Development of superconducting planar components for the focal plane units of CCAT-prime Heterodyne Array Instrument

Inaugural-Dissertation

zur Erlangung des Doktorgrades

der Mathematisch-Naturwissenschaftlichen Fakultät

der Universität zu Köln

Vorgelegt von

Ignacio Alberto Hugo Barrueto González

aus Los Ángeles

I. Physikalisches Institut
Universität zu Köln
2023

Gutachter:

Prof. Dr. Jürgen Stutzki

Prof. Dr. Lucas Labadie

Tag der Disputation: 26.02.2024

Abstract

This thesis focuses on the development of superconducting planar components for the CCAT Heterodyne Array instrument (CHAI). Planned to operate in two bands simultaneously, CHAI will feature two independent 64-pixel arrays covering $455 - 495$ GHz (Low Frequency Array) and $780 - 820$ GHz (High Frequency Array). The basic unit composing the arrays are 4-pixel waveguide blocks, fabricated in split block technology and designed to house four planar mixers fabricated on silicon substrates, which are suspended inside waveguide cavities. Each 4-pixel block also contains the local oscillator distribution network. The two topics of this thesis are the development of a power divider based on superconducting planar chip technology to perform the 1-to-4 power division for the LFA and the design of an integrated balanced mixer for the HFA. For the power division, a total of five different power dividers were designed in planar technology and fabricated in the I. Physikalisches Institut (Ph.I) microstructure fabrication laboratory. The individual components of the balanced mixers for the HFA have been designed and simulated, but could not be manufactured yet due to time constraints.

Due to the impossibility of Vector Network Analyzer(VNA) measurement to characterise the power dividers fabricated in this work, the SIS junctions found in the **I**ntegrated **BA**lanced **MI**xer (IBAMI), the mixer of choice for the LFA, are used as power detectors. The experimental setup is then composed of two IBAMI connected by waveguides to the power divider's outputs. This configuration has the advantage that it represents half of the 4-pixel block for CHAI, allowing for testing the components meant to populate the LFA in a simpler setup. This setup allows only for power division measurements with no possibility for direct measurement of the reflections at the waveguide ports of the power divider. Four units of the 2-pixel test block were fabricated in the mechanical workshop of the I. Physikalisches Institut. Three of the blocks have beamlead pockets to reduce the wear on the beamleads and the chips.

The fabricated power dividers were based on 90° hybrids and a Wilkinson

power divider. The experimental and simulated results showed how the transmission to the junctions in the IBAMI mixers is affected by the phase difference between the power divider outputs and the phase difference introduced by the coupler in the balanced mixer. Of the five power dividers fabricated only the Wilkinson power divider has the highest potential to achieve a balanced power division. Furthermore, it is concluded that the best choice of components for a heterodyne array is in-phase power dividers, such as the Wilkinson power divider, in combination with balanced mixers based on 180° couplers

Contents

List of Tables

List of Figures

Acronyms

CCAT Cerro Chajnantor Atacama Telescope

CHAI CCAT Heterodyne Array Instrument

CPW Coplanar Waveguide

FFT Fast Fourier Transform

FTS Fourier Transform Spectrometer

FYST Fred Young Submillimeter Telescope

HFA High Frequency Array

IBAMI Integrated Balanced Mixer

IF Intermediate Frequency

LFA Low Frequency Array

LO Local Oscillator

Nb Niobium

NbTiN Niobium Titanium Nitride

RF Radio Frequency

SiO_2 Silicon Dioxide

SIS Superconductor-Isolator-Superconductor

VDI Virginia Diodes

VNA Vector Network Analyzer

Chapter 1

Introduction

1.1 Brief history of astronomy of the interstellar medium

The study of the interstellar medium is a relatively young branch of astronomy ($\sim$ 19th Century). The first intentional discovery was only enabled by the development of spectroscopy when William Huggins, in 1864, observed the spectra of the Orion nebula and proved it was a cloud of gas [Huggins, 1864]. Later, in 1899, Edward Barnard discovered dark regions in pictures of the Milky Way and hypothesized that the background starlight was blocked by an interstellar cloud [Barnard, 1899]. Support for this came from the work of Johannes Hartmann in the study of the spectra of $\delta-$Orionis. In 1904 he noticed that the spectra of the system had a particularity, the calcium lines did not share the motion-induced shifts of the other spectral lines. This fact led to his realization that the calcium lines were not a feature of the star system but rather external; the Lines were caused when the radiation from $\delta-$Orionis passed through an external cloud of gas along the line of sight [Hartmann, 1904]. The next important contribution came in 1909 from the hand of the Dutch astrophysicist Jacobus Kapteyn, where he proposed the existence of gas in regions of space and it would produce "space lines" that did not share the motion characteristics of star lines [Kapteyn, 1909]. The same year Vesto Slipher would find evidence supporting Kapteyn's hypothesis when he discovered more calcium lines in the spectra of stars in Scorpion, Orion, and Perseus [Slipher, 1911]. Slipher contributions to the understanding of interstellar medium did not stop there, in 1912 he discovered the first reflection nebula in the Pleiades. He noticed that the nebula was shining only by reflecting the radiation from the star Merope; This discovery led him to conclude the existence of dust in the interstellar medium [Slipher, 1912].

Subsequent advancements in the study of the ISM came with the discovery

of quantum mechanics at the dawn of the 20th century. Two of the most important theoretical advancements were: the black body radiation law, developed in 1900 by German physicist Max Planck [Planck, 1901] and the new theory of Quantum mechanics, developed between 1920 and 1930. This new theory was able to explain the black body continuum emission from dust as well as the line emission from atoms and molecules.

Ira Bowen put this new theory to use when, in 1927, explained the hypothetical Nebulium lines as forbidden transition lines from [OIII] [Bowen, 1927]. A few years later, Karl Jansky detected the first extra-solar source of radio waves [Jansky, 1933] in 1932. This event marked the birth of Radio astronomy. Before this milestone, physicists thought that the Ionosphere would block any extraterrestrial radio waves, hence, no efforts were made to observe in these frequencies [Ghigo, 2023]. Even though Jansky's discovery marks the birth of radioastronomy as its own branch of astronomy, prominence to it would arrive after WWII. When Harold Ewen and Edward Purcell, in 1951, observed the 21 cm hydrogen line [Ewen and Purcell, 1951], [Hellwig et al., 1970], predicted in 1944 by Dutch astronomer Hendrik van de Hulst [van de Hulst, 1945]. This observation was of paramount importance as its observations shone light on the spiral structure of the Milky Way. Further development of the structure of the galaxy came in 1970 with the detection of molecular Hydrogen H_2 by George Carruthers [Carruthers, 1970], and more importantly, carbon monoxide CO by Arno Penzias and Robert Wilson [Wilson et al., 1970].

Molecular hydrogen lacks a permanent dipole moment, hence its direct observation must be based on the weak quadrupole spectrum (mid-infrared) and the high electronic transitions (UV). These transitions are too energetic to be significantly excited in the cold ISM, where the temperature is around 10 to 15K. Here is where CO states its importance. Even when its abundance in the interstellar medium is not as great as molecular hydrogen[Williams, 2003], CO rotational transitions are easily excited in the cold medium. For example, the lowest transition of $^{12}C^{16}O$ is at $f = 115.27120$ GHz and has an associated excitation temperature of 5.5 K. Around this time, it was when the first models of the ISM were conceived after years of observation of atomic and molecular species in the ISM. Astronomers George Field, Donald Goldsmith, and Harm Habing proposed the first model of the ISM in 1969 [Field et al., 1969] where radiative cooling is balanced by cosmic ray heating. This model had success in describing the physical conditions in neutral atomic phases both cold and warm. Eight years later a three-component model of the ISM was proposed by astronomers Christopher McKee and Jeremiah Os-

triker where the ISM is regulated by the Supernova explosion. In this model the ISM is classified by temperature with cold ISM, warm (including neutral and ionized), and hot ISM [McKee and Ostriker, 1977]. In 1985, after observations of massive star-forming regions in Orion and M17, astronomers Alexander Tielens and David Hollenbach proposed a model of Photo dissociation regions (PDR) [Tielens and Hollenbach, 1985]. This model attains mostly neutral gas in the ISM where far ultraviolet (FUV) photons play a significant role in the heating and chemistry of the region.

Even though astronomy is a very old discipline of human knowledge, most of the advances have been made in the last 200 years. Astronomers are limited by what they could observe. Progress was only possible with the help of new technological advances. Newer theories could only be corroborated by the observations and experiments made with the proper instrumentation. Nowadays Astronomers push the technical limits of telescopes and detectors, requiring improvements in speed, sensitivity, and frequency of operation. A prime example of this is the Atacama Large Millimetre/submillimetre Array (ALMA) [ALMA,] and the new generation of telescopes[Tyson, 2002, Güsten et al., 2006, Swetz et al., 2011, Johns, 2006]. ALMA with its 10 single pixel bands achieves sensitivities that are approaching the physical limit (detailed in section 1.3) in the millimetric and submillimetric range [ESO, 2022]. Not only single-pixel instruments are being pushed to the limit, but developments in multi-pixel array instruments demand an increase in the number of pixels. The I. Physikalisches Institut of the University of Cologne has been at the forefront of the development of heterodyne arrays, taking part in the development of heterodyne instruments. Examples of these are the mixers for Band 2 of the HIFI receiver [Pilbratt et al., 2010, de Graauw, Th. et al.,], The GREAT [Heyminck et al., 2012] and upGREAT[Risacher et al., 2016] receivers the Stratospheric Observatory for Infrared Astronomy (SOFIA), [Krabbe, 2000, Young et al., 2012, Risacher et al., 2017] and the SMART receiver the NANTEN2 telescope [Kawamura et al., 2005, Graf et al., 2002]. Now, the I. Physikalisches Institut is involved in the development of the CCAT-prime Heterodyne Array Instrument (CHAI), which with its dual-band operation with 64 pixels per array represents a significant step forward from the current state-of-the-art instruments.

1.2 Radiation and absorption of photons by matter

This section presents the main radiation mechanism of astronomical sources concerning this work and proceeds to give a brief explanation of it. An extensive explanation of all the other possible mechanisms of radiation by astronomical sources can be found in [Wilson et al., 2009] and [Rybicki and Lightman, 1985].

An absorber X (an atom or molecule) can transition between energy levels E_a and E_b ($E_a < E_b$) by the absorption or emission of a photon of energy $hf = \Delta E = E_b - E_a$. The probability per unit of time to undergo such transition is determined by the Einstein coefficients [Einstein, 1916], where these coefficients are an intrinsic property of the atom or molecule..

The absorption process involves the upward transition of X from energy level E_a to E_b by absorption of a photon of energy $hf = \Delta E$, whose probability is determined by the coefficient B_{ab}. This process is summarized as

$$X_a + hf \rightarrow X_b. \tag{1.1}$$

The emission of a photon happens when the particle X is in energy level E_b and transitions towards the lower energy level E_a, emitting a photon in the process. This decay can happen through spontaneous emission where

$$X_b \rightarrow X_a + hf\,, \tag{1.2}$$

where the probability of a spontaneous photon emission per unit of time is determined by the coefficient A_{ba}. A second process of decay is stimulated emission, where [Einstein, 1916] set the condition that photons of identical frequency, polarization, and direction of propagation must already be present,

$$X_b + hf \rightarrow X_a + 2hf\,, \tag{1.3}$$

whose probability per unit of time is determined by the B_{ba} coefficient. Both processes of absorption $X_a \rightarrow X_b$ (B_{ab}) and stimulated emission $X_b \rightarrow X_a$ (B_{ba}) transitions depend on the density of photons in the background. In contrast, the spontaneous emission (A_{ba}) is independent of the presence of a radiation field. In local thermodynamic equilibrium these coefficients are related by the following equations [Einstein, 1916]

$$B_{ba} = \frac{c^3}{8\pi h f^3} A_{ba}\,, \tag{1.4}$$

$$B_{ab} = \frac{g_a}{g_b} B_{ba} = \frac{g_a}{g_b} \frac{c^3}{8\pi h f^3} A_{ba}\,, \tag{1.5}$$

where g_a and g_b the statistical weights of the states.

Particular to the case of this thesis are the mid to low CO rotational lines and the low carbon ([CI]) atomic lines, since are the intended observational target of CHAI. [Simon et al., 2019] argues about the importance of observing these lines serve as tracers for dark and warm molecular gas. Their simultaneous observations in a multitude of environments are a missing piece in the understanding of the stellar feedback in the ISM. The set of spectral lines is

- CO $J = 4 - 3$ transition, f : 461.08 GHz.
- [C I] $^3\mathrm{P}_1 - ^3\mathrm{P}_0$ transition f : 492.16 GHz.
- CO $J = 7 - 6$ transition, f : 806.76 GHz.
- [C I] $^3\mathrm{P}_2 - ^3\mathrm{P}_1$ transition f : 809.34 GHz.

1.2.1 Black-body Radiation

The Planck spectrum describes the electromagnetic radiation emitted by a black body at temperature T. A black body is a theoretical body that absorbs all incident radiation, regardless of frequency or direction of incidence, and its spectral radiance is purely a function of its temperature. Eq. 1.6 shows the relationship between a black body's spectral radiance at a given frequency, $B(f, T)$, and its temperature T, where h is the Planck constant, c is the speed of light in the medium and k_B is the Boltzmann constant

$$B(f, T) = \frac{2hf^3}{c^2} \cdot \frac{1}{e^{\frac{hf}{k_B T}} - 1}. \tag{1.6}$$

The peak of the function can be found through the first derivative of the plank function. The resulting expression is known as Wien law (Eq. 1.7) and depicts how the maximum moves towards shorter wavelengths, with increasing body temperature (Fig. 1.1).

$$\lambda_{peak} = \frac{b}{T}, \tag{1.7}$$

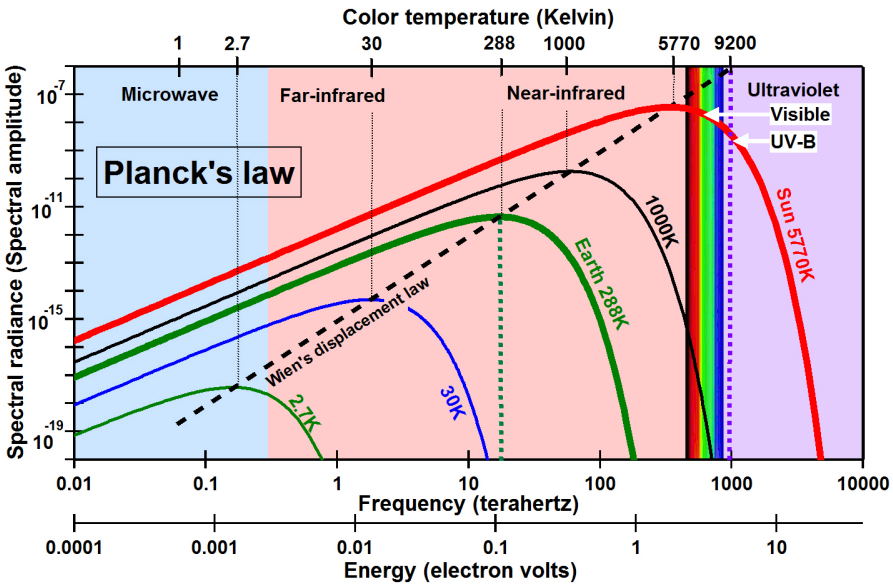

Figure 1.1: Black body spectral radiance for several temperatures [Ward,]. Here Wien's displacement law can be seen in the maxima of the spectra of bodies at different temperatures.

with λ_{peak} the wavelength of maximal radiance, T the body's temperature, and $b = 2.8977 \cdot 10^{-3} m \cdot K$ the Wien's displacement constant.

When it comes to the spectrum of a real body, it approaches the spectrum of a black body at the same temperature, this is because real bodies are not completely opaque and are not in thermodynamic equilibrium. One example of this is shown in Fig. 1.2 for the Sun's surface with the measured spectrum approximating the emission spectrum of a 5777 K black body.

1.3 Detectors for Radioastronomy and the need for arrays

The sensitivity of a receiver is one of its most important characteristics, it defines the weakest signal that can be distinguished from noise. It directly impacts the noise temperature (σ_{rms}) and the Signal-To-Noise ratio (SNR) of an observed signal. The SNR can be defined as

$$SNR = \frac{P_{signal}}{P_{noise}}, \tag{1.8}$$

where P_{signal} and P_{noise} are the power of the signal and noise, respectively. For astronomical sources in the $Rayleigh - Jeans$ limit ($hf \ll k_B T$), the intensity of an astronomical signal is directly proportional to the physical temperature of the body it radiates it ($P_{signal} \propto T_{src}$). On the other hand,

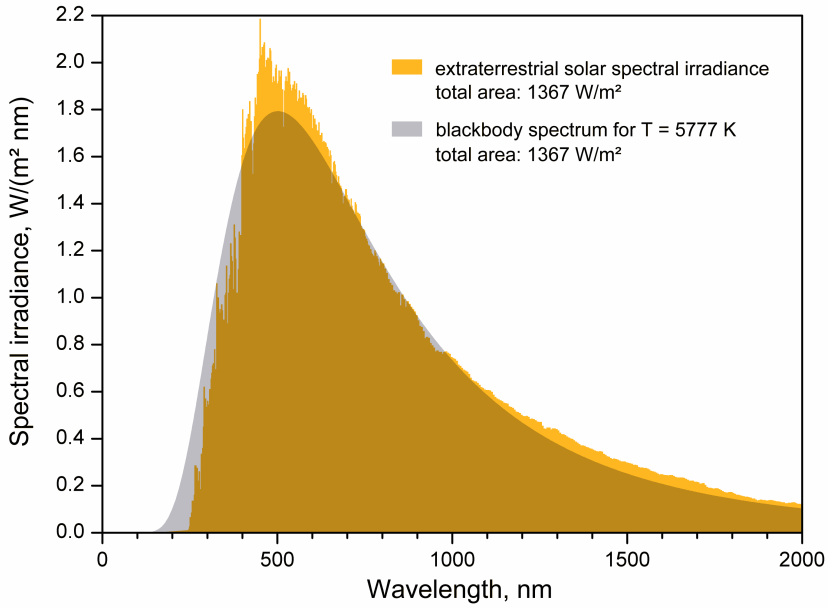

Figure 1.2: Solar spectrum [user Sch, , Iqbal, 2012]. The total power irradiated by the sun is equivalent to a $5777K$ black body. The irregularities in the solar spectra can be explained by the fact that the sun is not a homogeneous ideal black body.

the noise power can be expressed as [Dicke, 1946, Wilson et al., 2009]

$$\sigma_{rms} = \frac{T_{sys}}{\sqrt{\tau \Delta f}}, \tag{1.9}$$

with T_{sys} is the system temperature, τ is the integration time of the observation and Δf is the detector bandwidth. Hence, the SNR can be expressed as

$$SNR = \frac{T_{src}}{\sigma_{rms}} = \frac{T_{src}}{T_{sys}} \sqrt{\tau \Delta f}\,, \tag{1.10}$$

where T_{src} is the temperature of the source. Here T_{sys} represents the signal intensity that would produce an equivalent response in the receiver as the noise, it hence directly limits the sensitivity of the receiver, and it is the only other parameter, aside from the integration time τ, that can be modified to increase the SNR. The other parameters T_{src} and Δf are defined by the observation's source and scientific objective respectively. The T_{sys} is defined by the noise temperature of the receiver plus the contributions of the sky [Wilson et al., 2013]. eq 8.29

$$T_{sys} = T_r + T_{atm}\eta_1(1 - e^{-\tau_0 X(z)}) + T_{amb}(1 - \eta_1)\,, \tag{1.11}$$

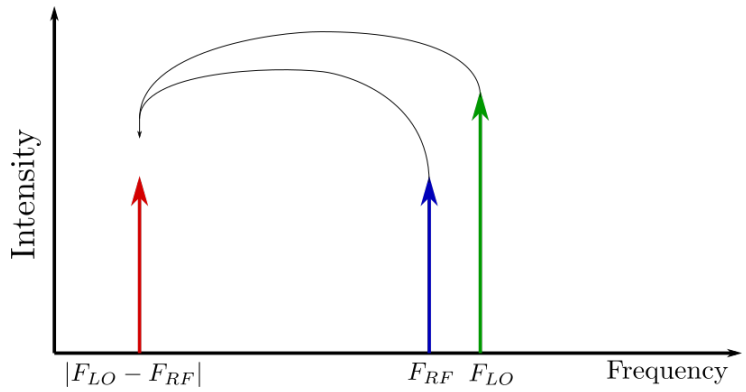

Figure 1.3: A basic example of the heterodyne principle: here the Radio frequency signal and Local oscillator are used to generate a new signal with frequency $|F_{LO} - F_{RF}|$

where, T_r is the receiver noise temperature, T_{atm} is the effective temperature of the atmosphere, T_{amb} is the ambient temperature, η_1 is the feed efficiency, τ_0 the zenith optical depth and $X(z)$ is the air mass at zenith distance z. This means that T_{sys} can be reduced by decreasing the noise temperature of the detector itself and reducing the effect of the atmosphere. The former parameter is addressed by optimizing and increasing the sensitivity of the detector itself, meanwhile, the latter is reduced by choosing an appropriate location for the observatory, in terms of opacity, this is explored later in the next section of this chapter.

The sensitivity limit of a detector depends on whether it performs coherent or incoherent detection. Coherent detectors measure both the amplitude and phase of the incoming radiation, meanwhile, incoherent detection only measures the amplitude. At lower frequencies up to the centimeter range ($\approx$ 30 [GHz]), coherent detection can be performed by an amplifier. At higher frequencies, coherent detection can only be carried out through the use of the *Hetedoryne* principle invented by *Reginald Fessenden* [Personnel, 1973] in 1904. This principle works by mixing the astronomical signal (RF) and a reference pump signal, called the Local Oscillator (LO), to generate a signal whose frequency is the difference between the frequencies of the RF and LO; This signal receives the name *Intermediate Frequency* (IF) signal (Fig. 1.3). The core element of this process is the *Mixer*, whose nonlinear characteristics enable the generation of the IF signal.

The sensitivity of coherent detectors is usually, measured in *Noise Temperature* (T_r), which is the equivalent temperature a resistor would require to produce thermal or *Johnshon-Nyquist* noise power equivalent to the one the detector is producing. This term comes from the fact that in the Rayleigh-jeans approximation, the available noise power spectral density from a resis-

tor at physical temperature T_p is

$$P_{noise} \approx k_B \cdot T_p, \tag{1.12}$$

thus, this leads to the definition of the noise temperature T_r

$$T_r = \frac{P_{noise}}{k_B}, \tag{1.13}$$

Where k_B is the Boltzmann constant, P_{noise} is the noise power per Hertz at the input of the detector. For a coherent detector, the minimum noise temperature is

$$T_r \geq \frac{\hbar \cdot \omega}{k_b}, \tag{1.14}$$

and it is a consequence of the Heisenberg uncertainty principle, due to measurement of both the amplitude and phase of the incoming radiation. On the other hand, incoherent detectors are not subject to this limit given that they only detect the power of the incoming radiation and their sensitivity is measured by the *Noise Equivalent Power* or NEP of the detector. NEP refers to the input signal power that would produce a response equivalent to the noise in the detector. It is usually quoted after detection averaging in a filter of 1 [Hz] bandwidth [Harris, 1990] and it has units of $[W/\sqrt{Hz}]$. The sensitivity limit of an incoherent detector is set by the fluctuations of the source, most sensitive incoherent detectors are called *background limited* when the noise of the source is larger than the noise of the detector.

An important consideration is that incoherent detectors need a filter to select the frequency of the incoming radiation to detect. The signal filtering must balance between frequency discrimination and available power for detection (SNR).

Comparison between the sensitivity of heterodyne and incoherent receivers can be done by converting the noise temperature of a heterodyne receiver to NEP using the equation 1.15

$$NEP = k_b \cdot T_r \cdot \sqrt{\Delta f} \tag{1.15}$$

For a conventional single sideband heterodyne receiver, the relation is ex-

pressed as

$$NEP = k_b \cdot 2T_r \cdot \sqrt{\Delta f_{IF}} \tag{1.16}$$

From a theoretical point of view, incoherent detectors have the sensitivity advantage over heterodyne receivers, since they do not have an intrinsic limit. In our case, this could reduce the system temperature and decrease the observing time. However, the implementation of the required frequency filters is not practical. For example, the upGREAT instrument achieved a frequency resolution $\geq 10^7$ in the $1.9 - 2.5$ THz range. To achieve the same spectral resolution with a grating spectrometer, it must be considered that its resolution is proportional to the number of slots/gratings with the distance between them being λ (for the first diffracted peak), resulting in a very large spectrometer (1200 m). The other possibility is using a Fabry-Perot interferometer to filter the incoming signal, which would be hard to implement due to the resolution required. Additionally, the narrower the filter, the more photons are rejected resulting in a loss of sensitivity, hence Fabry-Perot interferometers are used for very bright sources.

This means that, for single-pixel receivers, there are only a few possibilities to reduce the observing time for a desired SNR level. This is particularly onerous when considering the mapping of distributed sources since the switching and calibration times have to be added to the observing time. The only way to solve this is by increasing the number of pixels, this would reduce the mapping time of distributed sources bypassing the limitation set by the single-pixel sensitivity.

1.4 Atmospheric windows and locations for earthbound telescopes

As mentioned in the previous section, the atmosphere directly influences astronomical observations. Aside from atmospheric emission, which contributes to the noise, there is also atmospheric absorption. This absorption decreases the intensity of the source even completely absorbing it. The *Atmospheric windows* refer to the frequency ranges where the opacity of the atmosphere is the lowest: They are comprised of the visible range, the near-infrared and millimetre wave range, and the radio spectrum. Figs. 1.4 and 1.5 depict this phenomenon in two different ways. Fig.1.4 shows the height at which half of the radiation is absorbed across frequency. Meanwhile, Fig.1.5 shows the opacity across the wavelength of light.

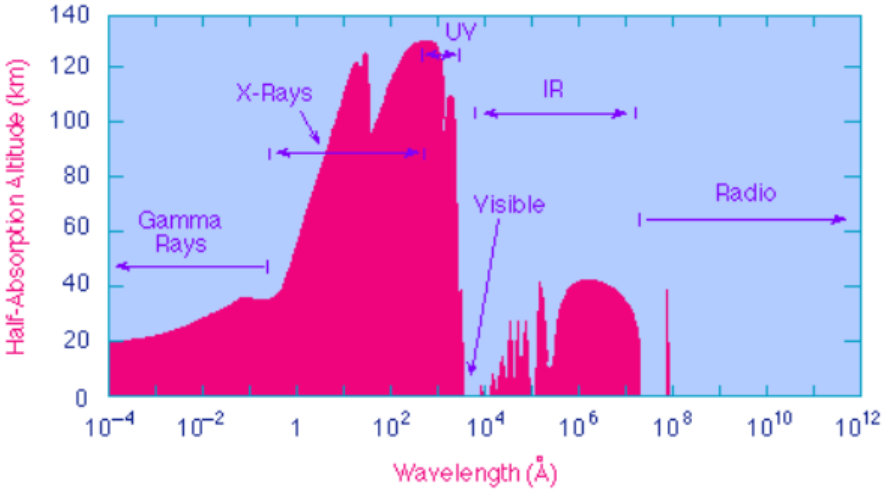

Figure 1.4: Half absorption altitude for the EM spectrum [Blackman,]. Most of the EM radiation is absorbed even before reaching the Troposphere, which contains about 75% of Earth's atmosphere [F.S., 1984]

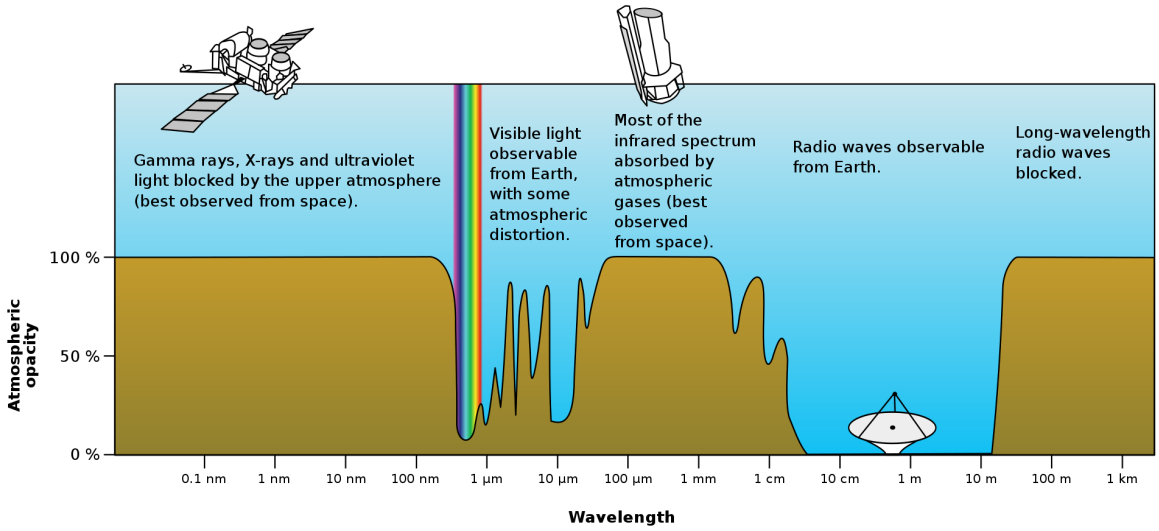

Figure 1.5: Atmospheric opacity [Nasa, 2008]. From this graph, the atmospheric window can be seen, only visible, radio and to some extent, microwave radiation can be observed from the earth's surface.

The only possible way to reduce atmospheric absorption is to locate the observatories in high and dry places. The latter requirement is particularly important for observatories that observe millimetre and submillimetre radiation as water vapor is the main absorption gas present in the atmosphere in those frequency ranges. The Chajnantor plateau in northern Chile is one of the best places for astronomy in the world. Its location in the high Andes mountains (over 5000 above sea level) and latitude (Atacama puna) results in a transparent atmosphere even in the millimetre and submillimetre range as shown in Fig. 1.6. These conditions attracted many observatories, among those are the Atacama Large Millimeter/submillimeter Array (ALMA), The Atacama Pathfinder Experiment (APEX) and the Atacama Cosmology Tele-

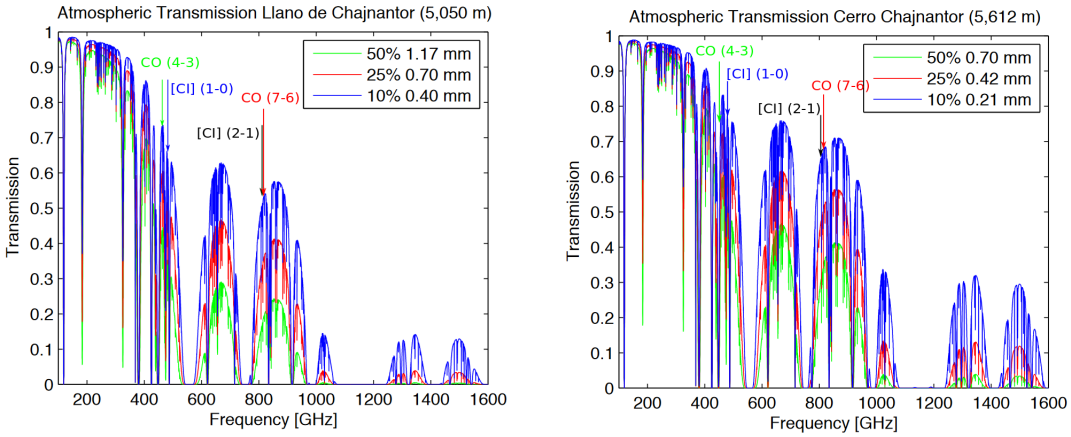

Figure 1.6: Atmospheric conditions on Chajnantor at different precipitable water vapour values at the llano Chajnantor (**Left**) and Cerro Chajnantor (**Right**) [Bustos et al., 2014, Pardo et al., 2001]. The molecular lines of interest for the GEVO science case are labelled. It can be seen how the peak altitude offers a better transmission characteristic than the plateau, especially for the higher frequency lines. This justifies the efforts to place an observatory at such altitudes.

scope (ACT). Even though the qualities at the plateau are excellent, there are still better places from an observational point of view. One example is the neighbouring Chajnantor peak (5,612 m.a.s.l) that exhibits an even better atmospheric transmission, shown in Fig.1.6. By the time of this writing, two telescopes are being built on this peak to take advantage of such good conditions; A 6.5 meter infrared telescope belonging to the Tokyo University Atacama Observatory (TAO) and the Fred Young telescope belonging to the Cerro Chajnantor Telescope Prime observatory (CCAT-prime).

Airborne and space telescopes are also a possibility, though their cost and lifetime become limiting factors. Prime examples of airborne observatories are SOFIA [Becklin, 2005] and KAO [Erickson, 2017]. Other types of airborne observatories are balloon-borne telescopes. They suffer from limited power and equipment due to weight considerations. Another potential problem with balloon-borne telescopes is data recovery as there may be problems with the landing procedure and the impact may damage the data storage units. In the case of Space telescopes, the required human and monetary resources are vast for a project with a limited lifetime.

1.5 CCAT observatory

The CCAT-prime consortium consists of Cornell University, the University of Cologne, the University of Bonn, Max-Planck-Institut für Astrophysik, and the Canadian Atacama Telescope Consortium (CATC) [Consortium,]. This consortium is responsible for the CCAT-prime observatory and its telescope is the Fred Young Telescope (FYST), named after Fred Young, whose generous

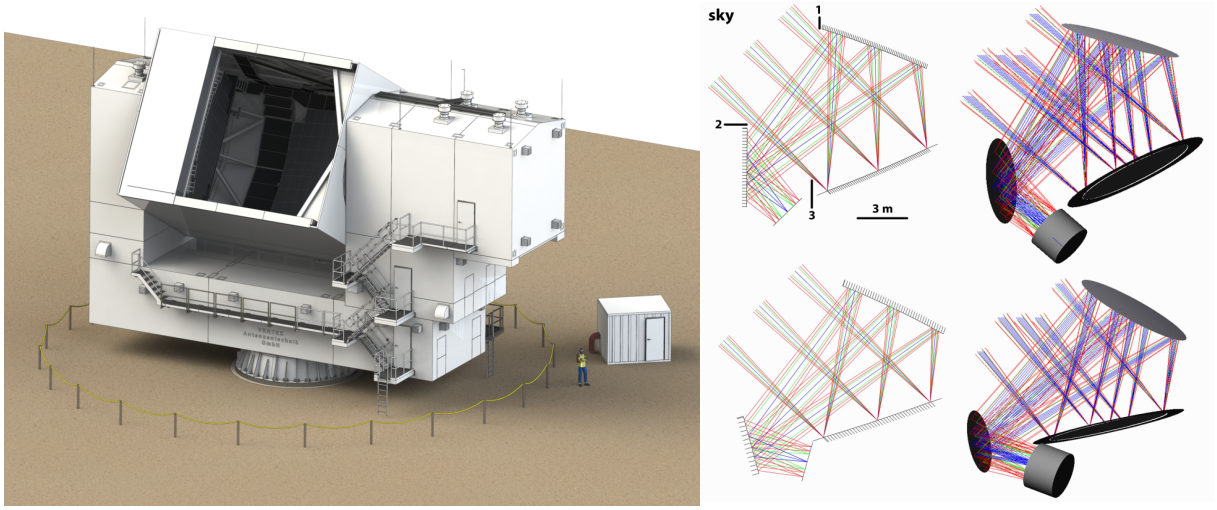

Figure 1.7: Left: 3D render of the Telescope *Credit: Vertex Antennentechnik GmbH.* **Right:**Crossed-Dagone off-axis optics[Niemack, 2016]

donations made the project possible. It features a six-meter off-axis crossed-Dagone design and a novel AZ-EL mount [Niemack, 2016, CCAT-prime, a] and a surface accuracy 10μm (7 μm goal) (Fig. 1.7) and it is designed as a surveying observatory.

The scientific goals of the observatory are [CCAT-prime, c]

- **Surveys of Kinetic Sunyaev-Zel'dovich effect** [CCAT-prime, b]. The Sunyaev-Zel-dovich effect is a cosmological phenomenon involving distortions of the CMB photons caused by interactions with the hot interstellar medium (Inverse Compton scattering).
- **Intensity Mapping of [CII] from the Epoch of Reionization** (IM/EOR) [Riechers,]. Intensity mapping is an observational technique to survey large-scale structures of the universe. Spectral line intensity mapping yields spatial information, allowing the study of the process of structure formation and the absorption/emission fluctuations can be used as a probe to study the dark matter density variations. This survey will address these objectives by observing [CII] fine line at 158 μm redshifts $z = 6 - 8$, whose brightness and the fact that is a tracer of star formation, allows direct mapping of the sources of reionization.
- **Galactic Ecology of the Dynamic Inter Stellar Medium** (GEco) [Simon et al., 2019] The study the process of star formation and how it is affected by its environs demands the analysis of the fine spectral lines of [CI] as well as medium/high excitations of CO. These species are agents of cooling in star formation clouds so they act as tracers of the process carried out in molecular clouds.

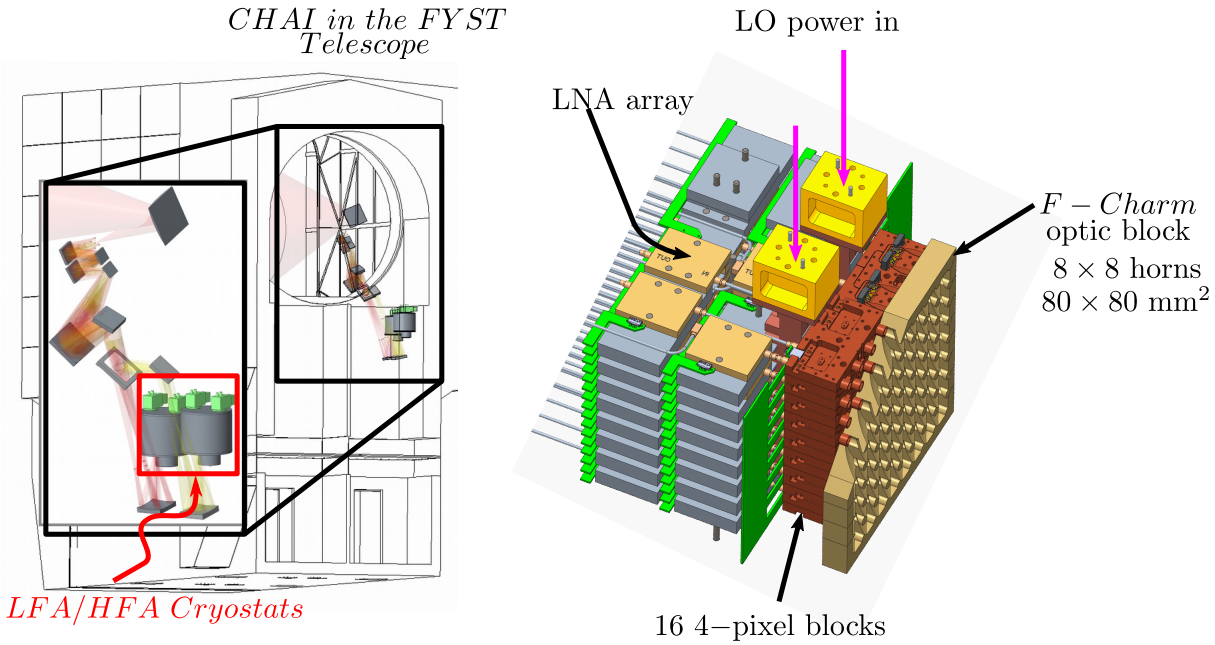

Figure 1.8: CCAT-prime heterodyne instrument (CHAI). **Left:** Position of CHAI inside of the FYST telescope. **Rigth:** CAD model of the LFA with the components labelled.

The University of Cologne is currently developing the instrument to address the **GEco** science case. This instrument is the CCAT-prime Heterodyne Array, and it is detailed in the next section. The University of Cologne will also develop an MKID camera to address the **IM/EOR** science case led by Prof. Dominik Riechers.

1.6 CCAT Heterodyne Array Instrument (CHAI)

The CCAT-prime Heterodyne Array Instrument (CHAI) is a modular, dual-frequency band array receiver conceived to operate in simultaneous observation with its two bands, each with 64 pixels. The bands are named as the Low-Frequency Array (LFA) intended to observe the CO $J = 4 - 3$ and [CI] $^3P_1$-$^3P_0$ transitions meanwhile the High-frequency Array (HFA) will observe the CO $J = 7 - 6$ and [CI] $^3P_2$-$^3P_1$ transitions. The specifications set for these arrays are listed in table 1.1

Both the LFA and HFA consist of 64 pixels in a square array. This array is assembled from 16 4-pixel blocks, arranged in 2 stacks of 8 blocks each. Since these are heterodyne receives, each mixer requires a local oscillator signal to perform the frequency down-converting. The natural approach would be to have a dedicated LO source for each mixer. This method is the most expensive and blunt solution; it comes with the difficulties of locking all LOs to the same reference and the possible interference between them. Hence, this alternative is discarded. This prompts the development of a LO distri-

Table 1.1: Requirements for the LFA and HFA band of CHAI

Sepecification	LFA	HFA
Frequency range [GHz]	$455 - 495$	$780 - 820$
Noise Temperature T_{DSB} [K]	< 100	< 200
IF band [GHz]	$4 - 8$	$4 - 8$
Resolution [kHz]/[km/s]	100/0.06	100/0.04
Velocity coverage [km/s]	2500	1500
Beam size ["]	26	15
Field of view ['x']	7.5×7.5	4.5×4.5

bution network that would allow for the optimum mixer operation. Before detailing the chosen LO distribution scheme for the LFA, a brief review of contemporary array receivers is given to see the approach taken to solve the LO distribution conundrum.

1.6.1 Modern Heterodyne receiver arrays

The first heterodyne array arose in 1988, it was an 8 Schottky diode array, developed by NRAO at Kitty Peak, Arizona [Payne, 1988]. It took a decade after the second array was developed.

BEARS (25-BEam Array Receiver System) was developed by NAOJ for operation on the $82 - 116$ GHz band in the year 2000. Bears featured SIS mixers in a DSB configuration [Sunada et al., 2000].

PoleStar is a receiver developed by the University of Arizona. It was a 2x2 SIS array, designed to operate at 810 GHz [Walker et al., 2001]. The LO distribution and coupling with the RF signal are done by quasi-optical means.

HERA is a 9 SIS pixel array for observations between $215 - 270$ GHz developed by IRAM. It was arranged in a 3×3 array where the LO division was achieved by a waveguide power splitter [Schuster et al., 2004].

SMART is a dual-band SIS receiver developed at KOSMA. It features a 2×4 array operating in the $460 - 490$ and $800 - 880$ GHz bands. In this receiver, the LO distribution and LO-RF coupling were achieved by quasi-optical means.[Graf et al., 2002]

CHAMP receiver [Güsten et al., 1998], originally a 4×4 pixel array was upgraded to CHAMP$^+$ in 2007[Kasemann et al., 2006]. **CHAMP$^+$** featured two 7 pixel arrays at the 450 and 350 μm bands, where the LO 67distribution was achieved by collimating phase gratings[Graf and Heyminck, 2001].

DesertStar is a 7-pixel detector developed by the University of Arizona. The 7 pixels are SIS mixers in a hexagonal array, where the LO multiplexing is done through quasioptical means using a reflective phase grating. [Groppi et al., 2003].

HARP is a receiver developed by the University of Cambridge in collaboration with other European and North American institutes. It has a 4×4 SIS mixer array where the LO is coupled through quasi-optical means. The LO is injected in a LO meander structure with a load at the end.[Buckle et al., 2009].

SuperCam is an 8×8 SIS heterodyne receiver developed by the University of Arizona. This array was conceived for observations in the 870 μm window. The LO coupling to the mixers is done by quasioptical means using the same scheme of using the LO meander structure as the **HARP** receiver [Groppi et al., 2009].

IRAM developed heterodyne arrays for the **2** and **3** mm bands. The 2mm receiver is a 1×4 pixel receiver and the 3mm band is a 5×5 array. For both these arrays, the LO coupling was achieved by waveguide 90° coupler [Fontana et al., 2010, Fontana et al., 2012].

Argus is a 4×4 pixel array developed for observations in the $85 - 116$ GHz band. It features Schottky diode mixers and the LO distribution was performed by a combination of multi-layer printed circuit boards and coaxial technology [Sieth et al., 2014].

upGREAT, the upgrade to the receiver **Great**, designed to operate at the Stratospheric Observatory for Infrared Astronomy (Sofia). It was designed for operation at 1.9 and 4.7 THz, with 2×7 and 7 pixels arrays, respectively. The LO distribution was based on beam splitters [Risacher et al., 2017].

NAOJ proposed in 2020 a 2×2 SIS array to be operated in the $130 - 160$ GHz frequency range. This array features a double polarization receiver based on SIS mixers and has a waveguide LO distribution network based on 90° couplers [Shan et al., 2020].

GUSTO is a dual band instrument designed to observe the 1.47 and 1.9 THz bands. each band consist of a 2×4 rectangular array. The LO division is achieved by the use of a phase grating [Mirzaei et al., 2021].

1.6.2 LO distribution for the LFA

The most common strategy used for distribution and coupling the LO power to the array of mixers are quasi-optical methods, like by phase gratings, or

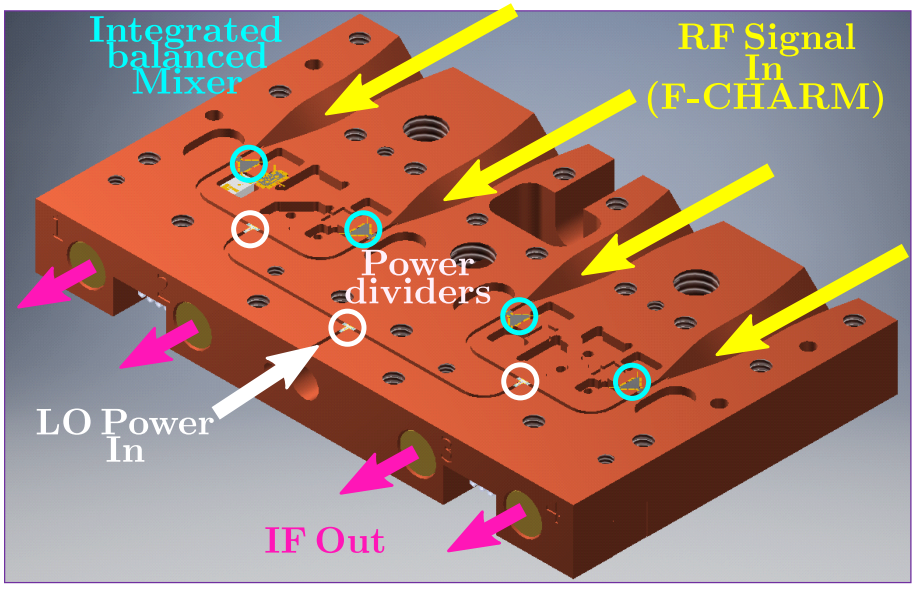

Figure 1.9: 4-pixel block and the main components therein. The LO power is received from the back of the block, and it is subsequently divided by three power dividers in a cascade configuration and delivered to the mixers. The mixers down-convert the RF signal received from the F-CHARM optic block and deliver the IF signal from the back of the blocks. The signal is subsequently amplified by the LNA array behind the mixer blocks.

a Martin-Pupplet diplexer [Walker et al., 2001, Graf et al., 2002] [Groppi et al., 2003, Buckle et al., 2009],[Graf and Heyminck, 2001] [Groppi et al., 2009, Risacher et al., 2017]. Fewer arrays have the LO division performed in waveguide technology with the number of pixels being under 10 pixels and the frequency range not surpassing 300 GHz [Schuster et al., 2004], [Fontana et al., 2010, Fontana et al., 2012] [Shan et al., 2020]. CHAI intends to develop the entire LO distribution network in waveguides to come to a compact array of 64 pixels. The high frequency means that the dimensions of the waveguide components are under 1mm. This means that the feasibility of construction is now an important consideration for the success of the fabricated component. This consideration is even more critical with the HFA components.

The CHAI developments start with the Low-Frequency Array (Table 1.1) because the lower frequency band eases the fabrication of components. Integrated balanced SIS waveguide mixers([Westig, 2013]) have already been developed in our group. The LFA array comprises 16 blocks stacked in two columns of 8 blocks each. This individual block constitutes the basic element of the array and 1×4 pixels (Fig.1.9). For the LO power division, the requirements are set by the most basic block, in this case, the 4-pixel block the set that 1 to 4 power division must be achieved.

1.7 Frame and scope of this thesis

This thesis finds itself embedded in the efforts of the I. Physics Institute of the University of Cologne of developing the CHAI receiver. During this thesis, the overall efforts were concentrated on delivering the LFA for the FYST telescope's first light.

In this frame, the scope of this work is twofold. First, is the design and test of a power divider to be used to achieve the 1-4 power division necessary for the 4-pixel block. The second objective concerns the preparations for the development of the HFA. It consists of the design of all components required for the 4-pixel blocks of the HFA array, that being the integrated balanced mixer and the LO power dividers.

This thesis consists of 6 chapters, including the present one. The layout of the thesis is as follows.

- Chapter 2 lays the theoretical background required to understand the working principles used in the design and test of the power dividers and design of the mixer for the HFA.
- Chapter 3 presents the design process of the components required for the LFA power divider and the HFA mixer.
- Chapter 4 presents the experimental methods and equipment used to characterize the LFA mixers and power dividers.
- Chapter 5 shows the measured results and their interpretation.
- Chapter 6 presents the conclusions of this work and lays the ideas on how to expand the work here presented.

Chapter 2

Background and theory

This chapter presents the theoretical background required to understand the choices taken in the design of the superconducting devices. This chapter can be divided into two main parts: The superconductivity part and the microwave part. The first part starts with a brief historical review of superconductivity, its discovery and the first attempts at a phenomenological description by the London brothers. It follows the non-local generalization made by A. Pippard and the Barden-Cooper-Schrieffer (BCS) microscopic theory of superconductivity. It continues with the application of the BCS theory for the calculation of the superconducting thin film properties in the microwave regime and a brief description of Superconductor-Isolator-Superconductor (SIS) tunnel junctions. The second part starts with the Maxwell equations and their application to transmission line theory. Then it introduces the S and Z- -network parameters and basic mixers architecture. The chapter ends with a description of the performance parameters of a heterodyne receiver.

2.1 Superconductivity

Superconductivity is an important topic for the work developed in this thesis as its properties allow for the operation of all devices contained in this work. The fabrication and optimization of the superconducting materials are handled by the personnel that fabricate the devices in the micro-structure laboratory of the institute. The superconducting materials of choice are Niobium (Nb) and Niobium Titanium Nitrate (NbTiN) due their gap frequencies (more details in sec.2.1.3). The framework provided by the BCS theory is required for the calculation of the surface impedance of thin Nb and NbTiN films in the 400 and 800 GHz ranges. The description of the theory of superconductors is mainly based on [Tinkham, 2004] and [Annett, 2004]. Additionally, a thorough and comprehensive review of the literature surrounding

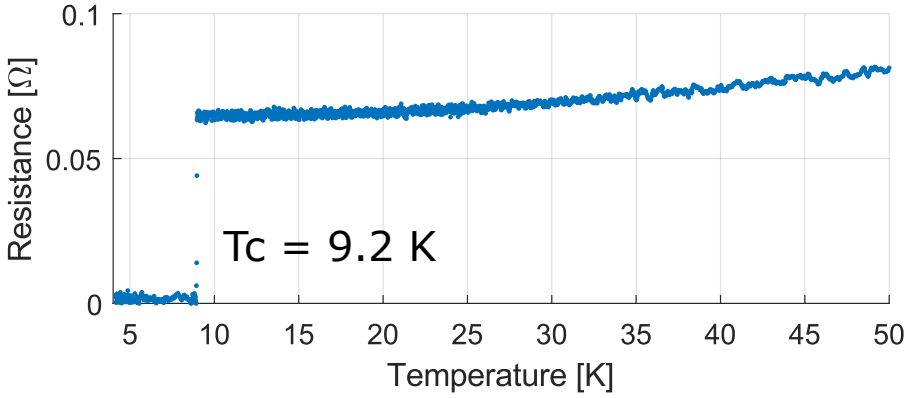

Figure 2.1: Measured resistance as a function of temperature for amorphous Niobium on Silicon. It can be seen how at temperatures well above the critical temperature of 9.2 K the Nb follows the normal metal resistivity function, which is governed by the phonon scattering of electrons. At the critical temperature, the resistivity sharply decreases to $m\Omega$. The Nb film is fabricated in the micro-structure of the I. Physical Institute of the University of Cologne.

superconductivity can be found in [Westig, 2013].

2.1.1 Discovery and phenomenological hallmarks

The phenomenon of superconductivity was discovered by the Dutch *Heike Kamerlingh Onnes*, the first to liquefy Helium. He studied the resistance of solid mercury at cryogenic temperatures and noticed that at the point at which the mercury had reached 4.19 K, the resistance vanished abruptly [Kamerlingh Onnes, 1911]. What happened there is that mercury experienced a phase transition to the superconductor state when it reached its critical temperature T_c of 4.2 K. This discovery earned Kamerlingh Onnes the Nobel prize in 1913 and started the study of superconductivity.

The zero resistance is the first hallmark of a superconductor. The second one is the expulsion of the magnetic field from a superconductor the moment the phase transition to the superconducting state occurs. It was discovered by the German scientists *Walther Meißner* and *Robert Ochsenfeld* in 1933 [Meissner and Ochsenfeld, 1933].

2.1.2 The London equations and the two-fluid model

The London equations are the first attempt to describe the demeanour of electromagnetic fields in the superconductor and their relation to the superconducting currents [London et al., 1935]. They are based on the classical Drude model of conductivity [Drude, 1900a], [Drude, 1900b] assuming the existence of superconducting electrons with an infinite free path in the material. The classical Drude model proposes that the motion of electrons is influenced by the Lorentz force and the collisions with the atom cores.

The collisions between the electrons and atom cores provide a term that is responsible for the resistance observed in a material. These collisions are summarized as a scattering term with a finite relaxation time or mean time between collisions.

$$m_e\ddot{\mathbf{r}} = -q_e\mathbf{E} - \frac{m_e\dot{\mathbf{r}}}{\tau} \tag{2.1}$$

For the superconductor case, it is assumed that there exist a population of electrons that does not collide with the atoms cores, hence their mean time between collisions (τ) is infinite. This leads to an acceleration of the charge $\ddot{\mathbf{r}} = e\mathbf{E}/m_e$. By taking the time derivative, using the current density $\mathbf{J}_s = n_s e\dot{\mathbf{r}}$, and replacing $\ddot{\mathbf{r}}$ from Eq.2.1 we obtain

$$\partial_t \mathbf{J}_s = \frac{n_s e^2}{m_e}\mathbf{E}, \tag{2.2}$$

which is known as the first London equation. Here n_s is the number of *superconducting electrons*, e the electron charge and m_e the electron mass. The second London equation is obtained by taking the curl of Eq. 2.2 and using Faraday's law

$$\nabla \times \mathbf{J}_s = -\frac{n_s e^2}{m_e}\mathbf{B} \tag{2.3}$$

The London equations describe the Meissner effect, showing how the magnetic field is screened from the inside of the superconductor. To obtain the behaviour of the magnetic field in the superconductor, $\mathbf{J}_s$ is obtained from the modified Ampere law and replaced in 2.3, leading to

$$\nabla^2\mathbf{B} = \frac{\mu_0 n_s e^2}{m_e}\mathbf{B} + \nabla \times (\mu_0\varepsilon_0\partial_t\mathbf{E}). \tag{2.4}$$

where μ_0 is the vacuum permeability. Remembering that $\varepsilon_0\mu_0 = 1/c^2$ and assuming that the field varies slowly, the second term can be neglected leading to

$$\nabla^2\mathbf{B} = \frac{\mu_0 n_s e^2}{m_e}\mathbf{B} = \frac{1}{\lambda_L^2}\mathbf{B} \tag{2.5}$$

$$\lambda_L = \sqrt{\frac{m}{\mu_0 n_s e^2}} \tag{2.6}$$

where λ_L is the *London penetration depth*. Equation 2.5 is know as the *Helmholtz equation for the magnetic field*, its solutions are of the kind $\mathbf{B} = B_0\, e^{-r/\lambda_L}\hat{r}$, with $\mathbf{r}$ being the direction of propagation. This implies that the magnetic field is exponentially attenuated inside the superconductor, explaining the observed Meissner effect detailed before.

The London eq.2.2 and 2.3 can be summarized in one equation by the use of a vector potential $\mathbf{A}$

$$\mathbf{J} = -\frac{\mathbf{A}}{\mu_0 \lambda_L^2} \tag{2.7}$$

A is defined as a vector potential $\mathbf{B} = \nabla \times \mathbf{A}$ that must fulfill the **London gauge** $\nabla \cdot \mathbf{A} = 0$.

The only unknown variable in eq. 2.6 for a prediction of the penetration depth is the number of superconducting electrons n_s. [Tinkham, 2004] argues that even if the quantity n_s is not initially defined, one can assume the natural limit of n_s is the total electron population density n. This yields the theoretical limit for λ_s when $T \to 0\text{K}$

$$\lambda_L(0) = \sqrt{\frac{mc^2}{\mu_0 n e^2}} \tag{2.8}$$

For $0 < T < T_c$ the dependence of $\lambda_s(T)$ can be approximated by [Tinkham, 2004]

$$\lambda_L(T) \approx \frac{\lambda_L(0)}{\sqrt{1 - \left(\frac{T}{T_c}\right)^4}} \tag{2.9}$$

The London equations provide a good phenomenological approximation for the superconducting state in the bulk regime and an operation point below its critical parameters, that is a temperature $T \ll T_c$ and in the presence of an EM field of moderately high frequency. The determination of the critical parameters of the superconductor was only possible after the introduction

of the Baarden-Cooper-Schrieffer(BCS) theory, briefly summarized in the following section.

2.1.3 The Bardeen–Cooper–Schrieffer (BCS) microscopic theory of superconductivity

The Bardeen–Cooper–Schrieffer (BCS) [Bardeen et al., 1957] theory of superconducting presents a microscopic explanation for the superconducting state. In the BCS theory, superconductivity is a consequence of the pairing of electrons through phonon interaction in the material. This phonon interaction allows for an attractive potential, making the Cooper pair binding possible. Aside from this interaction, the electrons do not have any further interaction with the atomic lattice. This theory describes the two hallmarks of superconductivity, those being the Meissner-Ochsenfeld effect and the almost null resistivity of conventional superconductors.

The underlying principle in the BCS theory is the existence of a bound electron pair, called *Cooper pairs*, due to an attractive interaction between them in the material ($V(\mathbf{k}-\mathbf{k}') < 0$). When considering a normal Coulomb interaction between free electrons ($U(\mathbf{r}) = e^2/r$), it always leads to a repulsive interaction [Tinkham, 2004].

$$V(\mathbf{k}-\mathbf{k}') = V_{\mathbf{k}\mathbf{k}'} = \Omega^{-1} \int U(\mathbf{r})\, e^{j(\mathbf{k}-\mathbf{k}')\cdot\mathbf{r}} d\mathbf{r} = \frac{4\pi e^2}{(|\mathbf{k}-\mathbf{k}'|)^2} > 0 \qquad (2.10)$$

Where $V_{\mathbf{k}\mathbf{k}'}$ is the interaction potential, $\mathbf{r}$ the distance between the electrons interacting,Ω, the normalization volume and $\mathbf{k}-\mathbf{k}'$ is the difference in wavevector of the electronic levels. However, by considering the screened Coulomb interaction between electrons and the screened Coulomb interaction between electrons and atom cores, an additional potential appears [Fröhlich, 1950],[Bardeen and Pines, 1955]([Tinkham, 2004] eq. 3.10)

$$V_{\mathbf{k}\mathbf{k}'}(\omega) = \underbrace{\frac{4\pi e^2}{q^2+k_s^2}}_{\text{Couloumb Interaction}} + \underbrace{\frac{4\pi e^2}{q^2+k_s^2}\frac{\omega_{\mathbf{q}}^2}{\omega^2-\omega_{\mathbf{q}}^2}}_{\text{phonon-mediated interaction}} \qquad (2.11)$$

Where k_s is the Thomas-Fermi wavevector [Ashcroft and Mermin, 1976], ω the frequency corresponding to the difference in energy levels $\hbar\omega = E_{\mathbf{k}} - E_{\mathbf{k}'}$, $\omega_{\mathbf{q}}$ the angular frequency of a phonon of wavevector **q=k-k'**. The potential has an attractive effect, meaning $V_{\mathbf{k}\mathbf{k}'}(\omega) < 0$, so long as $\omega < \omega_{\mathbf{q}}$, this

sets the cuttoff energy $\hbar\omega_c$, that is of the order of the Debye energy $\hbar\omega_D$ ($\hbar\omega_D = k_B\Theta_D$ where Θ_D is the *Debye temperature*, at which all phonon modes are excited). Qualitatively, this can be understood as that for an electron pair with $E_{\mathbf{k}} - E_{\mathbf{k}'} > \omega_D$ there is no phonon able to carry the momentum, and thus, no Cooper pair can be formed. It is worth mentioning that, meanwhile eq. 2.11 illustrates how the required attractive interaction between electrons may rise, it is too coarse to be used as a criterion for superconductivity [Tinkham, 2004].

Leon Cooper postulated that the background Fermi Sea was unstable against the formation of Cooper pairs [Cooper, 1956]. The pairs condense with a binding energy Δ until a new equilibrium point is reached where the binding energy for an additional pair is zero, reaching *the superconducting state.* The excitations above the the superconducting state are know as *Bogoliubov quasiparticles* with energy $E_{\mathbf{k}} = \sqrt{\xi_{\mathbf{k}}^2 + \Delta_{\mathbf{k}}^2}$ [Tinkham, 2004], p 61. Where and $\xi_k = \varepsilon_{\mathbf{k}} - \mu$ the single particle energy relative to the Fermi energy (ε the unperturbed Bloch energies, and μ is the Fermi energy). It becomes clear that $\Delta_{\mathbf{k}}$ is the minimum excitation energy, as the single particle energy of quasi-particles at the Fermi surface is $\xi_{\mathbf{k}} = 0 \implies E_{\mathbf{k}} = \Delta_{\mathbf{k}}$. Hence $2\Delta_{\mathbf{k}}$ is the minimum energy required to break a Cooper pair and create two quasiparticle excitations, each with energy $\Delta_{\mathbf{k}}$.

The determination of the gap energy $\Delta_{\mathbf{k}}$ is given by the BCS Gap equation or the condition for self-consistency, and it is simplified by the assumption of L. Cooper that $V = -\mathcal{V}$ ($\mathcal{V}$ a positive constant) for any state that was up to $\hbar\omega_D$ from the Fermi energy E_F[Cooper, 1956], [Bardeen et al., 1957]. This approximation leads to

$$\Delta_{\mathbf{k}} = \begin{cases} \Delta & \xi_{\mathbf{k}} < \hbar\omega_D \\ 0 & \xi_{\mathbf{k}} > \hbar\omega_D \end{cases} \tag{2.12}$$

Following the analysis done by [de Gennes, 1966]. p 112, leads to the equation for the gap energy at $T = 0$K

$$\Delta(0) = N(0)\mathcal{V}\int_{-\hbar\omega_D}^{\hbar\omega_D} \frac{\Delta(0)}{2}\frac{1}{\sqrt{\xi^2 + \Delta(0)^2}}d\xi \tag{2.13}$$

$$\Delta(0) = \frac{\hbar\omega_D}{sinh\left(\frac{1}{N(0)\mathcal{V}}\right)}\,.$$

Where $N(0)$ is the density of single spin density of states at $T = 0$K. For weak coupling superconductors, where $\hbar\omega_D \gg k_B T_c$, $N(0)\mathcal{V} \ll 1$ the gap energy can be approximated by

$$\Delta(0) \approx 1.764 \cdot k_B T_c \,. \tag{2.14}$$

For the case of Niobium, which is a strong coupling superconductor, the relationship in eq. 2.14 is modified to [Zheng and Walmsley, 2008]

$$\Delta(0) \approx 1.895 \cdot k_B T_c \,. \tag{2.15}$$

The gap energy is of vital importance in the calculation of the complex conductivity of superconductors in the microwave regime, detailed in the next section, since it gives the frequency at which the radiation has enough energy to break Cooper pairs and create quasiparticle excitations (Eq.2.16). The temperature dependence of the gap energy for weak coupling superconductors for $T \sim T_c$ is given by [Tinkham, 2004], Eq. 3.54 (Fig. 2.2)

$$f_{gap} = \frac{2\Delta(T)}{h} \tag{2.16}$$

$$\frac{\Delta(T)}{\Delta(0)} \approx 1.74\sqrt{1 - \frac{T}{T_c}} \tag{2.17}$$

2.1.4 Superconductor properties at microwave frequencies

The impedance of a medium is defined as the ratio between the electric field **E** and the magnetic field **H** of the EM wave that propagates through it. In the case of superconductors the fields are screened from their inside and EM waves can only propagate alongside their surface and in the medium around them. Hence it is useful to characterize the impedance for the fields at the surface of the superconductor as it is one of the key parameters in the design of the superconducting circuits. The general definition of surface impedance is

$$Z_s(\omega) = \frac{E_x(0,\omega)}{H_y(0,\omega)} = \frac{E_x(0,\omega)}{\int_0^\infty J_x(z,\omega)dz} \,. \tag{2.18}$$

The precise relationship between the current density **J** and the field in a superconductor depends on the characteristic lengths, λ_L, ξ, with the

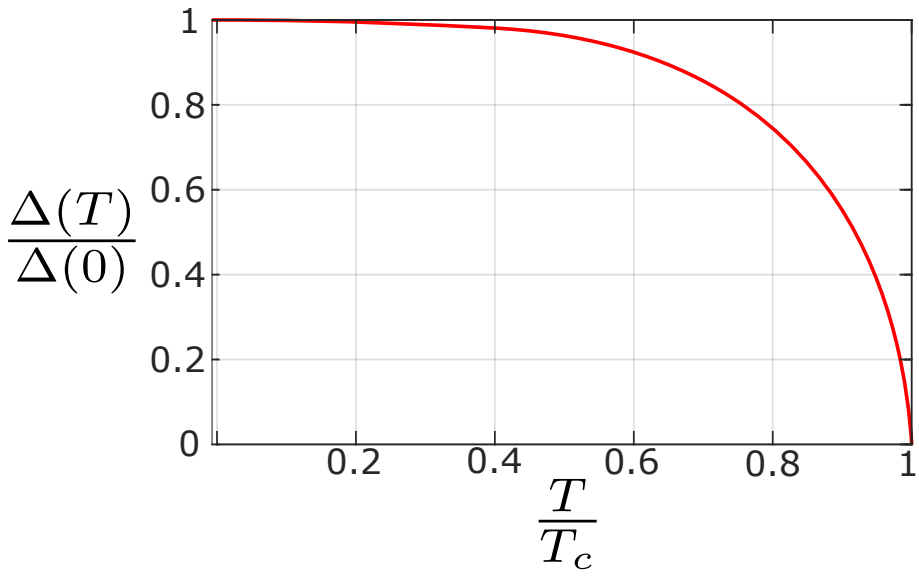

Figure 2.2: Temperature dependence of the Gap energy. The magnitude of the gap varies little from $\Delta(0)$ when $T \ll T_c$. The approximation $\Delta(T) \approx \Delta(0)$ hold up to $T/T_c \approx 0.6$. This also shows the reason behind the use of liquid Helium for cooling our devices, as the temperature achieved is lower than half the critical temperature of the Nb (Fig. 2.1)

former being the London penetration depth defined in eq.2.9 and the latter the coherence length of the superconductor, introduced by A. Pippard [Pippard and Bragg, 1953]. In Pippard's theory and BCS theory, the coherence length is related to the size of the Cooper pairs. Hence its role is comparable to the mean free path in normal conductors in the determination of the exact regime, either local or non-local, the metal should be modeled.

The *local regime* is defined when $\xi \ll \lambda_s$ which justifies the assumption that the fields are constant across ξ and the relationship for the current density and the vector potential, described in eq. 2.7), holds. The surface impedance for the local regime can be calculated by [Collin, 2007], Eq 2.105

$$Z_s(\omega) = \frac{E_x(0,\omega)}{\int_0^\infty J_x(z,\omega)dz} = \sqrt{\frac{j\omega\mu_0}{\sigma_1 - j\sigma_2}}, \tag{2.19}$$

with the conductivities σ_1 and σ_2 obtained from the two-fluid model, or the Mattis-Bardeen theory at frequencies closer to the gap frequency of the superconductor (Eq.2.16).

For the case $\xi \approx \lambda_L$ eq. 2.7 breaks down and equation 2.19 for the surface impedance is no longer valid. This is the *anomalous regime* and the current has to be obtained from the Mattis-Barden relationship (Eq. 2.26). For the case where $\xi \gg \lambda_L$, the superconductor is in the *extreme anomalous limit*

and the conductivity has to be obtained with the Mattis-Bardeen theory of the extreme anomalous skin effect (eqs. 2.28 and 2.29 of the following section). A brief analysis of the three regimes is presented in the following section.

The two fluid model of complex conductivity

The phenomenological theory of superconductors formulated by the London brothers did not only account for the screening of the magnetic field but it also provided an approximation for the bulk conductivity of the superconductors. When operating $T \ll T_c$, the conductivity can be approximated by a *Two fluid model*, initially proposed by [Gorter and Casimir, 1934]. In this model, two electron populations coexist, A superconducting n_s and a normal conducting population n_n, $n = n_s + n_n$. These two populations of electrons are responsible, respectively, for the imaginary part of the conductivity and the small dissipation observed at all frequencies. The conductivity σ_i can be approximated by

$$\sigma(\omega) = \sigma_1 - j\sigma_2 = \sigma_n(\omega) + \sigma_s(\omega) \tag{2.20}$$

$$\sigma_n(\omega) = \frac{n_n e^2 \tau_n}{m} \tag{2.21}$$

$$\sigma_s(\omega) = \frac{\pi n_s e^2}{m}\delta(\omega) - j\frac{n_s e^2}{m\omega} \tag{2.22}$$

With $\delta(\omega)$ the Dirac's Delta function at $\omega = 0$. This is meant to account for the DC demeanour of the superconducting electrons [Linden et al., 1994]. The limitation of this approximation is that only it describes the linear response of the superconductor. At temperatures $T \approx T_c$ or in very thin superconducting films ($d \ll \lambda_L$) the response of the superconductor cannot be approximated by this model.

Pippard non local extension of the London equations

The London equations provided a first approximation for the demeanour of superconductors and it was useful in predicting the bulk properties of the superconductor. However, the London equations limitations were discovered when A. Pippard noticed that by increasing the doping of Indium in a Sn

(tin) superconductor the penetration depth increased while the critical temperature remained constant [Pippard and Bragg, 1950]. This led him to the realization that the current density inside the superconductor could not be determined by the field at that point alone, meaning that the eq. 2.7 is no longer valid. Rather, the current density is mostly dependent on the field over a small volume inside the superconductor. Pippard formulation for the current in the non-local regime is

$$\mathbf{J}_s(\mathbf{r}) = -\frac{3e^2 n_s}{4\pi\xi_0 mc}\int \frac{(\mathbf{r}-\boldsymbol{\rho})[(\mathbf{r}-\boldsymbol{\rho})\cdot\mathbf{A}(\boldsymbol{\rho})]}{|\mathbf{r}-\boldsymbol{\rho}|^4} e^{-(|\mathbf{r}-\boldsymbol{\rho})|/\xi}\, d\boldsymbol{\rho}, \tag{2.23}$$

where the integral runs over the entire volume of the superconductor. This integral can be instead cut short and run over only some coherence lengths ξ for when $|\mathbf{r}-\boldsymbol{\rho}| > \xi$, the contribution of the field decays exponentially. With a a numerical fitting constant, v_F the Fermi velocity and ξ a constant introduced by Pippard called the coherence length of the superconductor, is defined as a combination between the electron mean free path (l_e) and the pure coherence length in clean systems ξ_0 [Pippard and Bragg, 1953]:

$$\xi_0 = a\frac{\hbar v_F}{k_B T_c}\,, \tag{2.24}$$

$$\frac{1}{\xi} = \frac{1}{\xi_0} + \frac{1}{l_e}. \tag{2.25}$$

The reasoning behind the definition of the coherence length ξ_0 is that Pippard argued that only electrons near the Fermi energy can participate in the formation of the superconducting state. Specifically, electrons whose energy is within $\sim k_b T_c$ of the Fermi level. This means that the momentum range of those electrons is $\Delta p = k_b T_c / v_F$. Taking this into account and using the Heisenberg uncertainty principle, a lower limit for the range of the position of the electrons is determined as $\Delta x \geq \hbar/2\Delta p = \hbar v_F / 2k_b T_c$. This motivates Pippard´s choice of the value for the coherence length. Qualitatively, ξ_0 can be understood as the distance between the electrons that form a superconducting charge carrier. In the microscopic BSC theory of superconductivity, the coherence length ξ_0 is defined as $\hbar\, v_f / \pi\, \Delta_0$ [Tinkham, 2004] (eq. 3.114)

The Mattis-Bardeen theory of the anomalous skin effect

Previous work on the determination of the superconductor conductivity did

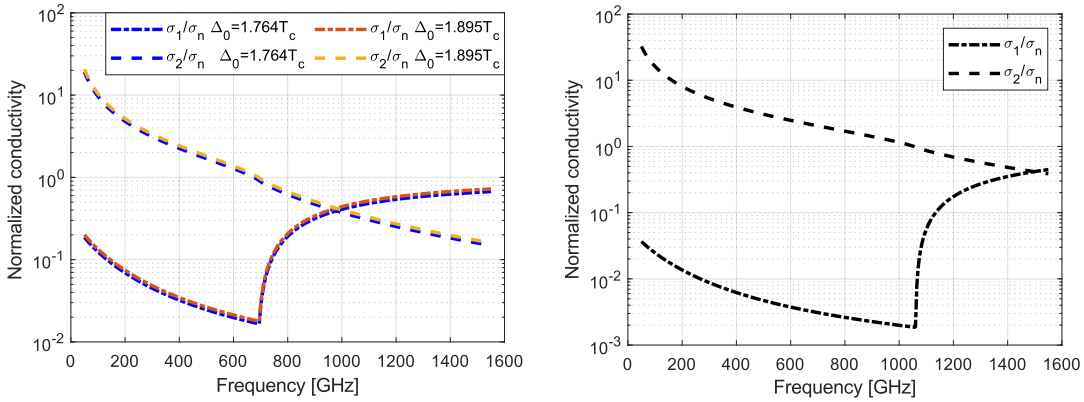

Figure 2.3: Normalized real and imaginary conductivity for Nb and NbTiN. The critical temperature of Nb and Nb and NbtiN are 9.2 and 14.7K respectively with a normal state resistivity of $\rho_{Nb} = 5.27\,\mu\Omega cm^{-1}$ and $\rho_{NbTiN} = 160\,\mu\Omega cm^{-1}$. For the Nb, the conductivity is obtained with the gap energy Δ_0 for a weak and strong coupling superconductor(eqs.2.14, 2.15) and it can be seen that the difference is not significant for our purposes. Hence the expression in eq.2.14 is taken. It is seen that both the real and imaginary parts of the conductivity decrease with frequency. This continues until the *Gap frequency* ($\hbar\omega = 2\Delta_0$) is reached. At this point, the radiation has enough energy to break cooper pairs and generate quasiparticle excitations in the superconductor. These quasiparticle motions are responsible for the sudden increase in the real conductivity of the superconductor and, more importantly, increased losses. For this reason, the operation of the superconductor should remain below its gap frequency.

not include the energy gap $\Delta(T)$ parameter in their calculations and hence could not predict its effects on the conductivity of superconducting films near the gap frequency. After the BCS theory was developed,
[Mattis and Bardeen, 1958] proposed a microscopic relationship between the current in the superconductor and the field, based on the work of Pippard

$$\mathbf{J}(\mathbf{r}) = \frac{e^2 N(0) v_F}{2\pi^2 \hbar} \int \frac{\mathbf{R}[\mathbf{R}\cdot\mathbf{A}(\boldsymbol{\rho})] I(\omega, |\mathbf{R}|, T)}{|\mathbf{R}|^4} e^{-|\mathbf{R}|/l_e}\, d\boldsymbol{\rho} \tag{2.26}$$

where $\mathbf{R} = \mathbf{r} - \boldsymbol{\rho}$ and $I(\omega, |\mathbf{R}|, T)$ from [Mattis and Bardeen, 1958] eq. 3.4, and T is the temperature. For the extreme anomalous regime, where $\xi \gg \lambda_L$ [Mattis and Bardeen, 1958] establish a relationship between the complex and normal conductivity of the superconductor that is also valid for the local regime of the superconductor as the response kernel $I(\omega, |R|, T)$ can be approximated by the local response [Barends, 2009], leading to the following relationships

$$\frac{\sigma_1(\omega) - j\sigma_2(\omega)}{\sigma_n} = \frac{I(\omega, 0, T)}{-j\pi\hbar\omega}, \tag{2.27}$$

$$\frac{\sigma_1(\omega)}{\sigma_n} = \frac{2}{\hbar\omega}\int_{\Delta(T)}^{\infty} dE[f(E)+f(E+\hbar\omega)]\frac{E^2+\hbar\omega E+\Delta^2(T)}{\sqrt{E^2-\Delta^2(T)}\sqrt{(E+\hbar\omega)^2-\Delta^2(T)}}+$$

$$\frac{1}{\hbar\omega}\int_{min\{\Delta(T)-\hbar\omega,-\Delta(T)\}}^{-\Delta(T)} dE[1-2f(E+\hbar\omega)]\frac{E^2+\hbar\omega E+\Delta^2(T)}{\sqrt{E^2-\Delta^2(T)}\sqrt{(E-\hbar\omega)^2-\Delta^2(T)}}, \tag{2.28}$$

$$\frac{\sigma_2(\omega)}{\sigma_n} = \frac{1}{\hbar\omega}\int_{max\{\Delta(T)-\hbar\omega,-\Delta(T)\}}^{\Delta(T)} dE[1-2f(E+\hbar\omega)]\cdot \frac{E^2+E\hbar\omega+\Delta^2(T)}{\sqrt{\Delta^2(T)-E^2}\sqrt{(E+\hbar\omega)^2-\Delta(T)^2}}, \tag{2.29}$$

where σ_n is the normal state conductivity as in the Drude model [Drude, 1900a], $\Delta(T)$ the gap energy of the superconductor and $f(E)$ the Fermi distribution. Similar to the two-fluid model introduced before, σ_1 represents the contribution of quasiparticles to the overall conductivity, thermally excited (first term) and the generation of quasiparticles by radiation (second term) above the gap frequency $f_{gap} = 2\Delta/h$. It is worth noting that above the gap frequency, the excited quasiparticles are subject to classic motion in the solid, this is visible in the sudden increase in losses in the superconductor. σ_2 contains the contribution of the superconducting cooper pairs. The previous relationships between the superconducting and normal current(eqs.2.28 and 2.29) are also valid for the local regime of the superconductor, as remarked by R. Barends [Barends, 2009], where the kernel $I(\omega, |\mathbf{R}|, T)$ can be approximated by the local response only ($I(\omega, \mathbf{0}, T)$).

Determination of the surface impedance for Nb at 480 GHz and NbTiN at 800 GHz

Once the possible regimes for the conductivity of a superconductor have been reviewed it is possible to calculate its surface impedance Z_s. This is to use it as the input parameter in the design of superconducting microwave components.

The first step in the calculation is the comparison between the coherence length and the magnetic penetration depth of the materials. This defines the operating regime of the superconductor to be either local, anomalous or extreme-anomalous. For Niobium, the reported coherence length ξ_0 is about 38 nm [Van Duzer and Turner, 1981] and the electron mean free path is $l_e \sim$

11 nm. This gives a coherence length $\xi \sim 9$ nm (Eq. 2.25). On the other hand, the reported values for λ_L range from 120 to 68 nm [Chang, 1979, Lea and Lichtenberger, 1996]. This leads to the assumption that, four our case, Nb is in the local regime ($\xi \ll \lambda_L$) [Gao, 2008]. In light of the previous information presented, it is deemed that the eqs. 2.28 and 2.29, provide a good approximation for the calculation of the conductivity in the local regime.

For the case of NbTiN, the operation at 800 GHz is also in the local regime since the coherence length is $\xi \sim 3$ nm [Yu et al., 2002] meanwhile the measured values for the penetration depth the values range from 200 to 500 nm [Yu et al., 2005, Tolpygo et al., 2018]. It is assumed then that eqs.2.28,2.29 provides a good approximation as well for the conductivity of NbTiN at 800 GHz.

In the local regime Eq. 2.19 is modified by R. Kautz [Kautz, 1978],[Kautz, 1979] for the case of a film of finite thickness d with vanishing magnetic field at d.

$$Z_s(\omega) = \sqrt{\frac{j\omega\mu_0}{\sigma}} coth(\sqrt{j\omega\mu_0\sigma}d) \tag{2.30}$$

For these equations to be consistent and apply to the electromagnetic design we have to make sure that the dimensions of the superconducting layers are thick enough to allow for a local treatment of the current. Considering that $Z_s = R_s + jX_s$, with $X_s = \omega L_s$ and that for the local regime, the magnetic penetration depth can be defined as [Broom and Wolf, 1977]

$$\lambda(\omega, T) = \frac{L_s}{\mu_0} \tag{2.31}$$

The results for the magnetic penetration depth, calculated with eqs. 2.30 and 2.31 (σ obtained from DC resistivity measures), for the Nb and NbTiN materials is $\lambda_{Nb}(500GHz, 4.2\,K) \approx 100$ nm and $\lambda_{NbTiN}(800GHz, 4.2\,K) \approx 430$ nm (Fig. 2.5). It can be seen that for frequencies below the gap frequency ($f \ll f_{gap}$) the magnetic penetration depth is rather constant. This λ_{mag} is an important parameter as it sets the thickness of the superconducting material for the local treatment to be valid and to avoid increased losses in the superconductors. Otherwise, the losses will be higher and the validity of the values for the surface impedance starts to break down.

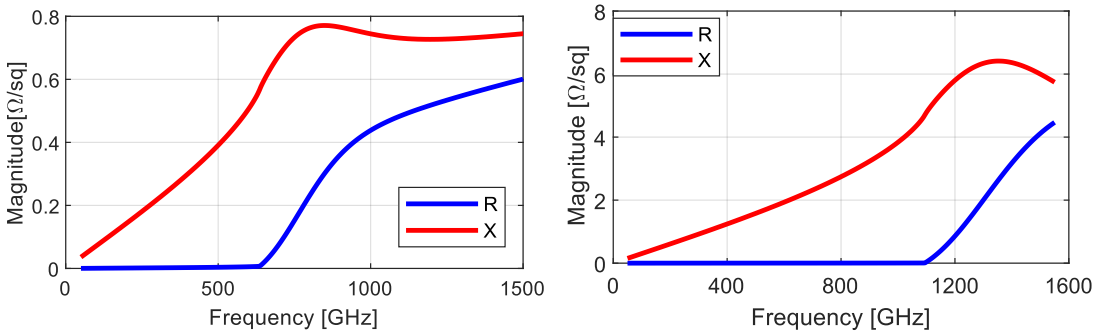

Figure 2.4: Surface impedance at microwave frequencies for Nb (**Left**) and NbTiN (**Right**), processed by *Clean room personnel* at I.Physikalisches Institut, Universität zu Köln. The critical temperature of Nb and NbTiN are 9.2 and 14.7K respectively with a normal state resistivity of $\rho_{Nb} = 5.27\,\mu\Omega cm^{-1}$ and $\rho_{NbTiN} = 160\,\mu\Omega cm^{-1}$. The *Gap frequency* $f = h/2\Delta_0$ can be seen as the surface resistance of the material suddenly increases. This is due to the fact the photons above this frequency possess enough energy to break the cooper pairs and create quasiparticles.

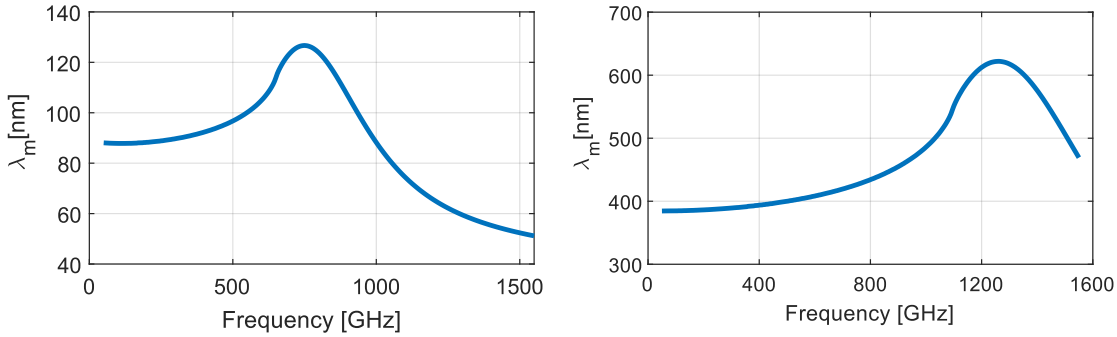

Figure 2.5: Magnetic penetration depth of Nb (**Left**) and NbTiN (**Right**). It can be seen that for frequencies below the gap frequency ($f \ll f_{gap}$) the magnetic penetration depth is rather constant. The λ_{mag} is an important parameter as it sets the thickness of the superconducting material for the local treatment to be valid and to avoid increased losses in the superconductors. For the critical temperature and normal state conductivity of the Nb and NbTiN fabricated, the magnetic penetration depths are $\lambda_{mag}^{Nb} \approx 100nm$ and $\lambda_{mag}^{NbTiN} \approx 430$nm. Those results were obtained with eqs. 2.30 and 2.31 , where σ is obtained from DC resistivity measures

2.1.5 Josephson and Superconductor-Isolator-Superconductor (SIS) tunnel junctions

In the context of the experimental work here presented, Superconductor-Isolator-Superconductor (SIS) junctions are used as the direct power detectors in the characterization of the passive superconducting devices designed in this thesis. Additionally, they are the nonlinear elements of choice for the HFA mixers. Thus it is necessary to characterize the behaviour of these superconducting devices in the presence of RF field.

Superconductor-Isolator-Superconductor (SIS) junctions are two superconducting electrodes separated by a weak link, where the weak link may be, for

example, an isolator barrier or a constriction of the superconductor material itself. The characteristics of these devices have placed them at the heart of heterodyne detectors, serving as the low noise mixer [Kerr et al., 2015].

These tunnel junctions display quasiparticle [Tien and Gordon, 1963] and Cooper pairs tunnelling between the electrodes. The tunnelling of Cooper pairs across the weak link is called *Josephson effect* after Brian Josephson, who predicted it in 1962 [Josephson, 1962], and it is a property of weak links between two superconductors. The supercurrent predicted is an oscillating current at zero voltage

$$I_s = I_c sin(\Delta\varphi) \tag{2.32}$$

$$I_c = \frac{\pi\Delta}{2eR_n} tanh\left(\frac{\Delta}{2k_bT}\right) \tag{2.33}$$

$$\frac{d\Delta\varphi}{dt} = \frac{2eV}{\hbar} \tag{2.34}$$

With I_c the *critical current* of the junction; that is the maximum supercurrent that the junction supports. $\Delta\varphi = \varphi_1 - \varphi_2$, the difference in phase of the *Ginzburg-Landau* wavefunctions $\psi_\chi = \sqrt{n_\chi}\, e^{j\varphi_\chi}$ of the superconducting electrodes [Landau and Ginzburg, 1950]. For a symmetrical tunnel junction ($\Delta_1 = \Delta_2 = \Delta$) the supercurrent is given in
[Ambegaokar and Baratoff, 1963]. Equations 2.32 and 2.34 are known as the *DC* and *AC Josephson* effects.

The supercurrent can be suppressed by the application of magnetic flux parallel to the plane of the tunnel barrier. For a rectangular junction, the supercurrent relationship with the flux Φ (Fig.2.6) is

$$I_c(\Phi) = I_c(0)\left|\frac{sin(\pi\Phi/\Phi_0)}{\pi\Phi/\Phi_0}\right|, \tag{2.35}$$

where $\Phi_0 = h/2e$ the fluxon, the elementary quantum of magnetic flux.

The tunnelling of quasiparticles, that coexist with the Cooper pairs in the superconducting electrodes, across a barrier is described by the *semiconductor model* of the tunnel junction [Tinkham, 2004] section 3.8.1 (Fig. 2.7).

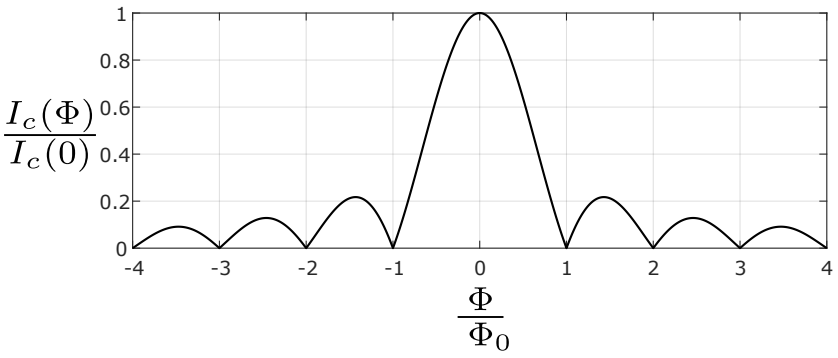

Figure 2.6: Critical current in the presence of magnetic flux.For the cases where $\Phi = \pm n\Phi_0$ and the critical current is zero $I_c = 0$, it does not mean that Cooper pair tunnelling across the junction is suppressed or impeded. Rather the case is that the total supercurrent amounts to zero.

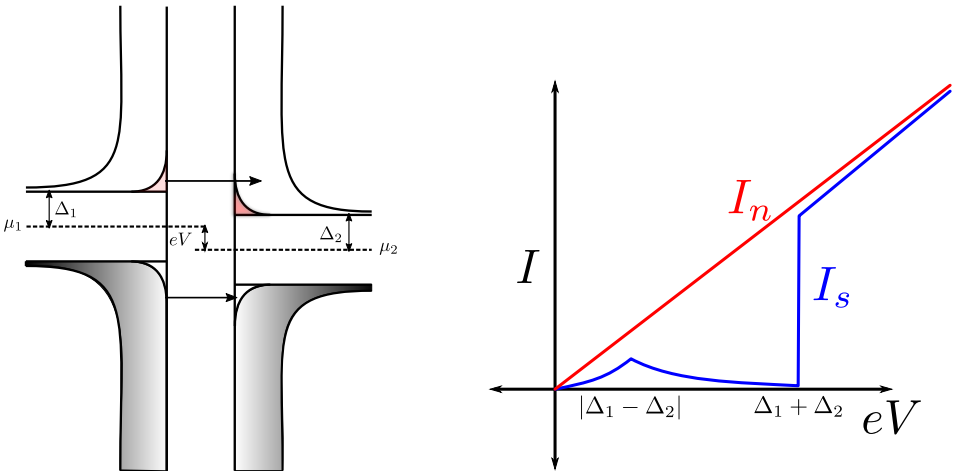

Figure 2.7: Depiction of the semiconductor model of an SIS tunnel junction for electron tunnelling. **Left:** Depiction of the density of states across the junction at $T > 0$ and with an applied bias voltage across the junction. The shaded areas represent the electron-occupied states. **Right:** SIS quasiparticles tunneling characteristic at $T > 0$.

$$I_s = \frac{G_{nn}}{e} \int_{-\infty}^{\infty} \frac{N_{1s}(E)}{N_1(0)} \frac{N_{2s}(E+eV)}{N_2(0)} [f(E) - f(E+eV)] dE \,, \qquad (2.36)$$

with G_{nn} the normal state conductance of the junction. For a SIS junction at $T > 0$, there is a non-zero current due to the tunnelling of thermally excited quasiparticles. The sharp peak at $\Delta_1 + \Delta_2$ is due to the singularity in the density of states at the gap edges. At voltages $eV \gg \Delta_1 + \Delta_2$ the current follows the normal stated characteristics. The local maximum at $|\Delta_1 - \Delta_2|$ (Fig. 2.7 **Right**)is because the thermally excited quasiparticles at the gap edge in the first superconductor are given enough energy to tunnel to the available states at the gap edge of the second superconductor.

When an SIS junction is irradiated by high-frequency radiation two effects

appear; the first is the *Shapiro steps*, corresponding to the interaction of the radiation and the Cooper pairs [Shapiro, 1963], and the second are the *Photon steps* that rise due the interaction between the quasiparticles and the impinging radiation, called photon assisted tunnelling [Tien and Gordon, 1963].

Photon assisted tunneling

An AC voltage $V_{rf}(t) = V_{dc} + V_{ac}cos(\omega_{rf}t)$ has the effect of assisting the tunnelling of quasiparticles in a tunnel junction as the radiation provides energy for tunnelling across it. [Tien and Gordon, 1963] describe the process where it is assumed that a microwave field applied between the junctions electrodes only modulates the energy levels of the quasiparticles, meaning that a quasiparticle with energy $E_{\mathbf{k}}$ becomes $E_{\mathbf{k}} + eV_{ac}cos(\omega_{rf}t)$. This modifies the wave function of quasiparticles in a way that a quasiparticles at level $E_{\mathbf{k}}$ splits into levels at $E_{\mathbf{k}} \pm n\omega_{rf}\hbar$. This betrays the quantum mechanical nature of this effect, where the energy is divided into discrete energy levels separated by $\hbar \cdot \omega$. Using the modified wave function for quasiparticles and the previously described semiconductor model the tunnelling current in the presence of RF field I_{qp}^{rf} can be calculated as follows [Tien and Gordon, 1963].

$$I_{qp}^{rf} = \sum_{n=-\infty}^{\infty} J_n^2\left(\frac{eV_{rf}}{\hbar\omega_{rf}}\right) I_{qp}^{dc}\left(V_{dc} + n\frac{\hbar\omega_{rf}}{e}\right), \tag{2.37}$$

$$I_{qp}^{dc} = C\int_{-\infty}^{\infty}[f(E - eV_{dc}) - f(E)]\rho_1(E - eV_{dc})\rho_2(E)\,dE\,, \tag{2.38}$$

where I_{qp}^{dc} the tunneling current in absence of RF field, C is a proportionality constant, ρ_1 and ρ_2 the density of states in the two superconducting electrodes. Due to the precise density of states of the superconductor being generally unknown, in practice, the value of I_{qp}^{dc} is experimentally measured with the supercurrent carefully suppressed

The RF field has the effect of producing current steps at $V_{gap} \pm \hbar\omega_{rf}/e$ called *Photon steps* (Fig. 2.8). In practice, knowing the exact density of states of a superconductor is not always possible, to circumvent this, I_{qp}^{dc} is measured and used in Eq.2.37, where the supercurrent is carefully suppressed by a magnetic field.

The SIS can then be used as a direct detector for the RF radiation impinging on it. When $eV_{rf}/\hbar\omega_{rf} \ll 1$ and $V_{dc} + \hbar\omega_{rf}/e > V_\Delta$ the terms greater than $n = 2$ are neglectable, leaving equation 2.37 as

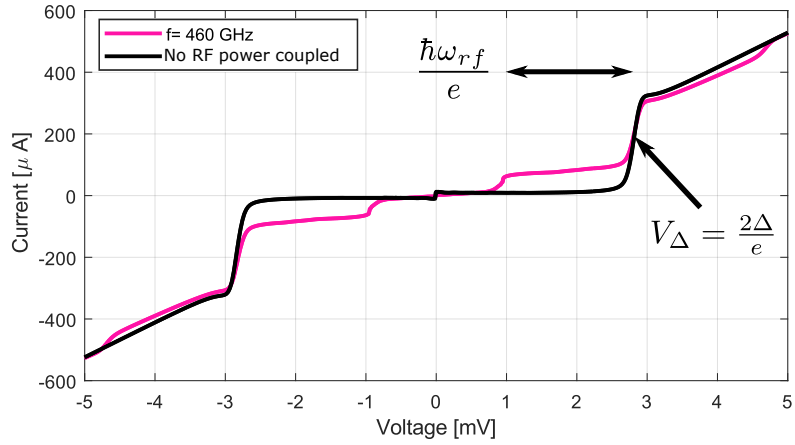

Figure 2.8: Example of an SIS tunnel junction displaying photon steps. The black curve is the junction in the absence of an RF field while the coloured one is irradiated with a monochromatic field at 460 GHz. The photon-assisted tunneling steps are visible below and above the gap voltage for this junction ($V_\Delta = 2.8$ mV)

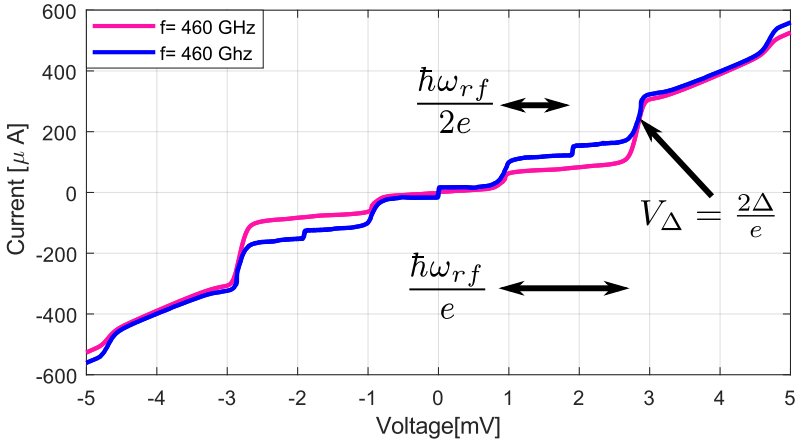

Figure 2.9: Example of an SIS junction exhibiting both Shapiro and photon steps in the presence of RF field of 460 GHz. Due to the fact that Shapiro steps result from the tunnelling of Cooper pairs, the width of a Shapiro is half of a photon step. Biasing the junction on a voltage where a Shapiro step appears results in an excess of noise in the receiver due to the fact that the amplitude of the Shapiro steps oscillates with increased RF power. In this case, the third Shapiro step falls in the middle of the first photon step, making the biasing for direct and heterodyne detection noisy and unstable.

$$I_{rf}(V_{dc}) \approx I_{dc}(V_{dc}) + \left(\frac{eV_{rf}}{\hbar\omega_{rf}}\right)^2 I_{dc}\left(V_{dc} + \frac{\hbar\omega_{rf}}{e}\right). \tag{2.39}$$

For low irradiation power, when $eV_{rf}/\hbar\omega_{rf}$ is small, the second term of Eq. 2.39, know as the direct response, is linearly dependent on the power of the RF signal. This is used as the basis for using the SIS tunnel junctions as a direct detector for the local oscillator power division measurements later in this thesis.

Shapiro Steps

Microwave radiation does not only affect the tunnelling of quasiparticles across the barrier it also affects the tunnelling of Cooper pairs. The relationship between the phase difference ($\phi = \Delta\varphi$) and the voltage across the junction is given by the Ac Josephson effect equation Eq. 2.34). By integrating V_{rf} in time, the phase difference in the presence of the RF field can be obtained

$$\phi(t) = \frac{2eV_{dc}}{\hbar}t + \frac{2eV_{ac}}{\hbar\omega_{rf}}sin(\omega_{rf}t) + \phi_0 \tag{2.40}$$

with ι_0 an integration constant and $\omega_0 = 2eV_{ac}/\hbar$. Using the DC Josephson (Eq. 2.32) and the Bessel function expansions to obtain the supercurrent leads to

$$I_s = I_c \sum_{n=-\infty}^{\infty} (-1)^2 J_n(2eV_{ac}/\hbar\omega_{rf})sin(\omega_0 t - n\omega_{rf}t + \phi_0) \tag{2.41}$$

The supercurrent of Eq.2.41 only introduces a DC contribution when V_{dc} the is equal to

$$V_{dc} = \frac{n\hbar\omega_{rf}}{2e} \tag{2.42}$$

The half amplitude of the n-th Shapiro step is

$$I_s^n = I_c J_n\left(\frac{2eV_{rf}}{\hbar\omega_{rf}}\right) \tag{2.43}$$

The amplitude of the step oscillates as the RF field increases. This is an undesired effect in the junction when operating it either as a direct detector or as a mixer due to the noise and instability of the iv relationship at the point where the Shapiro steps appear. Fortunately, this supercurrent property can be suppressed by the use of a magnetic field, as detailed in the previous section.

2.1.6 SIS junction as mixing element: Tucker theory

The IV-characteristic of a SIS tunnel junction shows a very high non-linearity (Fig.2.8). This near-perfect switch behaviour points to the fact that the SIS

junction could be used as a mixer. the quantum mixing was developed and presented in [Tucker and Feldman, 1985]. Here it is stated that SIS mixers can have a very low conversion loss, and even mixer gain, and can reach the quantum noise limit. the quantum limit is an inherent and fundamental limit of one quantum of noise.

The work here presented focuses on microwave components for the heterodyne mixer focal plane array, including components for a balanced mixer for the HFA. However, given the time constraints and the Covid-19 pandemic, no significant work was made on the fabrication and characterization of an 800 GHz balanced mixer. Hence the quantum theory of mixing is not detailed any further.

2.2 Electromagnetic Waves and Transmission lines

The relationships describing the electrical and magnetic fields were originally enunciated by James Clerk Maxwell [Maxwell, 1873] and later reworked into the four modern equations by Oliver Heaviside [Heaviside, 1893, Hunt, 2012]. From these equations, it is possible to predict the propagation of EM waves, in the form of the *Helmholtz* equation.

$$\nabla^2\mathbf{E} + \omega^2\mu\varepsilon\mathbf{E} = 0 \tag{2.44}$$

$$\nabla^2\mathbf{H} + \omega^2\mu\varepsilon\mathbf{H} = 0, \tag{2.45}$$

where $\mathbf{E}$ and $\mathbf{B}$ are the phasor-electric and -magnetic fields respectively ($\mathbf{\Lambda}(\mathbf{r},t) = \mathbf{\Lambda}_0(\mathbf{r})cos(\omega t + \phi)$). the standard solution for the wave equation is the superposition of two travelling waves in opposite directions $\mathbf{\Lambda} = \mathbf{\Lambda}_0^+ e^{-\boldsymbol{\gamma}\cdot\mathbf{r}} + \mathbf{\Lambda}_0^- e^{\boldsymbol{\gamma}\cdot\mathbf{r}}$, with $\boldsymbol{\gamma}$ the direction of propagation of the wave. These are equations that describe the wave propagation through a general medium.

For the case of propagation through a medium where the dimensions involved are comparable to the wavelength of the waves, the *Transmission line* treatment is required. Transmission lines can be modelled as distributed parameter networks where the parameters of the line are captured in *per length* parameters in the configuration shown in Fig.2.10. The parameters are resistance R, Inductance L, Conductance G and capacitance C. The equations that describe the voltage and current along the transmission line model shown

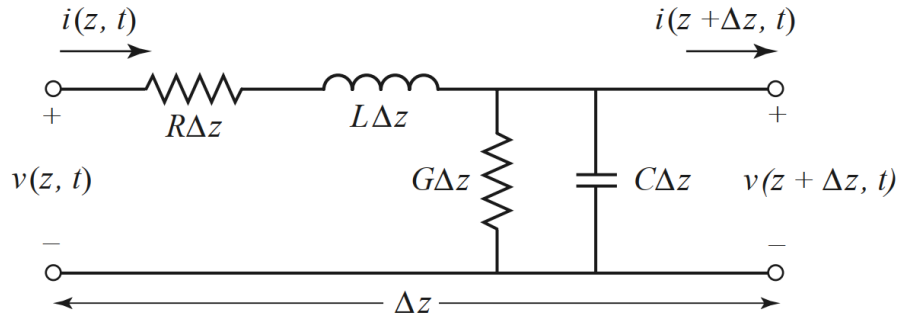

Figure 2.10: Equivalent lumped element circuit for a transmission line of incremental length.

in Fig.2.10 are the *Telegrapher equations* [Pozar, 2011, Collin, 2007]

$$\frac{\partial v(z,t)}{\partial z} = -Ri(z,t) - L\frac{\partial i(z,t)}{\partial t} \tag{2.46}$$

$$\frac{\partial i(z,t)}{\partial z} = -Gv(z,t) - C\frac{\partial v(z,t)}{\partial t} \tag{2.47}$$

Assuming sinusoidal voltages and a steady state regime, replacing the field with cosine-based phasors, meaning $V(z) = V_0 cos(\omega t + \theta)$, $I(z) = I_0 cos(\omega t + \phi)$ and combining the equations yields the wave equation for the voltage and current

$$\begin{aligned} \frac{d^2V(z)}{dz^2} - \gamma^2 V(z) = 0 \\ \frac{d^2I(z)}{dz^2} - \gamma^2 I(z) = 0 \end{aligned} \tag{2.48}$$

$$\gamma = \alpha + j\beta = \sqrt{(R + j\omega L)(G + j\omega C)} \tag{2.49}$$

With γ the propagation constant of the line, defining the attenuation (α) and phase β properties of it. For the lossless transmission line γ reduces to $\beta = j\omega\sqrt{LC}$. This in turn, defines the wavelength in the transmission line λ_g (Eq.2.52) and the phase velocity v_{ph} (Eq.2.53). For a lossy line, the wave is attenuated by a factor of $e^{-\alpha}$. The solution to the telegrapher equation consists of a superposition of travelling waves along the $\hat{z}$ axis (Eq.2.50). From this solution, the *characteristic impedance* Z_0 of the line Eq.2.51 is defined.

$$I(z) = \frac{R + j\omega L}{\gamma}(V_0^+ e^{-\gamma z} - V_0^- e^{\gamma z}) \tag{2.50}$$

$$Z_0 = \frac{R + j\omega L}{\gamma} = \sqrt{\frac{R + j\omega L}{G + j\omega C}} \tag{2.51}$$

$$\lambda_g = \frac{2\pi}{\beta} \tag{2.52}$$

$$v_{ph} = \frac{\omega}{\beta} \tag{2.53}$$

A particularly useful application of Transmission line theory is the determination of the input impedance of terminated transmission lines. When a losses transmission line of impedance Z_0 is terminated on a load of impedance Z_L at $z = 0$, the input impedance seen at a distance $z = l$ is [Collin, 2007] eq.3.47

$$Z_{in}(z = l) = Z_0 \frac{Z_L + jZ_0 tan(\beta l)}{Z_0 + jZ_L tan(\beta l)}, \tag{2.54}$$

for a lossy line, eq2.54 becomes [Collin, 2007] eq. 352

$$Z_{in}(z = l) = Z_0 \frac{Z_L + Z_0 tanh(\gamma l)}{Z_0 + Z_L tanh(\gamma l)}, \tag{2.55}$$

In the context of this work, four kinds of transmission lines are utilized. Hollow waveguide, coplanar waveguide, microstrip and to a lesser extent, slotline. All these transmission lines possess a different geometry, leading to their unique properties, which in turn induce different propagation modes along them. In the following section, the standard equations for the utilized transmission lines are given, as well as the required modifications introduced by the material of choice for that particular transmission line.

2.2.1 Rectangular waveguides

Waveguides are a transmission line composed of only one hollow conductor to propagate waves [Pozar, 2011, Collin, 2007]. The geometry of a rectangular waveguide as used in this work shown in figure 2.11, the propagation of the electromagnetic wave is along the $\hat{z}$ direction. Standard waveguide geometry

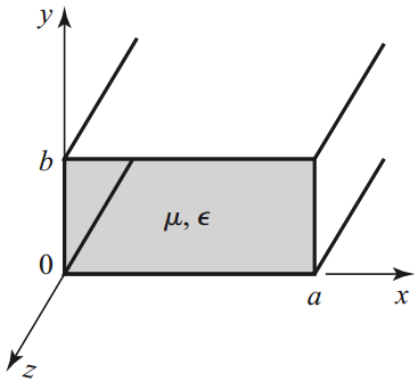

Figure 2.11: Geometry of a rectangular waveguide [Pozar, 2011].

has $a = 2b$, the reason for this is to maximize the single mode bandwidth of the waveguide.

Transverse Modes

Rectangular waveguides support *Transversal Electric* (TE) and *Transversal Magnetic* (TM) modes. The modes are defined by the *Helmholtz equation* for the TE and TM cases.

$$\left(\frac{\partial^2}{\partial x^2} + \frac{\partial^2}{\partial y^2} + k_c^2\right) h_z(x, y) = 0 \tag{2.56}$$

$$\left(\frac{\partial^2}{\partial x^2} + \frac{\partial^2}{\partial y^2} + k_c^2\right) e_z(x, y) = 0 \tag{2.57}$$

For the TE modes, $E_z = 0$ and H_z must comply with Eq.2.56, On the other hand for TM modes $H_z = 0$ and E_z is determined by Eq.2.57. The solution for those equation takes the form of $H_z(x, y, z) = h_z(x, y, z)e^{-j\beta z}$, and $E_z(x, y, z) = e_z(x, y, z)h^{-j\beta z}$. Here $k_c = \sqrt{k^2 - \beta^2}$ is the cutoff wavenumber and β given in 2.49. The cutoff wavenumber defines a cutoff frequency (Eq.2.59) for both TE and TM modes. Modes with frequency $f < f_{cutoff}$ are *evanecent modes* and experience exponential decay along waveguide [Pozar, 2011].

For a rectangular waveguide the fundamental mode, the one with the lowest f_{cutoff}, is the TE10. In the case of the TM modes, the TM11 is the mode with the lowest cutoff frequency. In this work, rectangular waveguides with dimension $a = 2 \cdot b$ are used. The bandwidth is limited to that of the fundamental mode. These waveguide dimensions give the following cutoff frequency for the first modes (TE11, TE20 and TM11) $f_{cutoff} = 2 \cdot f^{10}_{cutoff}$.

$$\beta = \sqrt{k^2 - k_c^2} = \sqrt{k^2 - \left(\frac{m\pi}{a}\right)^2 - \left(\frac{n\pi}{b}\right)^2} \tag{2.58}$$

$$f_{cutoff} = \frac{k_c}{2\pi\sqrt{\mu\varepsilon}} = \frac{1}{2\pi\sqrt{\mu\varepsilon}}\sqrt{\left(\frac{m\pi}{a}\right)^2 + \left(\frac{n\pi}{b}\right)^2} \tag{2.59}$$

2.2.2 Superconducting planar transmission lines

Coplanar Waveguide

Coplanar waveguides (CPW) are planar transmission lines that consist of a main line of width W between two ground planes separated by a gap s. The lines and the ground plane are supported by a dielectric substrate ((Fig.2.12)). The particular advantage of a CPW is that it only requires metallization on one side of the substrate, facilitating the fabrication of the circuits. CPW lines support Quasi TEM mode propagation with no intrinsic frequency cutoff, in contrast to hollow waveguides. Given the geometry of a CPW, it displays degeneracy in the mode propagation supporting both the even (the fundamental mode, displayed in Fig.2.13) mode and the odd mode. Mode degeneracy exists when two or more modes can propagate simultaneously and it is often undesired, as the additional modes deplete the signal transmission on the fundamental mode. The power that leaks to the wrong modes can easily produce undesired cavity resonances. The field configuration of the odd mode demands the existence of a potential difference between the two ground planes of the CPW, hence by having a *grounding bridge* between the two ground planes it is possible to avoid the propagation of the odd mode. These grounding bridges must be placed before and after any discontinuity in the CPW, where the excitation of the odd mode is inexorable. A disadvantage of the grounding bridges is that they add a capacitance to the ground in the line.

Standard CPW analysis involves the quasistatic approximation and the use of conformal mapping of the CPW geometry into another easier analysis. Following the steps proposed in [Bahl et al., 2013],[Simons, 2001], the relevant parameters of the CPW lines can be obtained. Equations 2.60 to 2.63 give the parameters of a CPW with a finite substrate thickness.

$$\lambda_{guided} = \frac{\lambda_0}{\sqrt{\varepsilon_{eff}}} \tag{2.60}$$

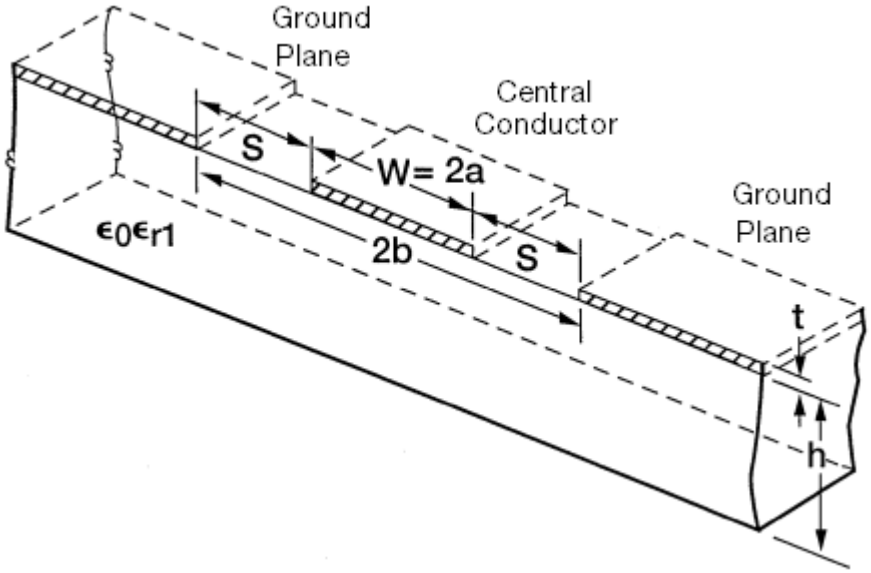

Figure 2.12: Scheme of a CPW with a substrate of finite thickness [Simons, 2004].

$$v_{ph}^{CPW} = \frac{c}{\sqrt{\varepsilon_{eff}}} \tag{2.61}$$

$$Z_0 = \frac{1}{C_{cpw} v_{ph}} = \frac{30 \cdot \pi}{\sqrt{\varepsilon_{eff}}} \frac{K'(k_0)}{K(k_0)} \tag{2.62}$$

$$\varepsilon_{eff} = \frac{C_{cpw}}{C_{air}} = 1 + \frac{\varepsilon_r - 1}{2} \cdot \frac{K(k_1)}{K'(k_1)} \frac{K'(k_0)}{K(k_0)} \tag{2.63}$$

where λ is the free space wavelength, ε_{eff} is the geometry dependent effective dielectric constant of the CPW. $K(k)$, $K'(k)$ along with the pairs k_0/k_0' and k_1/k_1' are detailed in [Simons, 2001] (**Section 2.2.3**).

$$\frac{K(k)}{K'(k)} = \begin{cases} \dfrac{\pi}{ln\left[2 \cdot \dfrac{1+\sqrt{k'}}{1-\sqrt{k'}}\right]} & k \in [0\ ,\ 1/\sqrt{2}] \\ \dfrac{ln\left[2 \cdot \dfrac{1+\sqrt{k}}{1-\sqrt{k}}\right]}{\pi} & k \in [1/\sqrt{2}\ ,\ 1] \end{cases} \tag{2.64}$$

$$k_1 = \frac{W}{W + 2s}\,, \tag{2.65}$$

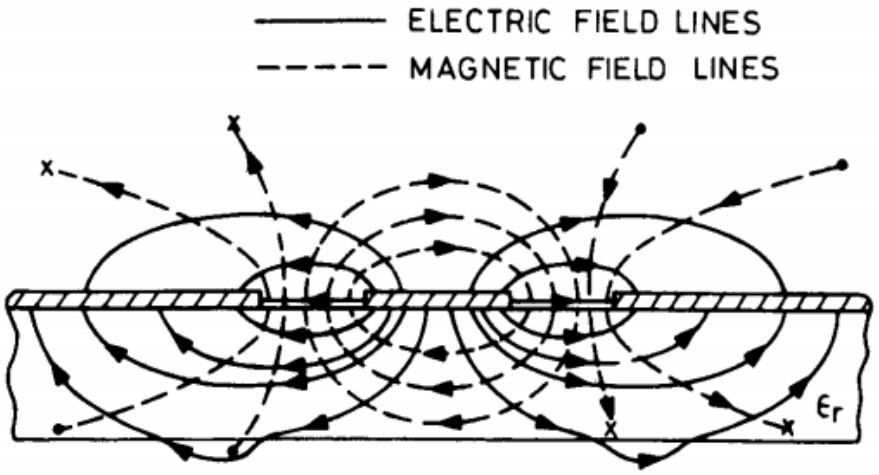

Figure 2.13: Fundamental mode (Even) of the CPW. [Gupta et al., 1996]

$$k_1 = \frac{sinh\left(\frac{W\pi}{4h}\right)}{sinh\left(\frac{\pi(W+2s)}{4h}\right)}\,, \tag{2.66}$$

$$k'_x = 1 - \sqrt{k_x}\,. \tag{2.67}$$

The k_1 and k_2 parameters depend on the geometrical parameters of the CPW Eqs. 2.65 - 2.66. The parameter $k' = 1 - \sqrt{k}$ is the complementary modulus. The complete analysis of a CPW line can be found in [Collin, 2007].

The modifications introduced by the superconducting state can be summarized as the addition of a kinetic inductance to the geometric inductance of the line.

$$L = L_{CPW} + L_k \tag{2.68}$$

From Eq.2.53, and using the approximation of a lossless line ($v_{ph} = 1/\sqrt{LC}$) the geometric contribution to the total inductance is $L_{CPW} = \mu_0\varepsilon_0\varepsilon_{eff}/C_{CPW}$. The contribution to the total inductance of the line is obtained from the contributions of the centre plane and ground planes of the CPW $L_k = (g_{line} + g_{ground})L_s$, with g_{line} and g_{ground} the geometric factors derived for the series resistance per unit length of the centre line and ground planes ([Simons, 2001], Section 8.2.1). L_s is the surface inductance of the superconductor in the local limit.

After the calculation of the total inductance per length, the impedance of the CPW can be calculated by Eq. 2.51 using the lossless approximation.

$$Z_0 = \sqrt{\frac{L}{C_{cpw}}} \tag{2.69}$$

Microstrip Lines

Microstrip lines are another type of planar transmission line, where the main line and the ground plane are separated by a dielectric substrate(Fig.2.14 **Left**). This particular design requires metallization in both faces of the substrate which, in our case, introduces some limitations on the application and use of this transmission line. The fundamental mode of the microstrip is a Quasi-TEM mode, displayed in Fig.2.14 **Right**. The standard microstrip analysis uses quasistatic approximation and conformal mapping to give an estimation of the line impedance [Gupta et al., 1996]. For the superconducting microstrip lines used in this work, the quasistatic analysis has to be corrected for the influence of the superconductor. An analysis that takes into consideration the geometry and superconducting properties in the local limit is given in [Chang, 1979]. There the corrected inductance and capacitance in terms of a *fringing factor* are given. The total inductance and capacitance per length of the line are.

$$L = \frac{\mu_0}{WK(W,h,t)}\left[h + \lambda_1\left[coth\left(\frac{t_1}{\lambda_1}\right) + \frac{2\sqrt{p}}{r_b}csch\left(\frac{t_1}{\lambda_1}\right)\right] + \lambda_2\, coth\left(\frac{t_2}{\lambda_2}\right)\right] \tag{2.70}$$

$$C = \frac{\varepsilon_r\varepsilon_0 W}{h}K(W,h,t) \tag{2.71}$$

Where W and h parameters are defined in 2.14 and t the thickness of the metallization layer of the microstrip. the parameters r_a and r_b are given in [Yassin and Withington, 1995], correcting a misprint in [Chang, 1979].

2.3 Network parameters

The treatment and analysis of distributed circuit networks are usually done with a network equivalent of the component, where the properties and characteristics of each component are summarized in an equivalent network matrix

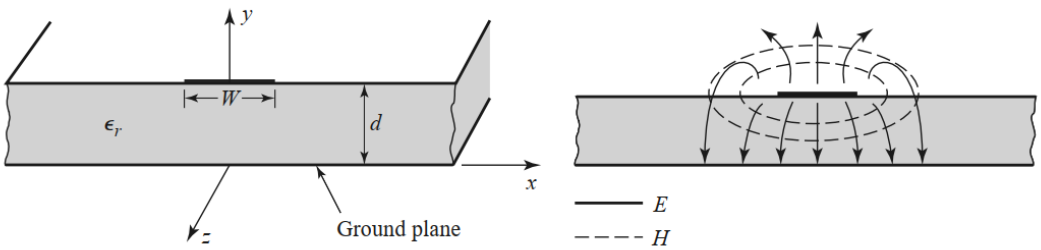

Figure 2.14: Left: Schematic of a infinitesimally thin microstrip of width W over a dielectric substrate of thickness h. **Right:** Field lines in the microstrip [Pozar, 2011]

obtained from the transmission line analysis, 3D simulation or direct measurement of such component. Common representations of networks are the *Impedance/Admittance* equivalents and the Scattering matrix[Pozar, 2011, Collin, 2007]. A representation of an N-port network is shown in Fig. 2.15 where the Voltage and current waves incoming and outcoming from the port are depicted. Impedance/ admittance matrix relates the voltage at one specific port i ($V_i = V_i^+ + V_i^-$) generated by driving a current I at port j ($I_j = I_j^+ + I_j^-$) while all the other ports are open circuited (including port i). This defines the impedance element Z_{ij}, that is the transfer impedance from port i to port j. The special case of Z_{kk} is the input impedance seen at port k when all other ports are in an open circuit state.

$$[V] = [Z][I] \tag{2.72}$$

$$Z_{ij} = \left.\frac{V_i}{I_j}\right|_{I_k=0, k\neq j} \tag{2.73}$$

Another matrix representation of a network is the *Scattering parameter* matrix. It relates the voltage waves incident at port j (V_j^+) and the waves coming out from port i (V_i^-) meanwhile all the other ports are terminated in matched loads, that is, no voltage waves reflected at those ports.

$$[V^-] = [S][V^+] \tag{2.74}$$

$$S_{ij} = \left.\frac{V_i^-}{V_j^+}\right|_{V_k^+=0, k\neq j} \tag{2.75}$$

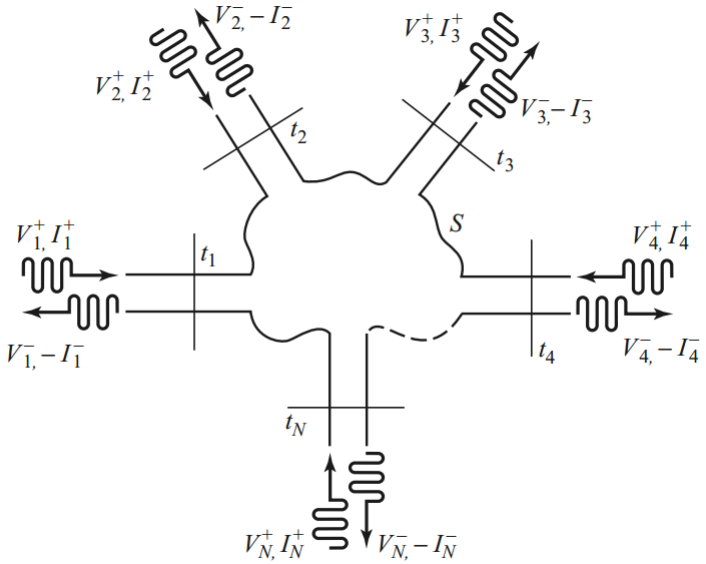

Figure 2.15: Portrayal of an arbitrary network of N ports. V_m^+ is the magnitude of the input wave at the port m and V_n^- is the magnitude of the output wave at the port n [Pozar, 2011].

2.4 Mixer architectures

One of the goals of this thesis is the design of a SIS mixer for the HFA array of CHAI. In general, a mixer is composed of a circuit network and a non-linear element. The network allows for the manipulation and the physical coupling of the Local Oscillator (LO) and Radiofrequency (RF) signal, while the non-linear element, be that a simple diode, Schottky or SIS junction, generates signals at frequencies $|\omega_{LO} \pm \omega_{RF}|$. To understand the choice of mixers done in this thesis, the basic properties of the most common mixer configurations are presented.

The most basic mixer architecture corresponds to a diode and a resistance in parallel, shown in Fig. 2.16. For classical mixers, the non-linear relationship allows for its power expansion. Let $V_{in} = V_{LO}cos(\omega_{LO}t) + V_{RF}cos(\omega_{RF}t)$ be the signal feed to the mixer. The response can be expressed in a power series as

$$V_{out} = \sum_{n=0}^{\infty} \chi_n V_{in}^n \tag{2.76}$$

Concentrating in the second order term $\chi_2 V_{in}^2$ we get

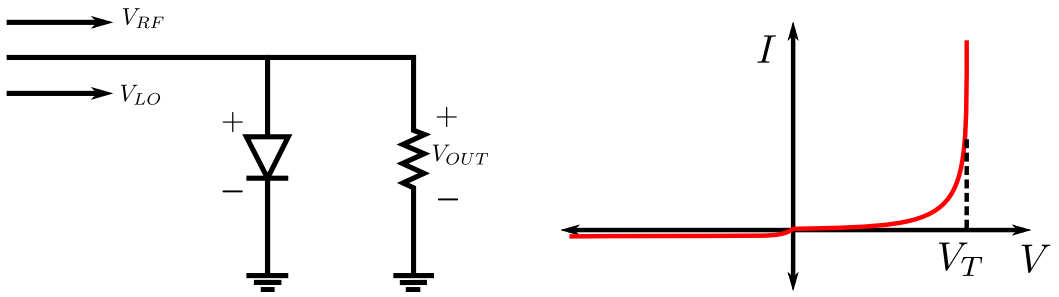

Figure 2.16: Simple single diode as a mixer.**Left:** Schematic of the diode as mixing element where the Voltages from the RF and LO signals are superimposed and fed to the diode. V_{out} contains the signal that is shifted in frequency. **Rigth:** I-V characteristic of an ideal diode. For the forward bias, no current can flow through the diode until the voltage reaches a certain threshold ($V_[t]$) where there is a strong non-linear relationship between the voltage and the current. This nonlinearity allows for mixing the V_{RF} and V_{LO} signals.

$$\chi_2 V_{in}^2 = \chi_2\big(V_{lo}cos(\omega_{lo}t) + V_{rf}cos(\omega_{rf}t)\big)^2 = \frac{V_{lo}^2}{2}\big(1 + cos(2\omega_{lo})\big) + \frac{V_{lo}V_{rf}}{2}\big(cos(\omega_{lo}t + \omega_{rf}t) + cos(\omega_{lo}t - \omega_{rf}t)\big) + \frac{V_{rf}^2}{2}\big(1 + cos(2\omega_{rf}t)\big) \quad (2.77)$$

The higher order components of Eq.2.76 yield components with frequencies multiples of ω_{RF}, ω_{LO} and its difference and sum, $m\omega_{LO}$, $n\omega_{RF}$ and $m\omega_{LO} \pm \omega_{RF}$. These components are not desired, and hence, they are filtered out. The particular component of interest is the product obtained by the product of cosines, particularly the $cos\big((\omega_{LO} - \omega_{RF})t\big)$. By selecting this term, the following output signal is obtained

$$V_{out} = Xcos(\omega_{if}t)\,, \quad (2.78)$$

where X a constant and $\omega_{IF} = |\omega_{LO} - \omega_{RF}|$. Mixing elements based on SIS tunnel junctions can not be described by the classical analysis presented here since its IV relationship in the presence of the Rf field can only be described in a quantum mechanical picture. Instead, they are described by the quantum theory of mixer [Tucker and Feldman, 1985]. The described mixer architecture allows for the frequency shifting of the RF signal to lower frequencies (*Downshifting*) by selecting the proper LO frequency and producing a new signal at $\omega_{IF} = |\omega_{LO} - \omega_{RF}|$. The bandwidth of the IF path is limited and determined by the frequency response of the IF components after the mixer. in particular the low noise amplifiers. For our case, the IF bandwidth

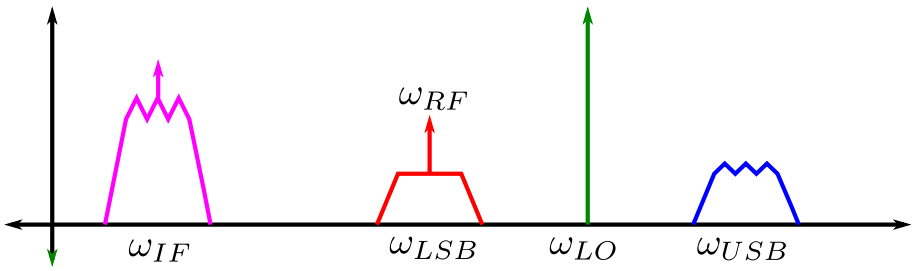

Figure 2.17: The spectrum of a conventional double side band receiver with the RF band and the Image band. In this configuration, both the USB and LSB are superimposed in the IF band. This means that any feature or noise present in any of the sidebands is added to the IF band, increasing its noise floor.

is 4-8 GHz. The fact that $\omega_{IF} = \omega_{LO} - \omega_{RF}$ defines the *Upper Side Band* (USB), for $\omega_{RF} > \omega_{LO}$ and the *Lower Side Band* (LSB), for $|\omega_{RF} < \omega_{LO}|$ The sideband which contains the desired RF signal is referred to as the *RF band*, meanwhile its mirror band concerning the LO signal is the *Image band*. The Image band is often undesired as it does not contain useful information and its addition increases the noise at the IF band. However, a more complex mixer configuration can filter this image band out (Single Sideband SSB) or even produce two different outputs for both sidebands of the receiver (Sideband separating 2SB). The mixer setup in Fig. 2.16 is a *Double Sideband mixer* (DSB) given that the output IF signal is a superposition of the USB and LSB bands.

2.4.1 Single Sideband mixer (SSB) and Sideband separating mixers (2SB)

Depending on how the image band is handled, it differentiates between these two kinds of mixers. The SSB mixer configuration is similar to the DSB configuration with the difference being that in this case the image band is filtered out before the RF signal is downconverted. In the 2SB mixers, the image and the RF band are separated and the imaged band can be rejected or processed, depending on preference, after the mixing process is done (Fig.2.18).

The SSB mixer first requires a filter, either a high- or low-pass filter before the detection is done. This is often not ideal as achieving a filter with the desired frequency response for the RF band is a difficult task, especially for submilimetre frequencies. Another fact is that having a filter before the signal is detected, limits the frequency operation of the receiver onto a certain band, either LSB or USB. The second requires a more convoluted configuration to achieve the separation of the sidebands.

In a 2SB mixer, the RF signal can be decomposed as a superposition of both

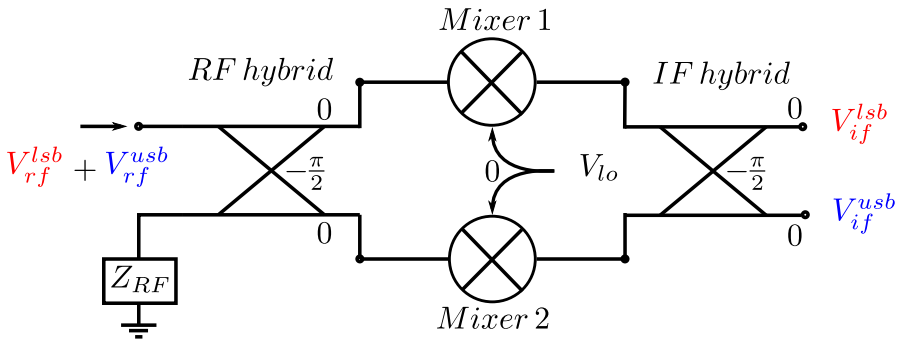

Figure 2.18: Schematic of a Sideband separating mixer, where Z_{RF} is a high frequency load. The input V_{RF} can be decomposed in the side bands $V_{RF}cos(\omega_{RF}^{USB}t)$ and $V_{RF}cos(\omega_{RF}^{LSB}t)$ and a subsequently separated by the mixer in V_{IF}^{LSB} and V_{IF}^{USB}. This mixer architecture is considerably more intricate than the simple DSB mixer, requiring 90° at both the RF and IF ends and two non-linear components for the separations of the sidebands.

the lower and upper sidebands

$$V_{rf} = V_{rf}cos(\omega_{rf}^{usb}t) + V_{rf}cos(\omega_{rf}^{lsb}t)\,, \tag{2.79}$$

where $\omega_{RF}^{USB} = \omega_{LO} + \omega_{IF}^{USB}$ and $\omega_{RF}^{LSB} = \omega_{LO} - \omega_{IF}^{LSB}$. The signal is then fed through an RF hybrid, that splits the signal in equal parts and introduces a $\pi/4$ phase difference between them. These two signals are mixed down to the IF by two mixers with two LO signals of the same frequency and phase. Consequently, the resulting IF signals of the mixers have a well defined phase difference, as visible in eq.2.80. When the V_{if}^{lsb} and V_{if}^{usb} outputs are then coupled through another hybrid, either the LSB or the USB is cancelled out, depending on the output port used. Meanwhile, the other sideband is added in phase at that same port.

The separation of the sidebands is achieved when the IF output signal from the mixers is recombined by the IF hybrid. The output signals from the hybrid are

$$\begin{aligned} V_{if}^{lsb} &= V_{if}\, cos(\omega_{if}^{lsb}t) \\ V_{if}^{usb} &= V_{if}\, cos(\omega_{if}^{usb}t - \pi/2) \end{aligned} \tag{2.80}$$

2.4.2 Balanced mixer

The balanced mixer is an architecture that addresses a reduction of noise in the IF signal by manipulation of the phase of the LO and RF signals rather than by manipulation of the IF bands. This kind of mixer requires either a 180° or a 90° hybrid to couple the V_{LO} and V_{RF} signals before feeding them to two non-linear elements. In contrast, In the previous mixer architectures, the LO and RF signals where already coupled before being fed to the mixer. [Kooi, 2008] gives a mathematical description of the IF current using a classical approach and a resumed version of it is presented in this text as well. The current in the mixers can be expanded as polynomial

$$I_{Mixer_{+bias}} = \sum_{k=0}^{\infty} \frac{a_k V^k_{Mixer_{+bias}}(t)}{k!}\,, \tag{2.81}$$

$$I_{Mixer_{-bias}} = \sum_{k=0}^{\infty} (-1)^k \cdot \frac{b_k V^k_{Mixer_{-bias}}(t)}{k!}\,, \tag{2.82}$$

where the a_k, b_k are the mixer conversion gain, assuming that the mixers have the same gain $a_k = b_k$, the IF currents for the 180° and 90° balanced mixers are

$$\begin{aligned} I^{\pi}_{if} = a_1 V_{rf} e^{j\omega_{rf}t} + \frac{a_2}{2!}\left[V_{rf} V_{lo} e^{j(\omega_{rf}+m\omega_{lo})t}\right] + \\ \frac{a_3}{4\cdot 3!}\left[V^3_{rf} e^{3j\omega_{rf}t} + 3V_{rf}V^2_{lo} e^{j(\omega_{rf}+2m\omega_{lo})t}\right] \end{aligned} \tag{2.83}$$

$$\begin{aligned} I^{\pi/2}_{if} = \frac{a_1}{\sqrt{2}}\left[V_{rf} e^{j(\omega_{rf}-\pi/4)} - V_{lo} e^{j(m\omega_{lo}t+\pi/4)}\right] + \frac{a_2}{2!}\left[V_{lo} V_{rf} e^{j(m\omega_{lo}+\omega_{rf})t}\right] + \\ \frac{8\cdot 3! a_3}{\sqrt{2} e^{j\pi/4}}\left[V^3_{rf} e^{3j\omega_{rf}t} + 3V^2_{lo} V_{rf} e^{j(2m\omega_{lo}+\omega_{rf})t} - 3jV_{lo}V^2_{rf} e^{j(2\omega_{rf}+m\omega_{lo}t)} - jV^3_{lo} e^{3j\omega_{lo}t}\right] \end{aligned} \tag{2.84}$$

In the case of both balanced mixers, the phase difference introduced by the hybrid, either 180° or 90°, and the reversely polarized mixers are responsible for the LO noise immunity. The LO and RF delivered to the two reversely biased mixers have a specific phase difference between them. This difference is responsible for the properties of the balanced mixers.

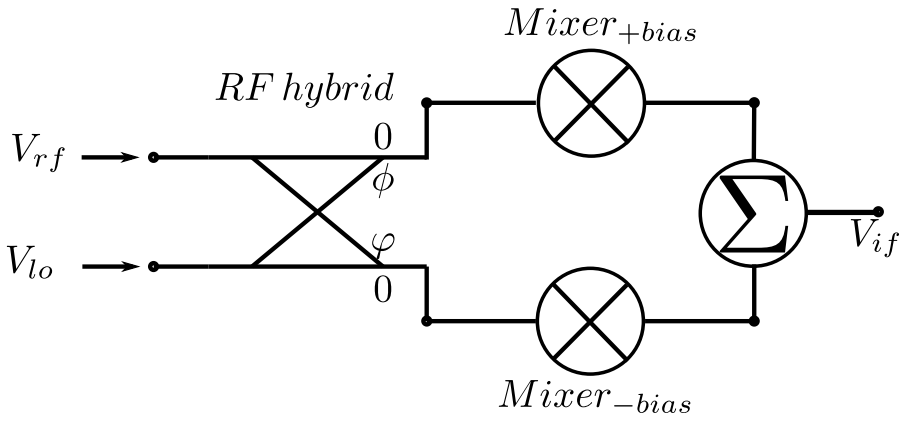

Figure 2.19: Schematic of a balanced mixer. The V_{LO} and V_{RF} are combined by the RF hybrid. For a 90° hybrid $\phi = \varphi = 90°$, meanwhile for a 180° $\phi = 180°$ and $\varphi = 0°$. The signal is then fed to the two mixers in reverse bias and then recombined by the IF combiner.

The choice of which architecture to use from a pure performance point of view is the 180° hybrid as it has superior isolation between the local oscillator and radio frequency signal. However, the implementation and integration of such a hybrid is a difficult task in submillimetric receivers. For that reason, the 90° hybrid is chosen for balanced mixers even if the isolation between the LO and RF signals and harmonic intermodulation are worse [Kooi, 2008].

2.5 Sensitivity of heterodyne receivers for radio astronomy

The noise that the detector adds to the signal limits the weakest signal that can be detected. It can be Johnson-Nyquist (Thermal noise), shot or flicker noise. The spectrum of these different kinds of noise is not necessarily the same, However, for simplicity's sake, it will be assumed here that the noise power is independent of the frequency over the bandwidth of interest (White noise). For the analysis and treatment of the noise, the noisy detector is seen as a combination of a noiseless detector with a noise source at its input that is responsible for delivering the noise power at the input of the device. This source is often represented as a noisy resistance that delivers *noise power* P_{in} at the input of the detector. This in turn produces an equivalent noise power P_n at the output of the device(Fig. 2.20). Viewed from a classical standpoint, the noise power P_n available from a resistor R at a temperature T over a given frequency bandwidth B is

$$P_n^{RJ} = k_B T B\,, \tag{2.85}$$

where k_B the Boltzmann constant. This is the *Rayleigh-Jeans* approximation for the power produced by the resistor. It is important to notice that this is only valid for the regime where $\hbar\omega \ll k_B T$. For the case where the previous condition does not hold, the Planck black body radiation law has to be used to calculate the power per Hertz available from the resistor [Pozar, 2011] p. 499.

$$P_n^P = \frac{\hbar\omega}{e^{\hbar\omega/k_B T} - 1} \tag{2.86}$$

There is another definition for the calculation of this power if the vacuum fluctuations are considered to be part of the power delivered by the resistor. This is the Callen-Welton definition for noise power, given by Equation 2.87. The matter of whether to use the Planck or the Callen-Welton definition for the noise power is convention and it is explored in [Kerr, 1999] and [Kerr and Randa, 2010], The difference lies in which process the zero point fluctuations are attributed to. Either to the emitted power generated by the black body or to the heterodyne detection process. In this work, the Planck definition is preferred, due to corresponding to the power emitted by a black body at temperature T and angular frequency ω,

$$P_n^{CW} = \frac{\hbar\omega}{e^{\hbar\omega/k_B T} - 1} + \frac{\hbar\omega}{2} \tag{2.87}$$

This noise power defines a *Noise Temperature* T_n as the available noise power per hertz of bandwidth ($B = 1$ Hz) divided by the Boltzmann constant. The noise temperature is the usual parameter to express the added noise of a heterodyne receiver

$$T_n \equiv \frac{P_n}{k_B} \tag{2.88}$$

Determination of Noise parameters

The measuring of the P_n or T_n of a detector is done using the Y-factor method, where the noise power generated by two black body radiators at different temperatures is delivered to the device and the output power is measured. The Y-factor is then defined as

$$Y = \frac{P_H}{P_C} = \frac{P_n(T_H) + P_n}{P_n(T_C) + P_n} \tag{2.89}$$

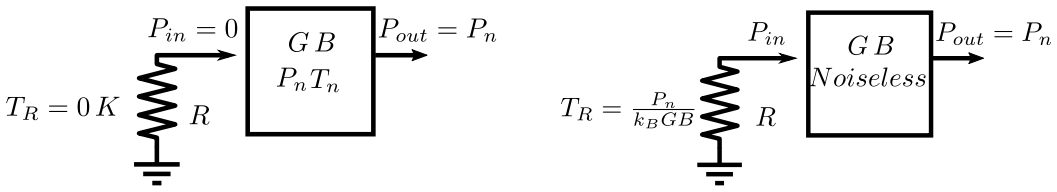

Figure 2.20: The output noise power P_n coming from a device can be seen as a combination of a noiseless device with a black body radiator at the input. This resistor produces a noise power at the input of the device that generates the same output power P_n at the output of the device. Image inspired on [Pozar, 2011] Figure 10.5.

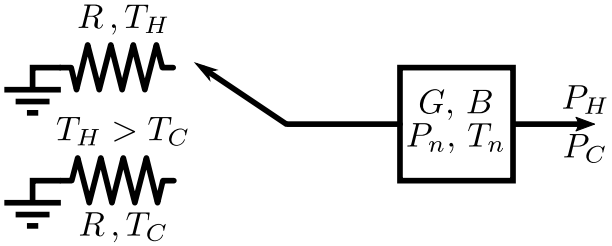

Figure 2.21: Y-factor measurement scheme. Here the device under test is coupled to the two loads at different temperatures and the output power is measured. The output power with both loads is then compared and it receives the name of *Y-factor* $Y = P_H/P_C$.

After the Y-factor has been determined, the equivalent noise power and noise temperature of the device can be obtained as

$$P_n = \frac{P_H - Y \cdot P_C}{Y - 1} \tag{2.90}$$

$$T_e = \frac{T_H - Y \cdot T_C}{Y - 1}\,. \tag{2.91}$$

The determination of the noise parameters of a network can be calculated if the noise parameters of the individual components are known. The noise temperature of a cascade of M devices, each with noise temperature T_χ and gain G_χ is

$$T_{cascade} = T_1 + \frac{T_2}{G_1} + \frac{T_3}{G_1 \cdot G_2} + \ldots \frac{T_m}{G_1 \cdot G_2 \ldots G_{m-1}} \tag{2.92}$$

The noise temperature of the cascade of elements is dominated by the characteristics of the first device. Assuming $G_i \gg 1$ can be seen that the gain of the i component in the cascade does attenuate the noise contribution of the $M - i$ following components It is then of great interest to have the gain of the

first component as large as possible as it will decrease the noise contribution of all the other components in the cascade.

The mixer noise temperature is referred to as the output IF band and it depends on the exact mixer configuration, as it determines how the image and RF band are handled. For example, an SSB mixer that terminates one of the Image bands in a low temperature load may have a lower noise temperature than a DSB that merges both the Image and RF bands into the IF band.

Chapter 3

Design of superconducting planar components

This chapter details the design process of the superconducting planar components for the LFA (460-500 GHz) and HFA (780-820 GHz) arrays. First, the software tools with the considerations and parameters required for simulation are introduced. Subsequently, the designs for the LFA components are presented with their parameters and, afterwards the performance of the integrated component. Finally, the designs for the HFA components are presented.

3.1 Commercial Electromagnetic 3D/2D simulators

The use of electromagnetic simulators yields a preliminary result of the characteristics of the components to fabricate, permitting their adjustment and optimization before fabrication. They are a valuable tool that not only permits a faster design process but also the troubleshooting and debugging of components. The simulators used in this thesis are the 3D high frequency suite from *CST - Computer Simulation Technology GmbH.*, The 2D Sonnet software and the 2D/ schematic simulator from *AWR microwave office software.*

The CST high frequency suite was used as the main software for the design of the superconducting planar membranes for both the LFA and HFA components. The superconducting parameters of the niobium (Nb) and niobium titanium nitrate (NbTiN) are implemented as a complex surface impedance as a function of frequency. The surface impedance is calculated in Sec. 2.1.4 using the Mattis-Bardeen approximation.

The 2D Sonnet is used for the design of a preliminary HFA SIS tuning struc-

ture. Sonnet does not allow for the implementation of the surface impedance table as CST. Instead, it allows a frequency independent surface impedance in units of $\Omega/\square$ (Ohm·square^{-1}). The superconductor properties are calculated by the use of the DC resistance and the surface reactance in the following equation

$$Z_s = R_{DC} + j\omega L_s, \tag{3.1}$$

where the surface inductance is obtained from eq. 2.31 with λ_L the London penetration depth calculated from eq. 2.9. In practice the values for the R_{DC} and L_s are taken so the resulting surface impedance complies with the calculated surface impedance obtained from the Mattis-Bardeen approximation (eqs. 2.28, 2.29).

Another software utilized for 2D planar components design is the AWR microwave office software. It is utilized for the tuning and matching of a microstrip Wilkinson power divider. AWR allows for the use of generalized transmission lines where the input parameters are the propagation constant of the line and the impedance. For superconducting microstrip lines both parameters can be obtained theoretically from equations described in section 2.2.2 or can be simulated using a 3D solver.

3.2 Design philosophy

The components designed are classified as the passive devices required for the LO distribution network for both the LFA and HFA arrays and for the HFA balanced mixer. For the power distribution components, it must be considered how CHAI is intended to operate the 64 heterodyne pixels. The 64 pixels are arranged in a 8×8 square array composed of 16 blocks, each with 4 pixels. Inside the 4-pixel block, three 3 dB power dividers are required to distribute the LO signal delivered to the block (Section 1.5). This means that a total of 48 individual 3 dB power dividers are required for the 16 4-pixel blocks. This poses a challenge for the fabrication of the power dividers as it means that the chosen design needs to have a repeatable performance. Hence it is desired that the components designed are modular, have a fast production time and allow for modifications with backwards compatibility. Another restraint is that the chosen design has to be able to be replaced or repaired without interfering with the performance of the mixers that lay on the same block. For this reason and the current technical capabilities at hand at the *I. Physikalisches Institut*, power dividers based on superconductor

films over silicon membranes are chosen instead of waveguide components.

The evaluation of any given component is done by quantifying its S-parameters. The transcendent goal is to achieve a specified pixel sensitivity (sec. 1.5). Still, there is no straightforward way to translate this sensitivity requirement into the realistic performance specifications on the S-parameters of the individual components constituting the network, especially considering them in a complex network scenario. For this reason, there was an incentive to fabricate and test an early batch of components, and from the results obtained, make the necessary adaptations for the next batch. This incentive is strengthened by the availability of resources in the microfabrication laboratory. The first batch/ generation of power dividers was designed and fabricated in late 2019/ early 2020, just before the COVID-19 pandemic, which abruptly interrupted the testing and characterisation. This meant that the second batch/generation of components would come three years later.

For the LFA components, the superconductor of choice is niobium given its gap frequency ($\sim$ 650 GHz) falls above the LFA frequency. The metallization thickness is 150 nm over a 9 μm silicon membrane. The operating frequency of the HFA (800 GHz) means that NbTiN ($f_{Gap} = 1095$ GHz) has to be used instead of Nb ($f_{Gap} = 650$ GHz). components are to be fabricated on a 350 nm niobium titanium nitrate film on top of a 5 μm silicon membrane.

3.3 400-500 GHz planar components

The current section describes the design of microwave components that are required for the power distribution scheme proposed for the 4-pixel block (section 1.6.2). Planar superconducting technology has been chosen over machined waveguides to be the components fabrication scheme. CPW lines and microstrip lines stand over other planar transmission lines like slotlines or striplines due to the ease of design and manufacture. Given the fact that the current size limitation for a substrate to be processed at the Institute clean room is about 30 mm, the ambitious idea of implementing all planar components (LO distribution network and mixers) in one chip is quickly discarded.

The present science case for the CHAI receiver sets the centre frequencies for the LFA, are $f_c^{LFA} = 480$ GHz, and HFA, $f_c^{HFA} = 800$. Even though the components required for the LFA and HFA are of the same kind, the operational frequency of the HFA does not only mean a reduction in dimensions but also the use of NbTiN instead of Nb as superconducting film, whose characteristics must be taken into account in the optimization of the planar

components here presented. The components for the LFA 460-500 GHz are

- 3 dB power divider - CPW 90° Hybrid
- Waveguide-slotline-CPW transition
- Compact termination
- Compact CPW-microstrip transition
- Microstrip Wilkinson

The HFA 780-820 GHz components are

- Mixer hybrid 1 - CPW 90° Hybrid
- Mixer hybrid 2 - CPW 180° Hybrid
- Waveguide-slotline-CPW transition
- Compact CPW-microstrip transition
- Power divider - Microstrip Wilkinson
- RF blocking filter
- SIS twin parallel Tuning structure

3.3.1 First generation 3 dB Power divider

The CHAI focal plane array architecture, at its most basic block, established that the LO radiation must be distributed to four mixers (detailed in section 1.6.2, Fig.1.9 and Fig.3.1). A symmetric 2-stage cascade scheme comprising three 3 dB dividers is selected. Here the input power is divided in two equal parts by the first power divider and subsequently delivered to another two 3 dB power dividers which deliver the power to the mixers. For the choice of power divider based on planar transmission lines, the two most commonly used are the Wilkinson power divider [Wilkinson, 1960] and a 3 dB branch line hybrid [Reed and Wheeler, 1956]. The selection of which one to use depends mostly on the ease of implementation in the transmission line of choice. A comprehensive analysis of more modern designs of the Wilkinson divider can be found on [Pozar, 2011] as well as the analysis of the simplest of branch line hybrid models.

First is the selection of the transmission line in which to implement the power dividers, either CPW or microstrip lines. This decision depends on its feasibility and ease of fabrication given the current capabilities at the microfabrication lab. In this regard, CPW has a clear advantage over standard microstrip lines given that CPW requires metallization on only one plane. Standard microstrip lines require metallization on both sides of the silicon substrate, jeopardizing the feasibility of any design. Nonetheless, this incon-

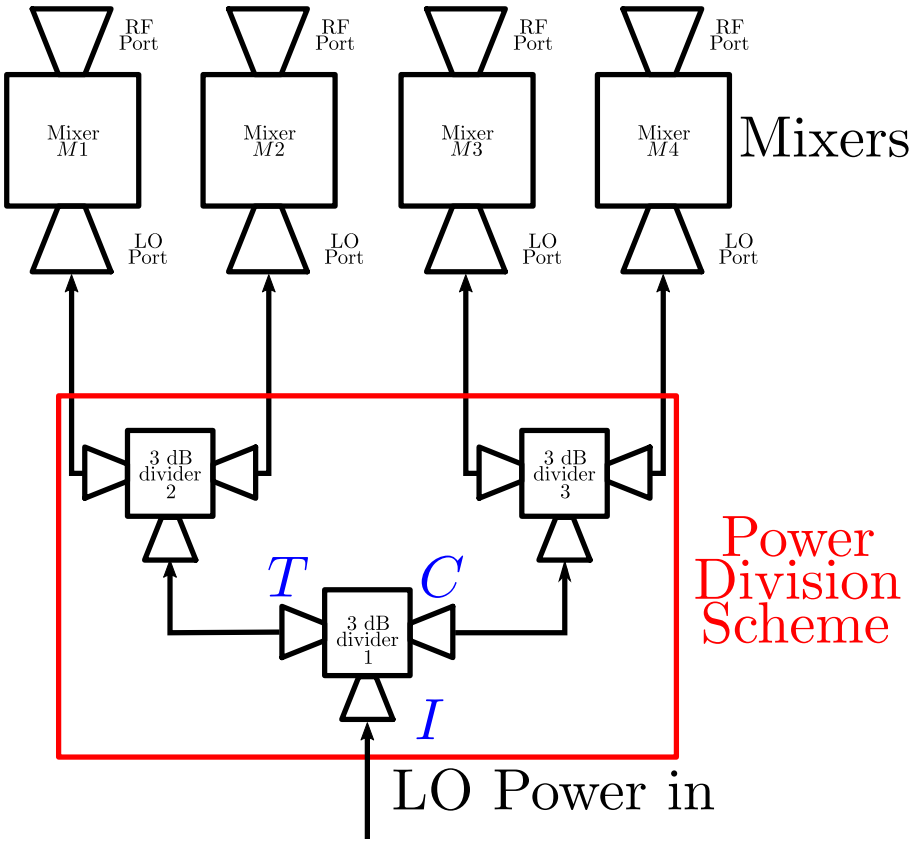

Figure 3.1: Schematic of the 4-pixel block with the 4 mixers. Enclosed in the red box is the power division scheme. This work's proposed power division scheme comprises three 3dB power dividers in a cascade configuration. Blue letters label the ports of the 3 dB power divider. The LO power is received at the input port (labelled with *I*), and it is divided equally to the transmitted port (T) and the coupled port (C)

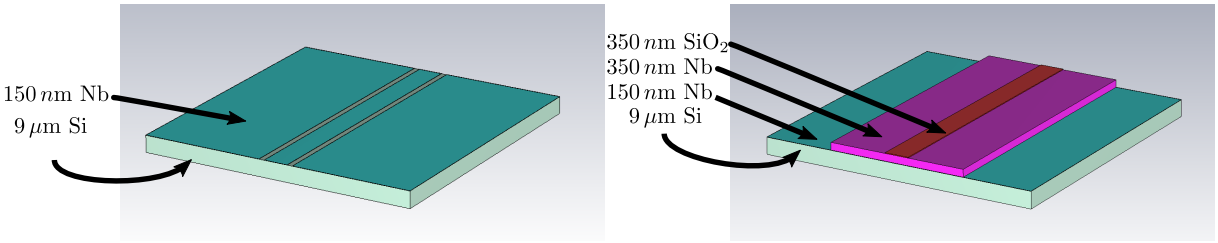

Figure 3.2: Schematic of the CPW and SiO_2 microstrip. **Left:** Schematic of the CPW line. **Right:** Schematic of the SiO_2 microstrip with the layers labeled. The SiO_2 layer thickness is exaggerated for a better display.

venience can be avoided by having a microstrip whose substrate is not silicon, but silicon dioxide (SiO_2) (Fig. CPW and sio2 microstrip **Right**). By sputtering silicon dioxide over a bottom niobium layer it is possible to use this layer as the ground plane and have a microstrip line that requires fabrication on only one side of the substrate. This kind of microstrip line is from here on called SiO_2 microstrip to differentiate it from the standard microstrip on a 9 μm silicon substrate. The caveat of the SiO_2 microstrip is that the silicon dioxide layer can crack and peel off of the ground niobium layer; the risk of

this happening increases the larger the silicon dioxide patch is. Additionally, the coverage of the niobium ground layer may not be perfect and there may be a connection between the ground and top layer of the microstrip line, rendering the line useless. For this reason, the first batch of power dividers, made in Q4 2019, is fabricated on CPW lines as the chances of defects on the fabrication are fewer. For the second batch of power dividers, made in Q4 2023, the devices are built in a combination of CPW and microstrip over SiO_2.

Once the transmission line type has been selected, it is time to choose the power divider itself. It is important to consider the effect the substrate has on the electrical parameters of a coplanar line. Silicon, with its high relative permittivity of 11.9 (Standard value at room temperature, 11.7 at 4 K), reduces the guided wavelength by a factor of ~ 2.7, placing limitations on the geometry of transmission lines. This characteristic of silicon is inconvenient to planar designs, especially when the lines have length constraints and/or have to be bent in special geometries. This will play an important role in the election of the power divider.

A possible candidate for the power division is the branch line coupler. It is a symmetric four-port device proposed by J. Reed and J. Wheeler [Reed and Wheeler, 1956], shown in Fig.3.3 **Top**. The input signal incident on port 1 is divided into ports 2-*transmitted port* and 3-*coupled port*. The ratio between power delivered to these ports can be tuned by the characteristics of the branch lines, with the number of branch lines increasing the operational bandwidth of the device. Port 4 ideally does not receive any signal coming from port 1 and it is called the *isolated port*. A three-branch line design has been selected as it is a good compromise between bandwidth and fabrication feasibility. The reason why not to pursue a design with a broader bandwidth is twofold. First is that with an increasing number of branch lines, the respective impedance becomes larger, leading to impractical lines with extreme dimensions; to the point where the line's dimensions preclude the design of the branch line coupler. For example, a four-branch line coupler with a feed line impedance $Z_0 = 40\,\Omega$ would require lines with an impedance of $\sim 180\ \Omega$. This high impedance value falls beyond a feasible limit of impedance achievable for CPW lines. Second, with an increasing number of branch lines, their impedance has smaller and smaller differences between them, resulting in similar line dimensions for two successive branch lines. This leads to tighter tolerances in the fabrication, resulting in a design whose comparative advantages over a three-branch line coupler do not justify its selection over the latter.

The fact that the branch line coupler only requires straight lines and it is relatively easy to implement in coplanar waveguides drives its selection as the core component for the first batch of power dividers. This design is still nonetheless subject to the silicon effect, Although its effects are not as aggravating as with the Wilkinson divider. This is due that no bent lines are required for this design. This is further detailed in later in this text in section 3.3.2.

The implemented CPW branch line coupler is shown in Fig.3.3. The feed line coming from port 1 has the reference characteristics Z_0 and $\beta_0\,(480GHz)$. These parameters are used for the calculation of the branch line dimensions. from now on, Z_0, β_0 will refer to the main CPW feed/output line that will connect all other CPW components. Following the equations for a three-branch line coupler given in[Reed and Wheeler, 1956], the initial impedance for the branch lines is calculated and given in table 3.1.

There are two important things to consider at this point, before the assembly of the branch line coupler in the 3D simulation software. First, the theoretical analysis of the branch line hybrid done by [Reed and Wheeler, 1956] made several simplifications to ease the analysis of the device. It assumes that there are no fringing effects at the connections between the branch lines (lines Z_a and Z_c) and the main lines (line Z_0). This is usually the case when the dimensions of the line are very small compared to the guided wavelength. In our case, the guided wavelength is $\lambda_{g0} \approx 267$ μm and comparing to dimensions of the lines (table 3.1), especially line Z_c, it can be seen that this statement does not hold any longer, since its width is about $> \lambda_{guided}/10$. This does, effectively, decrease the precision of the analysis done. Second, as discussed in section 2.2.2, the even and odd modes of the CPW are degenerate and both will propagate through the line if the conditions allow it. To suppress the odd mode, grounding bridges are placed at discontinuities in the line, ideally at everyone (section 2.2.2). This solution, however, comes at a cost. It does not only make the fabrication of the device more elaborate but also affects its performance by altering the electrical properties of the transmission line. Grounding bridges introduce a considerable parallel capacitance to ground in the line increasing its capacitance per length. This has the effect of shortening its electric length and lowering the intrinsic impedance of the line at that point (eqs. 2.49, 2.52 and 2.69).

These two factors detune the initial design of the branch line coupler. The effect of the grounding bridges in the CPW lines can be partially compensated by the introduction of an inductive section, which is a thinner section of

line just under the grounding bridge. This section not only reduces the effective capacitance of the bridges but also increases the inductance of the line in that particular section. For the three-branch line coupler, the inductive compensation was not implemented since it was not deemed necessary.

The model is optimized in CST taking the initial dimensions (Table 3.1) as the starting point. The optimization parameters are the impedance of the lines Z_a and Z_c, and the lengths l_0 and l_b. To avoid the introduction of yet another optimization variable, the lines Z_c and Z_a remain with the same length l_b. The final dimensions for the branch line coupler are tabulated in table 3.2). The simulated results of the optimized version are shown in Fig. 3.4. The reflections are below -10 dB in the LFA band as well as the isolation between ports 1 and 4. The balance in power distribution shows that the points of balance achieved at 432 GHz with -3.33 dB and 557 GHz with -3.7 dB. At 480 GHz there is a difference of 0.34 dB in the balance approx.

3.3.1.1 Waveguide to CPW transition

The CHAI focal plane unit and its dimensions set the need for a waveguide to CPW transition. Even if the complete cascade division and the mixer would be carried out in one single chip, the incoming LO power and RF signal are still coupled by a rectangular waveguide. The performance of a waveguide to CPW transition has been proven in [Westig, 2013], by using it as the waveguide interface of the 3 dB coupler of the balanced mixer. Hence the same design is taken for the waveguide to CPW transition and the model developed by Marc Westig is taken as the starting point for a new design.

The feasibility of a tapered slotline antenna was first demonstrated in [Acharya et al., 1993] as a free space antenna. The waveguide-slotline-CPW model that was used in [Westig, 2013], and in this work, was proposed by [Lin and Wu, 2001]. A transmission line schematic and the actual model are presented in Fig.3.5. In this transition, the waveguide TE_{10} couples the 460×230 μm^2 to the silicon substrate through a tapered slotline, whose length is about $\lambda/4$, matching the waveguide to a slotline of impedance 70 Ω. Subsequently, the $\lambda_{slotline}/4$ slotline section ends in a slotline-CPW transition made by the $\lambda/4$ crooked balun and a grounding bridge [Ho et al., 1994a]. [Lin and Wu, 2001] bends the slotline balun to fit in the silicon substrate. For the case of the Waveguide-CPW transition, an inductive compensation for the grounding bridge does not introduce any additional problems to the design, hence it is done by having a reduced CPW main line of 6 μ laying a 3 μm wide Nb film over a 800 nm thick SiO2 section. The dimension of the waveguide-CPW transition is labelled in fig.3.5 and tabulated in 3.3.

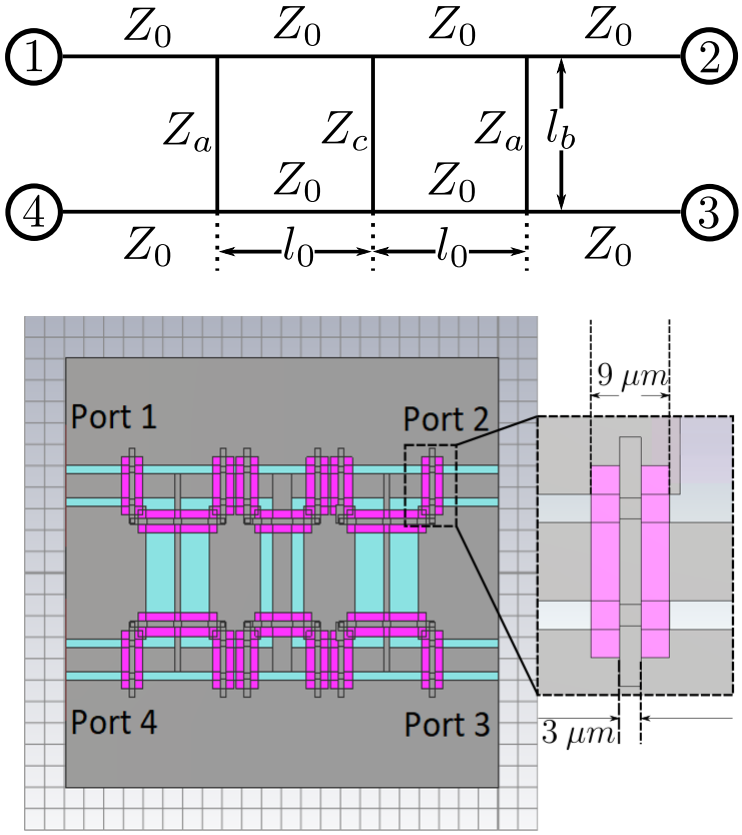

Figure 3.3: **Top:** Schematic of a branch line coupler with the characteristic impedance and length for all sections. Here, port 1 is designated as the input port, The signal is then divided into ports 2 and 3, meanwhile port 4 ideally does not receive any power. Due to the geometry and layout of the branch lines ports 2 and 3 are $\pi/2$ off phase ($\phi_2 - \phi_3 = -\pi/2$). Since the guided wavelength of a given line depends on its impedance, lines Z_a and Z_c should have different lengths ($Lambda_a/4$ and $Lambda_c/4$ respectively). In order not to add complexity to the design they are the same length l_b, corresponding to the design length for line Z_c. **Bottom:** Model of the hybrid on CST. One of the main issues with the model is the modification of the line parameters introduced by the necessary grounding bridges. Here all bridges are 3 μm wide placed on top of a 0.8 μm thick SiO_2 patch

Table 3.1: Initial parameters of the hybrid

Line	Width (W) [μm]	Gap (g) [μm]	Impedance [Ω]	Length [μm]
Z_0	13	3	38.7	$l_0 = 66.6$
Z_a	2	16	105.03	$l_b = 68$
Z_c	8	7	57.15	$l_b = 68$

Table 3.2: Final parameters the hybrid

Line	Width (W) [μm]	Gap (g) [μm]	Impedance [Ω]	Length [μm]
Z_0	13	4	42.05	$l_0 = 53$
Z_a	2.9	14.9	95.11	$l_b = 62$
Z_c	10	5.8	53.68	$l_b = 62$

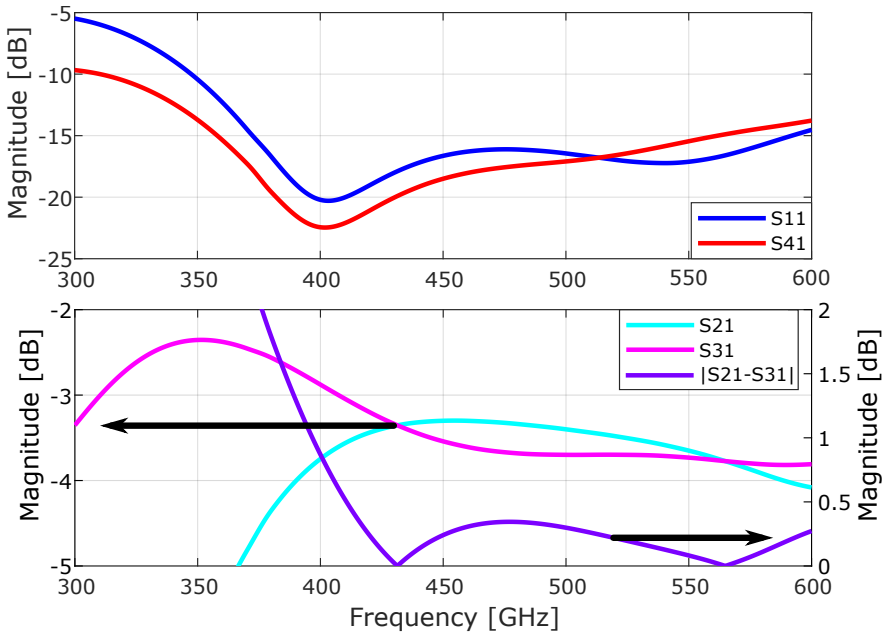

Figure 3.4: Parameters of the three branch line coupler. **Top:** Reflection and transmission to isolated port, both parameters are well below the requirements of −10 dB. **Bottom:** Transmission to transmitted and coupled port.

An aspect that was not explored in the design process done by [Westig, 2013] is the interaction between the waveguide cavity and the membrane cavity. The membrane cavity is defined as the cavity that houses the silicon membrane. It differentiates from the waveguide as it has a reduced height of 200 μm and starts immediately after the tapered slotline antenna. The interface between the membrane cavity and the waveguide is marked with the dotted red line in Fig. 3.6. The effect of the milling tool is incorporated into the design and it has a milling radius of 100 μm in the corners of the waveguides. By increasing the distance that the waveguide enters into the membrane cavity it is possible to further tune the parameters of the antenna. The optimum distance that the waveguide enters the membrane cavity is 60 μm. The simulation results of the antenna are shown in Fig. 3.7. Reflection over the band from both ports, the CPW and the waveguide ports are below −20 dB and the transmission from CPW to the waveguide is above −0.4 dB in the LFA band. This model of the slotline antenna is used for the first generation of power dividers based on the three-branch line coupler.

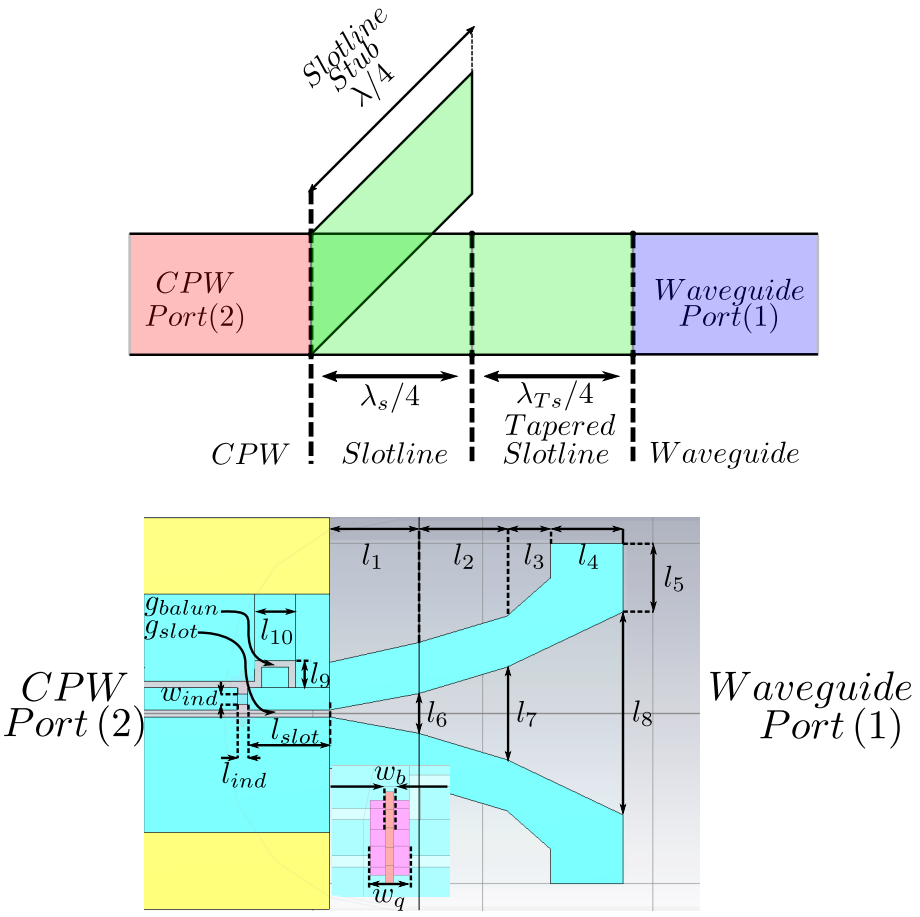

Figure 3.5: Waveguide to CPW transition. **Top:** Transmission line schematic of the waveguide to CPW transition. For clarity's sake, the different transmission line types have been marked with different colours. **Bottom:** Model of the Slot antenna with the dimensions labelled. The slotline serves as a $\lambda/4$ transformer between the waveguide and the slotline section, labelled with l_{slot}. The slotline is then adapted to the CPW by the use of a $\lambda/4$ slotline balun. There is a grounding bridge to impede the excitation of the CPW odd mode at the interface between the slotline and the CPW lines.

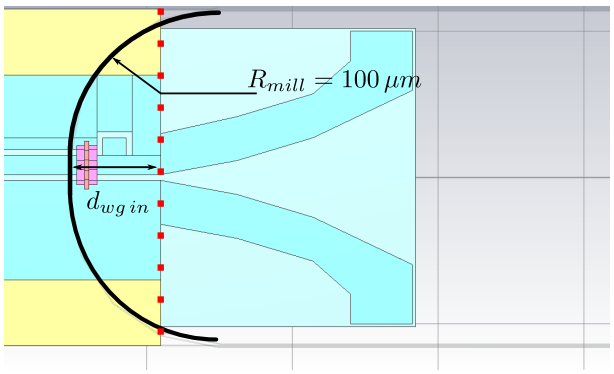

Figure 3.6: Top view of the waveguide-CPW transition. Here the limit between the membrane cavity and the waveguide is marked by the red dotted line. Standard waveguide-slotline transitions have the waveguide ending where the membrane cavity starts.

Table 3.3: Parameters of the Waveguide-CPW transition

Parameter	length [μm]	Parameter	Length [μm]	Parameter	Length [μm]
l_1	52.2	l_7	54.4	g_{balun}	4
l_2	52.2	l_8	119.2	l_{ind}	6
l_3	25.7	l_9	16.1	w_{ind}	6
l_4	42.4	l_{10}	24.1	w_b	3
l_5	40.4	l_{slot}	47.9	w_q	9
l_6	23.2	g_{slot}	4	$d_{wg\,in}$	60

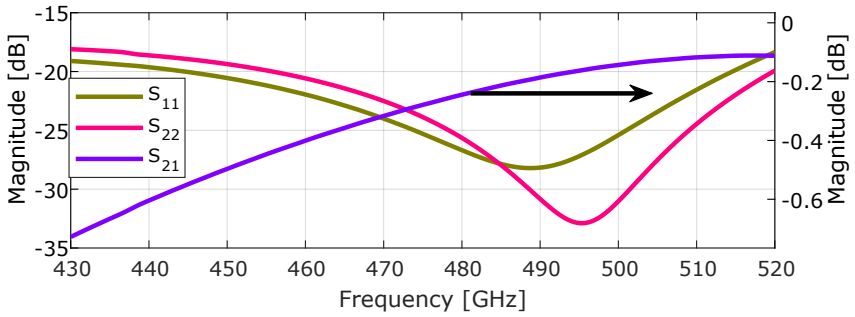

Figure 3.7: Parameter of the tapered slotline antenna. Both reflections at the waveguide port (S_{11}) and the CPW port (S_{22}) are below -20 dB of reflections in the band.

3.3.1.2 CPW bends

For the integration of the three-branch line coupler and the waveguide to CPW transitions, it is necessary to incorporate 90° and 45° bends. To reduce the footprint of the membrane, a compact 90° CPW chamfered bend is selected (Fig. 3.8). The bend requires two grounding bridges to hinder the odd mode propagation and ensure the wavefront remains symmetric concerning the propagation direction of the line [Lahiji et al., 2010]. The added capacitance of the airbridges is then compensated with inductive sections under them. The bend has a chamfer in both the main line as well in the outer ground plane, with the gap of the line remaining constant. The depth of the chamfer is such that the chamfered sections are 1.86 times the width of the main line [Rida et al., 2009, Zou et al., 2010]. The dimensions of the 90° can be found in table 3.4.

A double 45° bend, or S-bend, is also designed to centre the CPW-waveguide transition concerning the branch line coupler. This bend requires two pairs of grounding bridges, a pair for each bend. Since the required dimension for the chamfer in this 45° bend moves into the location of the grounding bridges, these bridges do not have direct inductive compensations as is the case for the 90° bend.

The reflection at the ports of both bends is below -15 and -25 dB respectively. This design allows for the integration of the three-branch line coupler,

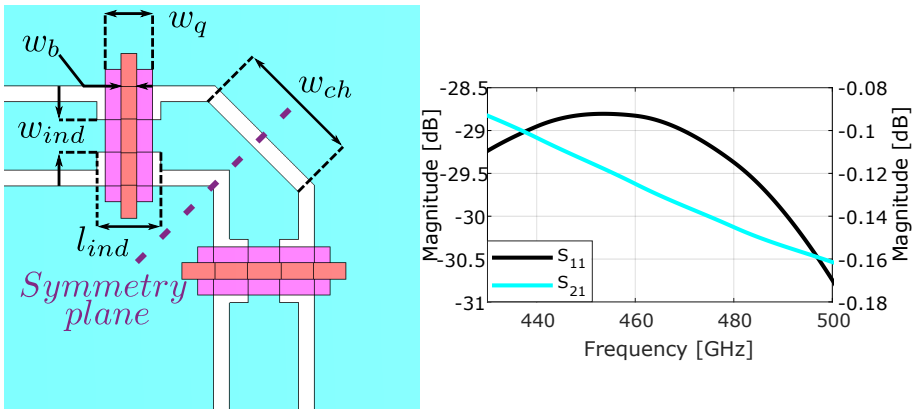

Figure 3.8: Mdeol of the CPW 90° bend. This kind of bend requires grounding bridges before and after it to avoid the excitation and propagation of the odd mode. This also ensures the wavefront remains symmetric concerning the direction of the wave propagation. The grounding bridges are the same as the ones used in the branch line couplers and the slotline antenna. Their placement is symmetric concerning the plane denoted in the image.

Table 3.4: Parameters of the CPW 90°

Parameter	length [μm]
w_{ind}	6
l_{ind}	12
w_b	3
w_q	9
w_{ch}	24.18

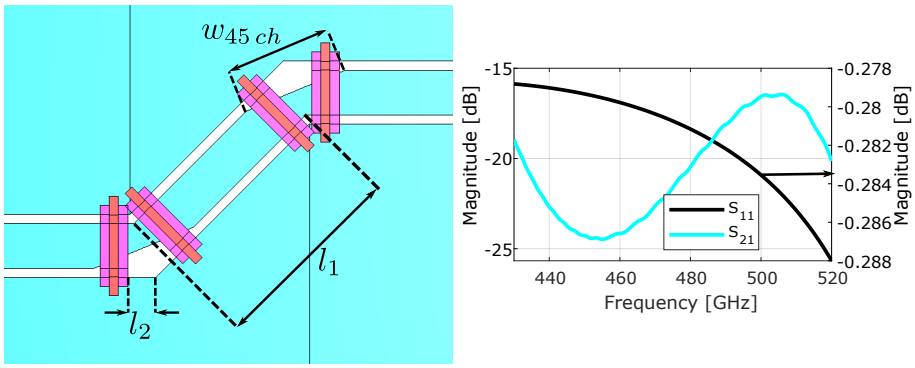

Figure 3.9: CPW 45° S-bend. Since this S-bend is composed of two consecutive 45° bends it does require four grounding bridges in total. In contrast to the 90° bend case, the air bridges are not directly compensated by an inductive section under them. Instead, only the main line has a chamfer and the ground is left without it. This produces an inductive loading of the line that compensates for the added capacitance introduced by the grounding bridges.

Table 3.5: Parameters of the CPW S-bend

Parameter	length [μm]
$w_{45\,ch}$	65.3
l_1	12
l_2	9.3

the load and the CPW-waveguide transitions on one membrane.

3.3.1.3 Termination of the isolated port (Port 4)

The branch line coupler design presented in section 3.3.1 (Fig. 3.3) makes use of the power division from port 1 to ports 2-3 to distribute the LO power to all mixers and leaves port 4 unused. Since the branch line coupler itself is a symmetric device, any power reflected from port 4 will be retransmitted to ports 2 and 3. At first glance, this feature does not seem so important that it needs special attention after all the incoming power is delivered through port 1, which is isolated from port 4 by design and reflections from ports 2 and 3 are not expected at this stage. However, considering the coupler embedded in the distribution network and recalling mixer operation conditions, those statements do not hold any longer. This is because a low-noise SIS mixer, in general, is not well matched to its input port over the complete frequency band of interest.

For the design and construction of terminations, there are two approaches depending on its dimension. There is the distributed load, whose dimensions are comparable to the guided wavelength, and hence, must be treated as distributed elements. The second approach is lumped element approximation, in which the dimensions of the termination are small compared to the guided wavelength. These elements are treated as *lumped/concentrated* elements such as resistors, capacitors or inductors.

There is also the consideration of which transmission line the termination will be implemented, as the geometry of the termination depends on the transmission line. Waveguide terminations are an example of the distributed approach. These kinds of terminations usually involve an absorptive conical/pyramidal wedge structure placed in the waveguide. They have been extensively used and tested, where usual reflection from such structures are under -30 dB [Mena and Barishev, 2005, Kerr et al., 2014, Hesper et al., 2017]. Such results make this kind of termination an attractive possibility to terminate the isolated port of the hybrid. On the other hand, for planar circuit loads, usually the lumped element approach is used, mainly due to the ease of integration with the branch line coupler. At the time of designing the power divider, no implementation of a CPW termination in a high frequency scenario was found in academic literature. For microstrip lines termination and attenuators based on thin film resistors have been developed for frequencies up to 50 GHz [Monje et al., 2005, Cuong et al., 2007, Lopez-Berrocal et al., 2009, Li et al., 2021]

Since waveguide termination technology is an already mature technology with proven performance in the microwave frequency range and astronomical receivers, it is the first termination to be studied as a possible termination for the branch line coupler. The feasibility of a waveguide termination depends on the possibility of having a branch line coupler with four waveguide transitions. This since 3 waveguide ports are required to receive and divide the incoming power and the fourth waveguide port has to be terminated in a waveguide load. An initial integrated model with four waveguide transitions is shown in Fig. 3.10 with promising results (Fig.3.11). Nevertheless, this model runs into the problem that the distance between the output waveguides is too small compared to the recommended distance by manufacturing personnel of 700 μm [Mechanikwerkstatt, 2018]. The fact that the footprint of the CPW branch line coupler is comparable to the footprint of the waveguide to CPW transition makes it difficult to adhere to this distance requirement. A possible solution for this is to increase the length of the lines between the branch line coupler and the waveguide transitions. Additionally, the orientation of this transition can be changed to increase the distance between waveguide walls. These solutions come with the problem that longer CPW lines require grounding bridges to hinder the propagation of the odd mode, otherwise it couples to the cavity generating a myriad of resonances. A model with these considerations implemented is shown in Fig.3.12 with results shown in Fig. 3.13. This model is the seventh iteration of the design in an attempt to remove the cavity resonances of the model. Still, a resonance is visible at 487.5 GHz. The modifications added to maximize the distance between the waveguide and the suppression of the CPW odd mode deteriorates the performance of this model, the reflections are under -13 dB and the amplitude imbalance is about 1.2 dB.

The antagonistic goals of increasing the cavity size, maximising the distance between the output waveguides, and minimizing the circuit footprint, to avoid the coupling to cavity resonances, set a trade-off where neither of the outcomes is acceptable. Given the time constrictions and resources at hand, designing a power divider with a waveguide termination is therefore deemed not feasible.

Moving to an on-chip CPW termination requires a resistive material first. Titanium Nitrate is a superconducting material whose bulk transition temperature is 5.3 K. In thin films of TiN, the critical temperature and DC resistance depend on the thickness of the film. For a 90 nm thin film the critical temperature measured is 1.8 K and has a DC sheet resistance of 25 $\Omega/\square$. It is assumed that the electrical properties of TiN at 500 GHz do not

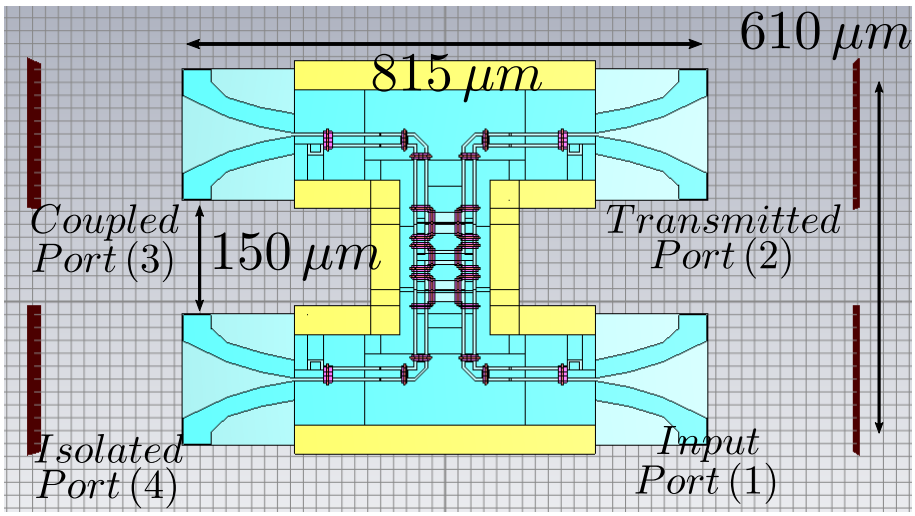

Figure 3.10: CST model of 90° branch line coupler with four waveguide transitions. Here the transitions are placed symmetrically without the addition of an extended CPW line to separate the waveguide-CPW transitions. This presents a challenge for the manufacture of the cavity as the distance between the waveguide should be at least 700 μm.

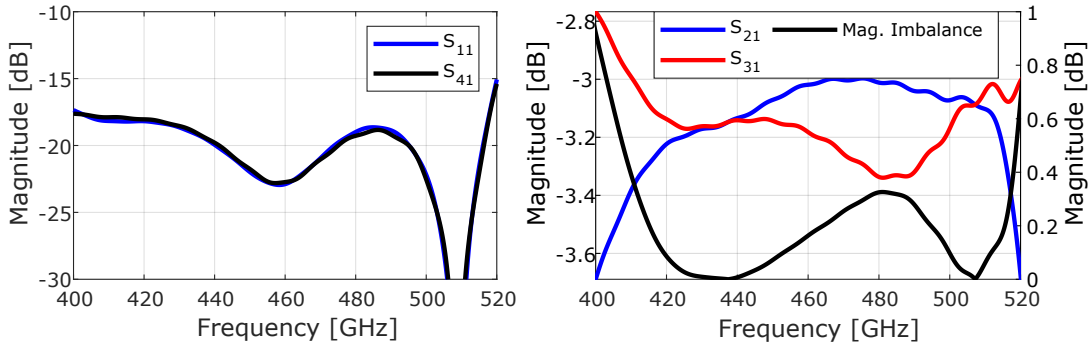

Figure 3.11: S-parameters of the 90° branch line coupler with four waveguide transitions.

vary significantly from its DC characteristics. Taking these values for the sheet resistance a load of dimensions 13×20 μm^2 (Fig. 3.14) is designed by using the sheet resistance equation $Z_L = R_\square \cdot L$. The width, and hence length, of the termination has the same width of the feed line Z_0 to avoid fringing effects and parasitic caused by the corners of the line. The 13×20 μm^2 dimensions give a resistance of $R_{lumped} = 38\,\Omega$. The small difference between R_{lumped} and Z_0 is due to a mistake that was made in the calculation of the line impedance at the moment of designing and integrating the load. Another important point to consider is that for the lumped element approximation to hold, the length of the element must be small compared to the guided wavelength. In general, the lumped element approximation is summarized as $l_{component} \ll \lambda_{guided}$. Considering that $\lambda_{guided}(480GHz) = 266.4$ μm, the length of the load is about one-thirteenth of the λ_{guided}. Considering these dimensions, the lumped element approximation is expected to

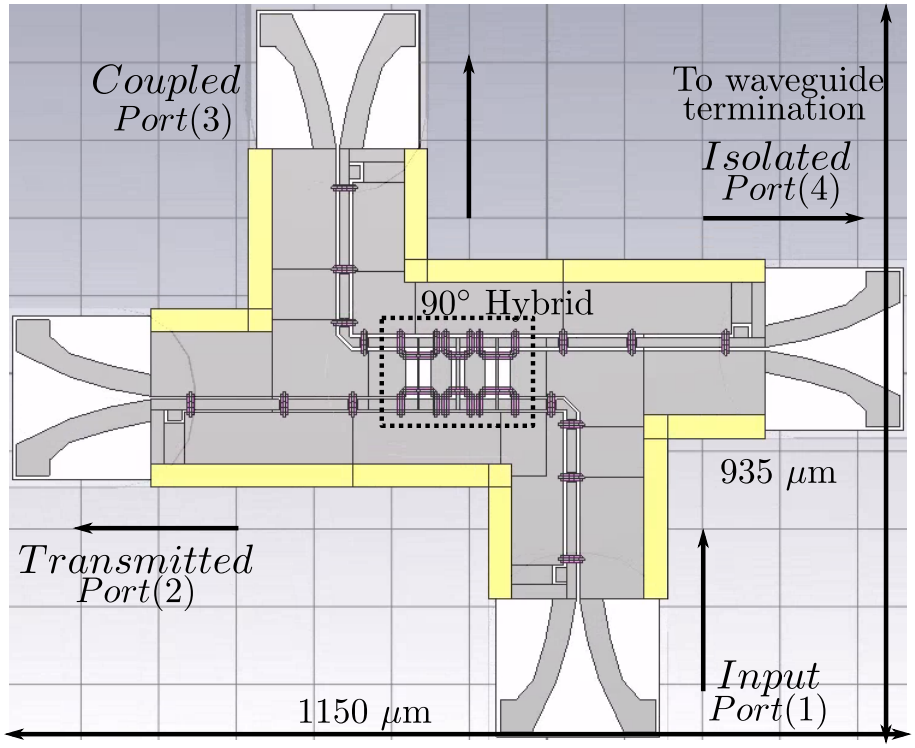

Figure 3.12: 90° hybrid with four waveguide interfaces. The arrangement of the four outputs follows the necessity for a structurally sound cavity, where the thickness of the walls separating the waveguides should be greater than 700 μm. The additional grounding bridges on the CPW lines between the antennas and the 90° hybrid are added to prevent the CPW odd mode, which easily couples to cavity resonances.

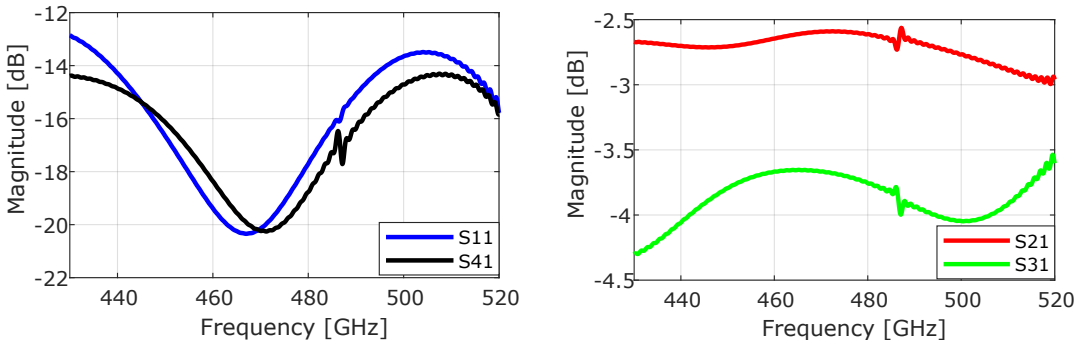

Figure 3.13: S-parameters of the 7th iteration of the 4 antenna hybrid. **Right:** Reflections at the input port 1 and transmission to the isolated port 4. **Left:** Transmission to port 2 and coupling to port 3 from the input port 1. A clear resonance can be seen at 487.5 GHz. Even though the magnitude may seem insignificant in the simulation, it is still an undesired feature in the design given that interactions in the complete power division block may enhance its effect. Additionally, the amplitude imbalance (S_{21}/S_{31}) is larger than 1 dB.

hold. The simulation results show that the reflections of the load are below -10 dB Fig.3.7. However, the simulated results suggest a deviation from the expected behaviour as a simple lumped resistance of $Z_l = 42\ \Omega$, since termination of that $Z_{load} = 38\,\Omega$ would not produce low reflections at all, since $\Gamma = (Z_0 - Z_l)/(Z_0 + Z_l) = (42 - 38)/(42 + 38) = 0.05 = -26$ dB. This load is implemented despite this fact in a branch line coupler to test its

characteristics and find out its behaviour at microwave frequencies.

The second type of termination consists of a lossy resonator termination. It is the same as the TiN film lumped element load, but in this case has a wide grounding bridge partially over it. This is expected to increase the losses turning the termination into a lossy resonator. The results are in Fig.3.7 and it shows a better performance than with the lossy resonator as the reflections are below −15 dB in the LFA band.

The last termination is the short circuit termination as it will serve as a calibration termination. This termination produces a complete reflection at that point. Additionally, a power divider with a short circuit termination is a component with one fewer uncertainty. A short circuit has known parameters, contrary to the other loads where the properties of the TiN at the LFA frequencies are still uncertain.

3.3.1.4 CPW branch line power divider with integrated load

Three branch line coupler designs are integrated, one with every different termination. For convenience, they are referred to as **H2N**, model terminated with the concentrated resistor, **H2L**, terminated with the lossy resonator and **H2S**, terminated with the short circuit. The parameters for the H2N model are presented in Fig.3.16. Results for power dividers terminated with a lossy resonator and a short circuit are presented in Sec.5.2 where the simulations of all fabricated models are presented. The reflections of the model **H2N** are below −12 dB and the isolation between output ports. The transmission towards the output ports has the points of equal division at 420 and 489 GHz with an overall magnitude imbalance under −0.5 dB in the 460-500 GHz band. It can be seen that the magnitude imbalance quickly increases after 490 GHz. This and the concern that if there is a frequency downshift between the designed and fabricated model, the magnitude imbalance at 490 GHz may be greater than expected. For this reason, a power divider where the dimensions of the lines have been reduced by 3% is integrated. This change in the dimensions shifts the frequency response of the device about 3%. The simulated results of this model are shown in Fig.3.17 and labelled as **H3N**. This model exhibits higher overall reflections over the band. The magnitude imbalance of this model is under 0.3 dB in the LFA band with the points of equal power division at 450 and 503 GHz. The model has an imbalance of 0.5 dB over the 440-510 GHz band.

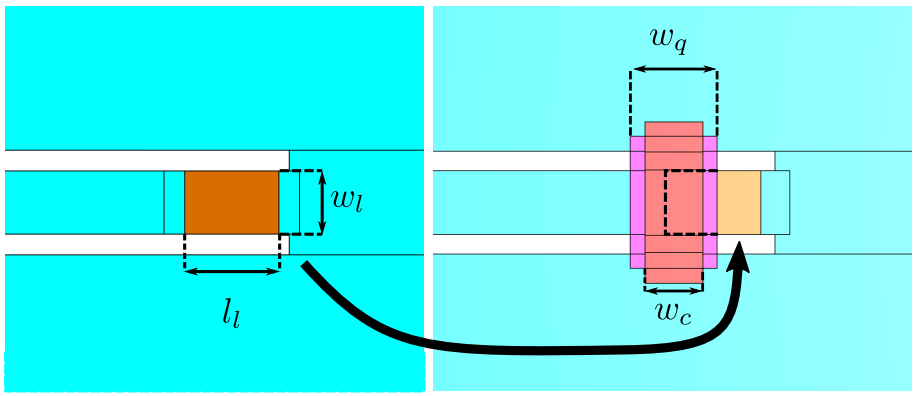

Figure 3.14: Models of the CPW line terminations **Left:** CST implementation of the concentrated resistor. **Right:** CST implementation of the lossy resonator termination. Here the underlying assumption on these terminations is that they are small enough to be treated as lumped element terminations. That is, these terminations can be represented as a combination of resistor, capacitance and inductance elements.

Table 3.6: Parameters concentrated and lossy resonator termination

Parameter	length [μm]	Parameter	length [μm]
w_l	6	w_1	12
l_l	12	w_c	18

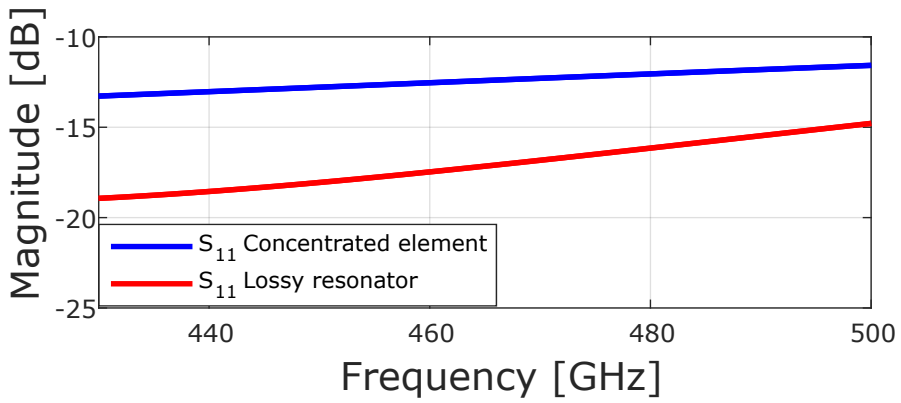

Table 3.7: Parameters of the CPW terminations. The short circuit termination parameters are not included in the graph as they are already known.

3.3.2 Second generation 3 dB Power divider

The results obtained from the simulation show that models **H2N** and **H3N** should work as standalone components. Reflections of -13dB mean that only 5% of the power gets reflected and transmissions of 3 ± 0.5 dB equate to a $50.45 \pm 5.79\%$ of power transmitted. In light of these facts and considering the aforementioned interest in a quick fabrication and characterization (in particular, to test the concentrated terminations on the coupler) led to the fabrication of the devices before any complete receiver description was made. In Chapter 5, a study on how the network's overall parameters are affected by the properties of its individual components is presented. This study serves

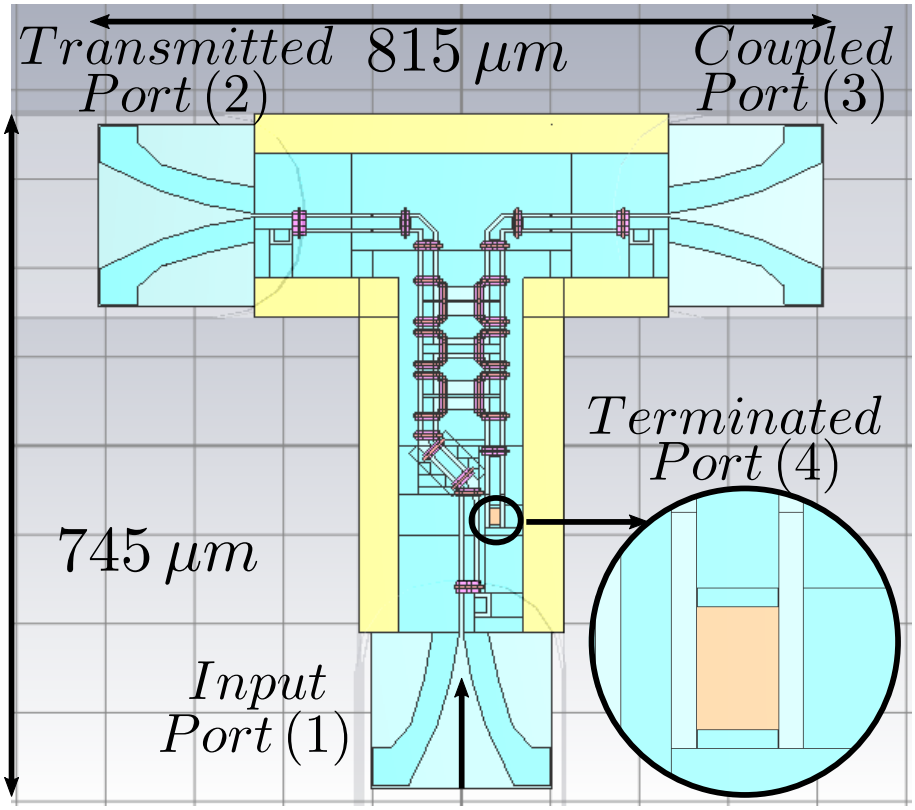

Figure 3.15: CST model of an integrated power divider based on a three-branch line coupler with the isolated port terminated on a concentrated resistor load.

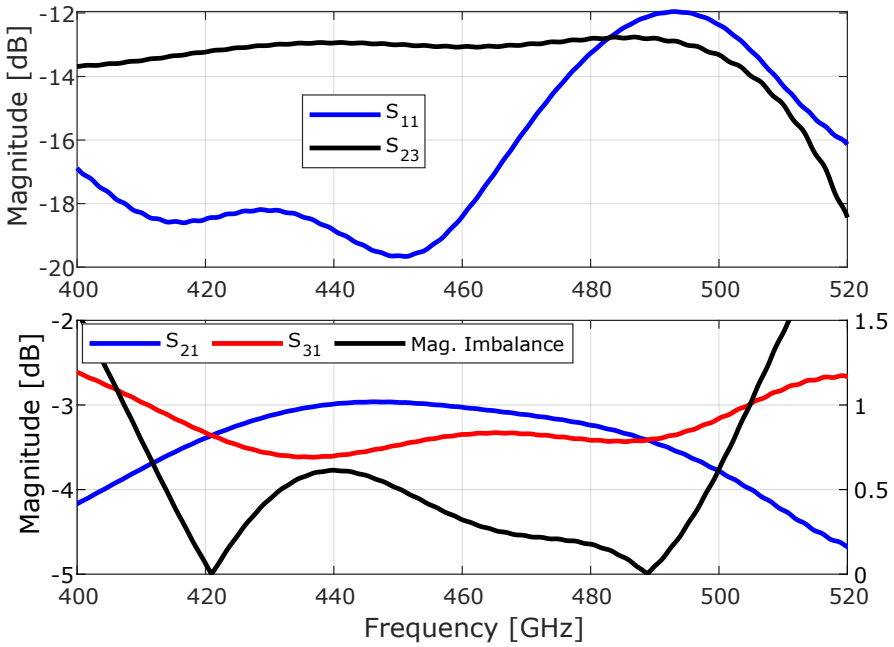

Figure 3.16: S-parameters of the power divider terminated on a concentrated resistor (H2N).

to evaluate the effect of individual mismatches and imbalances and set a desirable limit for them. Additionally, After testing the first batch of devices in the 2-pixel block it turned out that the overall performance was not as desired, prompting the search for an alternative power divider model.

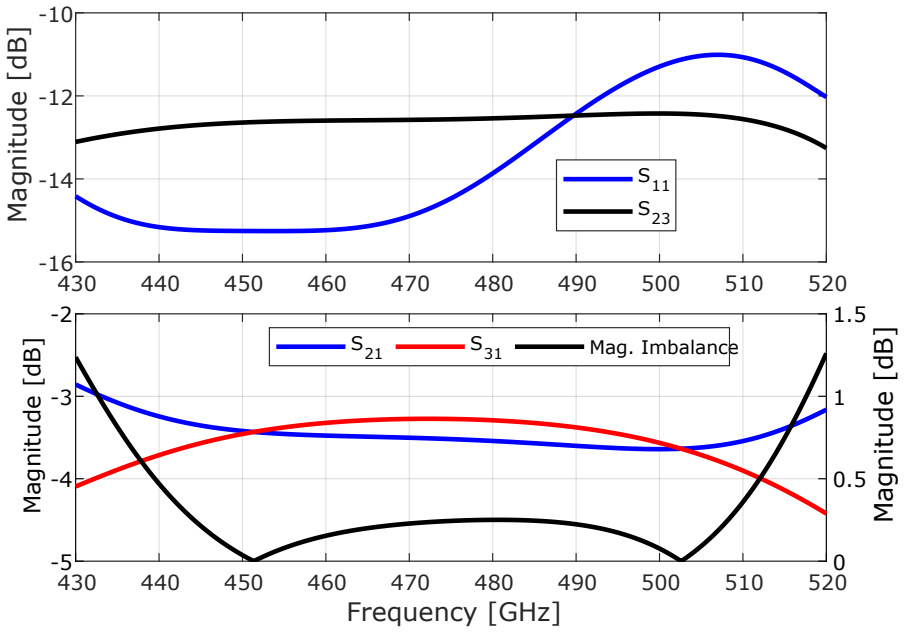

Figure 3.17: S-parameters of the up-shifted H3N power divider terminated on a concentrated resistor.

The other possibility mentioned at the beginning of sec. 3.3.1 for a power divider is the Wilkinson power divider [Wilkinson, 1960]. Since it is a three-port component, it dispenses with a transmission line termination and it has, in principle, a balanced power division. A CPW microstrip Wilkinson was not considered due to the difficulties of implementing it on CPW transmission lines (Fig 3.18). Here both output lines have to be connected by a small lumped resistor $\lambda/4$ from the point of division for the device to work properly. The inherent architecture and distribution of the CPW lines and their ground planes complicate the implementation since it requires bends in a relatively short and wide line. This leads to increased fringing effects in the fields of the structure. Furthermore, the CPW lines require grounding bridges between the three ground planes, this not only makes the design mode difficult but also negatively affects the parameters of the design, possibly jeopardizing its functioning. This elicits the question of whether it is possible to implement a design based on microstrip lines.

The first problem this idea comes across is the fact that microstrip lines require a ground plane on the bottom of the substrate. Currently, is not possible to have a design which has superconducting Nb on both faces of the silicon membrane. This poses a considerable complication for a possible microstrip Wilkinson design. The solution is to have both the microstrip line and the ground plane in the same face of the substrate. This is achieved by sputtering SiO_2 over the Nb (the microstrip ground plane) and then sputtering a second layer of Nb (the microstrip line) on top of it. This has already

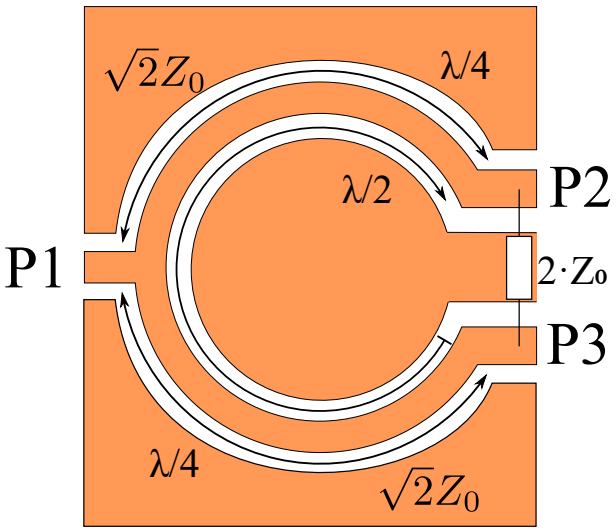

Figure 3.18: Schematic of a Wilkinson divider *Source: provided by Wikipedia user Stündle.* The geometry required for the Wilkinson power divider demands that the branches are connected by a resistor of value $R = 2 \cdot Z_0$. For the case of CPW lines, achieving this geometry is particularly hard given how comparatively wide the lines are in comparison with λ_g. The design is also negatively affected by the addition of grounding bridges at every discontinuity. These two factors reduce the performance and bandwidth of the design, and hence, the attractiveness of a possible implementation in CPW lines

been done on [Westig, 2013] where the tuning structure of the twin parallel SIS junctions was done on a microstrip over Nb film.

Using this fabrication scheme, a Wilkinson power divider is then designed in a 400 nm superconducting Nb microstrip line over 300 nm $Si0_2$ and 150 nm Nb ground plane (Fig.3.19). This line is chosen because it represents a compromise between the impedance of the main line and its width. This line has an impedance of $Z_{micro} = 19\,\Omega$. This traduced on an impedance value for the output arms of $Z_{arm} = \sqrt{2} \cdot Z_{micro} = 26.8\,\Omega$, which is achieved by a $2\,\mu$m wide line.

What differentiates the Wilkinson divider from a standard Y divider is the isolation between the output ports. The isolation is achieved by connecting the output arms with a resistance of $R = 2 \cdot Z_0$ at $\lambda_g/4$ from the division (Fig. 3.19). The output has to be curved to be connected by the small resistor. For this case, the chosen design dispenses with the use of compact 90° bends and uses round arms instead. The reason for this is that compact bends require a chamfer compensation similar to the ones used in the CPW designs (Fig.3.8) that has a depth of $\sim$ 70% of the width of the line [Rida et al., 2009]. For a $2\,\mu$m line this means that at the narrowest section, there is only a $0.6\,\mu$m width line. This tightens the tolerances in the manufacturing process and increases the chances of an open line in the manufactured device. The designed Wilkinson power divider is shown in Fig.3.19. It is important to remember

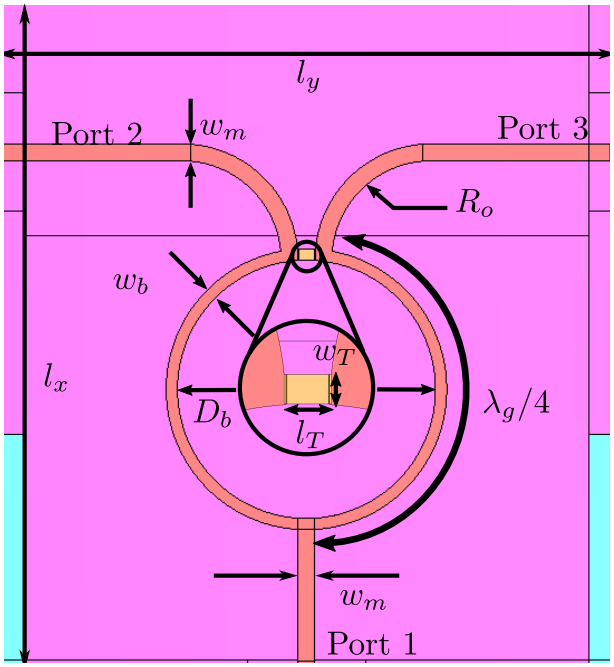

Figure 3.19: Microstrip Wilkinson design with the tree ports labelled. The signal is injected through port 1 and it is divided equally towards ports 2 and 3. The resistor situated at $\lambda_g/4$ from the division ensures the isolation between the output ports 2 and 3.

Table 3.8: Parameters of the microstrip Wilkinson power divider

Parameter	length [μm]	Parameter	length [μm]	Parameter	length [μm]
w_m	3	w_T	2	l_x	105
w_b	2	l_T	2.8	l_y	108
D_b	46	R_o	19.1	λ_g	299

the effect the superconductivity has on the transmission lines, by increasing the inductance of the line the wavelength is smaller than a a comparable line with normal conducting lines. This feature is an advantage in this setting as it helps reduce the overall footprint of the SiO_2 patch required.

The properties of the Wilkinson make it a promising device for the second generation of power dividers. This provided that the waveguide-microstrip interface could be designed and fabricated.

3.3.2.1 Waveguide-Microstrip transition

The problem with structures over an extended SiO_2 patch is that the layer is prone to break and flake off. The larger the patch, the greater the chance of this happening. This does not pose a considerable problem for the Wilkinson divider itself, which has a footprint around 110 x110 μm^2 (Fig.3.24). However, any design with a direct microstrip-waveguide interface runs the very plausible risk of failing due to the SiO_2 patch flaking off of the membrane and taking the Nb layer with it. This is mainly due to the larger dimensions required for a waveguide transition. The minimization of this problem in-

volves the reduction of the patch diameter; A solution that directly clashes with the maximization of the distance between waveguide outputs set by the manufacturing capabilities at hand. Additionally, such waveguide-microstrip transition has yet to be designed and optimized. In light of these facts and the scarcity of time, pursuing a power divider design based purely on SiO_2 microstrip transmission lines is not a feasible option. The solution that circumvents the aforementioned problems is having a design that makes use of the already designed waveguide-CPW transitions. Then, only a CPW-microstrip transition is required to deliver the power to the microstrip Wilkinson power divider. This is achieved by a $\lambda/12$ transformer. The advantage is that both, the Waveguide-CPW transition and the concept of $\lambda/12$ transition, have been tested.

The CPW to microstrip transition concept was originally proposed by Marc Westig for his balanced mixer design [Westig, 2013] where a $42\,\Omega$ CPW is matched to a $21\,\Omega$ microstrip line. It is a design that takes advantage of the compact impedance transformer proposed by [Braham, 1961] and it uses it to adapt two different transmission lines of different impedance Z_{CPW} and Z_{micro}.

This compact 12th λ transformer 3.20 matches line Z_a to line Z_b by two sections of impedance and length Z_b,l_b and Z_a,l_a. The matching condition is that, at the symmetry point of the transformer, the input impedance seen towards lines a (Z_a^{in}) and b (Z_b^{in}) has to be the same. This yields the condition for the electrical lengths, shown in eq.3.2. The limit case of equal impedance gives the largest electrical length required for impedance matching, that is $l = \lambda_g/12$, for every other case the electrical lengths will be shorter than 1/12th of the guided wavelength.

$$\frac{l_a}{\lambda_a} = \frac{l_b}{\lambda_b} = \frac{1}{2\pi} atan \sqrt{\frac{\xi}{\xi^2 + \xi + 1}} \tag{3.2}$$

where $\xi = Z_a/Z_b$. For the implementation of this transformer, the input lines to be matched are a CPW and microstrip, where $Z_{CPW} = Z_a$ and $Z_{micro} = Z_b$. The CPW line is the standard $Z_0 = 42\,\Omega$ meanwhile the microstrip line is the SiO_2 microstrip line. A $3\,\mu$m line over the 300 nm SiO yields $Z_{micro} = 19\ \Omega$. From a theoretical point of view, this transformer only requires that the conditions set on matching sections are met. This means that the Z_b line of the matching section does not necessarily have to be a SiO_2 microstrip, but it can be any line that meets the impedance and electrical length requirement. The line selected is an inverted microstrip line, where

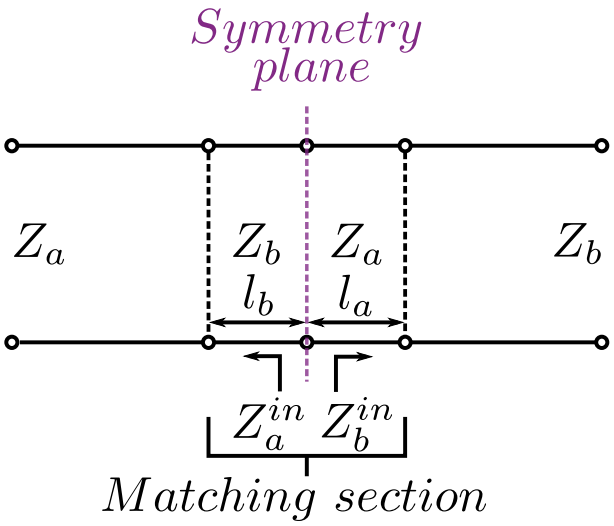

Figure 3.20: Schematic of the compact 12th transformer. The matching condition is set by equating the input impedance $Z_a^{in} = Z_b^{in}$

the main CPW line is covered by a grounding bridge that acts as the ground plane of a microstrip.

The designed transformer is shown in Fig.3.21. The reflections seen from both ports, the CPW and the microstrip are below −20 dB over the LFA band.

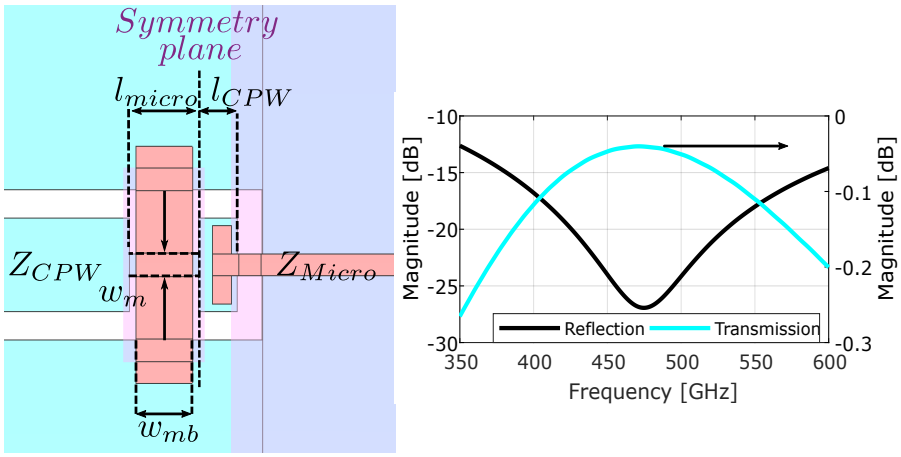

Figure 3.21: CPW to microstrip transition. The design uses an inverted microstrip section to achieve the required impedance of the first section of the transformer. For the second section of the transformer, the design uses the standard CPW line.

Table 3.9: Parameters of the 12th transition

Parameter	length [μm]
l_{micros}	11.1
l_{CPW}	6.2
w_m	3
w_{mb}	9.1

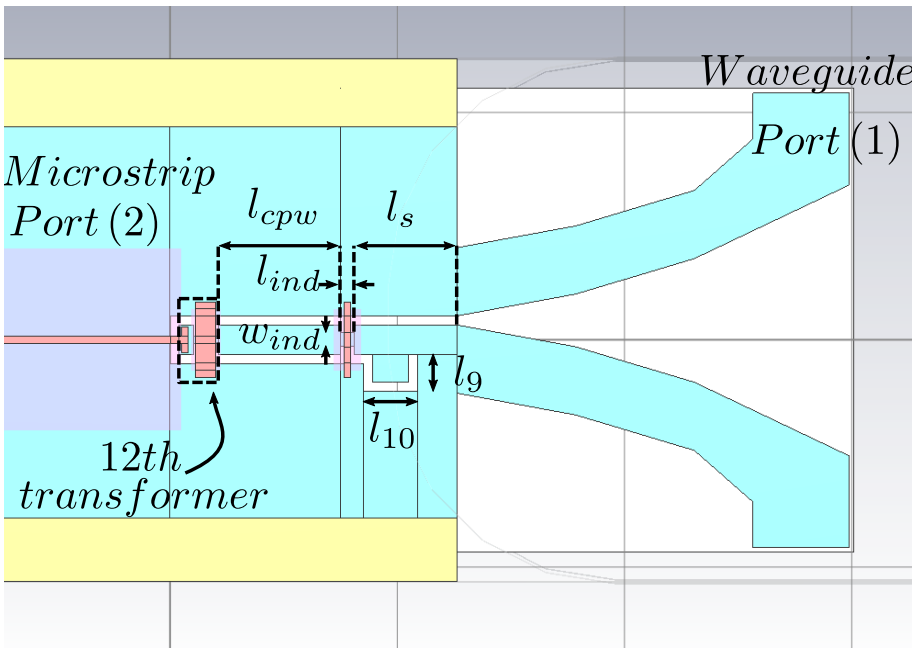

Figure 3.22: CST model of the waveguide-microstrip transition. This mode differs from the waveguide-CPW transition since the input impedance is no longer the CPW impedance but it adds the 12th λ transformer. The distance the waveguide enters the membrane cavity is 30 μm in contrast to the 60 μm for the waveguide-CPW transition for the branch line power divider.

Table 3.10: Parameters of the Waveguide-microstrip transition

Parameter	length [μm]	Parameter	Length [μm]
l_{cpw}	43.8	w_{ind}	6
l_s	45.4	l_{ind}	6
l_9	18.1	l_{10}	26.1

3.3.2.2 Waveguide-CPW-microstrip transition

The waveguide-CPW interface used for the second generation of power dividers is of the same kind as the one in the three-branch line coupler power divider. That is a waveguide-slotline-CPW transition. The difference is that now the input line is not a CPW, but a microstrip instead (Fig. 3.22). This means that the input impedance seen from the slotline sections is no longer the impedance of the Z_{cpw} but the impedance of the complete CPW-microstrip transition.

The waveguide-slotline transition remains unaltered as well as the dimension of the grounding bridge at the CPW-slotline interface. The matching between the 12th transformer and the slotline antenna is done by adjusting the dimensions of the bent slotline balun, modifying the inductive compensation of the grounding bridge and changing the distance the waveguide enters the membrane cavity. The results show reflections below -20 dB in the LFA band at both, the waveguide and microstrip port. These results make the transition suitable to be used in the Wilkinson power divider (Fig. 3.23).

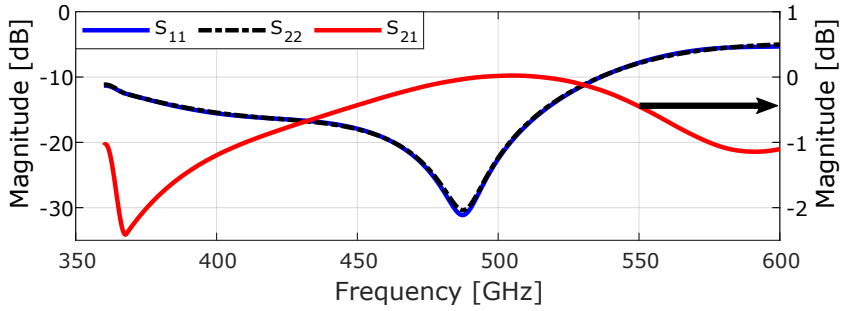

Figure 3.23: Parameters of the waveguide-microstrip transition

3.3.2.3 Complete microstrip Wilkinson power divider

Fig. 3.24 shows the integrated Wilkinson power divider designed. Results are shown in Fig.3.25. This design shows reflections under −20 dB at the input and output ports meanwhile the transmission between the transmitted and coupled port is below −30 dB in the LFA band (Fig.3.25 **Top**). On the other hand, the power division to both output ports is about −3dB across the band. Simulations show that there is a resonance coupled to the cavity at 550 GHz. This resonance is well above the band of interest, hence no attempts to eliminate it are made. The results achieved with the Wilkinson power divider make it a promising component for the power division on the 4-pixel block.

3.4 780-820 GHz planar components

This section describes the design of the microwave components required for the HFA CHAI mixer and power divider. The reasons and motives for choosing planar components in the HFA are even stronger than in the LFA given the smaller dimension of the components. Since the HFA frequency band falls above the gap frequency of Nb (f_{Gap} = 650 GHz), it is not possible to have the main components fabricated on this material. Instead, Niobium Titanium Nitrate (NbTiN) is used as it has a gap frequency above 1 THz (Fig.2.4 **Right**). The larger magnetic penetration depth of NbTiN (Fig.2.5 **Right**) demands thicker superconducting films. Given the current fabrication capabilities at hand, the thickness of the NbTiN films is 350 nm for both the bottom and top layers. This value is smaller than the calculated magnetic penetration depth for the material, hence, increased losses are expected in the superconducting circuits. Another point to consider is the fact that even though the operational frequency of the HFA is almost twice that of the LFA, the planar transmission lines for the HFA are only reduced in length but not in width. This effect and the increased thickness of the NbTiN enhance fringing effects and hinder the design process of passive components.

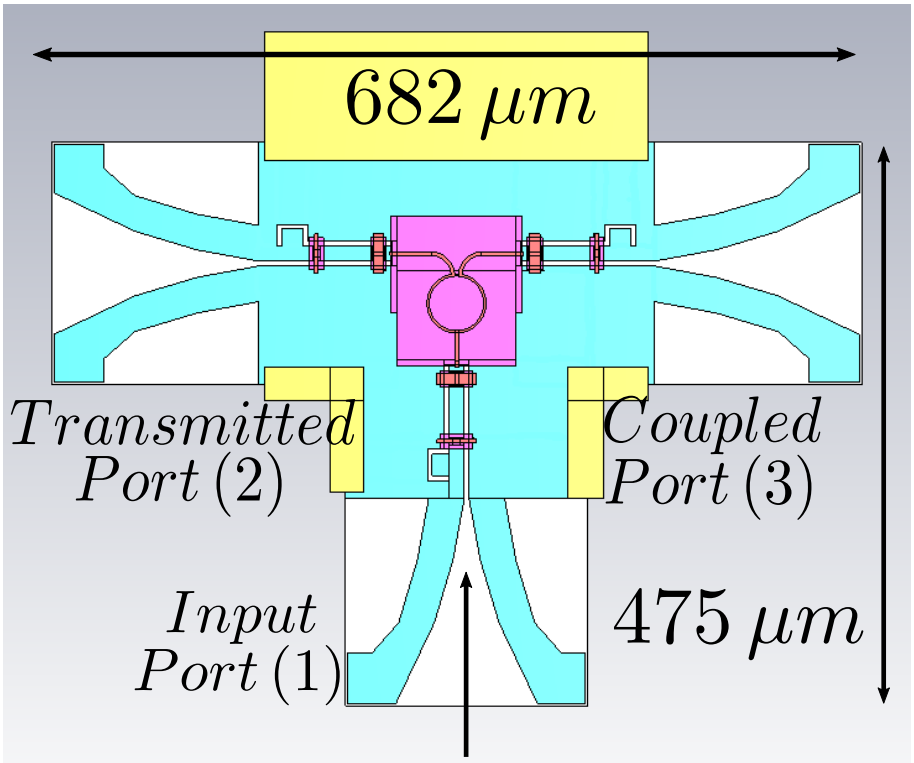

Figure 3.24: Design of a power divider based on a microstrip Wilkinson over amorphous SiO2. Due to the added superconducting kinetic inductance, the dimensions of the Wilkinson differ from the dimensions of a design on a normal conductor, particularly the length of the branches and the impedance of the line. Here the Wilkinson power divider is adapted to CPW lines by a $\lambda/12$ λ transformer initially designed by M. P. Westig

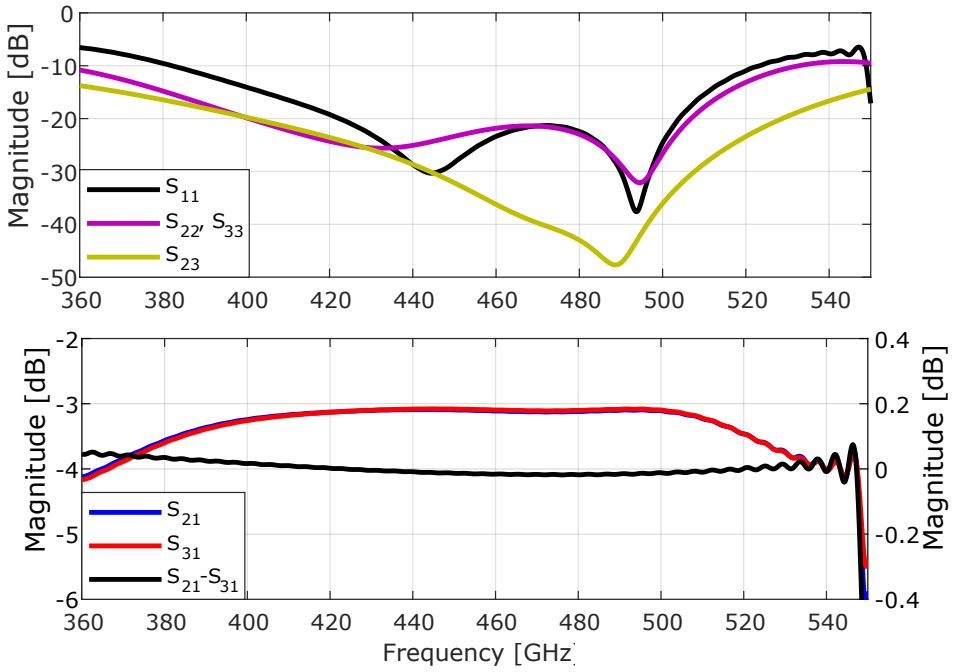

Figure 3.25: S-parameters of the complete microstrip Wilkinson power divider on a 9μm Si substrate. **Top:** Reflections at the waveguide ports and isolation between the two outputs. **Bottom:** Transmission from input to output ports and amplitude imbalance of the divider.

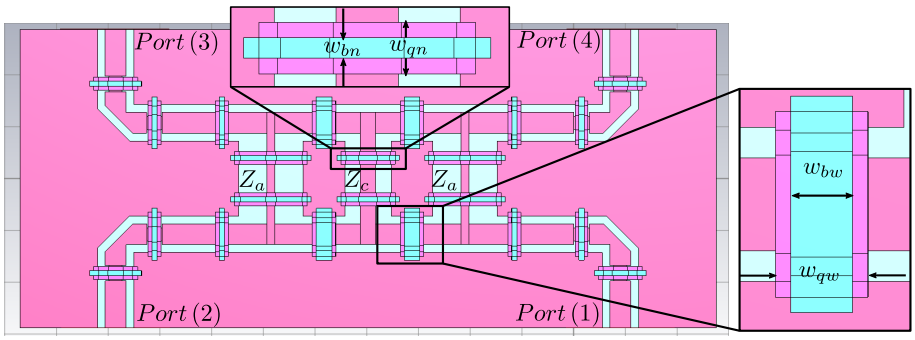

Figure 3.26: HFA branch line CPW coupler. The wider grounding bridges in the lines connecting the branch lines replace the two narrower bridges seen in the branch line coupler for the LFA. The width of this grounding bridge serves as an extra tuning parameter to tune and adjust the characteristics of the coupler.

Table 3.11: Parameters of the 800 GHz branch line Coupler

Line	Width (W) [μm]	Gap (g) [μm]	Impedance [Ω]	Length [μm]
Z_0	9	3	43	$l_0 = 33$
Z_c	4	11	87.4	$l_b = 35$
Z_a	8	6	58.7	$l_b = 35$

The CPW 90^{circ} and 180^{circ} couplers presented in this section are intended to be used to couple the LO and the RF signal before being delivered to the SIS junctions. The promising simulations of the microstrip Wilkinson power divider at the LFA prompt the design of a similar model for the HFA.

3.4.1 90° three branch line coupler

The three branch line coupler used for the HFA balanced mixers follows the same design as the branch line coupler used in the IBAMI mixer for the LFA. The design is shown in Fig. 3.26. One difference compared to the LFA components is that this design features one grounding bridge in the lines connecting the Z_a and Z_c branch lines. The reason for this is to avoid having two separate grounding bridges that would be too close to one another, due to the small ground plane between the branch lines. The larger capacitance introduced by this wider grounding bridge is used as an additional tuning parameter. Given the reduced fractional bandwidth required for the HFA, it is desired that the point of equal power division of the branch line coupler is at 800 GHz. The simulated results are shown in Fig.3.27. The reflections at the input port and the transmission to the isolated port are under -15 dB in the band. The transmission toward the transmitted and coupled ports has the point of equal transmission and the maximum imbalance in the band is about 1 dB at 780 GHz. The phase imbalance is about is about $\phi_{21} - \phi_{32} = 91°$.

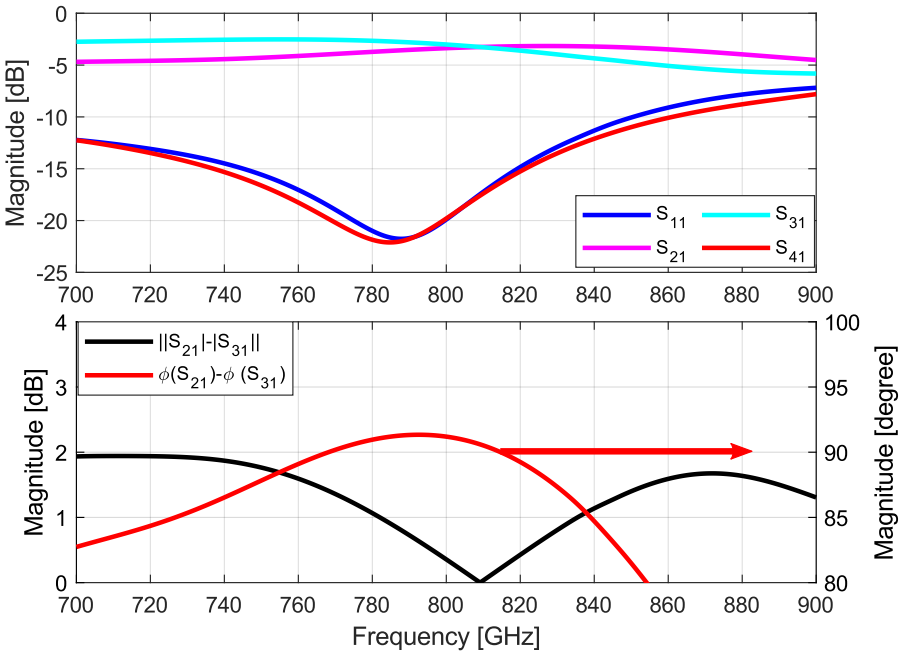

Figure 3.27: S-parameter of the 800 GHz three branch line CPW coupler. **Top:** S-parameters of the branch line coupler. **Bottom:** Transmission imbalance between the transmitted (2) and coupled (3) ports on both magnitude and phase.

3.4.2 180° CPW coupler

In the Mixer architectures section2.4, it was mentioned how a balanced mixer based on a 180° has advantages over a 90° one, mainly an improved LO-RF isolation and it is less sensitive to the noise in the phase of the LO [Kooi, 2008]. The 180° hybrid, originally proposed in [Tyrrell, 1947], is a four-port device with some additional features over the 90° coupler granted by the geometry and phase relationship between the outputs. This coupler receives its namesake due to the property of equally dividing a signal and adding a 180° phase between them. Port 4 receives an input signal and it is divided towards ports 2 and 3 with $\phi_2 - \phi_3 = 180°$, meanwhile, Port 1 is the isolated port. For the case that port 1 is the input port, the signal is then divided towards ports 2 and 3 with $\phi_2 - \phi_3 = 0°$ and port 4 is the isolated port. Fig.3.28 **Right** depicts a standard schematic of a 180° coupler. The rat race coupler does not only serve as a power divider but also as a signal combiner/subtracter. When two signals are injected into ports 2 and 3 the combination of them comes at port 1, meanwhile, its difference comes out at port 4. Hence the denominations of Σ and Δ ports. A mixer based on this kind of coupler has the SIS junctions at ports 2 and 3 and the LO and RF signals at ports 4 and 1 respectively. This means that ports 1 and 4 require a waveguide transition. This complicates the design of a mixer chip. A modification of this rat-race hybrid is proposed by [Ho et al., 1994b] (Fig.3.28 **Left**) where the layout of the output lines is changed for a symmet-

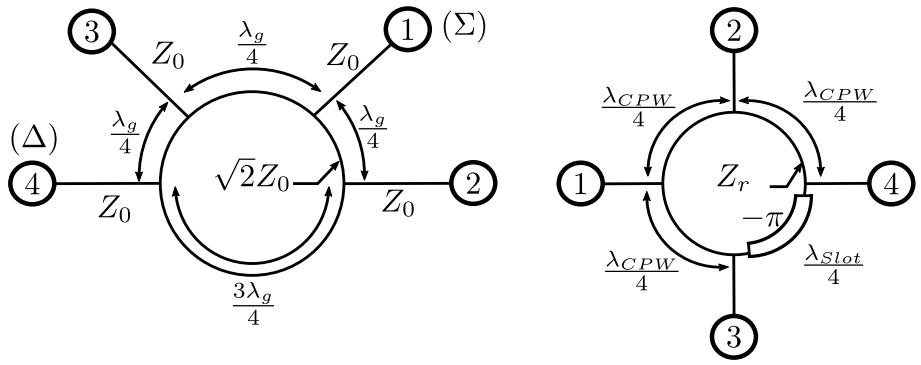

Figure 3.28: Rat race coupler schematics and port layout. **Left:** Schematic of a standard rat-race hybrid. The distance between the output branches is what gives the power division and phase properties of this design. **Right:** Compact CPW 180° hybrid design proposed by [Ho et al., 1994b]. To preserve the phase properties of the design it requires the use of a phase inverter between ports 3 and 4, marked with $-\pi$.

ric one with the impedance of the lines composing the rat race $Z_r = \sqrt{2}Z_0$. The phase properties are preserved by the use of a reverse phase CPW-slotline T-junction [Ho et al., 1994b] section B. This design is further modified by[Fan et al., 1995] where the impedance and electrical length of the rat race is given by $Z_r = \sqrt{2(1 - cot^2\theta)}$, where [Fan et al., 1995] proposes $\theta = 2\pi/5 = 72°$, resulting in the reduced $\lambda/5$ lines of its design. In the course of the development of HEB mixers for SOFIA in our group, a modified version of this coupler was developed and tested in a 1.9 THz balanced HEB mixer [Fathi, 2018].

In this work, for the SIS mixer for the HFA, I implemented the proposed architecture of Fan in CST following the design recommendation of [Fan et al., 1995] (Fig.3.29). The main CPW line has an impedance $Z_0 = 42\Omega$ ($w_{cpw} = 8$ μm, $g_{cpw} = 3$ μm) meanwhile the slotline impedance is $Z_s = 56.2\,\Omega$. To facilitate the design of this model, the guided wavelengths in the CPW and the slot line have the same value $\lambda_{cpw} = \lambda_{slot}$ The dimensions of the optimized design are tabulated in table 3.11 and its results shown in Fig.3.30. The reflections at the input port are under -12 dB and the transmission to the isolated port is under -40 dB. The transmission to the transmitted (2) and coupled (3) ports are about -3 dB with an amplitude imbalance lower than -0.2 dB over the band and a phase difference of $-175°$ across the band.

3.4.3 Waveguide - CPW transition

The waveguide-CPW transition for the HFA is of the same kind as the one used in the LFA. The waveguide dimension used is 240x140 μm^2. The original dimension was 240 x 120 μm^2 and were changed to the current ones due to manufacturing concerns. Two versions of this transition are designed, one

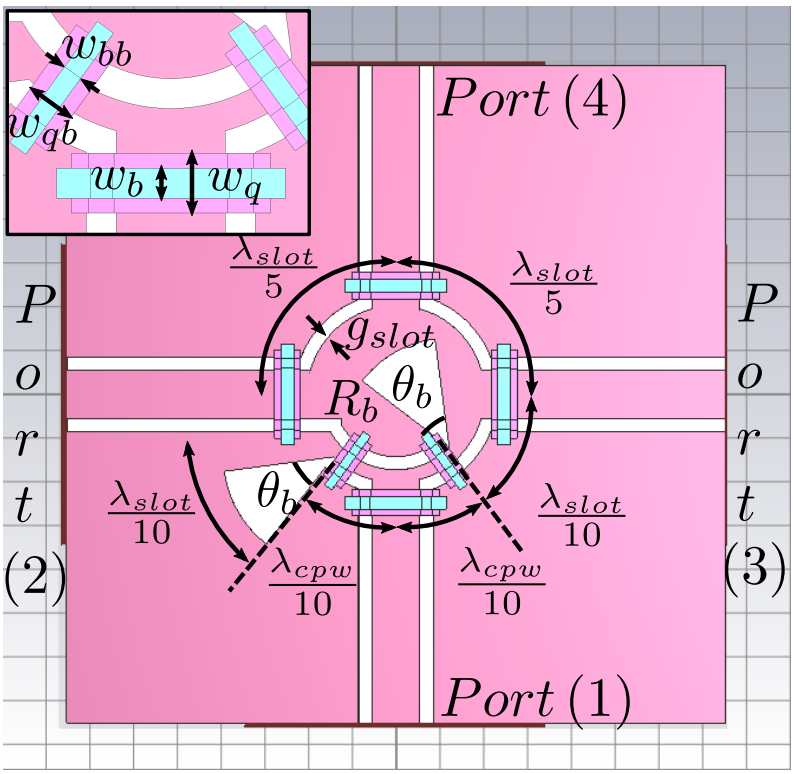

Figure 3.29: Rat-race coupler implemented in planar circuitry in CST.

Table 3.12: Parameters of the 180° ratrace hybrid

Parameter	length/angle [μm/ Radian]	Parameter	Length [μm]	Parameter	Length [μm]
g_{slot}	3	R_b	25	w_q	6
λ_{cpw}	155	θ_b	$\pi/4$	w_{bb}	12.9
λ_{slot}	155	w_b	3	w_{bq}	5

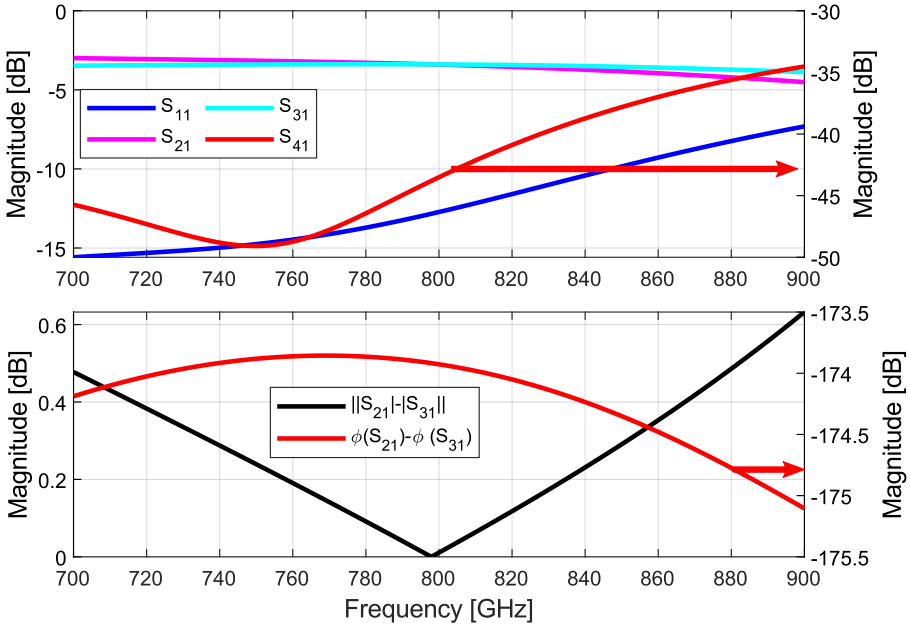

Figure 3.30: S-parameters of the 800 GHz rat race CPW coupler. **Top:** S-parameter of the branch line coupler. **Bottom:** Transmission imbalance between the transmitted (2) and coupled (3) ports on both magnitude and phase.

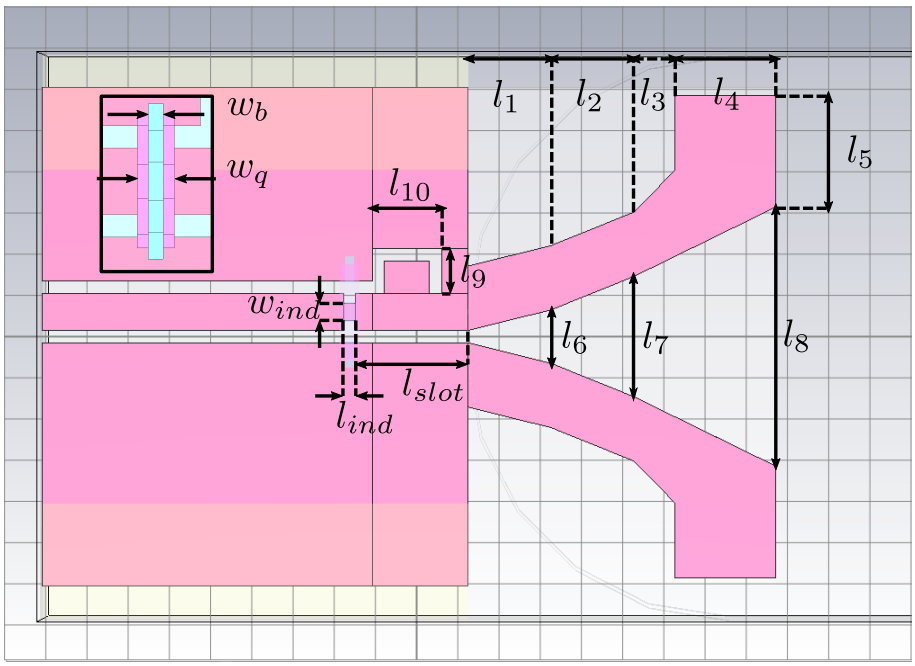

Figure 3.31: Model of the waveguide-CPW transition for the 800 GHz balanced mixer with the dimensions labelled. This model follows the same architecture as the waveguide-CPW transition used for the LFA components. This time it serves as a match between the 240×140 μm^2 waveguide and the CPW. The 3 μm slotline serves as a $\lambda/4$ transformer between the waveguide and the slotline section labelled with l_{slot}. is then adapted to the CPW by the use of a $\lambda/4$ slotline balun. at the interface between the slotline and the CPW, there is a grounding bridge to impede the excitation of the CPW odd mode.

Table 3.13: Parameters of the Waveguide-CPW transition

Parameter	length [μm]	Parameter	Length [μm]	Parameter	Length [μm]
l_1	20.1	l_6	12.9	l_{slot}	27.3
l_2	20.1	l_7	29.2	l_{ind}	4
l_3	9.9	l_8	62.9	w_{ind}	4
l_4	24.54	l_9	10.8	w_b	2
l_5	26.9	l_{10}	16.9	w_q	6

with a crooked balun and another with a radial stub at the CPW-Slotline transition. The slotline antenna with a bent balun is presented in Fig.3.31. The results for this waveguide-CPW transition show reflection losses at the Waveguide port below -20 dB (Fig.3.32) and below -17 at the CPW ports. The results for the second model of the transition are shown in Appendix A.

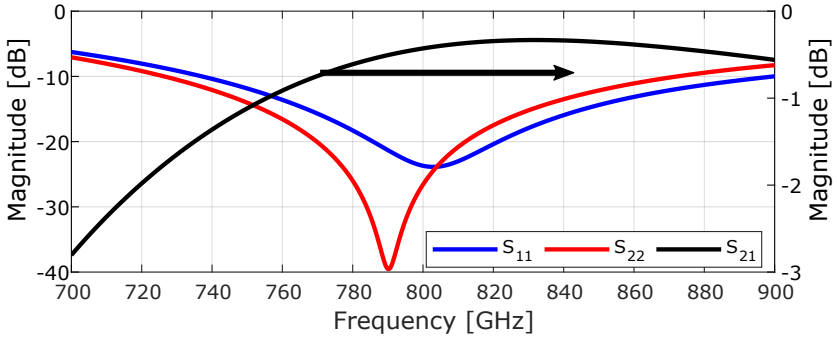

Figure 3.32: S-parameters of the 800 GHz waveguide-CPW transition

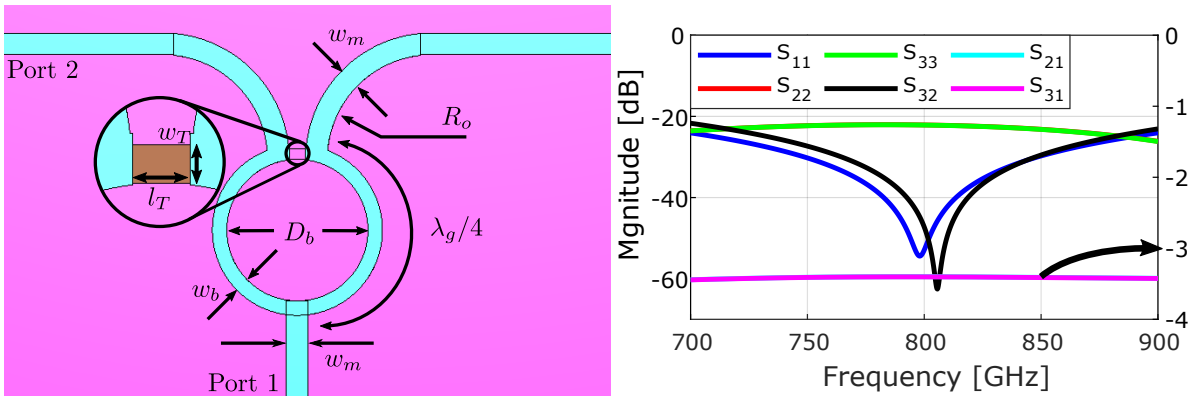

Figure 3.33: Design of the HFA microstrip Wilkinson. **Right:** Model of the microstrip wilkinson in CST. **Left:**S-parameters of the design.

Table 3.14: Parameters of the microstrip Wilkinson power divider

Parameter	length [μm]	Parameter	length [μm]	Parameter	length [μm]
w_m	3	w_T	2	l_x	50
w_b	2	l_T	3.8	l_y	80
D_b	25	R_o	15.9	λ_g	145

3.4.4 Microstrip Wilkinson

The Wilkinson power divider for the HFA is to be fabricated in 400 nm NbTiN over 300 nm SiO_2. The main line is 3 μm, which gives an impedance of 24 Ω. the side lines have a width of 2 and impedance of 35 Ω. The simulated results show reflections at all ports under -20 dB and isolation better than -30 dB in the HFA band (Fig.3.33).

3.4.5 Compact CPW- microstrip transition

The compact CPW-microstrip transition is, again, based on 12th λ transformer. The lines to be matched are a 45 Ω CPW and a 3 μm microstrip over 300 nm SiO_2, giving an impedance of 24 Ω. The high operating frequency and the surface inductance of NbTiN translate to very short matching lines (Table 3.15). At this point, the first l_{micro} section cannot be considered as an inverted microstrip anymore and it is more like CPW with a grounding

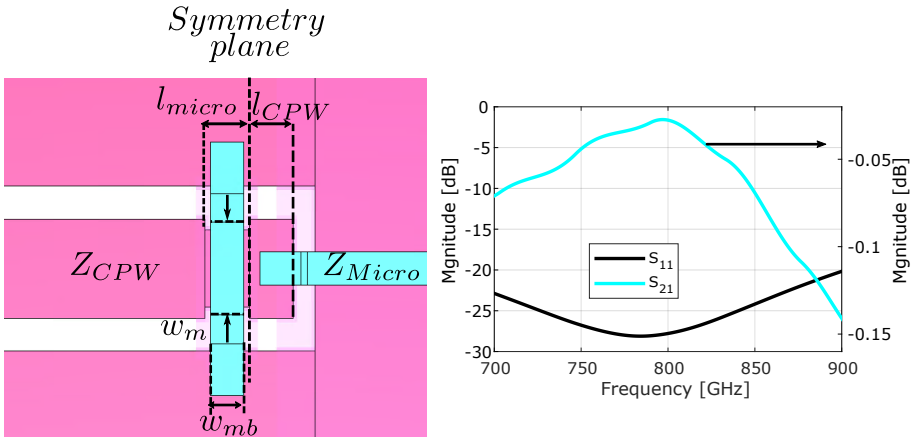

Figure 3.34: CPW to microstrip transition for the HFA. In this case, the high operation frequency and the material properties lead to very short lines for the Z_b and Z_a lines. At this point the first lines of the transition (l_{micro}) is a capacitive loaded CPW line rather than an inverted microstrip line.

Table 3.15: Parameters of the 12th transition

Parameter	length [μm]	Parameter	length [μm]
l_{micro}	3	l_{CPW}	5
w_m	7	w_{mb}	3

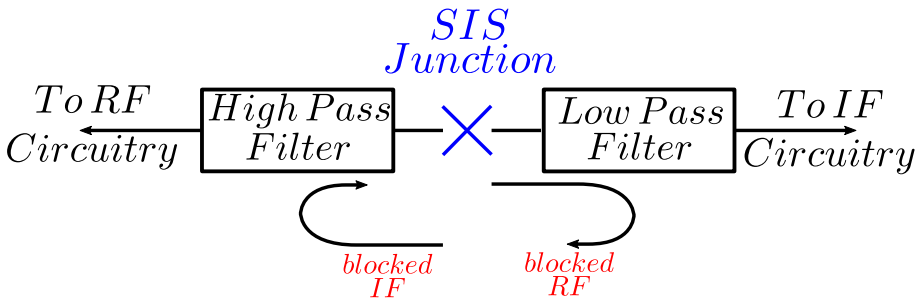

Figure 3.35: Frequency filters around SIS. The purpose of these filters is to isolate the RF and IF chains in order to avoid any possible interference caused by leaked microwave signals and DC biases.

bridge. The reflections of this transformer are below −20 dB over the 700-900 Ghz band.

3.4.6 IF and RF filters

The proper function of a mixer requires electrical isolation between the RF and IF circuits, as shown in Fig.3.35. The DC voltages and currents required to bias the SIS junctions should be blocked from the RF circuity since it would allow a DC connection between the two SIS junction structures and it would not be possible to bias them independently anymore. Additionally, an RF signal in the IF circuitry may excite a litany of resonances due to the generally larger dimensions of the IF cavities and lines. This isolation between RF and IF circuits is achieved by two filters, placed before and after the SIS junctions.

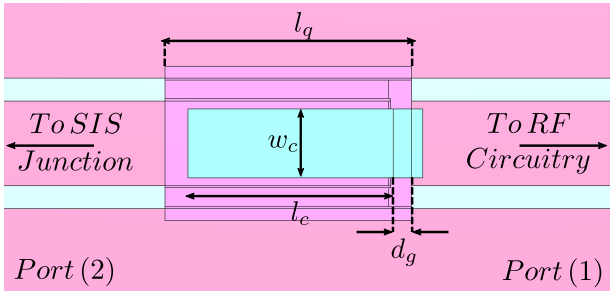

Figure 3.36: DC and IF blocking capacitor. This structure is the equivalent to a series capacitor which has an impedance of $Z_c = 1/j\omega C$, where C is determined by the overlapping area between the lines and the properties of the dielectric.In this case, the dielectric is a 300 nm thick layer of silicon dioxide

Table 3.16: Parameters of the Waveguide-CPW transition

Parameter	length [μm]	Parameter	Length [μm]
w_c	6	l_q	23
l_c	19	d_g	3

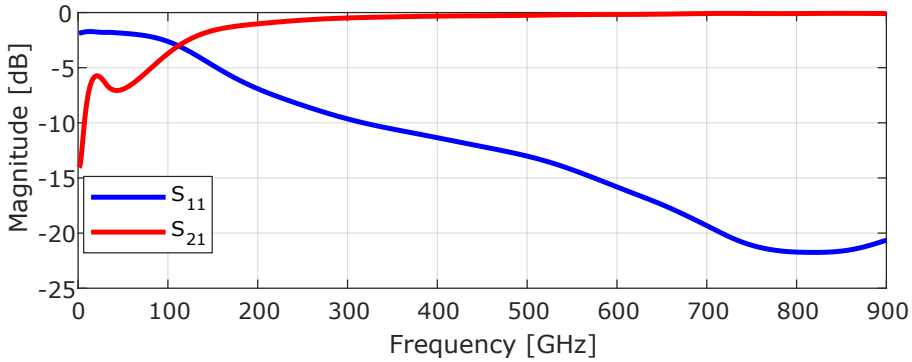

Figure 3.37: S-parameters of the IF blocking capacitor.

The High pass filter before the SIS junctions is implemented as a series capacitor. The impedance of this capacitor ($Z_c = 1/j\omega C$) is seen as a short circuit at RF frequencies but as an open circuit for IF frequencies and blocks the DC. The designed capacitor is shown in Fig.3.36. This blocking capacitor consists of an overlap between the lines separated by 300 nm dielectric layer of SiO_2. Its dimensions are such that the capacitive coupling between the lines assures good transmission at 800 GHz while blocking the IF and DC signals. Results are shown in Fig. 3.37, The blocking filter works as intended as the reflections at 800 GHz are below -20 dB. At the IF frequencies, the reflections are about -1.7 dB and the transmission is below -10 dB.

The lowpass filter is more complex than just a blocking capacitor, it is a six-stage binomial, or maximally flat, filter. The design corresponds to a double terminated maximally flat filter, calculated by the insertion loss method [Matthaei et al., 1980, Pozar, 2011]. The insertion loss in the filter can be specified as $P_{loss} = 1 + k^2(\omega/\omega_c)^{2N}$, where N is the order of the filter and ω_c is the frequency at which it is about $-3dB$. ω_c is called the cutoff frequency

of the filter and it is the design parameter that defines the filter dimensions. For this design, the order of the filter taken is $N = 6$ and the cutoff frequency is $\omega_c = 500$ GHz. The reason for the seemingly high cutoff frequency is that a lower cutoff frequency leads to considerably larger filter dimensions. This generates problems with the integration of the RF circuitry, whose operational frequency is a hundred times higher. Once the filter design and order have been chosen, the values for the normalized components can be obtained from [Matthaei et al., 1980] table 4.05-l(a) and the real value can be obtained by the following equations

$$C_\chi = \frac{1}{R_0}\frac{1}{\omega_c}C_\chi^{norm} \qquad (3.3) \qquad\qquad L_\chi = R_0\frac{1}{\omega_c}L_\chi^{norm}, \qquad (3.4)$$

where the values L_χ^{norm} and C_χ^{norm} are the normalized reactance values for the filter χth section. R_0 is the reference source impedance and for its selection, one must consider the resistance of the SIS junctions at different bias points. Since this resistance ranges from 10 to 110 Ω [Tucker, 1979, Tucker and Feldman, 1985], the reference source resistance is taken to be the average $R_0 = 60$ Ω. Once the reference resistance has been determined, the reactance values can be calculated from eqs.3.3,3.4. The implementation of the reactance values is done through the stepped impedance method. With this method, the filter can be implemented as a cascade of transmission line sections of high and low impedance. The underlying idea is that a short transmission line ($l < \lambda_g/8$ [Pozar, 2011]) of extreme characteristic impedance is equivalent to a purely reactive element. The lines of low impedance Z_l are used to implement capacitor, while the lines of high impedance Z_l are equivalent to inductance. The relationship between the dimension of the line and its reactance is

$$\beta l = \frac{LR_0}{Z_H} \qquad (3.5) \qquad\qquad \beta l = \frac{CZ_L}{R_0}, \qquad (3.6)$$

where l the length of the line, R_0 the reference resistance, $Z_{L,H}$ the Low/High impedance of the line and C, L the normalized reactance values (Table 3.17). The actual value for the impedance Z_L and Z_H is not defined but it is desired that the ratio Z_H/Z_L is as great as manufacture allows it [Pozar, 2011]. The filter is shown in Fig.3.39 and the important parameters are tabulated in Table 3.17. For the filter design, the low and high impedance values are $Z_L : 31$ Ω and $Z_H : 90$ Ω. These values are close to the limit values of what is feasible to achieve with CPW lines. It can also be seen that some of the lines are longer than $\lambda_{cpw}/8 \sim 22\,\mu$m. All these factors contribute to the fact that the filter does not exhibit a sharp cutoff or a transmission below −30 dB at 800 GHz. In any case, the filter does fulfil the requirements for its

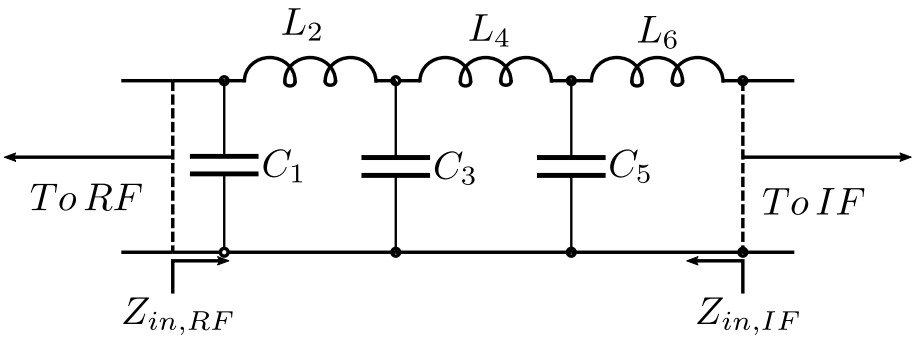

Figure 3.38: Schematic of the binomial filter of order $N = 6$. The numbering follows the stage number rather than the component itself with every capacitance and inductance representing a stage of the filter.

Table 3.17: Relative values for a sixth-order binomial filter, $R_0 = 60\ \Omega$

Capacitance	C^{norm}	Capacitance [pf]	Inductance	L^{norm}	Inductance [pH]
C_1	0.517	27.427	L_2	1.414	270.05
C_3	1.932	102.49	L_4	1.932	368.98
C_5	1.414	75.02	L_6	0.517	98.74

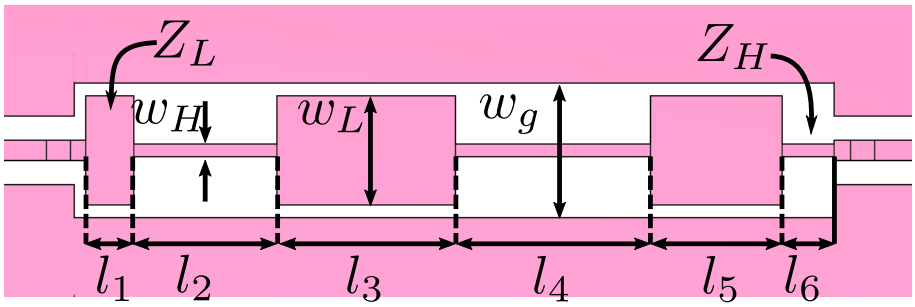

Figure 3.39: Stepped impedance binomial filter. The low and high impedance are Z_L : 31 Ω and Z_H : 90 Ω respectively. The low and high impedance sections take the role of capacitances and inductances respectively. The proper working of this design requires that the ratio Z_H/Z_L to be as high as fabrication allows it[Pozar, 2011].

Table 3.18: Relative values for a sixth-order binomial filter, $R_0 = 60\ \Omega$

Parameter	length [μm]	Parameter	length [μm]	Parameter	length [μm]
w_H	3	l_1	11.9	l_4	48.4
w_L	27	l_2	35.4	l_5	32.5
w_g	33	l_3	44.5	l_6	12.9

use in the IF circuitry. It is worth noting that it is possible to increase the order of the filter up to two additional orders without running into designs that require impractical impedance values [Matthaei et al., 1980] table 4.05-l(a). Another important point is that for the tuning structure and proper matching of the SIS, the input impedance seen from the Rf circuitry must be purely imaginary, even more so that it is an open circuit. The Smith chart of the reflections from the Rf port (Fig.3.40) reveal that this is not the case and the impedance has a real component at 800 GHz. Fortunately, the solution is quite simple just adjusting the length of the transmission line between the SIS tuning structure and the filter

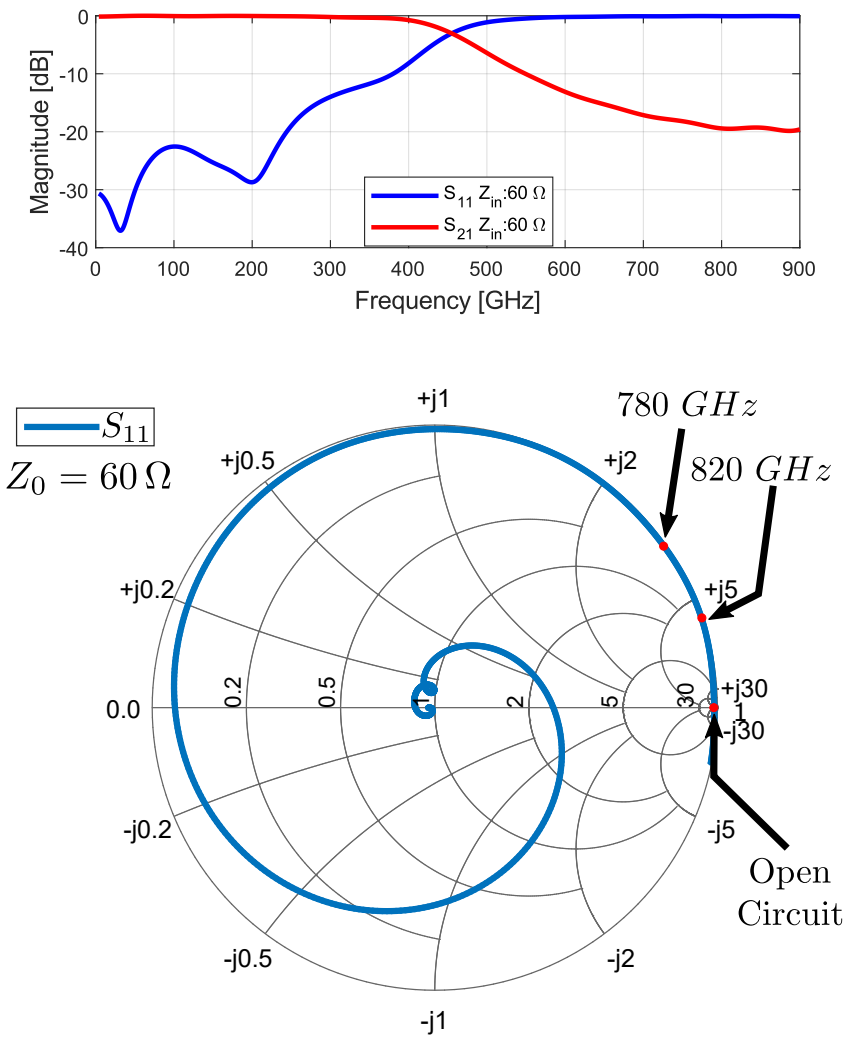

Figure 3.40: S-parameters of the stepped impedance filter.**Top:** Rectangular plot of the reflection at the Rf port(S_{11}) and transmission from the RF to the IF ports S_{21} with an input impedance of $Z_0 : 60\ \Omega$. **Bottom:** Smith chart plot of the reflections at the RF port (S_{11}). It can be seen that the input impedance seen at 800 GHz is not an open circuit. but rather a high complex impedance. For the correct operation of the SIS junctions, it is needed that the filter is seen as an open circuit, this is easily achieved by tuning the length of the transmission line that connects them.

3.4.7 SIS layout and tuning circuit

The last component required for a SIS mixer is the tuning structure to match the SIS junctions to the feed lines. The SIS junction consists of a tri-layer of a bottom electrode of niobium, an isolating layer of aluminium nitrate, and a top electrode of niobium nitrate. the junction is sandwiched between layers of NbTiN to provide an electrical connection between them and the lines. For this, a tuning structure is needed to match the lines to this impedance Z_J. The SIS junctions can be modelled as a resistance R_n in parallel with a capacitance C_j, which gives an impedance $Z_j = 1/R_n + j\omega R_n C_J$. In general, this results in a very reactive impedance with a very small resistance. In this work, only one tuning structure is proposed due to the tight time constraints

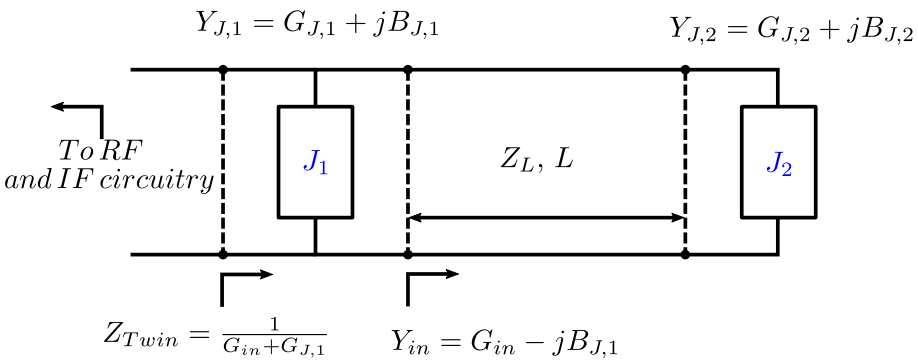

Figure 3.41: Schematic of a twin parallel tuning structure. Here the junctions are represented as an admittance composed by the normal state conductance and suceptance of the junctions. The tuning parameters of this structure are the length of the line connecting the junctions and its characteristic impedance. it must have values such that the admittance seen at the first junction J_1 has the opposite value of its susceptance, cancelling each other out. This results on a purely resistive input impedance for the complete structure.

encountered in the development of this thesis.

The twin parallel tuning structure (Fig. 3.41) is designed to eliminate the reactance of an SIS junction by using the transmission line between them. The tuning parameters of this particular network are the length and characteristic impedance of the line. The parameters have to be such that the susceptance of the SIS junctions cancels out and the total impedance of the structure is real. This allows for the use of simple matching networks, such as the classic $\lambda/4$ transformer, since it can only match resistive loads[Pozar, 2011].

The HFA SIS junctions have an area of $1\,\mu\text{m}^2$, a normal state resistance of $R_n = 10.05\,\Omega$, meanwhile the capacitance is $C_j = 85fF$. This value, at 800 GHz, gives an impedance of $Z_J = 0.5170 - j2.220\,\Omega$. The proposed tuning structure is implemented on microstrip lines given the difficulty of implementing parallel SIS junctions on coplanar waveguide. Additionally, a tuning structure like this has been proven to work in many receivers [Belitsky et al., 1995, Westig, 2013], albeit at a lower frequency. The implemented design is simulated in Sonnet software, shown in Fig.3.42, due to its convenience and faster solving time than CST. The tuning structure is connected to the RF circuitry at the CPW port of $Z_{CPW} = 42\,\Omega$. The junctions are simulated as through ports of $1\,\mu\text{m}^2$ with R_n and C_j as parameters. The connection to the Lowpass filter and the rest of the IF circuitry is yet to be done, it is likely that as in many other cases, there must be an adaptation of the design at the moment of integrating the components. The dimensions of the design are tabulated in Table 3.19 and the results are displayed in Fig.3.43. The reflections at the CPw port (1) are below -20 dB and the transmission balance has a point of equal power to each junction at 780 GHz.

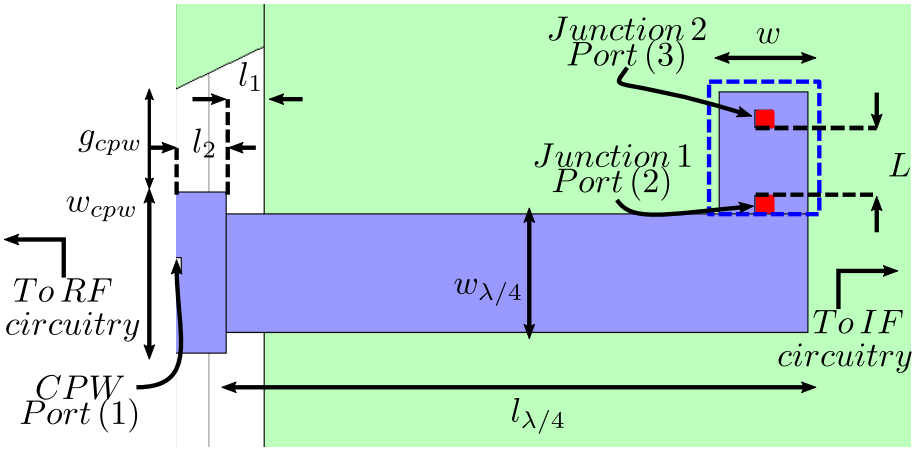

Figure 3.42: Sonnet model of the complete SIS junction tuning structure. Marked with the blue dashed line is the twin SIS junction tuning structure, connected to the CPW port by a $\lambda/4$ transformer. The SIS junctions are simulated as a port with a resistance and capacitance R_n and C_j respectively.

Table 3.19: Dimension of a twin SIS junction tuning structure

Parameter	length [μm]	Parameter	length [μm]
w_{CPW}	9	$w_{\lambda/4}$	7
g_{CPW}	5.8	w	4
$l_{\lambda/4}$	29	L	2.3
l_1	3	l_2	2

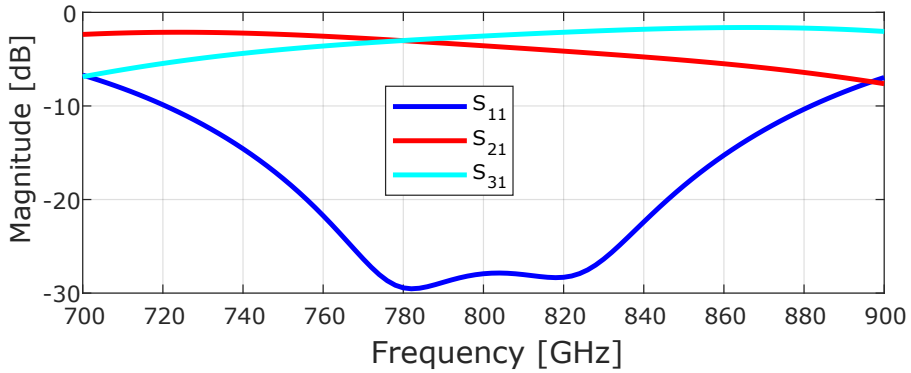

Figure 3.43: Simulations of the complete tuning structure in Sonnet software.

3.4.8 Integrated balanced mixer

The first version of a balanced mixer for the HFA is based on the CPW 90° hybrid, detailed previously in this chapter. Due to time constraints, only the RF components have been integrated. That corresponds to the 90° CPW hybrid plus the Waveguide -CPW transition and the IF blocking capacitors. The S-parameters of this model are presented in Fig.3.45. Reflections at the LO port and isolation between The LO and RF ports are below -12 dB and -14 dB respectively. The point of equal power distribution to ports 2 and 3 is at 800 GHz with a magnitude imbalance under 2 dB in the complete band. The phase imbalance is within 4° in the band of interest. It can

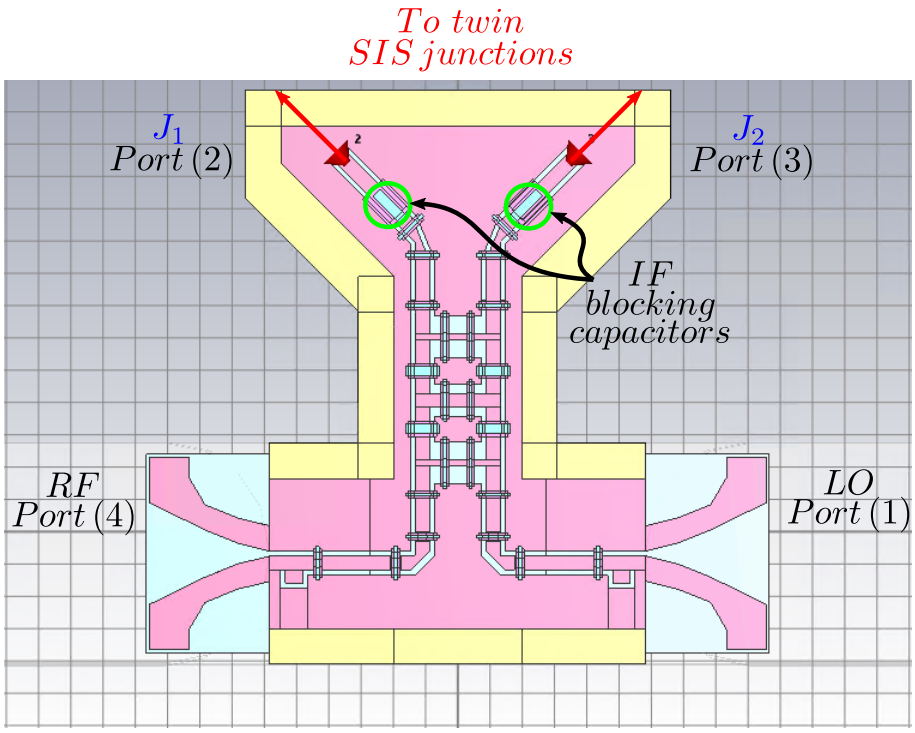

Figure 3.44: Integrated RF components of a CPW based balanced mixer. The junction ports J_1, J_2 represent the port where the twin SIS junctions with the designed tuning structure are to be connected.

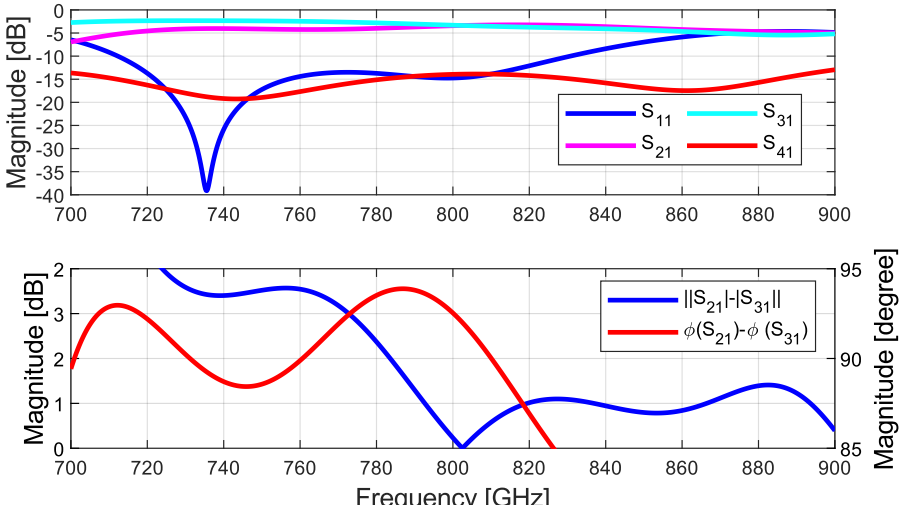

Figure 3.45: S-parameters of the integrated RF components

be seen that the point of equal power distribution does not coincide with the minima of the reflections and isolation between waveguide ports. One additional design is presented in the appendix A where the design is tuned so the lowest reflection is at 820 GHz. The models here presented can be integrated for a first design for a balanced mixer for the HFA, they may be used for testing purposes and, in case better performance is demanded, as an advanced starting point for further optimization.

3.5 Summary

This section presents the design for superconducting planar components for the LFA and HFA of CHAI. The components for the LFA consist entirely of components required for the proposed power divider to be used in the LO distribution. On the other hand, the components for the HFA are components required for the design of an integrated balanced mixer and a power divider.

The LFA power dividers are meant to be used in a 4-pixel block, where the LO has to be delivered to the four individual mixers. The technology chosen to manufacture the power dividers is superconducting Niobium film over a 9 μm silicon substrate. The reasons for this are the fast and adaptable series production and the modularity enabled by the superconducting chips. Two distinct designs are proposed, the first design for a power divider is based on a coplanar waveguide 90° branch line coupler whose isolated port is terminated with an on-chip load. Meanwhile, the second is based on a Wilkinson power divider manufactured on a Sio_2 microstrip line, which is a microstrip line that only requires processing on one side of the substrate. Since all designs are based on superconducting film over a silicon membrane, a Waveguide to CPW transition is designed. In this transition, the waveguide and slotline transition is matched by a slotline antenna. The slotline is subsequently matched to the CPW by the use of a $\lambda/4$ balun.

The power dividers are based on a CPW 90° branch line coupler which does require a termination for the isolated port. Initial ideas considered a waveguide load termination since the concept has been proven. This idea is discarded because of manufacturing constraints, in specific, the distance between two waveguide walls had to be larger than 700 μm. This constraint severely limits the design of the power diving chip, setting a minimum footprint size constraint. A design made complying with these constraints, suffered from resonances, excited by the CPW odd mode due to the increased size of the cavity. This leads to the discard of the waveguide termination and focuses on-chip terminations instead. Three terminations are implemented, a concentrated element one, a lossy resonator termination and a short circuit termination.

The second power divider came about as the power dividers based on the CPW 90° branch line couplers performance in the 2-pixel block was not satisfactory. The new power divider design is a Wilkinson power divider that does not require a termination since it is a three-port device. The divider itself is designed on a microstrip transmission line meanwhile the waveguide interface is done by adding a microstrip-CPW transition to the

existing waveguide interface. This microstrip line ground plane and main line are on the same side of the silicon substrate. This is achieved by sputtering a 300 mm thick SiO_2 layer and then sputtering another top Nb layer. The simulated performance of this power divider makes it a promising candidate for the power division in the 4-block.

The HFA components are designed for the frequency range between 780-820 GHz. This means that niobium titanium nitrate (NbTiN) has to be used instead of niobium given its higher gap frequency. They will be fabricated on a 5 μm Si wafer. A balanced mixer design requires a coupler that equally divides the signals and introduces a phase shift between them, either 180° or 90°. It also requires low-pass and high-filters to block and separate the RF and the IF circuitry from each other. Since the SIS tuning structure is fabricated on microstrip lines, a compact CPW-microstrip transition is proposed.

For the couplers, two kinds are considered, a 180° and a 90° couplers. After they have been designed, it is necessary to define a waveguide dimension and a CPW-waveguide transition. The waveguide dimensions are set on 240×140 μm^2 and the transition is a waveguide-CPW transition based on a slotline antenna as the one designed for the LFA. The filters required to separate the RF and IF circuitry are implemented on CPW lines. Finally, for the SIS junctions, a twin parallel tuning structure on the microstrip is chosen and designed. The CPW-microstrip transition is based on the concept of the 12th λ matching circuit. The complete integration, and subsequent optimization, of the balanced mixer and power divider was not possible due to the time constraints encountered in this thesis. However, the designs presented in this work, directly integrated into one circuit, show a performance that serves as a good starting point for further optimization or for a finished model to be used for fast manufacture and characterization.

Chapter 4

Experimental setup, measurement methods and data processing

This chapter details the current testing environment, its reach and limitations and the proposed measurement methods to characterise the fabricated devices. subsequently, it details the experimental setup required to perform the proposed experiments and the data processing required to extract the parameters of interest from the experimental results.

4.1 Measurement methods and available power detectors

For the characterization of the power divider designed it is required to measure the transmission between its ports and the power reflected from them. The information about these parameters is often resumed in the S-Parameter matrix of the device (Section 2.3). The standard manner to measure the S-parameters involves the use of a *Vector Network Analyzer* (VNA). This instrument can generate a signal and send it through one of the ports of the Device Under Test (DUT) and measure the amplitude and phase of the transmitted signal at another port. Additionally, it can measure the reflections generated at the input port of the DUT.

To do so, the 2-port VNA requires a continuous wave source, four receivers and four directional couplers. A signal is sent towards the DUT and it is split by the directional coupler R1. Here part of the signal is sent to a reference receiver while the second goes to through the second directional coupler M1 towards the DUT. At this point, part of the signal is reflected to port 1 of the VNA and is directed towards the measurement receiver 1 by the directional coupler M1. The comparison between the signal measured by reference 1 and measurement 1 receivers yields the S_{11} parameter. The signal coming out of

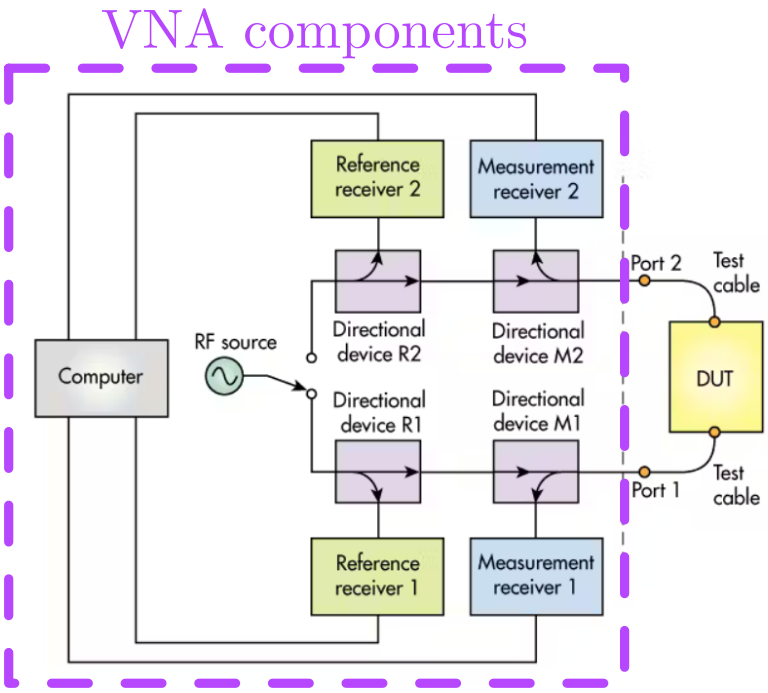

Figure 4.1: Schematic of a VNA with its main components. To measure the transmission and reflection characteristics of the DUT, the VNA makes use of a CW source, directional couplers and reference/measurement receivers. *Image source: Microwaves & RF: Brushing Up on Network Analyzer Fundamentals.*

DUT port 2 is received by the directional coupler M2 and is measured by receiver 2. Comparison between receivers 2 and 1 measurements yields the S_{21} parameter.

To provide accurate and precise measurements, the VNA requires calibration measurements to eliminate possible sources of error within it. Fig. 4.2 depicts the parameters of interest (S-parameters of the DUT) and the possible sources of error as well. They are removed by measuring special calibration devices with known characteristics. Usual devices for the calibration are one port terminations of a short-circuit, an open-circuit and a $50\,\Omega$ termination. Meanwhile, the standard two-port calibration device is a *through* between the two ports with a line whose transmission is known. Once the calibration has been performed, the errors in the two port measurements can be removed. However, these calibrations are not permanent, since stability and drift in the components of the VNA will degrade the measurement performed. It is then recommended to perform one, and two-port, calibrations regularly and every time the measurement setup changes.

The aforementioned capabilities of the VNA make it a powerful tool at the time to test microwave devices. However, for the testing of the devices designed in this thesis, a VNA has considerable limitations. The first of them is set by the nature of the devices themselves. they operate at a tempera-

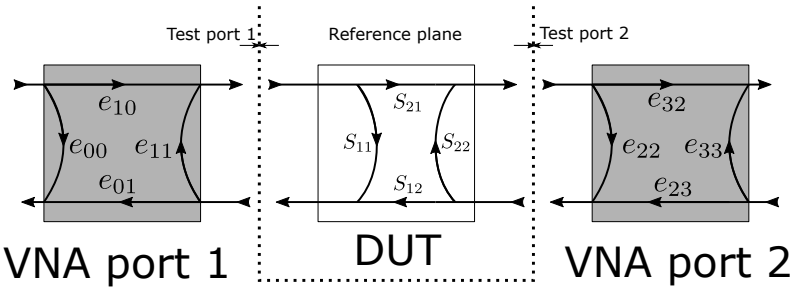

Figure 4.2: Schematic of the standard two-port error model of the network analyzer for measurement of transmission and reflection parameters of the DUT. The error parameters in the two VNA ports are depicted in the ports of the VNA. Standard one-port and two-port calibrations can determine, and subsequently, eliminate these errors from the measured data.

ture of 4.3 K. Hence, they need to be placed at the 4.3 K stage of a Dewar with limited accessibility from the exterior. The two main possibilities are coupling by free space propagation through the IF windows of the dewar and direct connection using electric wires (Fig. 4.3). In this scenario, any VNA calibration will be limited in the sense, that it is difficult to remove the errors that may arise in the connection to the interior of the dewar. This would not only require the dewar to be removed to perform the standard one and two-port calibrations but also would require the exchange of components at the 4 K stage for devices with known parameters. This exchange cannot be immediately done as the dewar has to be warmed up to room temperature, opened and closed again to be cooled to 4 Kelvin again to perform the test. This would increase the cost of operation in both operation time and cryogenic costs to a very high level. A second limitation, and perhaps the most important, is the availability and cost of VNAs operating in the microwave regime. Standard VNA operating band ranges from 100 MHz to 100 GHz, where access to higher frequencies requires expensive extension modules. The cooperation with other institutions that may have granted us access to a VNA was prevented by the COVID-19 pandemic, without considering the limitation set by the cryogenic temperature required for the operation of the devices.

4.1.1 SIS junctions as direct power detector

Since it is not practical and feasible to perform VNA measurements to characterise the devices fabricated, it is necessary to look for alternative measuring methods. The first step is to find a suitable detector to measure the power transmitted towards the output ports of the power divider. Here the SIS junctions in the Integrated Balanced Mixer(IBAMI) chip arise as a good candidate, for measuring the power coupled to them. In section 2.1.5, it was detailed how an incident RF field coupled to the junctions would pro-

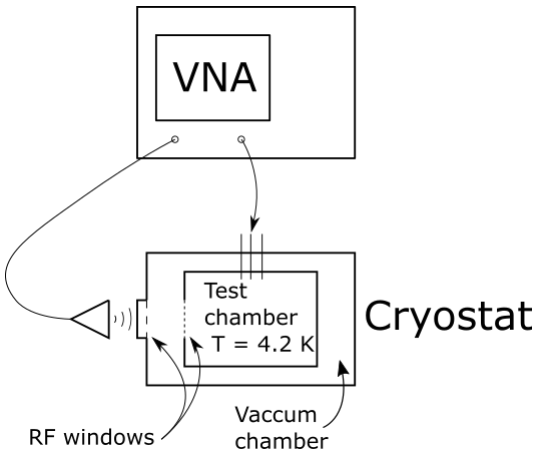

Figure 4.3: A simple schematic of a connection between a VNA and the devices under test depicting two possible ways of connecting the VNA and the cold chamber of the cryostat/dewar.

duce photon-assisted tunnelling. This phenomenon can be used to detect the power coupled to the junctions by recording the induced current at the first photon step of the SIS's I-V characteristic (Fig. 4.4). For our case in question, the SIS junctions used are the ones in the IBAMI mixer developed by [Westig, 2013](Fig. 4.5). IBAMI has a twin parallel SIS junction circuit as the nonlinear element required for mixing. In this work, for the sake of clarity, the twin parallel SIS structure is referred to as a single detector J_x. With this convention, the IBAMI chip has two non-linear detectors. Since the power divider chip has two outputs, two IBAMI chips are required to test the power divided by the power divider (Fig.4.6).

The advantage of this measurement scheme is that the IBAMI chips can be placed in the same testing block as the power divider. Additionally, a power divider and two IBAMI mixers represent half of the 4-pixel block intended to be used in the LFA of CHAI. This would allow for testing of the power divider in an environment similar to the intended, final one. This potentially yields useful information about the integrated system and the interaction between its components.

The limitations of this setup for the characterisation of the S-parameters are, first, this setup only allows for direct measurement of the induced current in the SIS junctions, where the transmission between the input port to its output ports of the branch line power divider is embedded. Measurement of the reflection parameters of the branch line power divider would require a different testing setup with the addition of a directional coupler with known characteristics.

The second limitation is that the detector is not characterised individually.

This fact limits the extraction of the branch line power divider's parameter and complicates the interpretation of experimental results. By doing the system integration before knowing the individual parameters of the components, it is not possible to completely discern which observed features are inherited from individual components' characteristics or if they arise from their interaction. Considering that the SIS junctions are devices susceptible to their immediate network, it is sensible to look for an additional power detector independent of the system.

4.1.2 Erickson power meter 3 (PM3)

As an additional detector, independent of the network, an Erickson power meter 3 (PM3) is borrowed from the Max Planck Institute for Radioastronomy (Fig. 4.8). This power meter would allow for independent measures of the transmission of the branch line power divider.

This power meter consists of a power sensor and an electronic readout. This detector is an incoherent detector which only detects power from 200 μW to 200 mW. The sensor detects the temperature of a thin resistive layer suspended in the sensor block that is coupled to the exterior through a rectangular horn. The readout block is responsible for converting the signal produced by the sensor to a voltage that can be read by any data recording electronics. To remove the detector offset, an *On-Off* measurement has to be done before performing power measurements with this detector.

The measurement scheme with this power meter is similar to the power division measurements executed with the IBAMI mixers, with the horn of the PM3 detector coupled to the mixer ports M1/M2 (Fig 4.6).

4.1.3 IBAMI mixer

So far the two detectors mentioned are meant to be used for power division measurements without addressing the, possibly, direct transmission between output ports (Transmission between ports T and C in Fig. 4.6). For this measurement scheme, The IBAMI chips are used as coherent detectors, as balanced mixers, more precisely. A thorough review of the component can be found in [Westig, 2013]. Two of them are placed at the output ports of the power divider and will measure the magnitude of the signal that is injected through one output port and what is transmitted to the other, which will be detected by the second IBAMI mixer (Fig.4.7). This a is measurement scheme more convoluted than the one required for the previous measurements, especially requiring two CW sources to act as the mock RF signal and the Local Oscillator signal.

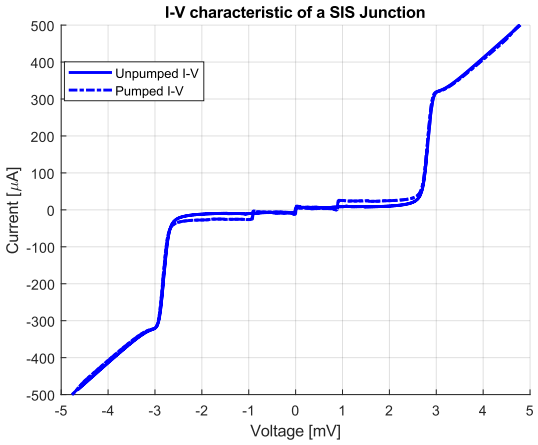

Figure 4.4: I-V characteristic of a SIS junction with magnetic field applied for cooper pair tunnelling suppression. The solid line depicts the electrical characteristics of the junction without any coupled photons. Aside from the suppressed cooper pair current, there is no current flowing through the junction before the gap voltage. The dashed one depicts the I-V when photons are coupled to the junction. This coupling changes the I-V characteristics of the junction by assisting the tunnelling of quasiparticles below the gap voltage. This is the phenomenon that allows the use of the SIS junctions as a direct detector.

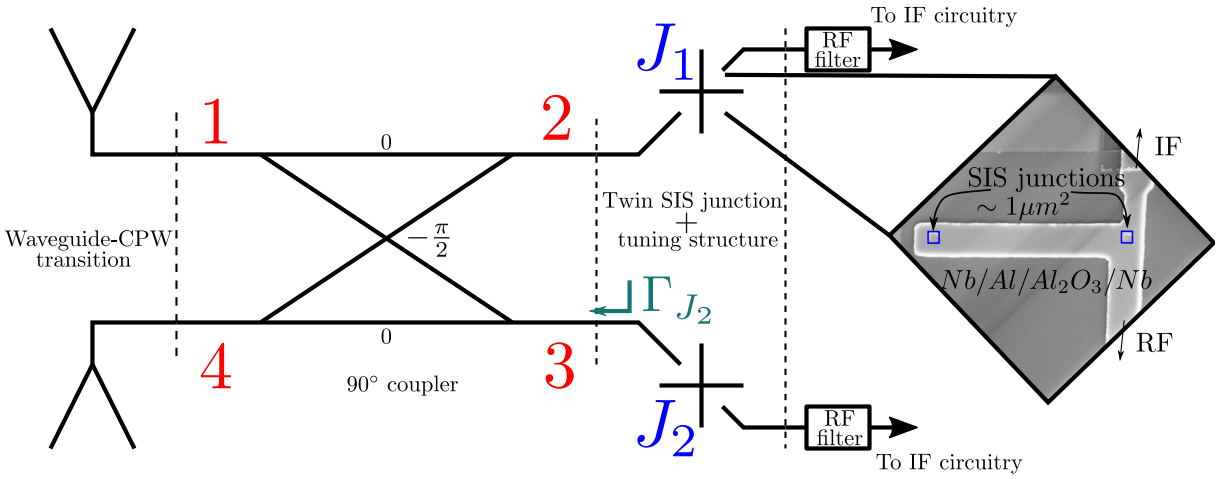

Figure 4.5: Schematic of an Integrated Balanced Mixer (IBAMI) developed by Marc Westing and the mixers to be used for the CHAI LFA, with the main parts labelled. Port 1 and 4 receive the signal coming from the waveguides and coupled them together in the 90° coupler.They are delivered for mixing to the nonlinear SIS circuitJ_1, J_2, in ports 2 and 3. The generated signal at IF frequencies is then delivered to the IF circuitry through an RF filter. Here J_x refers to the twin junction structure found after ports 2 and 3 as a whole circuit and not as an individual SIS junction. The electron scan image of the twin SIS [Westig, 2013] shows the layout of the junctions in the tuning structure. The two SIS junctions are placed in parallel and connected by a short transmission line that acts as a lumped inductance. This structure is meant to compensate for the capacitance of SIS junctions, making the input reactance as small as possible, and facilitating the matching of the SIS to the rest of the RF circuit.

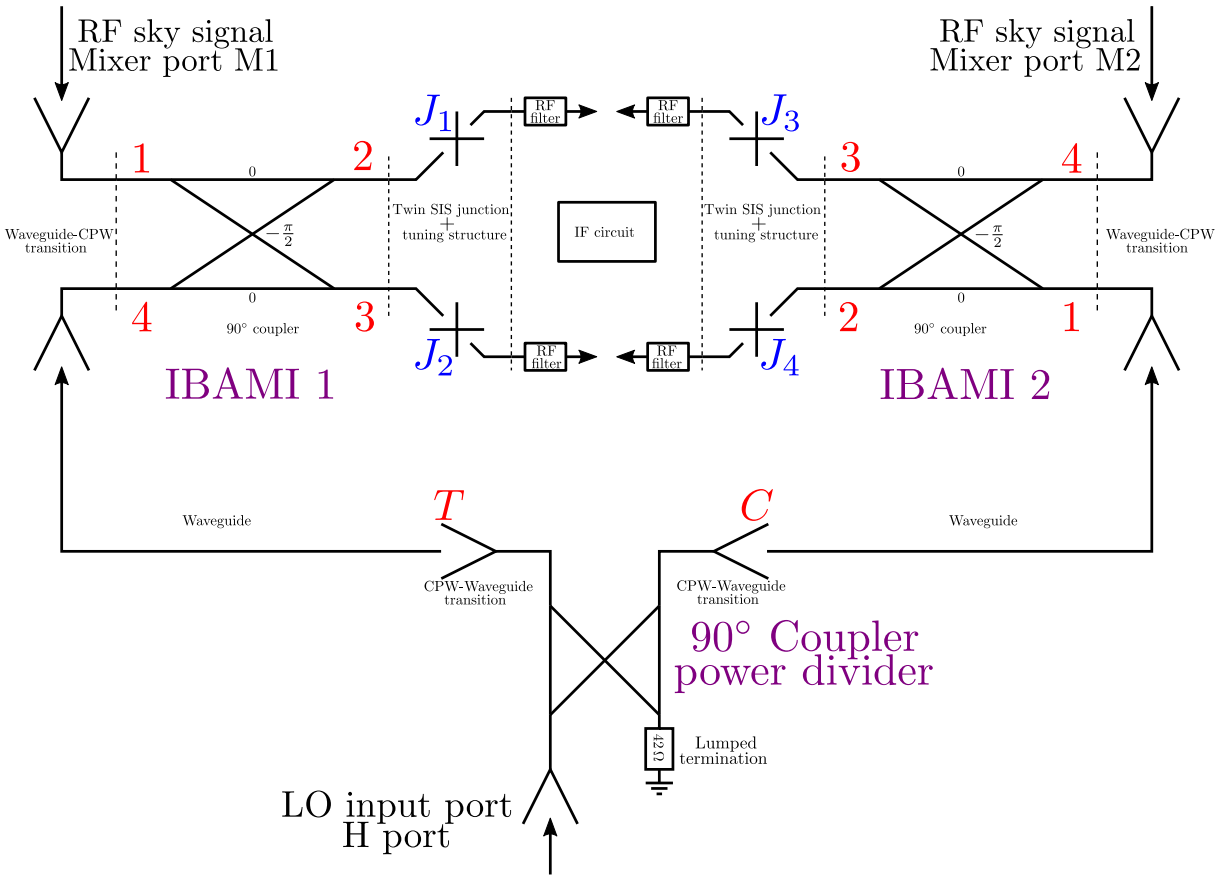

Figure 4.6: Schematic of the two-pixel block. The LO signal is received at the input port of the 90° Coupler and divided towards the two IBAMI. The ports of the IBAMI are labelled as well as each of their SIS junctions. The numbering of the coupler ports (coloured in red) in IBAMI2 follows the same numbering as in the simulation schematics. This arbitrary labelling was done to avoid confusion in the posterior analysis of the system.

4.2 Experimental Setup

In this section the equipment required to carry out the desired measurements is described, starting with the cryogenics, continuing with the testblocks, Software and recording electronics to finish with the radiation sources and external optics.

4.2.1 Cryogenics

The power divider and the IBAMI mixers are fabricated in superconducting thin film Nb (150 nm) on top of a 9μm silicon wafer. The operational temperature of superconductors has to be below half ofT_c, which for Nb is $4,8$ K. This sets an additional demand on the testing equipment and there are two approaches to achieve such low temperatures. The first one is the use of liquid Helium-cooled dewars and the second is the use of closed system cryocoolers. For this work liquid helium dewars are used, given their availability in the group.

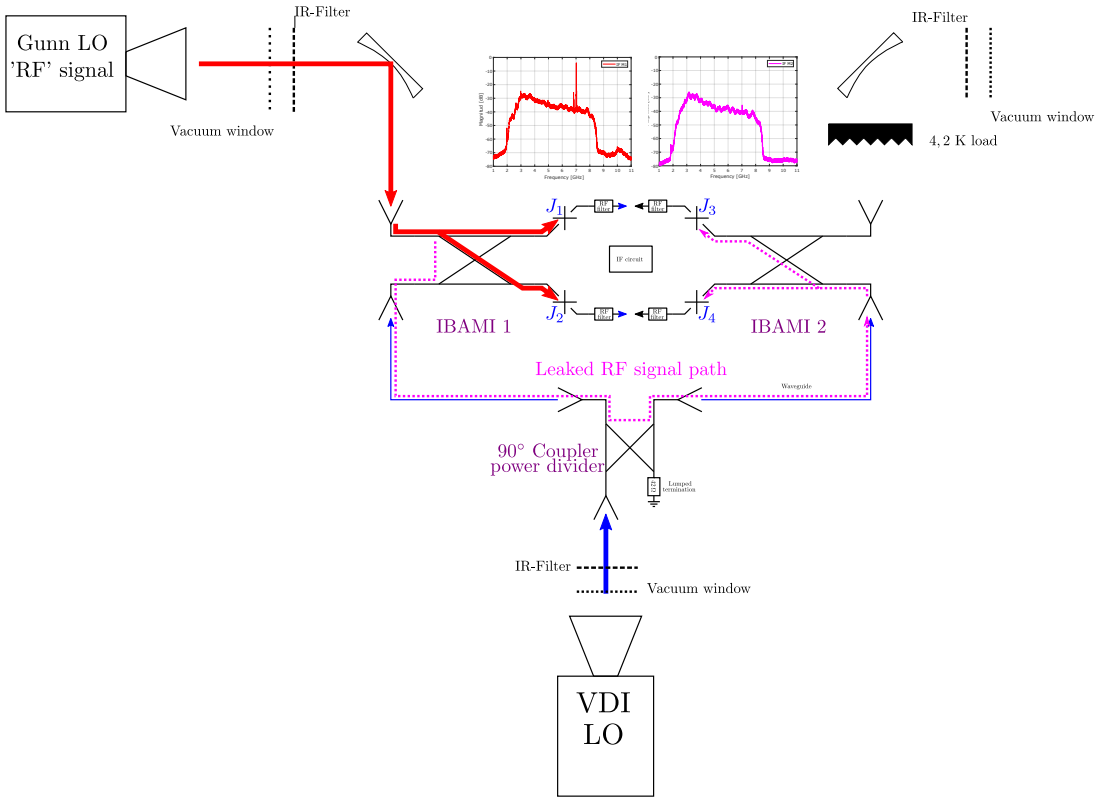

Figure 4.7: Setup for the characterization of the crosstalk over the LO path in the two-pixel block. Here only the xtalk over the LO path is shown. The CW signal from the Gunn LO leaks into the LO path and reaches the coupled transmitting through the output ports of the coupled and directed to the blinded mixer.

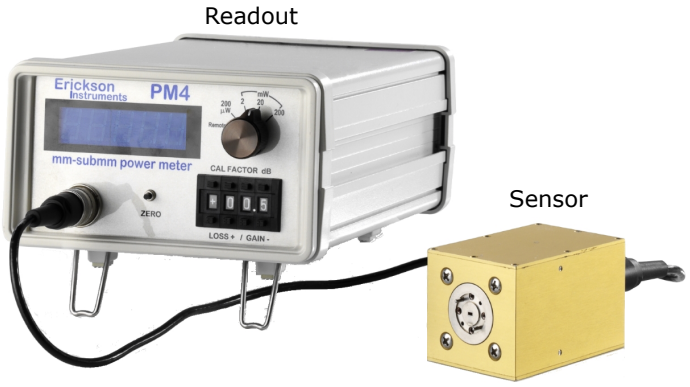

Figure 4.8: *Erickson power meter* model PM4 as no depiction of the model PM3 was found. The device has a coaxial output that allows for the recording of the displayed voltage corresponding to the measured power.

The dewar utilized is an Infrared Laboratories [infrared laboratories,], from the HDL-X series (Fig. 4.9a). It has two stages, at 77 K and 4.2 K respectively (Fig. 4.9b). The cold plate for mounting test devices is a gold-plated copper slab that is the bottom of the liquid Helium container inside the dewar. This ensures a good thermal link between the liquid helium and the superconducting devices. This test chamber has 4 windows for free space coupling to the exterior that can be sealed shut if needed.

4.2.2 Test blocks

The planar components designed and used in this work are meant to be suspended in cavities with waveguide interfaces at their ports, through which the RF and LO signals are coupled to the chips. 6 test blocks were used to test the components, one test block which houses only 1 IBAMI chip and 5 2-pixel blocks.

The first block used is the balanced mixer waveguide test block, detailed in [Westig, 2013], Chapter 4. This is a symmetric copper tellurium block that houses only one IBAMI chip. This allows for the characterization of the IBAMI chip by itself, without any interactions with other planar components. This block was originally used to test the noise temperature of the IBAMI chip and in this work, it is used to measure the power coupled from the waveguide ports of the IBAMI chip to the SIS junctions.

The five variations of the 2-pixel block are numbered 11.110.02, .03, .04 and .05. All these blocks contain one power divider and two IBAMI chips with two horns at the RF input of the mixer. Their dimensions are 19.8 x 24 x 9.6 mm^3 split blocks machined in copper tellurium by the workshop of the *I. Physikalisches Institut*. Blocks .02, 03. and .04 were fabricated in Q4 2019, while block .05 was fabricated in Q4 2023. Fabricated block .02 is shown in Fig.4.10.

The waveguide dimension in the 2-pixel blocks is 460x230 μm^2. The input LO signal is coupled in, and out of the block by diagonal horns. Within the block, there are two permanent magnets used to suppress the Josephson current in the SIS junction. The block has also the DC connections required to bias each individual junction (J_x) and to record its IV curve. The block is housed in the 4.2 K stage of Dewar 8, attached to the cold optics block for thermal link to the dewar cold plate and coupling to the outside (Fig. 4.11).

Blocks .02, .03 and .04 are designed to test branch line power dividers while block .05 is designed to test the microstrip Wilkinson. Almost every branch line power divider was tested in either block .02 or .03. Block .04 was meant to include a board that would allow biasing of the SIS junctions, and read out the LO-induced current in them. That board did not survive the first cool-down and broke down, effectively impeding the testing of any power dividers in that block. Blocks .02 and .03/.04 are almost identical with the exception that block .03/.04 has 5μm pockets milled in the upper half of the block that fits over the beamleads. This is done to reduce the mechanical stress applied to the silicon membranes during the assembly and disassembly of the

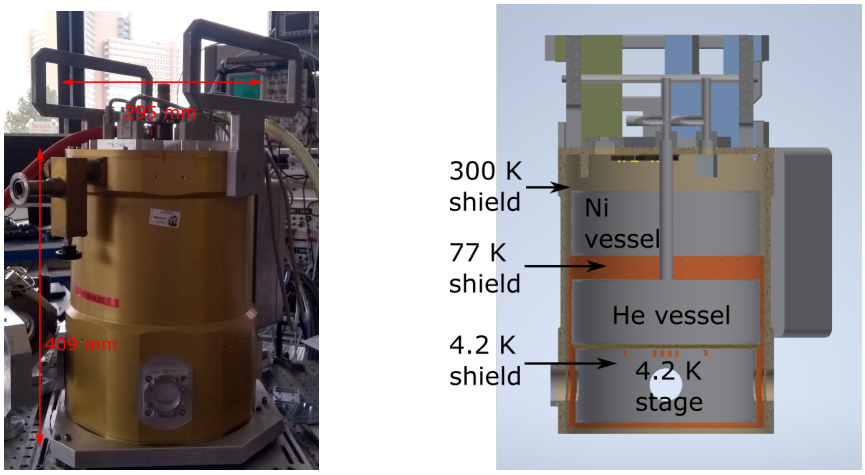

(a) (b)

Figure 4.9: Cryogenic dewar utilized for the power divider experiments. Photo of dewar 8 in the experimental setup.Schematic of the HDL dewar used with its stages and vessels labeled

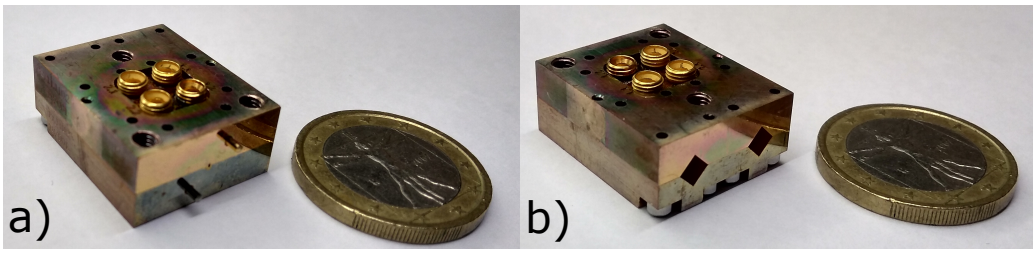

Figure 4.10: a): Rear of the 2-pixel block. **b):** Front of the 2-pixel block with a view of the two diagonal horns that lead to the mixers. On the top of the block are the four G3PO connections to bias the junctions and deliver the IF signal to the Cold Low Noise Amplifiers.

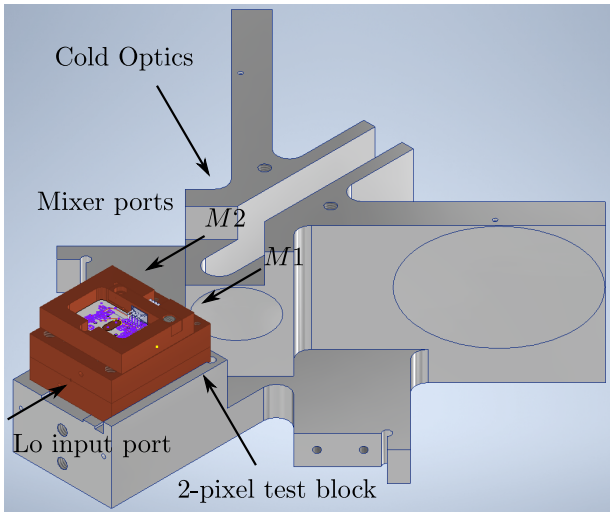

Figure 4.11: CAD schematic of the cold optics sledge plus the two-pixel block

block. Fig.4.12 shows the top half of blocks .03(**left**) and .02 (**right**) over the branch line power divider cavity. The beamleads leave a print on the surface of block .02 top half as they are pressed between the two halves. Block .05 also has 5, μm beamlead pockets over the beamleads of the IBAMI and the Wilkinson power divider, Fig.4.13 **Left** shows a schematic of the beamleads on top of the IBAMI cavity for both blocks .03 (**left**) and .05 (**right**). It can be seen how the beamlead in block .05 is divided into smaller beamlead pockets instead of having one large, continuous pocket as in .03/.04. The reason for this modification is that simulations (Showed Section 5.4, Fig.5.33) of this blocks shows a resonance behaviour where the field concentrated in the area that has been removed. The last difference between block .03/.04 and .05 is the fact that the waveguide interface of the IBAMI chip features a step discontinuity where the Waveguide cavity is reduced from 460to 200 μm (Indicated as waveguide step in Fig.4.13). More details about his can be found in [Westig, 2013], section 3.2.4.

4.2.3 Software, equipment and electronics

The initial code used to record the I-V characteristics was developed by former doctor student Florian Blauth 4.14. It was able to record the I-V curve of an SIS junction together with the IF power output. The program was initially designed for the characterization of the noise temperature of devices. It can record the SIS I-V, the IF power output and the noise temperature. Later, the software was modified by senior researcher Matthias Justen to allow an automatic sweep in frequency and recording of a single point of the IV curve.

The SIS I-V recording software receives the voltage and current signals from the HIFI warm electronics (Fig. 4.15). They allowed for the individual biasing of the SIS junction through the use of bias boxes inside the 4.3 K stage of the dewar (Fig.4.16).

Another software used for the characterization of the coupler is the IF software which allows for the recording of the IF band. It is connected to an Agilent technologies PXA Spectrum analyzer N9030A through LAN communication(Fig.4.17).

4.2.4 Radiation sources and external optics

To test the coupler characteristics it is required to use a continuous wave (CW) source. Two CW sources are used in this thesis, the first source is **Virginia Diodes inc.** signal generator extender module **sgx 494 WR 6.5**, from 110 to 170 GHz plus a frequency tripler. Since it is an extension module,

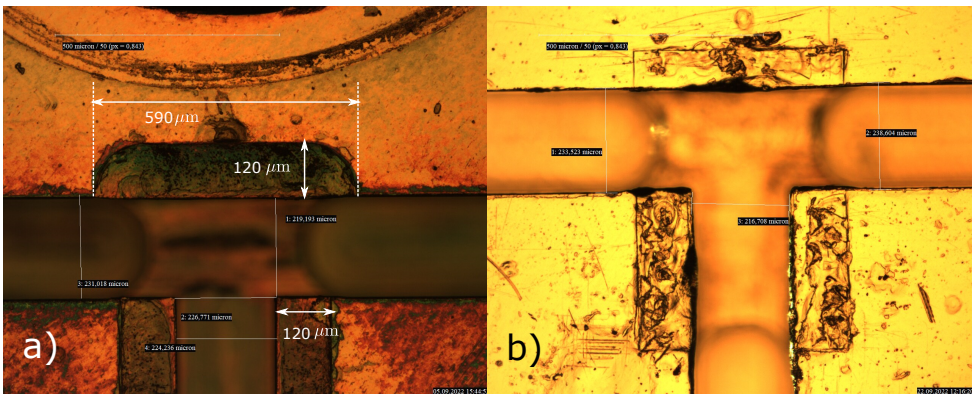

Figure 4.12: Pictures of the top half of the 2-pixel block over the branch line power divider cavity. **Left:** Top half of block .03 displaying the pockets over the branch line power divider cavity. **Right:** Top half of block .02 displaying the cavity of the branch line power divider. The beamleads leave a print on the surface of the block as they are pressed between the two halves of the block.

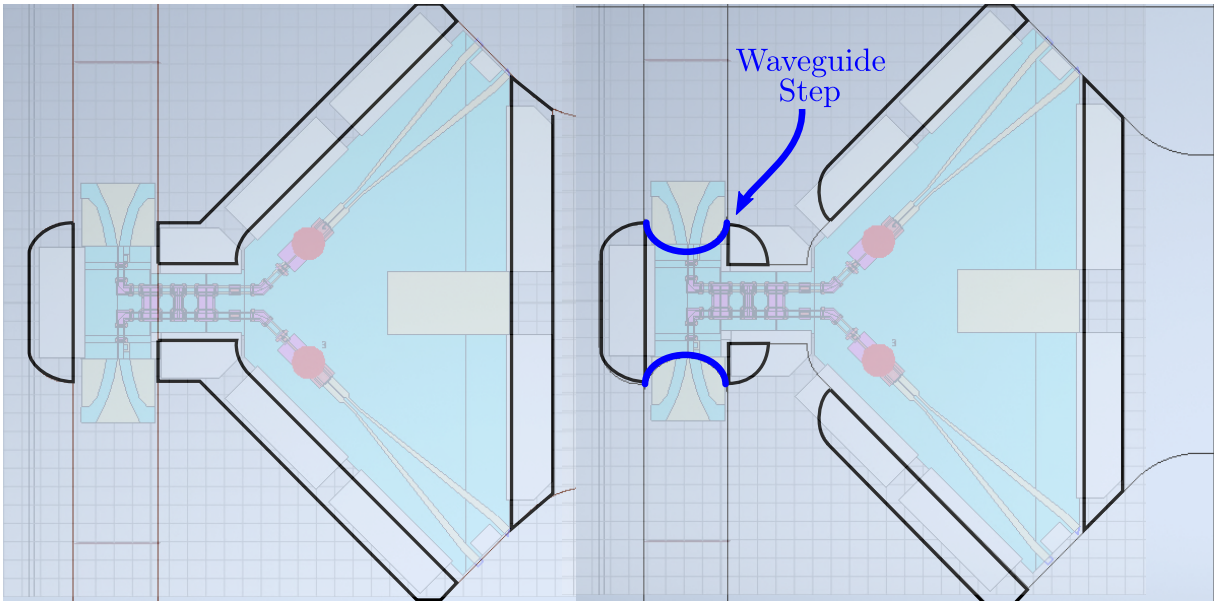

Figure 4.13: Footprint of the beamlead pockets in the IBAMI cavity. The beamlead pockets are highlighted in a black. **Left:** IBAMI cavity in block .03 and .04 . Here it can be seen how the lateral beamlead pocket extends along the entirety of the IBAMI cavity. **Right:** IBAMI cavity in block .05, in this case, the lateral pockets have been broken into two smaller pockets at the side of the coupler. The front and back beamlead pockets remain the same as in block .03/.04.

this source requires an input signal. This signal is provided by the *Anritsu MG3692C* signal generator (Fig. 4.18). The combined signal generator and the VDI extension module allow for CW emission in the frequency range of 330-510 GHz band (Fig. 4.19). This CW generator is from now on called *VDI LO*. The second CW generator used in this work is an **Radiometer Physics GmbH** Gunn diode CW generator, here on called Gunn LO. The operation frequency of this one ranges from 438-504 GHz and has the configuration for only 12 frequencies labelled. Among the frequencies labeled there is a setup for 462 and 491 GHz, two very important frequencies of interest for

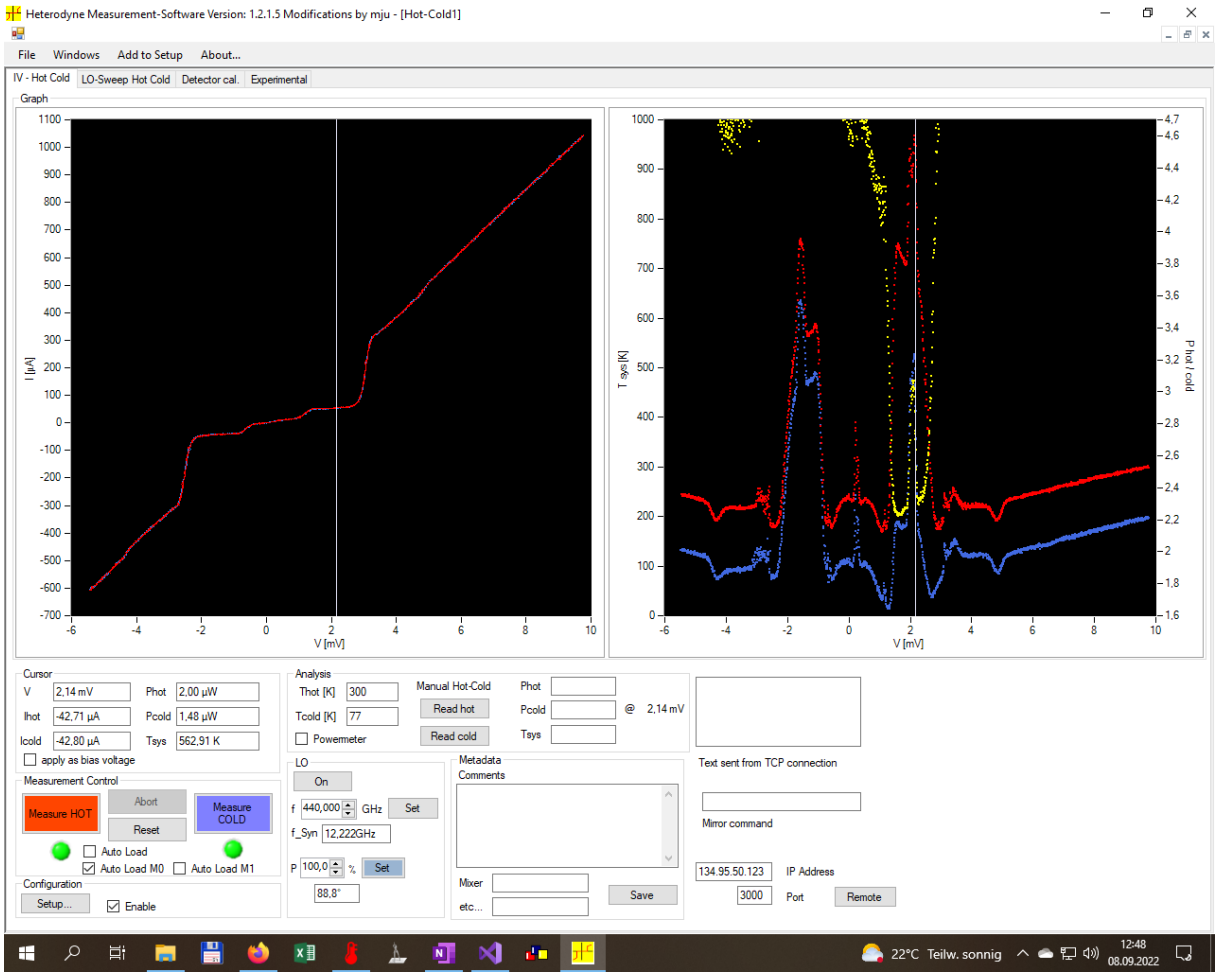

Figure 4.14: User interface of the software developed by Florian Blauth and later modified by Matthias Justen. It was initially used to record the pumped I-V curves of the SIS junctions for a given frequency (left window) and the IF power output (right window). The later modification was made to allow a frequency sweep with a CW source and record the I-V curve of an SIS junction at a desired bias point.

the receiver. The maximum output power of the Gunn LO is 80 μW.

Both CW generators are coupled to the mixers by free space coupling and the use of optics. The warm optics setup consists of concave and planar mirrors to focus the beam into the dewar and a grid to attenuate the CW power coupled to the dewar (Fig. 4.20). The VDI LO is coupled to the free space by the use of an in-house made diagonal horn antenna. The same antenna is used in the 2-pixel block. For the Gunn LO, no documentation detailing the parameters of the antenna was found. To focus the beam pattern into the dewar a convex mirror is used. The optics were designed only to extract and deliver the signals in and out of the 4.2 K chamber of the dewar and have not been optimized to reduce reflections and standing waves in the optic path leading to the two-pixel block.

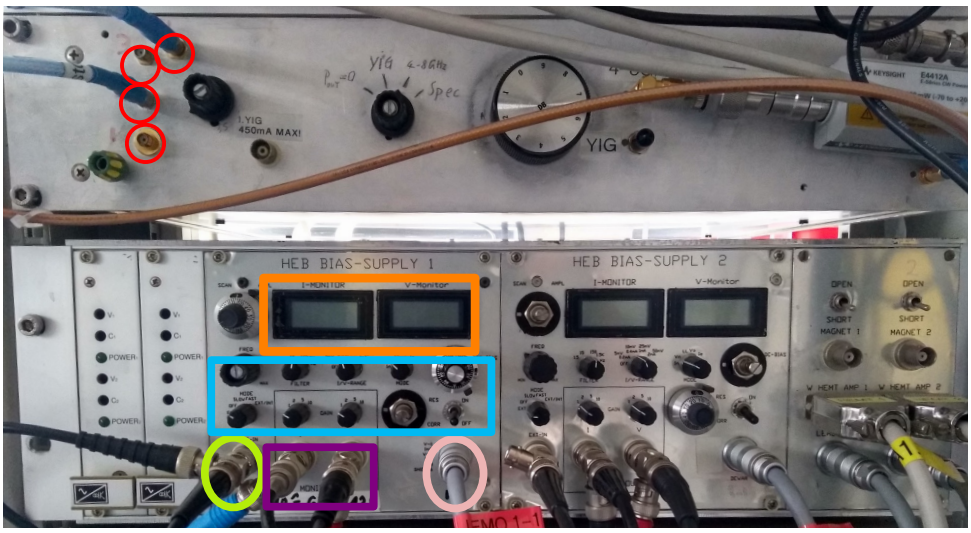

Figure 4.15: Warm electronics are used for the recording of the I-V characteristics. **Top:** IF board used to record the IF output of the mixers. Marked on red, the four IF inputs of the board. **Bottom:**Bias boxes 1 and 2 of the four bias boxes used. On orange: the voltage and current displays, marked on Cyan the voltage, current and sweep control knobs, Pink: the voltage and current connection to the cold electronics inside the 4K stage of the Dewar. Lime: External voltage reference connection.

4.2.5 Power division experiments

Power division experiments are intended to measure the S-parameters S_{21} and S_{31} of the coupler, or at least, detect a directly related variable across the band of interest, such as current induced in the SIS. There are two manners to achieve this. The first is to take a tunable CW source, the VDI LO, for example, tune it to the desired frequency, record the variable of interest and repeat for the desired frequency points. The second one is to use the SIS junctions of the IBAMI as a detector perform space-domain measurements and use the Fourier transform to calculate the frequency response of the SIS.

Frequency sweep of the Local Oscillator

Measuring the coupler characteristics with SIS junctions as detectors requires two IBAMI chips. The coupler and the IBAMIs are placed together in the 2-pixel blocks, the layout is shown in (Fig. 4.6). This setup has the advantage, that not only serves as an experimental setup for the coupler but also yields valuable insight into the integration of the components for the future array receiver. This is because the 2-pixel block emulates 2 adjacent pixels of the LFA.

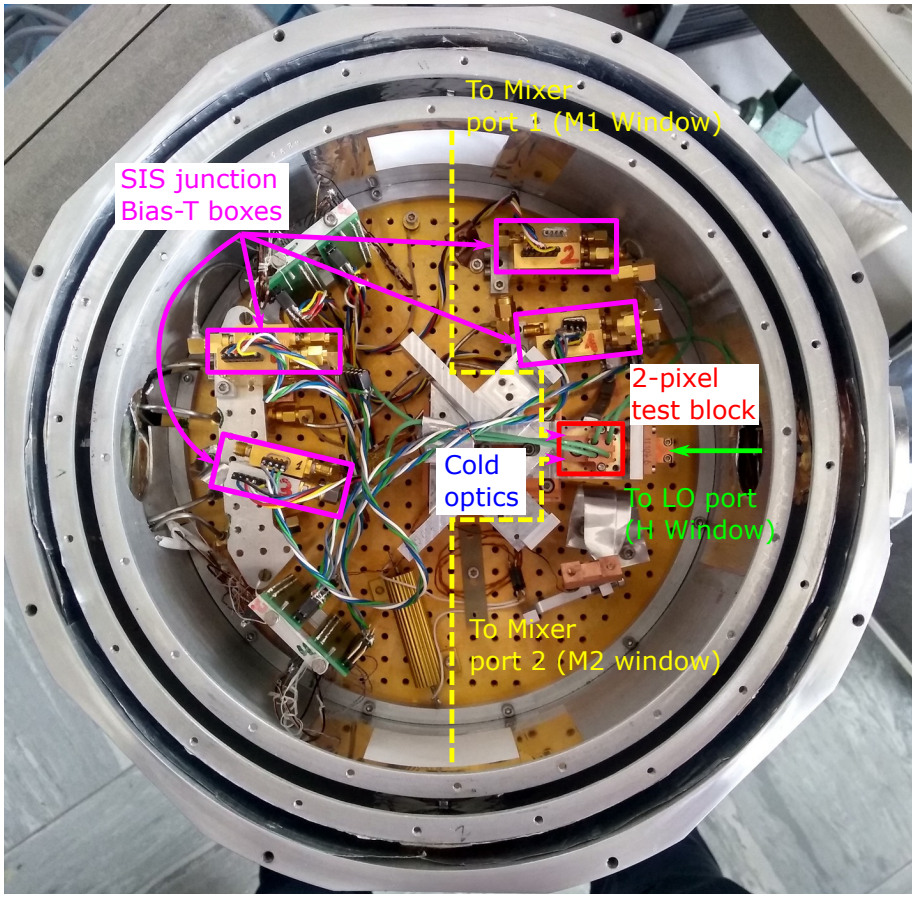

Figure 4.16: Top view of the 4.2 K stage of Dewar 8. Four bias-T boxes are used to set the bias and read out the I-V characteristics of the SIS junctions. The LO and Mixer ports are coupled out of the dewar through the three IF-blocking windows. The four bias-t boxes(marked with magenta) allow the biasing and the reading of the I-V characteristics of the SIS junctions as well as extraction of the IF signal generated in the mixers.

Figure 4.17: Agilent Technologies PXA Spectrum analyzer N9030A used to record the IF band of the IBAMI. The input is connected to an Agilent power meter that receives the combined outputs of the IBAMI.

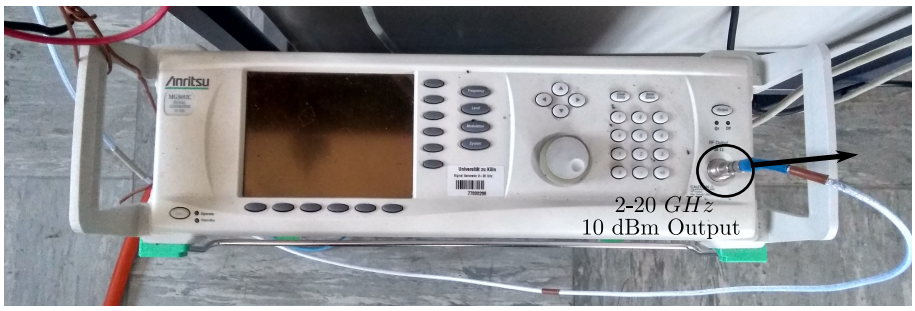

Figure 4.18: Anritsu MG3692C Signal generator used to generate the initial RF feed signal for the signal extensor. It is capable of delivering 10 dBm of output power in continuous wave mode has and has an output range from 2-20 GHz. This is the Signal generator used to produce the reference signal for the extensor module.

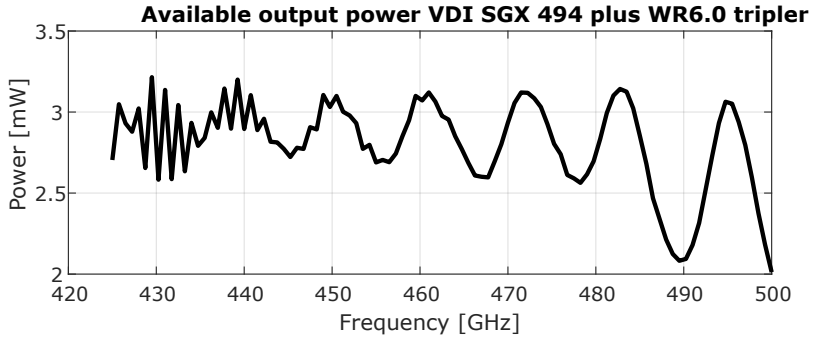

Figure 4.19: Measured output power for the VDI SGX 494 extensor module plus WR6.0 tripler. The measurement was made with a VDI PM5 power meter with a direct Waveguide connection. This corresponds to the maximum power available from the VDI extensor module.

Frequency sweeps with SIS detectors

The sweeps do not entail much more than selecting the frequency with the *Anritsu signal generator* (frequency resolution up to 1 Hz), recording the induced current at a specific voltage bias at the four detectors and continuing until the desired frequency band has been covered. Ideally, the available CW power and the optic coupling remain constant across frequency, allowing for an easier analysis of the experimental result. This is not the case, as visible from the measured output power from the VDI LO plus the frequency tripler(not with a diagonal horn antenna attached). Reflecting upon this fact, two clear options arise. The first is to adjust the VDI power at each frequency point so the coupled power to a detector of choice remains constant. On the other hand, the second is to only adjust the VDI LO power before each sweep with the adjustment made so all four detectors remain in the linear regime across the complete frequency band.

For the adjusted frequency sweeps it is necessary to choose a detector as the reference one, in this case, it is J_1. The VDI LO power coupled to the reference junction is adjusted at every frequency point so that the induced

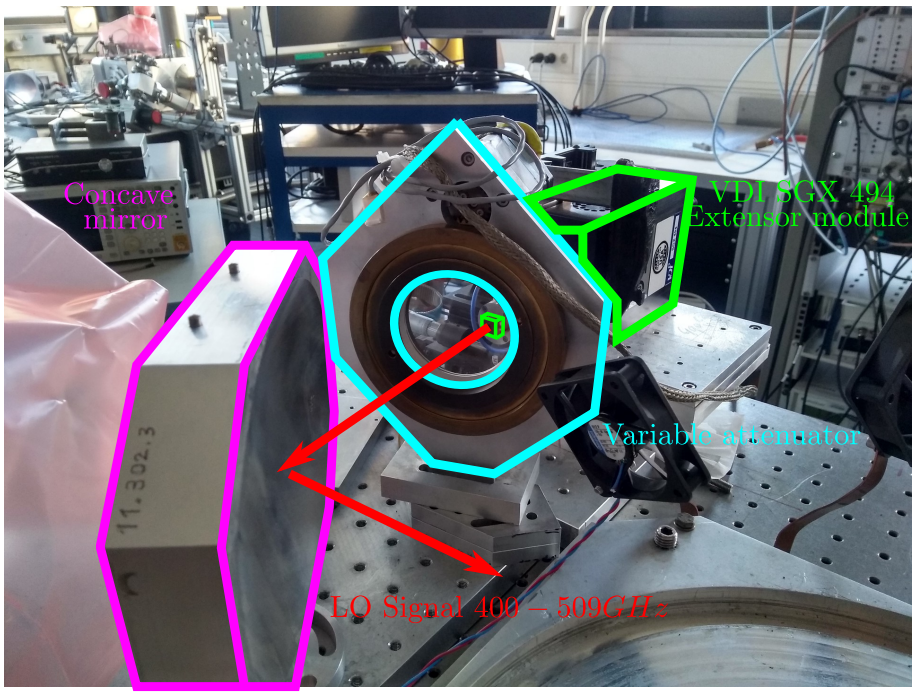

Figure 4.20: Optics setup used to characterize the LO power divider. The VDI extensor module deceives a reference signal from the *Anritsu signal generator* and generates a signal whose frequency is $36 \cdot f_0$ is mounted on a three-axis stage, allowing for position adjustments in the $x-$, $y-$ and $z-$axis. In front of it, there is a rotating grid that decreases the available power delivered to the dewar, Finally, there is a concave mirror that focuses the beam from the signal extensor into the dewar.

current at a specific voltage is kept at a constant value. The adjustment in coupled power is done employing the warm optics. The bias point chosen for the reference detector is V = 2.0 mV and I= 60 μA. The measurement is executed by tuning the VDI LO at the start frequency, recording the I-V curves for each of the four detectors and moving to the next point until the desired frequency range has been covered. The resolution of this frequency sweep is $\Delta f = 1$ GHz. This seemingly coarse resolution has its reason in the fact that, at the time of the execution of this experiment, there was no automated software capable of performing the required adjustment between each frequency point. The selection of the desired detector output to record was done manually and had to be done for the four detectors for every frequency point. This led to a very long execution time of around 4 hours in a setting where the hold time of the dewar was about 7 hours in the most ideal of cases.

A brief summary of the procedure of this frequency sweep is

- Record an Off-measurement of the IV curves of the four detectors
- Start at f_0 by tuning the VDI LO
- Select reference detector, voltage and associated induced current level

desired

- Adjust the warm optic to reach the desired induced current in the reference detector
- Record the I-V curves of the four detectors.
- Repeat for $f_0 + \Delta f$
- Record off measurement of the I-V curves of the four detectors at every predetermined frequency milestone.

The non-adjusted frequency sweep had the VDI power adjusted only before each frequency sweep. Hence, the initial adjustment of the VID LO coupled power had to ensure that all four detectors would remain in the linear regime across the entire frequency band. Due to the standing waves present in the optic path, such a requirement was not always achieved. At some frequency points the power coupled to the detector is so great that the SIS junction saturates. When this happens the induced current in the SIS junction is no longer linear concerning the coupled power. To avoid this, a preliminary sweep is executed. The four detectors are biased at 2.2 mV, below the gap voltage, and the induced current is recorded for the frequency band. The original software was modified by Matthias Justen to automatically tune the VDI frequency and record the induced current of a single detector. The bias voltage of the detector to be recorded had to be manually selected before the execution of the sweep. This modification to the software allowed for faster sweeps and an increased resolution. A brief summary of this frequency sweep is

- Bias the four detectors at between $2 - 2.2$ mV
- Run a preliminary trial to check the power coupling level in the four detectors
- Adjust the warm optics. This may take several adjustments
- Check that all four detectors remain in the linear regime
- Sweep the VDI LO for the four detectors without making further adjustment to the warm optics or to the VDI LO

Frequency sweeps with the Erickson PM3

The third frequency sweep involves the replacement of the SIS detectors in the mixer as direct detectors by an *Erickson PM-3* (Fig 4.8) power meter. As detailed in the previous section, the power meter is an incoherent detector and only detects the power coupled to the film in the sensor. The PM3 is placed outside the dewar in front of the windows leading to the mixer ports (Fig.4.16 in yellow) and the VDI LO is chopped On-Off. For this experiment,

the same 2-pixel blocks are used. For this, the IBAMI chips have to be removed from the block. The first trial run was made with the IBAMI chips inside the block, to detect any power coming out of the mixer port windows. Any power detected there would point to some anomaly where there would be power reflected or not coupled to the mixers and ejected to the mixer ports of the block. After the trial runs were performed the IBAMI chips are removed from the block and the LO sweeps are repeated. The software used for the recording of the voltage output of the PM3 detector is the same modified software used in the frequency sweeps with SIS junctions as detectors. To ensure stability the bandwidth was covered in small frequency ranges where an off-measurement of the background took place in between them.

A brief summary of this frequency sweep is

- Turn on the Erickson PM3 and wait until it stabilizes
- Select the desired frequency bandwidth and resolution
- Perform an initial Off measurement of the same duration as a complete frequency sweep
- From the previous measurement asses the stability of the PM3 sensor and select a frequency span that ensures the stability of the detector within the time frame T_meas
- Perform the frequency sweep $f_0 - \Delta f$
- Perform an off measurement lasting T_{meas}
- Perform frequency sweeps and Off-measurements until the desired frequency range has been covered

Fourier Transforms Spectrometer (FTS) experiments

The experiments with the FTS are done by replacing the sensors of the FTS with the IBAMI, either in the balanced mixer test block or in the 2-pixel block. Perform a spatial sweep without any sample and record the Fourier transform of the detected current of the IBAMI. For this setup, the test block is moved from Dewar 8 to Dewar 1. This is due to the fact there is no need to record the IF output of the IBAMI and, hence, they can be moved to a smaller dewar that requires fewer litres of liquid Helium to cool down.

4.2.6 Measurement of crosstalk between mixers

So far the experiments devised test parameters that are related to the transmission between the input and output ports of the coupler. Another parameter of interest is the transmission between the two output ports, namely, the S_{23} s-parameter. The current setup allows the injection of the CW signal

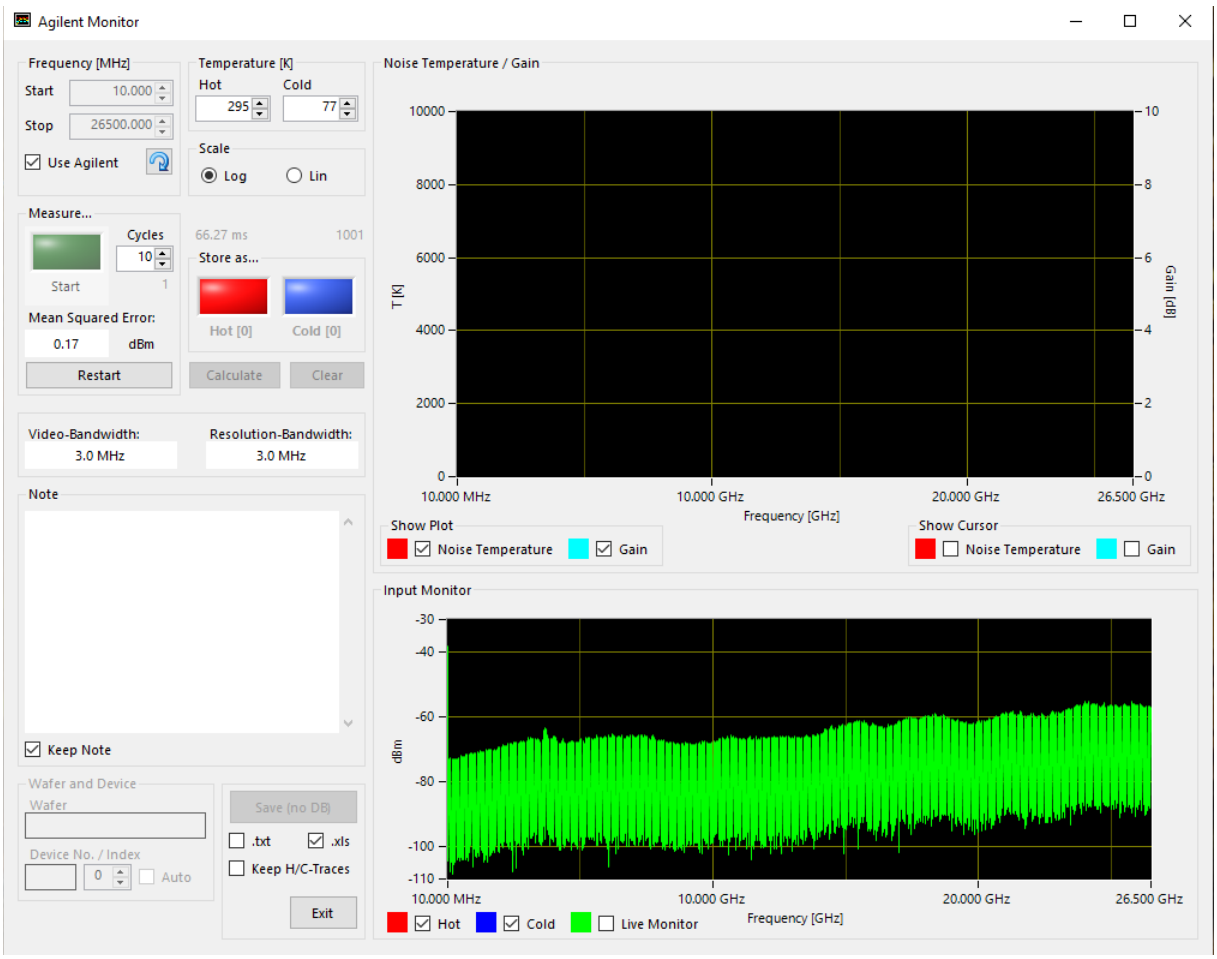

Figure 4.21: Custom Software made by M. Schulz to read the IF band and calculate the noise temperature and gain of a mixer (Top display). The spectrum captured by the signal analyzers is shown in the lower display.

through the three ports of the block. For this experiment, the SIS junctions are the detector of choice again. However, they are used in a balanced mixer configuration instead of as a direct detector. For this experiment another CW source is needed, in this case, it is a *RPG* Gunn LO. The VDI LO will be used as the signal enabling the mixing process in the SIS junctions meanwhile the Gunn LO acts as a signal to be detected in the IF band of the mixers. The test has the VDI LO injected through the LO input port while the Gunn LO shines into one of the mixer ports leading to an IBAMI. This mixer is referred to as the *sighted mixer*, meanwhile, the other mixers are referred to as the *blind mixer*. The spectrum of the IF band is recorded with an *Agilent PXA Signal Analyzer N9030A* (Fig.4.17). The Signal analyzer is then controlled using custom software developed by Michael Schulz to read and record the IF output of a mixer and to calculate its noise temperature and gain(Fig. 4.21).

Extra preparations were taken for this experiment. The actual variable measured in this test is the cross-talk between mixers. This is not only affected

by the properties of the coupler but also by the properties of the optics, the block, the IF circuitry and the IBAMI themselves. There are three possible paths where from one pixel may leak into the other. those are over the optic path, the IF path and the LO path. The first, Xtalk over the optic path refers to a signal being captured by the optics of both the sighted and blind pixel. This path is eliminated using blocking the aperture of the diagonal horn leading to the blinded pixel with an absorptive polymer, effectively *blinding* the mixer. The crosstalk over the IF path refers to unforeseen coupling in the IF circuitry. Characterization of crosstalk over the IF path requires two sighted pixels. The SIS junctions of one of them are biased on the resistive zone of the SIS (beyond the gap voltage), effectively deactivating the mixer. Then, any signal detected on the deactivated mixer IF band is due to coupling from the active pixel IF. For the experiments executed, the contribution to the crosstalk through the IF path was ruled out given that the other pixel was a blind pixel. Furthermore, the IF combination is done outside the dewar, and not inside the 2-pixel block. Crosstalk over the LO path means that the CW signal from the Gunn LO finds its way to the waveguides connecting the IBAMI and the coupler. From there it transmits through the output ports of the coupler and reaches the blind mixer. So indeed the talk over the LO path is influenced directly by the transmission between output ports of the coupler, particularly, the S_{23} parameter. A visualization of the Xtalk over the LO path is displayed in Fig. 4.7.

A complete characterization of the crosstalk over the entire frequency band of the LFA is not practical since the same tone of frequency f_0^{Gunn} can be detected with frequencies from $f^{VDI} \pm \nu$, with ν any value between 4 and 8 GHz. It was decided that Xtalk characterization would only be performed for scenarios relevant to the science case. Only two frequencies are selected, $f_1^{Gunn} = 461$ and $f_2^{Gunn} = 492$ GHZ, these frequencies are the CO $4-3$ and [CI]$1-0$ transition frequencies. The VDI LO is then swept from the lower and upper sideband covering the entirety of the IF bandwidth of $4-8$ GHz with a resolution of 1 GHz. Regarding the setup for the SIS junctions, they are biased at 2mV. For the adjustment of the VDI LO power one junction is chosen as a reference once again and the warm optics are adjusted so the first photon step shows a current of 60 μA at every frequency. The lower and upper sidebands of the mixer are then driven out of the dewar where they are recombined by a 180° coupler and detected by a power meter whose spectrum is analyzed by the signal analyzer.

a brief summary of this experiment is

- Select the Gunn LO frequency f_{Gunn}.
- Calibrate the power sensor
- Tune the VDI LO f_{DVI} a frequency within the one of the side bands of the f_{gunn}
- Set the bias voltage of all four SIS at 2mV and choose a reference junction.
- Adjust the warm optics so the reference junction displays the desired induced current level
- Adjust the Gunn LO power so the tine is detected in the IF of both mixers
- Record the IF output
- Tune the next f_{VDI}

4.3 Data processing: Extraction of parameters of interest

The previous section explained the experiments carried out. In this section, all the necessary steps taken to extract and evaluate the parameters of interest from the acquired data are presented.

4.3.1 Drift and gain corrections in SIS curves

The current and voltage of the SIS junctions are recorded by the use of the HIFI bias boxes (Fig.4.15). These electronics are not free of drift in the recorded voltage and current values. To eliminate such errors from the measured IV curves a sample I-C curve with no LO signal coupled to it is taken. From this measurement, it is possible to find out the drift in current and voltage and correct the measured I-V curves. The zeroing procedure is enabled by the features of the I-V curve: its odd symmetry, the remnants of the suppressed Cooper pair tunnelling and by knowing that the gap voltage of the SIS junctions is approximately 2.8 mV (Fig. 4.22). The correction for bias box current gain is corrected by comparing the current level in the resistivity regime immediately above the gap voltage.

4.3.2 Power division

The adjusted LO power sweeps have the complete LO-coupled I-V curve (pumped IV curves from now on) of the SIS detectors for every frequency point in the bandwidth. From the pumped I-V curves the bias voltage V_{bias} chosen to compare induced current levels is between 2 to 2.2 mV. Then for every frequency point and for every detector the induced current at this V_{bias}

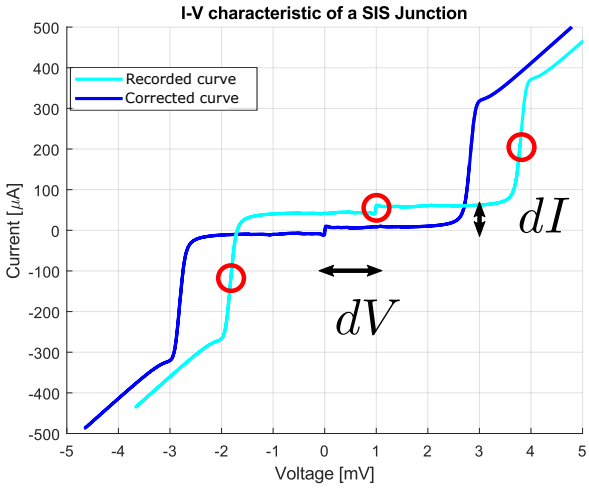

Figure 4.22: Example of drift in the recording electronics and its correction. The gap voltage ($\sim$ 2.8 mV) of the SIS junctions is an inherent property and is not affected by the bias. This property and the remnant of the Cooper pair tunnelling (marked with the red circle) are used to find the drift values of dV and dI and zero the I-V curve. The drift has been enhanced for the example purposes.

is obtained. This is done by a Matlab routine that reads the I-V files and extracts the current value at the desired voltage point. An example of the results obtained is in Fig. 4.23.

The non-adjusted LO sweeps immediately deliver the induced current at a specific voltage for the detector. No complete I-V curve is recorded. Ideally, these recordings could be used to asses directly to asses the power division of the coupler. They could be used to give a rough estimation of the power distribution. The raw data is first corrected for the drift in voltage and current as well as the correction for the current gain. Fig.4.24 **Top** shows the corrected data. To eliminate the external influences in the data, one detector is chosen as a reference and serves as normalization for the other three detectors. The relative measurement is shown in Fig. 4.24 **Bottom** and allows for a much easier data analysis especially when comparing the experimental results to simulation. Since an SIS junction with no coupled LO power still exhibits a small current under the gap, it is necessary to subtract this zero level for each junction before normalizing. This scheme is also performed for the Erickson PM3 experiments, where the power detected at one window is normalized by the power of the other. The zeroing of the power detected by the PM3 detector is done for every frequency band taken.

4.3.3 Evaluation of Xtalk

The data delivered by the spectrum analyzer is the IF spectrum of the mixers. The extraction of the xtalk is a direct comparison between the magnitude of the tone detected in both mixers (Fig.4.25). The sighted mixer detects the

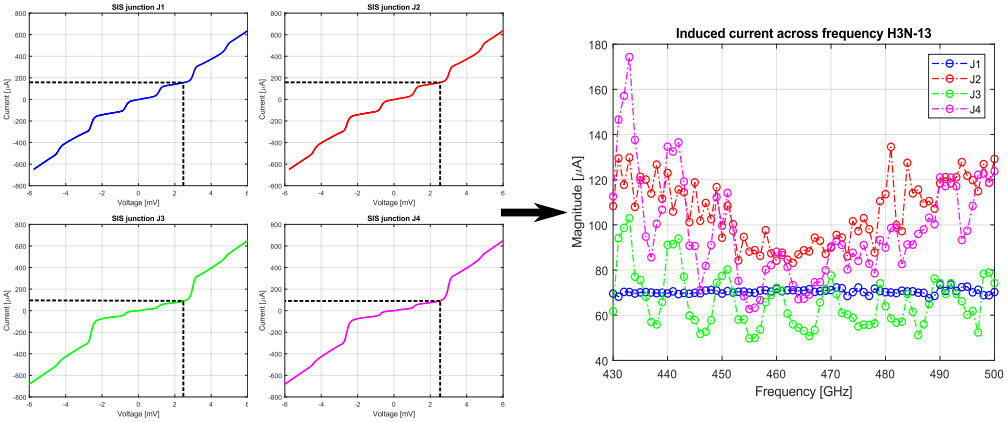

Figure 4.23: Example of how the measurements across frequency for four junctions. **Left**: The four junctions present in the two-pixel block with LO power coupled. The induced current is recorded at the desired voltage value (usually before the critical voltage, around 1.8-2 mV) at a given frequency f_0. **Right**: Recorded induced current at the four junctions from 460 to 490 GHz. The 1 GHz resolution seems enough to capture the overall performance of the power division on the two-pixel block. However, both the frequency span and the resolution are not sufficient for analysis and comparison with the 3D EM simulations.

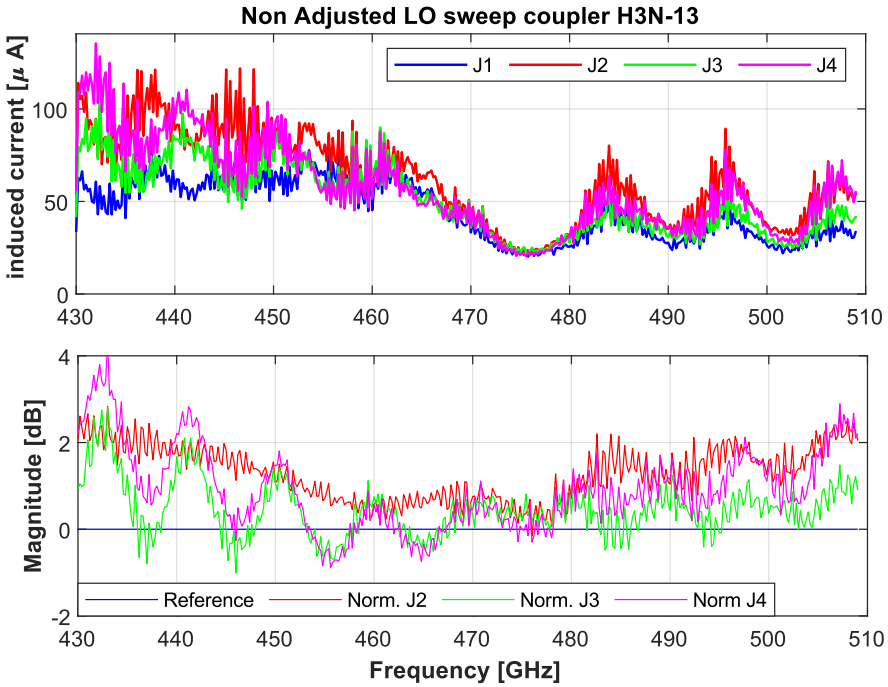

Figure 4.24: Example of the results from a non-adjusted LO sweep **Top**: Raw data recorded by the software. **Bottom**: Induced current for the junction normalized to the reference junction chosen, in the case J_1.

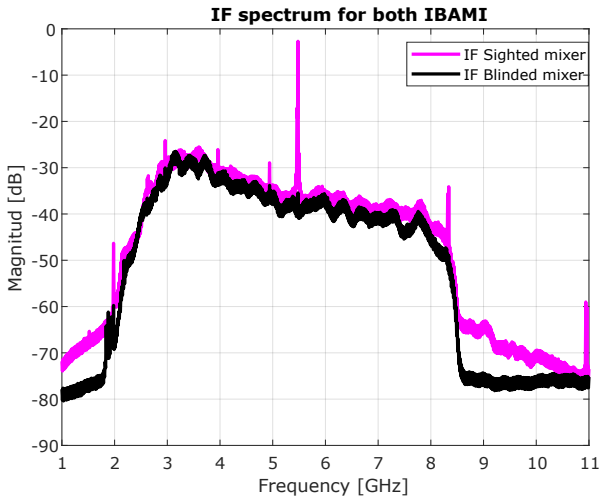

Figure 4.25: IF spectrum of the sighted and blind pixel for $f_{Gunn} = 491.58$ and $f_{VDI} = 497$ GHz. The difference in the average power in the IF band for the sighted and blinded pixel can be explained by the blind pixel being blocked by a piece of absorptive load inside the Dewar, acting like a 4K load. Meanwhile, the sighted mixer background is the IR-blocking windows. The magnitude of the Gunn LO tone in the blinded pixel IF is compared against the magnitude of the tone in the sighted pixel IF. The difference between them is the level of xtalk between the two adjacent mixers.

Gunn LO signal with X dB above the noise floor, meanwhile, the blinded mixers detect a signal with Y dB above the noise floor. In case there is no signal detected on the blinded pixel, the Gunn LO signal power is increased until the signal is detected. The difference between the magnitude X-Y is the level of crosstalk between adjacent mixers. This value is obtained for both the USB and LSB bands for every Gunn LO frequency.

4.4 Summary

The characterisation of the fabricated power divider design entails measuring the transmission from its input towards its output, its isolation between output ports and the reflections produced at any port. This information is resumed in the S-parameter matrix of the component and is usually measured with a Vector network analyzer (VNA). However, VNAs are expensive equipment, not readily available. Additionally, the cryogenic conditions required for the operation of the superconducting devices limit the applicability and practicality of VNA measurements.

The impracticability of VNA measurements to characterise the superconducting devices designed calls forth the search for alternative detectors. The detectors here proposed are the SIS junctions in the IBAMI mixer chips and are used as direct power detectors. For this scheme, two IBAMI chips are required to measure the power divided by the branch line power divider. The

IBAMI chip and the power divider are then placed in a block that represents half of the 4-pixel block. Since neither the power divider nor the IBAMI chips have been characterized in the 2-pixel block configuration, an external power divider that is not part of the network is required. This power meter is the Erickson PM3.

Aside from its use as a direct power detector, The SIS junctions are also used in a coherent detector configuration for measuring the crosstalk between pixels. In this setup one of the IBAMI mixers is blinded meanwhile the other has a direct line of sight of CW generated by the Gunn LO. Subsequently, the IF output is recorded for both pixels. The third detector used is an Erickson PM-3 power meter, this gives a detector that is external to the measurement setup and can measure the power division without the need for the IBAMI mixer chips.

The fact that the power devices and IBAMI chips are fabricated in superconducting materials sets the operating temperature requirements and mandates an operation temperature below 4.5 K. To meet such a requirement, we have chosen to use a liquid Helium cooled Dewar. The dewar chosen is an Infrared laboratory dewar, which has three IR-blocking windows that allow free space coupling to the 4K stage from the outside. The fabricated devices are then placed in a CuTe housing block. a total of 5 blocks are fabricated and used in this thesis. One text block that houses a single IBAMI chip and four 2-pixel blocks. The 2-pixel block represents two adjacent mixers of CHAI with two IBAMI mixers and one power divider. The 2-pixel blocks .02, .03 and .04 are designed to test the branch line power divider, while block .05 is for testing the Wilkinson power divider. Some of the blocks possess a 5 μm pocket over the beamleads that decreases the mechanical strain over them and the silicon membrane. This facilitates the opening and closing of the 2-pixel block.

The code used for the recording of the I-V characteristics of the devices is based on the routines written by former doctor student F. Blauth, modified by senior researcher M. Justen. The code controls a CW source and records the output of the HIFI bias boxes. The source is a VDI extender module that allows for a high-resolution frequency sweep between 400 and 509 GHz. A second CW source used is an RPG Gunn diode LO that is used as an RF signal to be detected and downconverted by the two IBAMI.

Finally, the extraction of the power division characteristics from the power division experiments consists of normalizing the induced current at three junctions concerning a chosen reference junction. For the evaluation of the crosstalk, the intensity of the peaks in the IF band of the blind mixer is

compared to the sighted one. Their difference is the level of isolation between two adjacent mixers.

Chapter 5

Fabricated devices, simulation and experimental results and interpretation

This chapter starts with a description of the fabricated devices, and the differences between the design parameters and the manufactured ones and presents an updated analysis in CST. It continues with the presentation of experimental results of the measurements performed on the IBAMI balanced test block and the fully populated 2-pixel block, with two IBAMIs and one LO divider [1]. Subsequently, a comparison between the measurement results and its simulations is done to finish with a brief study on possible improvements for future LO distribution networks.

5.1 Testing approach

In the previous chapter, it was detailed what the proposed tests and procedures entail. Ideally, every component designed would be tested and its result compared against the simulation. However, that was not the case. To understand what would, at first glance, seem an incomplete set of tested power dividers, it is important to remember the frame in which this thesis was embedded. The overarching goal of the detector group is to build and provide components to populate the 4-pixel block while complying with the required noise temperature (T_{DSB}). For this reason, the test performed were only on devices and in scenarios that would, potentially, be useful in the final receiver. This is the reason why no specialised testing block other than a 2-pixel block was made/designed. Additionally, because the test demands considerable time and consumable resources, it was required to be economical with the testing, pooling together as many experiments as possible in a test session. This is the reason that not all possibilities and combinations of

[1] The adjusted LO sweeps are not presented due being very limited with respect to their results and are not a significant contribution over the non-adjusted LO sweep.

power dividers and detectors were carried out.

5.2 Fabricated devices

The branch line power dividers are fabricated by photolithography in the cleanroom facilities of the I.physikalisches Institute of the University of Cologne. Due to the inherent process accuracy, the fabricated devices's dimensions deviate from the designed ones. The first deviation is that the SiO_2 layer under the grounding bridges is about 920 nm instead of the 800 nm initially intended. The second difference is that the CPW lines are narrower than designed, mostly due to underexposure in the photolithography process. This the narrowing of the CPW lines traduces in a higher impedance than designed. The effect of the underexposure is larger in the thinner branch lines of the coupler (Fig.5.1) since a change from $13 \rightarrow 12.2$ is done not change Z_{CPW} as much as $3 \rightarrow 2.4$ μm. The Waveguide-CPW transition is also affected by the underexposure, with the greatest effect on the slotline-CPW transition(Fig. 5.2). All these modifications are tabulated on tables 5.1,5.2. Additionally, model H2N, the model terminated with a concentrated resistive load has the inductive section under the grounding bridge in the isolated port 3 μm narrower than intended. This is due to a mistake in the export process from CST to the photolithography mask.

All these effects detune the power divider and it is necessary to simulate the fabricated models to have a reliable comparison with the measured results. The models with the fabrication variances included are then simulated with enhanced and more detailed parameters than used previously in the design stage. The reason for this is to try to capture all effects and interactions occurring in the device. This enhanced simulation is enabled by the availability of dedicated simulation computers detailed at the beginning of this chapter and the average computing time for one simulation was about 150 hours.

Another factor to add to the simulation of the fabricated devices is the beamlead pockets. The beamlead was added to blocks 11.110.03, 11.110.04 and 11.110.05. Initial simulation at the design stage does not hint at any significant problem with the addition of these structures neither to the branch line power divider nor the microstrip Wilkinson. Simulation results, shown in Fig.5.3, for the detailed simulation performed, reveal that there is little difference between the blocks. The models start to have a small diverge after 480 GHz that increases with frequency. A review of the 3D field distribution in the model at 500 GHz reveals that the E-field concentrates inside the beamlead pockets (Fig. 5.4). This effect does not seem to have a large effect

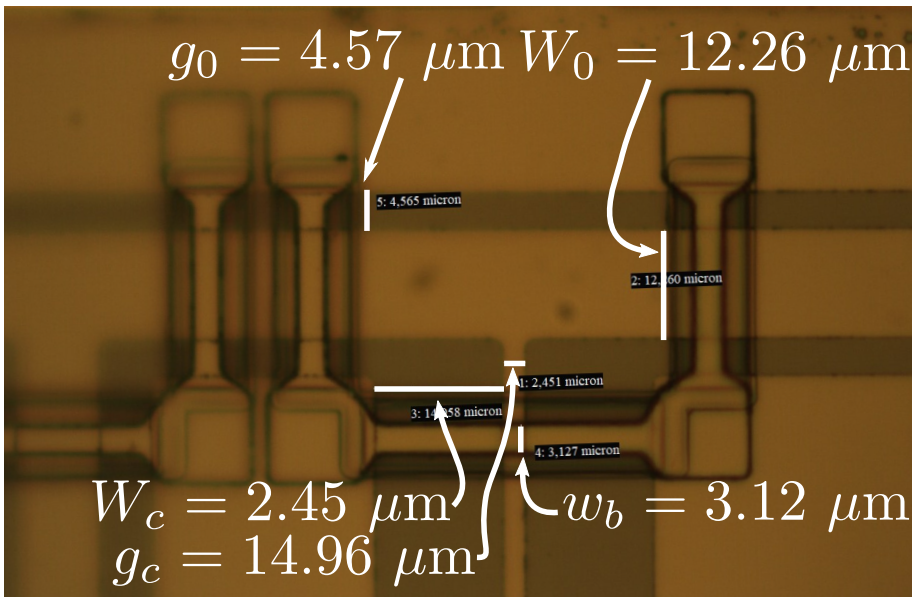

Figure 5.1: Photo of the center lines of a fabricated H2N branch line coupler. Due the difficulty to measure the exact dimension, an average of the measure is taken.

Table 5.1: Average fabricated dimension of the H2N/L/S CPW branch line couplers

Line	Designed (W) [μm]	Designed (g) [μm]	Fabricated (W) [μm]	Fabricated (g) [μm]
Z_0	13	4	12.4	4.4
Z_c	2.9	14.9	2.4	14.6
Z_a	10	5.8	9.6	6.1

on the S-parameters of the power divider within the LFA band. From the simulated power divider terminated with a short circuit, it can be seen that the effect is only noticeable at the higher end of the band.

The CST models for all the branch line power dividers (H2N, H2L, H2S and H3N) are updated, simulated and compared with the original results presented in Chapter 3. For the power divider terminated on a concentrated resistor, model H2N, there is the additional fact that the inductive section of the grounding bridge is 3 μm narrower than expected. For this device the deviation from original values means that the operational bandwidth is reduced, this can be seen by the imbalance (Fig.5.5 **Top left**) that has the points of equal power division at 436 and 480 GHz. The reflections at the input port (Fig.5.5**Middle left**) are under -12 dB for both models with the fabricated model suffering from an increase in the reflections at between 400 and 460 GHz. The isolation between output ports remains mostly the same between the two models up to 500 GHz when the fabricated model displays lower transmission between ports. The reflection at the output ports remains under -10 dB in the band of interest but has noticeable changes between models (Fig.5.5 **Bottom left**). These changes are mainly due to the changes in the termination at the isolated port.

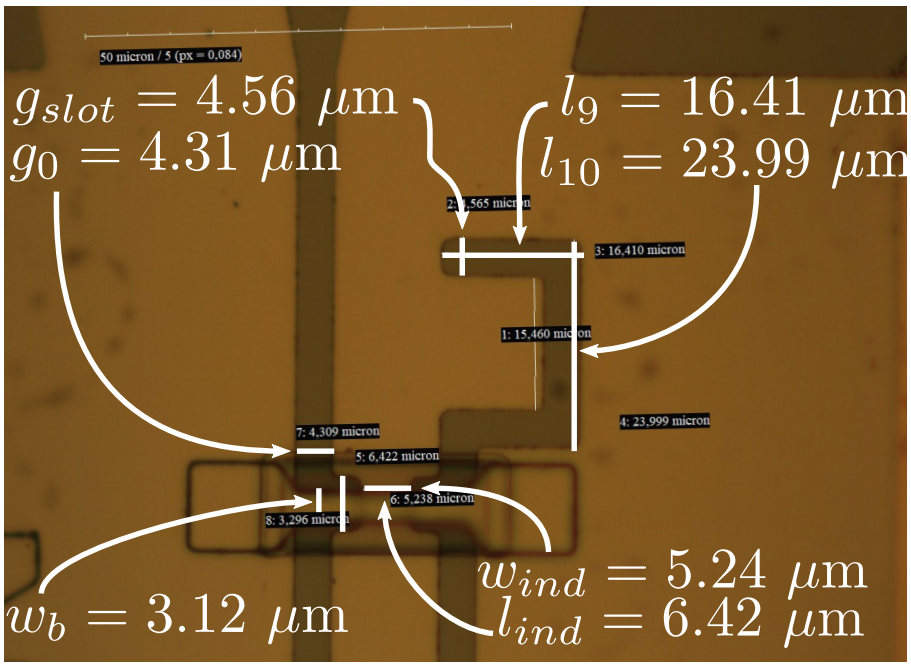

Figure 5.2: Photo of the slotline-CPW transition after the slotline antennas of every port of the power divider. Averages are taken to be implemented in the CST models.

Table 5.2: Average fabricated dimension of the H2N/L/S CPW branch line couplers

Parameter	Designed [μm]	Fabricated [μm]
g_{slot}	4	4.4
g_0	4	4.4
w_b	3	3.2
l_9	16.1	16.4
l_{10}	24.1	24.3
w_{ind}	6	5.6
l_{ind}	6	6.4

The model H2L has a noticeable variation between the simulations of the designed and the fabricated model (Fig.5.5 **Right**). The power transmission to output ports (S_{21}, S_{31})(Fig.5.5 **Right top**) sees an enhancement in the power division as the imbalance is reduced close to 1 dB in the band. Fig.5.5 **Right middle** shows the reflections at the input (S_{11}) port and the transmission between output ports (S_{32}). Here the S_{11} parameters do not change that much between the models, the fabricated model displays lower reflections at the lower end of the band where the reflections are the lowest. The S_{32} is the parameter that exhibits the greatest difference between the designed and fabricated model with the difference being at least 2 dB. The reflections at the output ports are shown in Fig.5.5 **Right bottom** where again, there is a noticeable difference between the designed and simulated model, where the difference between the s-parameters have an average of ~ 2.5 and ~ 2.4 for the S_{22} and S_{33} respectively in the LFA$(455 - 495)$ band.

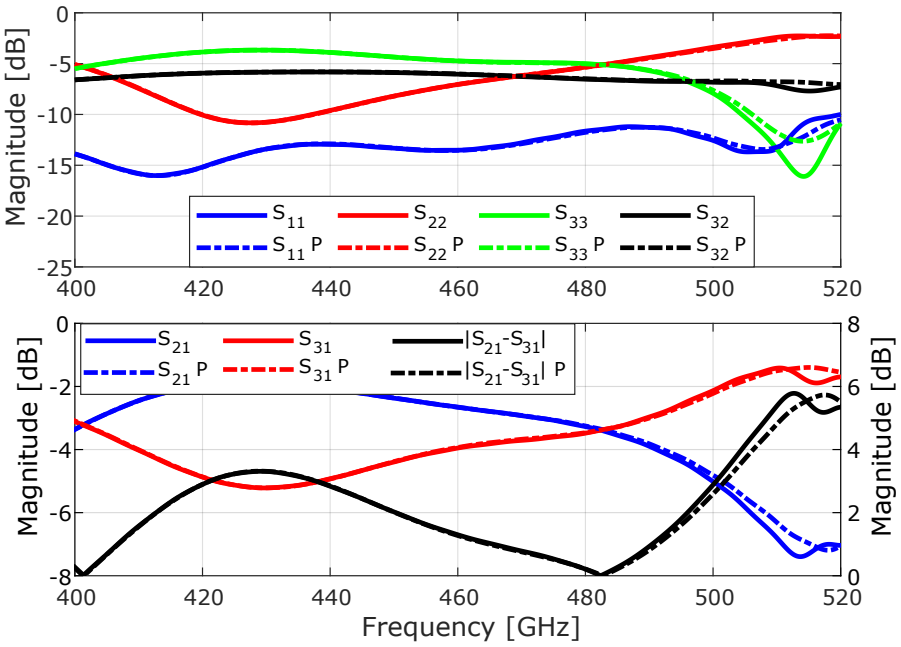

Figure 5.3: Detailed simulation of power divider terminated with a short circuit (H2S) in blocks 02 and 03. Result from block 03 that has beamlead pockets are labeled with the additional P.

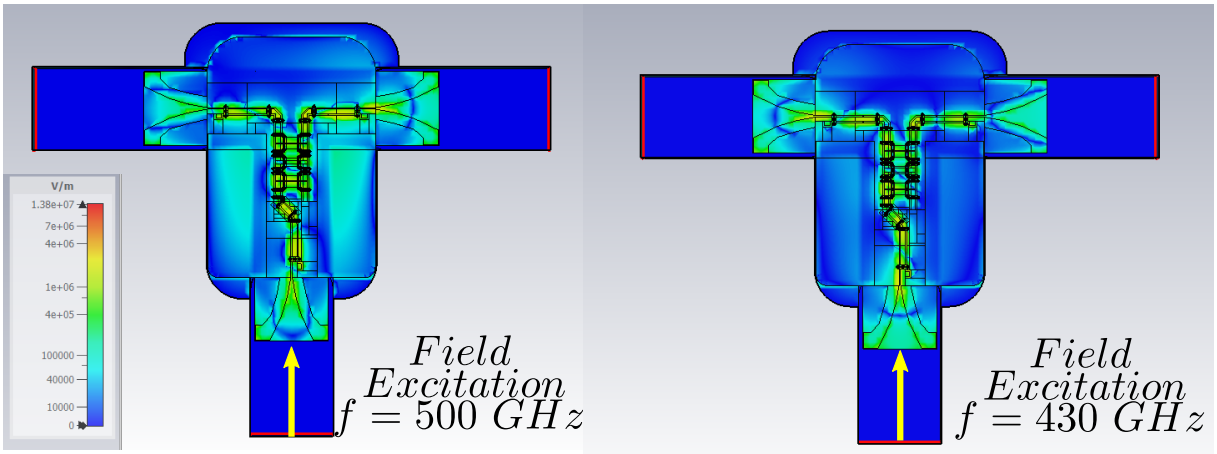

Figure 5.4: 3D simulation of a hybrid power divider terminated on a short circuit with beamlead pockets. Here the maximum field amplitude is shown at 500 and 430 GHz.

For the model terminated with a short circuit (H2S), the difference between the designed and fabricated models is mainly observed in the power division (Fig.5.6 **Left top**), since the point of equal division is at $\sim$ 480 GHz rather than at $\sim$ 490 GHz. The reflections at the input port and transmission between output ports (Fig.5.6 **Left middle**) remain similar, following the same behaviour across the frequency range. The reflections at the output ports are similar (Fig.5.6 **Left bottom**).

The last model, model H3N (Fig.5.6 **Right**), shows similar results between the designed and the fabricated model. The transmissions to the output

ports, shown in Fig.5.6 **Right top**, have a similar demeanour in the LFA band with the simulated model having a larger imbalance in the band with a maximum of 0.58 dB at 500 GHz. moving forward to the reflections at the input port and transmission towards the output port (Fig.5.6 **Right middle**) it can be seen that for the fabricated model the transmission between output ports increases on average 1.5 dB over the designed model. On the other hand, the reflections at the input port (S_{11}) do not change significantly between the designed and the fabricated models. The reflections at the output ports (S_{22} and S_{33} respectively), do no change significantly (Fig.5.6 **Right bottom**).

The differences between the designed and fabricated models can be explained as a combination of the coarser simulation parameters used in the design stage and the changes due to the fabrication process. Due to the error on the lithography mask, simulated results of H2N cannot be used to draw significant conclusions about the effects of the more detailed simulation and the fabrication changes. The changes in reflections at output ports (Fig.5.5 **Left bottom**) could be attributed to the change in the termination due to the high transmission between the isolated port and the output ports. The difference in the s-parameters S_{32} between the designed and fabricated models H2L and H3N could be because the behaviour of the TiN sheet was not detailed enough at the design stage. This is enforced by the fact that the model H2S, which is terminated on a short circuit, does not exhibit a significant variation in the S_{32} and S_{22} and S_{33}.

Overall, the difference between the result in a coarser, faster simulation setup and a finer, more detailed analysis and time-consuming do not justify the use of the finer parameters at the design stage given the time cost required. The detailed analysis may be run once a model has been selected in an attempt to capture all possible features before its preparation for fabrication.

5.3 Experimental characterization of the IBAMI as a direct power detector

The use of the SIS junctions in the Integrated Balanced Mixer (IBAMI) chips as direct power detectors makes it desirable to know their characteristics to better understand the measured results. By measuring its characteristics and comparing it to CST simulations it would be possible to develop a CST model of the IBAMI chip that could be used in the analysis of the measured results of the 2-pixel block. Up to this work, no experimental characterization of the IBAMI chip was done, mainly due to the lack of a CW source that would

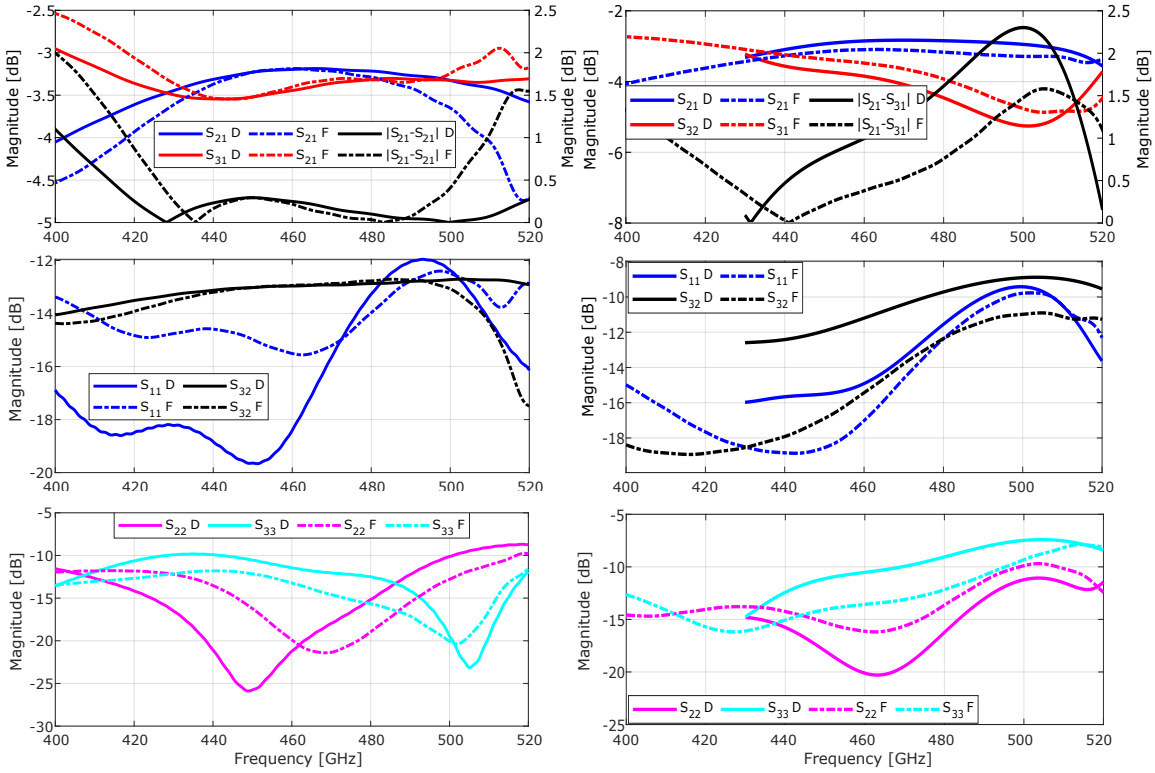

Figure 5.5: Comparison of simulated parameters of model H2N(**Left**) and H2L (**Right**) as designed (**D**) and fabricated (**F**). **Top:** Transmission to output ports and balance of the power divider. **Middle:** Reflections at the input port and transmission between the transmitted (S_{22}) and the coupled port (S_3). **Bottom:** Reflections at the Transmitted (S_{22}) and the coupled (S_{33}) ports.

cover the LFA band (the work presented by [Westig, 2013] only contains the simulated S-parameters). Hence, the IBAMI chip is characterized in this work. Considering the current capabilities and experimental methods, detailed in Chapter 4, means that only the transmission from the waveguide ports to the SIS junctions can be measured.

Before testing the IBAMI chip embedded in the 2-pixel block, it is placed inside its original balance mixer test block and the SIS junctions are used as a detector with the FTS. Fig.5.7 show the port and junction layout of the IBAMI chip in the IBAMI test block. Due the symmetric nature of the IBAMI chip, it is expected that the junctions exhibit a response that is symmetric between them at the moment of comparing results from ports H and M ($J_1^{H\,feed} \rightarrow J_2^{M\,feed}$ and $J_2^{H\,feed} \rightarrow J_1^{M\,feed}$). The response is shown in Fig. 5.8. The top graph shows the response of junctions as a direct detector and the lower graph shows the relative response of the junctions with respect to the other junction. It can be seen that the response of $J_1^{H\,feed}$ is the same as the response of $J_2^{M\,feed}$, meanwhile response of $J_1^{M\,feed}$ is lower than the mirror response of $J_2^{H\,feed}$. This is also seen in the relative response where the relative response of J_1 follows the same behaviour as J_2 but in lower

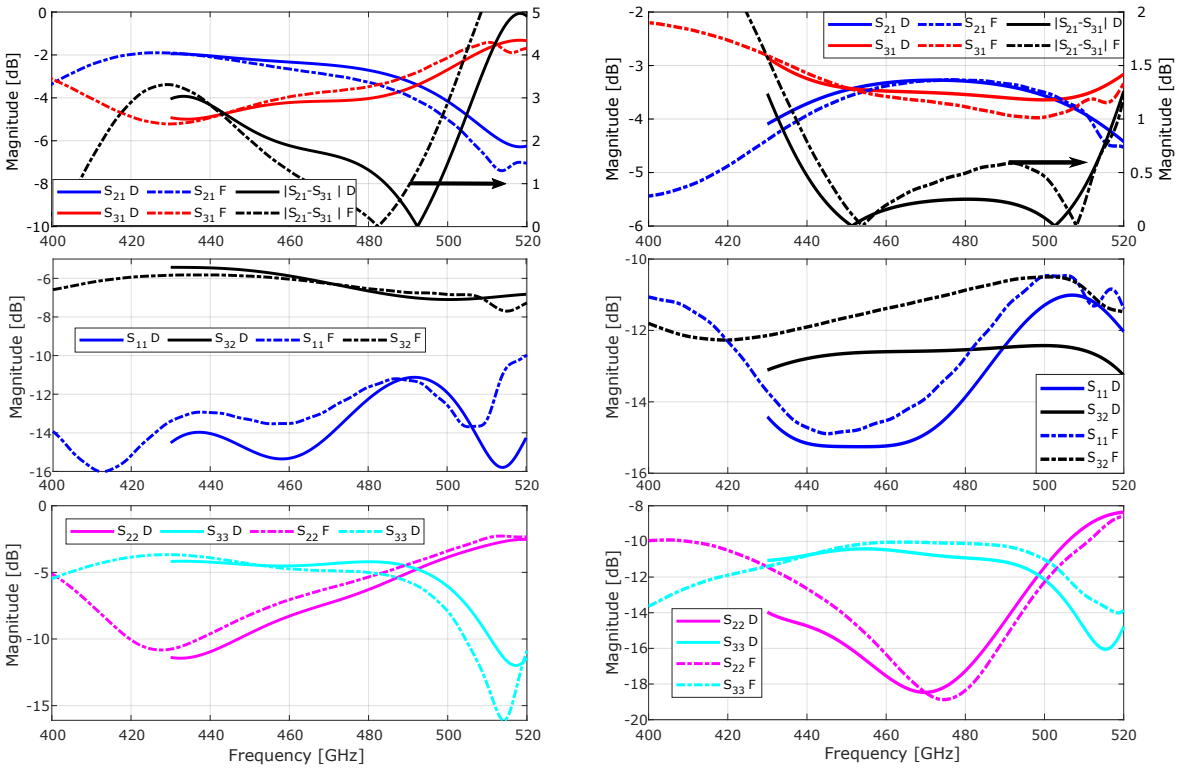

Figure 5.6: Comparison of simulated parameters of model H2S (**Left**) and H3N (**Right**) as designed (**D**) and fabricated (**F**).**Top:** Transmission to output ports and balance of the power divider. **Middle:** Reflections at the input port and transmission between the transmitted (S_{22}) and the coupled port (S_3). **Bottom:** Reflections at the Transmitted (S_{22}) and the coupled (S_{33}) ports

magnitude. This difference can be explained as a loss in sensitivity due to instability in the current bias of the junction during the FTS measurement.

After the FTS measurements are performed, the induced current across frequency in junctions J_1/J_2 is measured using an LO source sweep. Fig.5.9 presents the result obtained from a non-adjusted LO sweep for the IBAMI in its test block, together with the FTS measurement results. The induced current has been filtered with a moving mean filter with a 1 GHz window (5 points). From the induced current it is seen that the current induced to the junctions decreases in frequency (Fig.5.9 **Top**). Comparing the induced current in the junctions with the output power of the VDI source it is clear that the wave behaviour seen at the end of the band is caused by the variation in LO power (Fig.5.9 **Middle**). Another observation is that the induced current in both junctions decreases with frequency, despite the available power. Fig.5.9 **Bottom** shows the comparison between the relative response obtained from non-adjusted LO sweeps and the FTS experiments. Comparing the LO sweeps to the FTS direct response measurements (Fig.5.8) shows that the response of the junctions does not decrease considerably before 520 GHz, in contrast to the decreasing induced current in the LO sweep

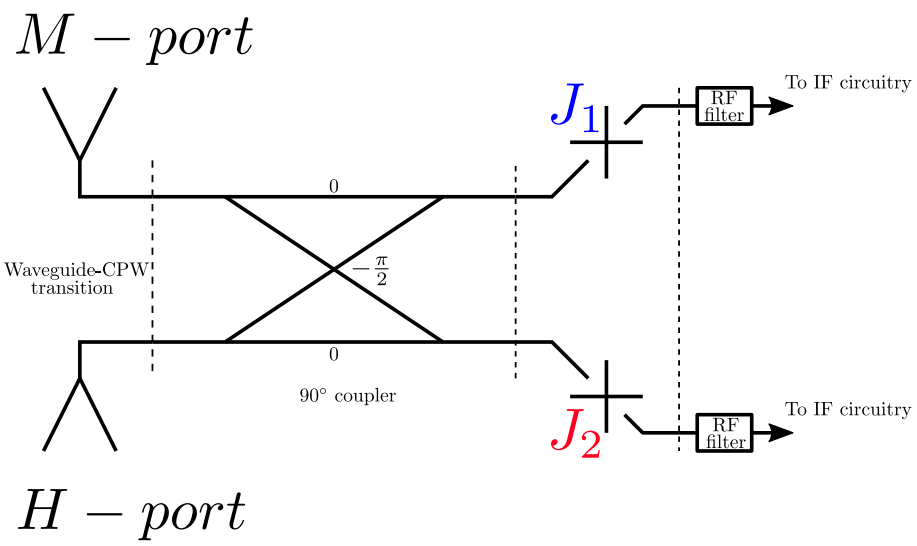

Figure 5.7: Port and junction layout of the IBAMI chip in its balanced mixer test block. Due to the symmetry of the IBAMI chip the H- and M-port can be interchanged in practice. H-port is also sometimes called the LO/In-port of the mixer since it is the port that receives the LO radiation divided by the power divider.

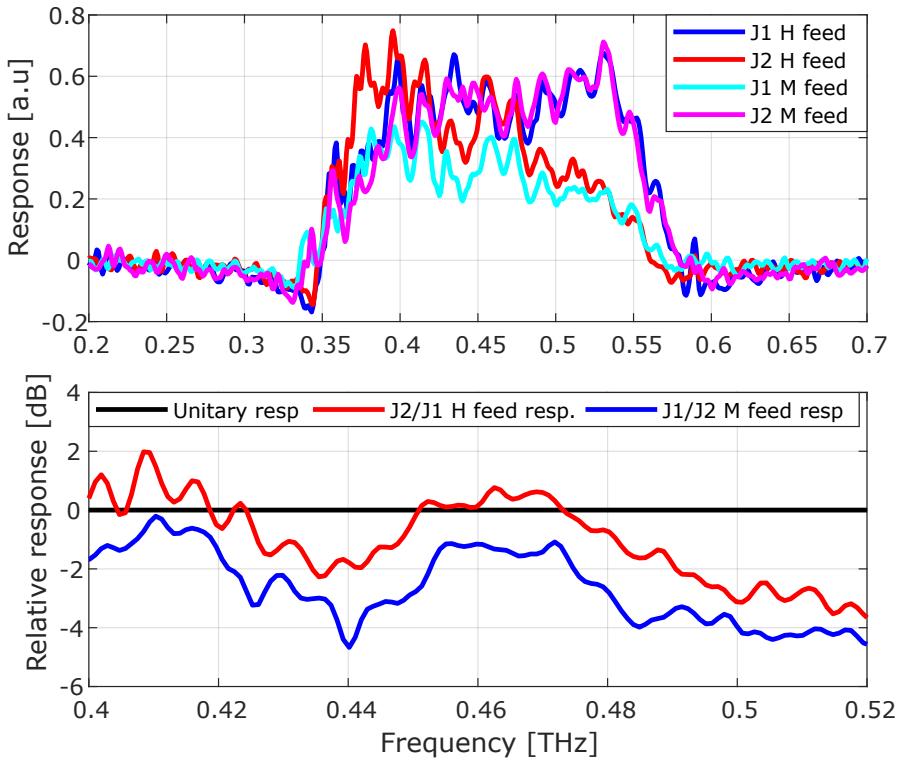

Figure 5.8: FTS measurement of the IBAMI measured in the original balanced mixer test block, detailed in [Westig, 2013] Fig 4.3. **Top:** The response of the two SIS of one IBAMI chip is recorded by the FTS and plotted. The blue and red graphs are the response of the SIS junctions J_1 and J_2 when the FTS source shines at the RF port of the IBAMI chip. The cyan and magenta lines are the response of the junctions J_1 and J_2 when the FTS source shines at the LO port of the IBAMI chip. **Bottom:** Relative response of the junctions. The **black** curve is the unitary response, and the red curve is the relative response of J_2 to J_1 when the FTS signal is injected through the H port of the dewar. The blue curve is the relative response of J_1 to J_2. The points of equal balance are taken at 420 and 460 GHz. These points are taken to fit the simulation to the measured results.

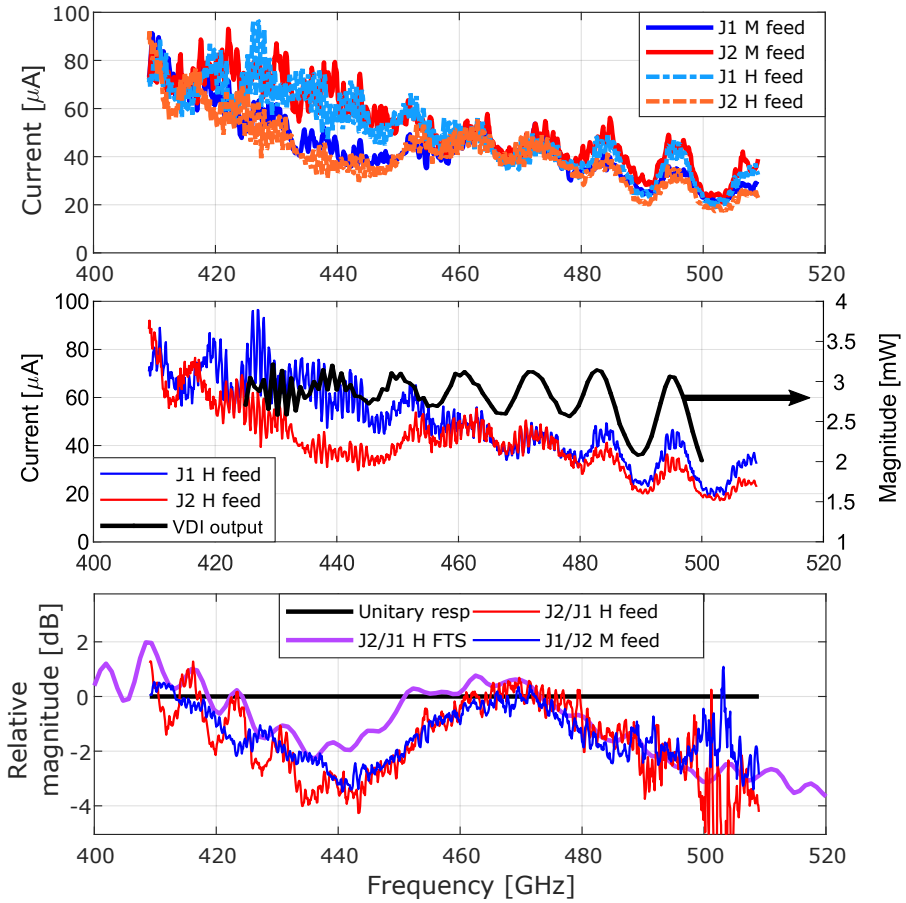

Figure 5.9: LO sweeps in the balance mixer test block. **Top:** Induced current across frequency in the two SIS junctions in the IBAMI chip H feed and M feed. **Middle:** Comparison of the induced current in the junctions and the available output power from the VDI LO. The variations in the output power of the VDI source are visible in the induced current in both junctions. Additionally, it can be seen how the induced current decreases with frequency, despite the available power. **Bottom:** Relative response of junctions for the LO sweep. Again, the black curve is the unitary response. In dashed red and blue the relative responses of the junctions for the LO sweep and in violet, the relative response of the junctions measured in the FTS. The LO sweeps and the FTS measurements are in good agreement, having a difference between 440-460 GHz where the junctions exhibit a more balanced response as in the LO sweeps.

results. Apart from that, the relative response of the junctions of both experiments is in good agreement, only differentiating themselves at 500 GHz. It is interesting to notice that the wave pattern (Fig.5.9 **bottom**) between $400-440$ GHZ seen in the LO sweep through the H-port are not seen in the LO sweep from M1 window(M-port sweep). This wave pattern is also seen in the FTS relative response. This suggests that this wave pattern could be caused by internal standing waves in the waveguide block, e.g. between the IBAMI chip and the diagonal horn, since the optics and the coupling to the source are very different in both cases.

One last experiment is performed in the balanced mixer test block. It consists

of injecting the LO signal through port M1 and placing a termination, either an absorptive load or a mirror, on port H (Fig.5.10). Results are shown in Fig. 5.11. It can be seen how the placement of a mirror at the other waveguide port affects the induced current in the junctions. This suggests that power leaks from one waveguide port to the other, as explained in Fig.5.10. Furthermore, this shows that the induced current in the junctions of an IBAMI chip is not only defined by the inherent properties of the mixer but it can be affected by the network in which the IBAMI chip is embedded.

Now that power coupled to the junctions in the IBAMI chip has been tested in a standalone scenario, this can be used as a reference for future experiments in the 2-pixel block. This reference will be compared against the response in the 2-pixel block allowing to assess the status of the IBAMI mixers in the 2-pixel blocks and hint at potential problems within. A schematic of the 2-pixel block was presented in Chapter 4 Fig.4.6 and it is included again in this chapter in Fig.5.12 for clarity's sake.

5.3.1 IBAMI characteristics in 2-pixel block 11.110.03

Coupler H3N-13

The results for LO sweeps on block 11.110.03 in conjunction with coupler H3N-13 are presented in Fig.5.13. The **Left** column shows results for an non-adjusted LO sweep through the H-port, meanwhile, the **Right** column shows the results for a sweep through the M-ports (M1 and M2 windows). For this occasion only, the raw induced current recorded in the junctions is shown in the **Top** graphs, this data is then filtered with a moving mean filter with a 1 GHz window (5 points). The LO sweeps through the H-port (Fig.5.13 **Left middle**) show a similar behaviour from 430 to 460 GHz, where from that point, the induced current decreases to a minimum at 475 GHz. At this point, the recorded value is close to the value observed in a junction with no LO power coupled (at the same bias point). After this minimum, the induced current rises again and exhibits a similar wave behaviour as the observed in the IBAMI reference measured in the test block. One difference is that the local maxima do not decrease with frequency. Moving on to the relative response of each mixer (Fig.5.13 **Left bottom**), it can be seen that the response of both mixers has the same behaviour but there is an offset between them. The relative response of M2 is closer to the unitary response. There is only some agreement between the M1/M2 port sweeps and the IBAMI reference response.

If only the results through H-port LO sweeps were considered, it could lead

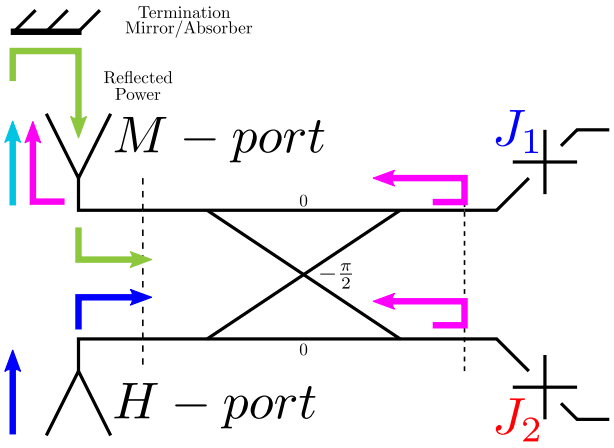

Figure 5.10: Schematic transmission waveguide ports of IBAMI. The input signal, marked as the blue arrow, is coupled to the IBAMI and delivered to the junctions J_1 and J_2. The dark cyan arrow represents the signal that leaks to port M, which has a waveguide interface, and it is launched from the IBAMI chip. By placing a mirror this power is reflected into the IBAMI chip, generating interference with the input power at the H-port. Another possible path is represented by the magenta arrow, which is the power that is reflected by the SIS junctions.

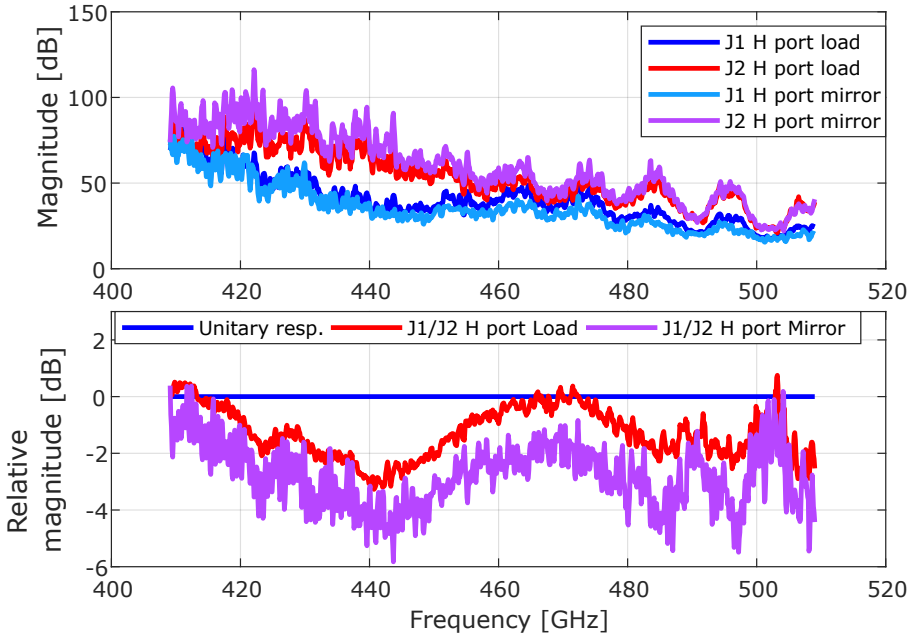

Figure 5.11: LO sweeps in the balanced mixer test block. the LO is injected through the M1 port and the H port is loaded, either with an absorptive load or a mirror. **Top:** Induced current with an absorptive and a mirror load. here the data has already been filtered with a 1 GHz window moving mean (5 points). It can be seen how the induced current changes between the loads. For the mirror load the induced current in J_2, is on average, higher than for an absorptive load. On the other hand, J_1 exhibits a lower induced current for the mirror load. **Bottom:** Relative response of the IBAMI for the absorptive and mirror load. The effects introduced by the mirror load at port H are an increase in the noise of the induced current and a change in the induced current at both junctions.

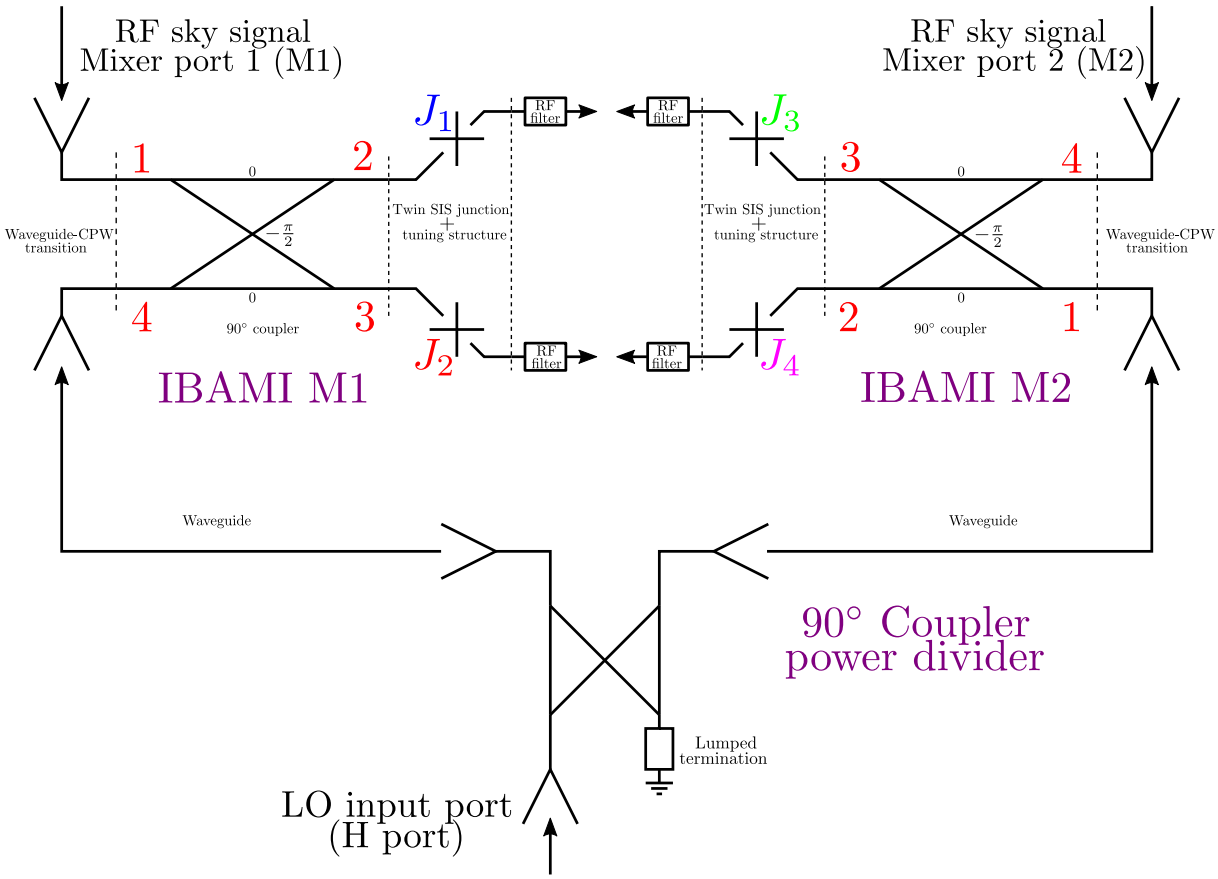

Figure 5.12: Schematic of the 2-pixel block. The ports of the IBAMI are labelled as well as each of their SIS junctions. The numbering of the coupler ports (coloured in red) in IBAMI M2 follows the same numbering as in the simulation schematics (Fig. 5.21). This arbitrary labelling was done to avoid confusion in the posterior analysis of the system. The junctions here have been coloured in blue, red, green and magenta, the same colour as their induced current is plotted in the LO sweeps. For the H-port sweeps, the LO signal is received at the input port of the 90° Coupler branch line power divider and divided towards the two IBAMI, hence, noticeable induced current is expected in all four junctions. For the M-port sweeps (sweeps through M1/M2 ports), it is expected that only the junctions of the respective mixer exhibit an induced current.

to the false conclusion that the mixers M1/M2 are defective and/or there is a problem with them. The result yielded by M-port sweeps helps to refute such an idea. These LO sweeps display a similar behaviour as the previously recorded IBAMI reference (Fig.5.13 **Right top**); that being the noticeable imbalance in induced current between 410 and 460 Ghz and the overall decrease in induced current towards the high end of the band. The relative response of the M1/M2 sweeps reveals that the mixers have a similar overall behaviour as the IBAMI reference (measured in the balanced mixer test block), with an added wave pattern across frequency. This pattern is out of phase for mixers M1 and M2(Fig.5.13 **Right bottom**) . This wave pattern is visible over the whole frequency band, with a maximum of a 4 dB amplitude between 470-480 GHz.

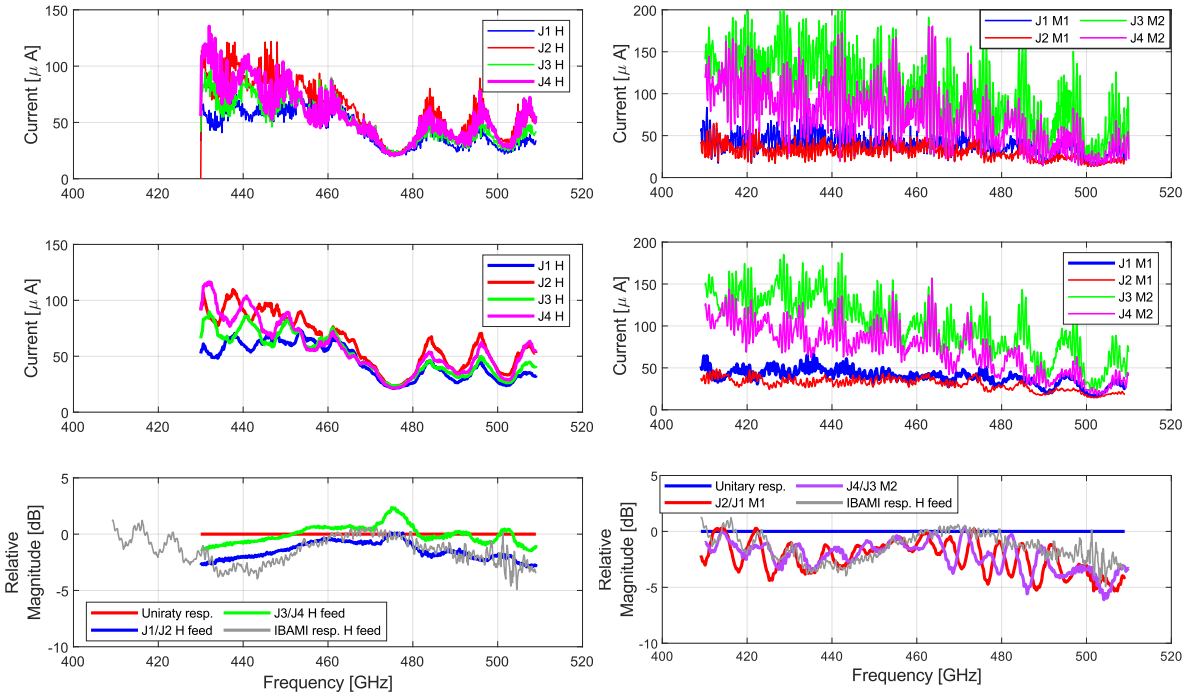

Figure 5.13: LO sweeps in block 11.110.03 with branch line coupler H3N-13. Coupler H3N-13 is the frequency-shifted coupler, terminated on a concentrated load. **Left:** LO sweeps through the H port **Right:** LO sweeps through the Mixer windows M1 and M2. **Left top:** Raw recorded current in the H-port sweep. **Left bottom:** Filtered recorded current. **Left bottom:** Relative response of junctions in the same IBAMI chip. The gray curve is the IBAMI reference response. **Right top:** Raw recorded current in all junctions. The M port sweep involves shining the LO directly to either M1/M2 ports. These sweep only yield information about the respective junctions of the IBAMI chip tested. **Right middle:** Filtered induced current. **Right bottom:** Relative response of the junctions in the same mixer compared to the measured reference response.

The results obtained from M-sweeps suggest that the mixers M1 and M2 are not defective, rather, their performance is affected by their placement in the 2-pixel block. This could suggest that the coupler H3N-13 is defective and/or there are unforeseen effects at play in the coupler. This coupler is then removed and a coupler with a lossy resonator load is placed to test whether or not coupler H3N-13 was defective.

Coupler H2L-8

A second power divider is tested in block 03, a H2L-8 model. The tests performed are the same as coupler H3N-13, with the recorded results shown in Fig.5.14. Only the filtered results are shown (filtered with a moving mean with 1 GHz/5 points window). The H-port sweeps (Fig.5.14 **Left top**) have similar behaviour as the H-port sweeps with coupler H3N-13. A range of low induced current is observed, again, in the same frequencies as with coupler H3N-13 ($460 - 480$ GHz), and it is followed by the same wave-like pattern

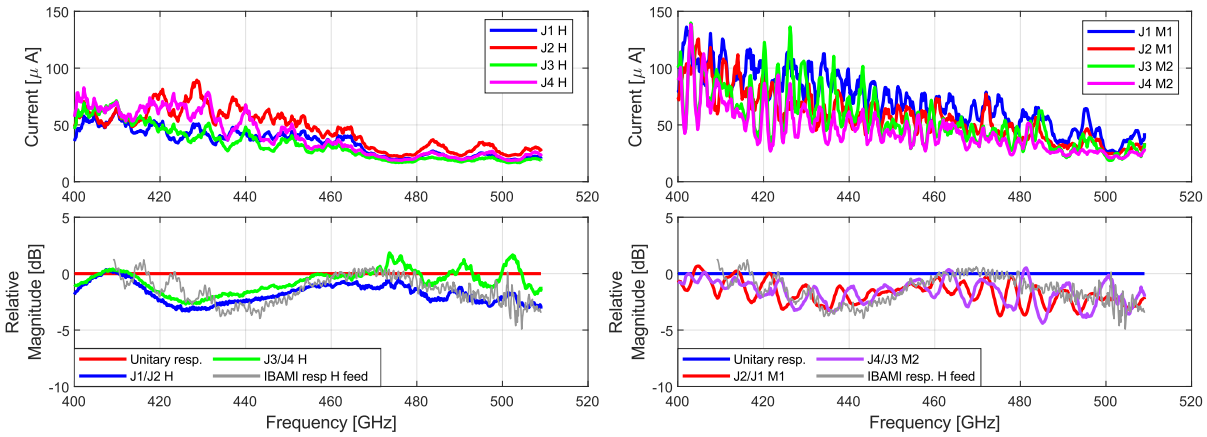

Figure 5.14: LO sweeps in block 11.110.03 with branch line coupler H2L-8 (terminated on a lossy resonator load). **Left top:** Filtered current sweeps through the H port. **Left bottom:** Relative response of the junctions compared with the IBAMI reference response. **Right:**LO sweeps through the Mixer windows M1 and M2. **Right top:** Filtered induced current in all junctions Mixer ports feed. **Right bottom:** The relative response of the junctions compared to the IBAMI reference response.

after 480 GHz. Checking the relative response (Fig.5.14 **Left bottom**) of both mixers shows they are similar and with less offset than for coupler H3N up to 460 GHz. They do exhibit a larger difference from 480 upwards, mainly because the induced current in the junctions J_3 and J_4 is close to the unpumped current level. Comparing these results with the relative response with coupler H3N-13, the fact that the response measured at the M2 port is more balanced than at the M1 port is also observed with coupler H2L-8. Additionally, this is the second branch line power divider in the 2-pixel block for which the standing waves observed in the IBAMI reference sweep between $410 - 440$ GHz are not seen.

The sweeps through the M1/M2 windows (Fig.5.14**Right top**) yield an induced current with a high frequency wave pattern embedded and a decreasing level towards the high end of the band. The relative response (Fig.5.14**Right bottom**) yields results similar to the one previously measured with the coupler H3N-13. One difference is that the standing waves recorded for the IBAMI mixer at port M1 are smaller in amplitude.

Coupler H2S-3

The fact that the two previously tested branch line power dividers (H3N-13 and H2L-8) displays the range of low induced current prompts the test of H2S branch line power divider. This model, contrary to the previously presented couplers, has a (CPW) short circuit where the TiN termination is in models H3N-13 and H2L-8. The LO sweeps in block 03 with model H2S-3 are shown

in Fig.5.15. The induced current in the H-port LO sweeps (Fig.5.15 **Left**) shows the results of two incomplete sets. A mistake in the recording and labelling of the sweeps means that J_3, J_4 from set 1 and J_1 from set 2 are not available. Only J_2 was properly recorded for both sets, and both are plotted to show that the LO power between sweeps did not differ significantly. Proof of this is the fact that both sweeps display a similar induced current in J_2. Observing the induced current with the H port sweeps (Fig.5.15**Left top**), the previously observed range of low induced current, between 460−480 GHz, is present again with this coupler. Additionally, the wave pattern starting at 480 GHz is also observed, albeit in a much smaller magnitude as with previous branch line power dividers. The relative response ((Fig.5.15 **Left bottom**)) is similar to what has already been measured with coupler H3N-13 and H2L-8, where the relative response of the IBAMI at port M2 has a slightly smaller imbalanced as the one mixer at port M1 has. The mirrored junctions response is again very similar, following the same pattern across frequency with an increased magnitude, reaching almost 5 dB of difference between mirrored junctions. For this power divider the amplitude of J_2/J_4 is larger than J_1/J_3.

Moving on to the M-port sweeps (Fig.5.15 **Right top**), it can be seen that the recorded current displays, again, a wave pattern with a considerable amplitude. The induced current in junctions J_1/J_3 is in counterphase to the current in junctions J_2/J_4. The relative response for M-port sweeps (Fig.5.15 **Right bottom**), shows the same wave pattern across frequency, but with an enhanced magnitude. For this coupler in question, the wave pattern is significantly different between sweeps M1 and M2. The IBAMI at M1-port exhibits a relative response with a wave pattern whose amplitude increases with frequency. On the other hand, the relative response of IBAMI at M2-port exhibits a wave pattern whose amplitude that decreases from $410 - 440$, is more or less constant from $440 - 470$ GHz and increases from $470 - 510$ GHz. It is important to notice that, at the high end of the band, the induced current in some junctions is close to the unpumped levels for some points. This enhances the magnitude of the wave pattern seen in the relative response.

The results obtained for the H-port sweeps with the coupler H2S-1 display the same overall behaviour observed with coupler H3N-13 and H2L-8. These three couplers tested so far, exhibit the same range of low induced current between $460 - 480$ GHz. The M-port sweeps results show the same overall behaviour as measured with previous couplers but with a wave pattern of considerable magnitude.

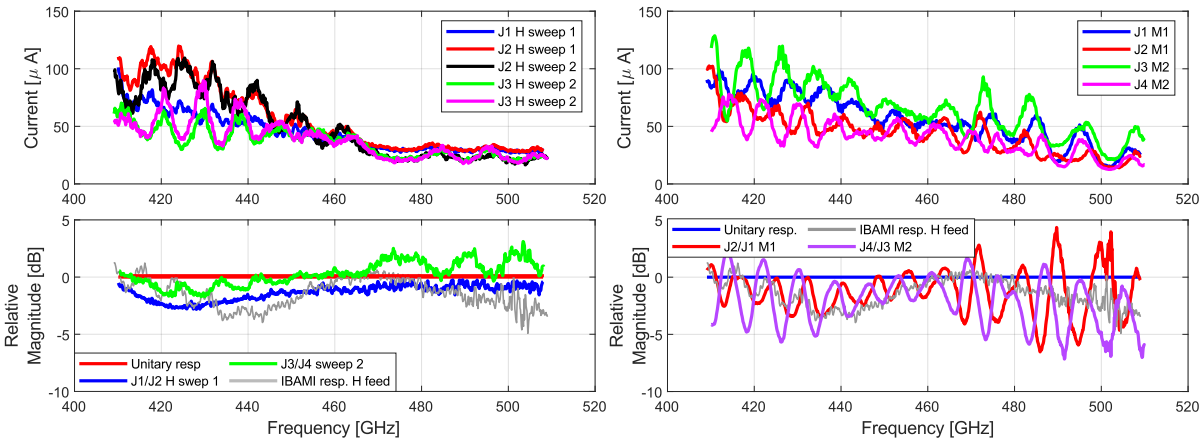

Figure 5.15: LO sweeps in block 11.110.03 with branch line coupler H2S-3 (terminated on a short circuit). **Left:** LO sweeps through the H-port. **Left top:** Filtered induced current in all junctions. Due to a problem in the recording of the sweeps, the results from two incomplete sets of H-port sweeps are presented. J_3, J_4 from sweep 1 and J_1 from sweep 2 were not recorded properly. Only J_2 was recorded in both sweeps and both recordings are plotted.**Left bottom:** Relative response of the junctions compared with the IBAMI reference response. **Right:** LO sweeps through the M-ports. **Right top:** Filtered induced current in all junctions with a M-port feed.**Right bottom:** Relative response for junctions in the same IBAMI chip compared to the IBAMI reference response.

Discussion

When comparing the M-port sweeps in block 11.110.03 for the three branch line power dividers tested, it is apparent that the relative response of the IBAMI chip exhibits a wave pattern. These patterns (for IBAMIs at M1 and M2 ports) are very similar between them and between power dividers H3N-13 and H2L-8. This is in contrast to power divider H2S-3, where the response of IBAMI chips at M1 and M2 ports is significantly different. This suggests two hypotheses, first, the coupling from M-ports to the junctions is influenced by the properties of the power divider, this agrees with the previously stated hypothesis that the induced current in the junctions depends on the network the IBAMI is embedded. Second, power dividers H3N-13 and H2L-8 have similar characteristics.

The H-port sweeps reveal that the three power dividers tested exhibit the same range of low induced current between $460 - 480$ GHz. Between $480 - 500$ GHz, the three couplers tested exhibited the same wave behaviour in the induced current, with only coupler H3N-13 having considerable induced current in this frequency range. The range of low induced current limits the range where the relative response for H-port sweeps is useful, after 460 GHz not much can be drawn from it. Between $400 - 460$ GHz, the mixer response with the H-port sweeps does not agree with the measured IBAMI reference response. This is the case for all three power dividers. Furthermore, the

response of J_3/J_4 is more balanced than J_1/J_2

Regarding the range of low induced current, it was initially suspected that coupler H3N-13 was defective. The fact that the H-port sweeps with coupler H2L-8 display the same phenomenon reduces the chances of H3N-13 being a defective device. Another hypothesis of what might be the cause of this range of low induced current is that the TiN may exhibit an unforeseen effect at those frequencies. This hypothesis is proven incorrect by the H-port sweeps with coupler H2S-3. Since H2S-3 does not have a TiN termination, rather a short circuit and exhibits the range of low induced current nonetheless, these results suggest that the observed phenomenon in the H-port sweeps is not caused directly by some unexpected behaviour of the TiN termination. Hence, these facts lead to the idea that this phenomenon stems from an interaction between the coupler and the chip block rather than an unexpected effect of any particular component. The observed induced current between $460 - 480$ GHz suggests that no power is coupled to the junctions in both IBAMI chips. Since no power is coupled to the junctions, it would mean that the power from the VDI LO either does not reach the IBAMI chips, suggesting a problem with the overall power divider design, or it is not coupled to the silicon chips it escapes through the M1/M2 ports.

To test the latter idea, a measurement with block 03 and the Erickson PM3 is executed. In this experiment, no power was measured coming from the M1/M2 window and the hypothesis that the power does not couple to the junctions and escapes through port M1/M2 is discarded. Since no power was detected, the idea that the power does not reach the IBAMI couplers gains weight. This would imply that there is a problem with the coupler design in the block since this frequency range of low induced current is observed with the three couplers, whose only significant difference is the termination. Another possibility is that there is an unexpected problem with block 03. To discard any possible mechanical problem with the current testing block, a power divider with a short circuit termination is tested on block 02 to find if the features observed with power divider H2S-3 will be present as well.

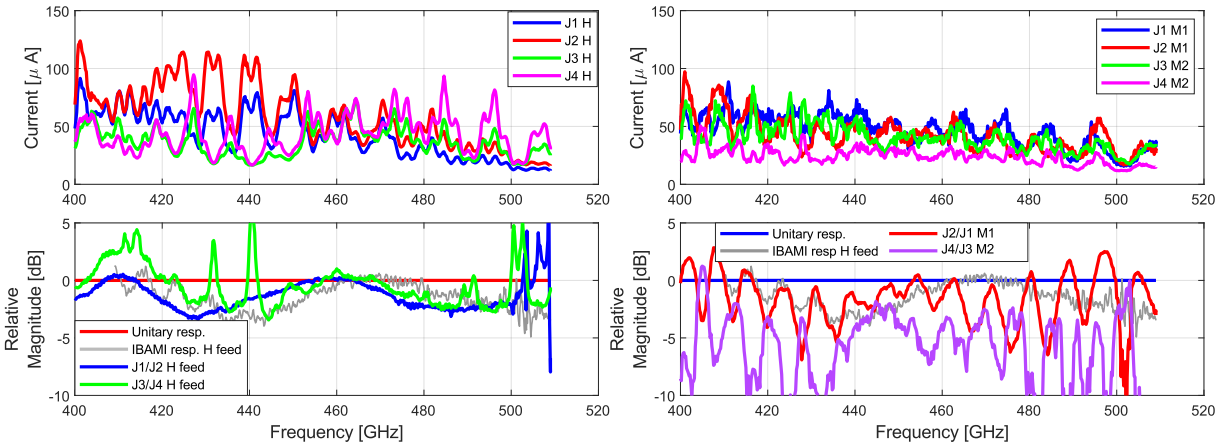

Figure 5.16: LO sweeps in Block 11.110.02 with branch line coupler H2S-1 (terminated on a short circuit). **Left top:** Filtered current sweeps through the H port. **Left bottom:** Relative response of the junctions compared with the IBAMI reference response.. **Right:**LO sweeps through the Mixer windows M1 and M2. **Right top:** Filtered induced current in all junctions Mixer ports feed. **Right bottom:** The relative response of the junctions compared to the IBAMI reference response.

5.3.2 IBAMI characteristics in 2-pixel block 11.110.02

Coupler H2S-1

The results of coupler H2S-1, in block 02, are shown in Fig.5.16. Before analyzing the results, it is important to remember the difference between block 02 and block 03 and it is that block 02 does not have the 5 μm beam-lead pockets milled on its top half block (Section 4.2.2). The H-port sweep (Fig.5.16**Left top**) does not display the range of low induced current between $460 - 480$ GHz. The wave pattern after 480 GHz is only observed in junctions J_3, J_4, meanwhile junctions J_1, J_2 experience only a decrease in induced current, reaching induced current values close to unpumped levels after 500 GHz. For the IBAMI chip at port M2 there are frequencies where the induced current in the junctions experience a sudden decrease in induced current. this is observed at frequencies 431, 440 and 500 GHz. This is seen clearly in the relative response (Fig.5.16 **Left bottom**) of junctions J3/J4, where the peaks in the relative response correspond to these points. Aside from these features, the relative response follows the same overall behaviour as the reference of the separate IBAMI mixer, like as the relative response of junctions J_1/J_2. This match is lost from 500 GHz upwards, where the junctions do not exhibit any induced current at all. The M1/M2-port sweeps (Fig.5.16 **Right top**) show an induced current that has an almost constant average level across the complete band, but it is not the same for all junctions. J_4, in particular, shows a low induced current compared to J_3 and almost no features at all. In contrast, the other junctions (J_1, J_2 and J_3) shows the features previously observed, such as the overall decrease in induced current

across frequency and the wave-pattern after 480 GHz. The relative response of the junctions (Fig.5.16**Right bottom**) shows that the junctions in the IBAMI at port M1 behave similarly as in block 03 with coupler H2S-3. The IBAMI at port M2 does exhibit a large imbalance, possibly cause by the induced current level in J_4 being very close to the zero level.

Coupler H3N-12

Block 02 is opened to remove the power divider H2S-1 and place power divider **H3N-12**. This is to compare it against the results measured with coupler H3N-13 in block .03. The results are shown in Fig.5.17. The H port sweeps (Fig.5.17 **Left top**) show two distinct features. Junctions J_1 and J_2 (from the IBAMI chip a port M1) do not display the range of low induced current, as observed with coupler H3N-13 in block 03. It also displays the standard decreasing induced current towards the high end of the band. Junctions J_3 and J_4 display a noticeable feature. J_3 experiences two ranges of low induced current, between $424 - 438$ GHz and $452 - 462$ GHz. The latter is also observed in the induced current at junction J_4. Since only the junctions in the IBAMI chip at M2 exhibit these features, it suggests that this feature has a different source than the low induced current observed with couplers in block 03. The relative response (Fig.5.17 **Left bottom**) shows that the junctions in the IBAMI chip at M1-port have a very similar response as the IBAMI reference response. Only losing the match after $500GHz$ where the current reaches levels close to the unpumped values. On the other hand, the feature previously observed in the H sweeps with the IBAMI chip at M2 port is seen even clearer. One possibility is that the IBAMI chip at M2 port is experiencing some mechanical wear due to the several opening/closing and thermal cycles it has been subjected to.

The M1/M2-ports (Fig.5.17 **Right top**) sweeps reveal a very different behaviour in the IBAMI chips at port M1 and M2, While the induced current in junctions $J_1 J_2$ display a similar behaviour as the one observed int he IBAMI test block, the induced current in $J_3 J_4$ shows a wave pattern with a small period. Now it is the induced current in J_4 that exhibit the low induced current between $424 - 438$ GHz. Moving on to the relative response (Fig.5.17 **Right bottom**) for the junctions of the IBAMI at M1-port are similar to the reference measurement of the IBAMI. On the other hand, the mixer at the M2 port displays the same behaviour as in the H-port sweep with a large imbalance due the range of low induced current between $424 - 438$ GHz.

Discussion

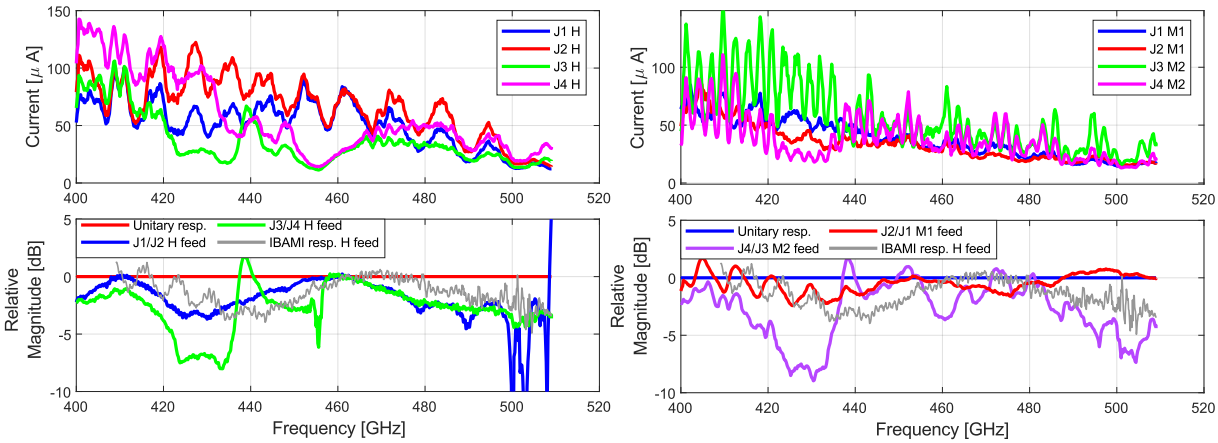

Figure 5.17: LO sweeps in Block 11.110.02 with branch line coupler H3N-12 (terminated on a concentrated load). response with variable power. **Left:** LO sweeps through the Mixer windows M1 and M2. **Left top:** Induced current in all junctions. **Left bottom:** The relative response of the junctions compared with the IBAMI reference response. **Right top:** Filtered induced current in all junctions Mixer ports feed. **Right bottom:** The relative response of the junctions compared to the IBAMI reference response.

In the measurements of coupler H2S-1 and H3N-12 in block .02, there are two important observations. First, the observed range of low induced current between 460−480 GHz in block 03 was not observed in the H-port LO sweeps, neither for power divider H2S-1 nor H3N-12. The junctions J_1 and J_2 in the IBAMI chip at port M1 display a very similar induced current and relative response to the IBAMI reference measurements. The IBAMI chip at port M2 does display a similar behaviour in the sweeps with coupler H3N-12. This leads to the second point and it is that this IBAMI chip does experience a significant degradation in its induced current characteristics between the measurements with coupler H2S-1 and H3N-12. This change is visible in sweeps from both H and M2 ports. This fact suggests that the problem observed in the sweeps of the IBAMI at port M2 is an issue of the mixer rather than being a phenomenon similar to the observed phenomenon in block 03.

These results suggest that the hypothesis that the range of low induced current was caused by a problem with the design of the power divider is not correct. The reason for this is, that for the same power divider models (H2S and H3N), the results were not reproduced when testing them in blocks 02 and 03. Remembering that the only difference between block 02 and 03 are the beamlead pockets, hints toward the possible cause of this feature. It also points towards a possible explanation for the sudden degradation of the IBAMI at mixer port M2, since that IBAMI chip had experienced at least 4 opening/ closing cycles.

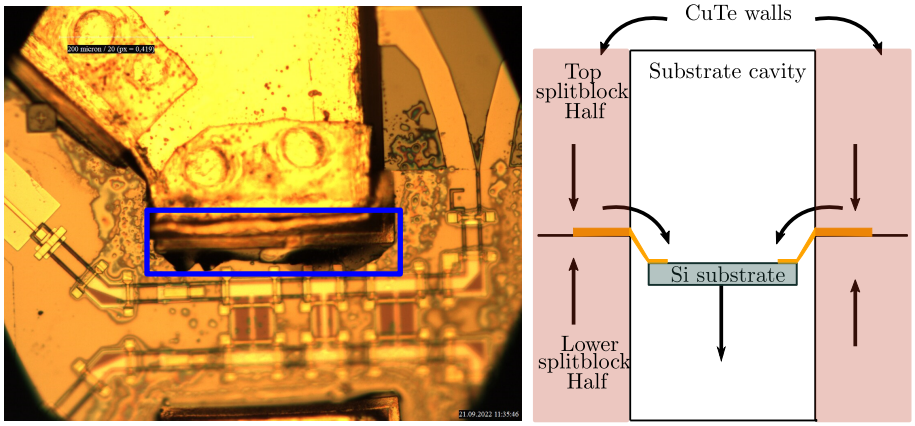

Figure 5.18: IBAMI chip in block 11.110.02 after several opening/closing cycles. **Left** Status of the membrane after about 5 opening/closing cycles. It can be seen that the complete model has sunk into the cavity. This increased the tension on the membrane and led to the beamlead peeling off the substrate, taking part of the Nb ground layer with it. **Right:** Schematic of the cross-section of the substrate cavity in block 11.110.02. In the current block, the gold beamlead is pressed between the CuTe waveguide walls. This pushes the material out to the substrate cavity, which in turn sinks the Si membrane. This process gets worse and worse the more opening/closing cycles the membrane experiences. this is the precise problem the addition of the beamlead pockets attempts to avoid.

Block 11.110.02 is opened and the status of the IBAMI chip at port M2 is checked (Fig.5.18). It was observed that IBAMI at M2-port was sunken in. The Nb layer was peeled off from the substrate by the gold beamlead. This is due to the lack of pockets means that, when the block is closed, the gold of the beamlead gets pushed into the waveguide cavity, putting progressively larger tension on the silicon membrane. eventually leading to it breaking. Even though the IBAMI chip at port M1 did not show any symptoms of a possible breaking of the chip, visual inspection shows that it was in a similar status to the IBAMI chip at port M2. Hence, both of them are removed from the block 02.

This opportunity is taken in order to test the power division performed by the coupler in block 02. The detector used is the Erickson PM3 power meter, and it is placed outside the M1/M2 windows. The results are shown in Fig.5.19. The power measured at the windows M1 and M2 is shown superimposed with the available power from the VDI source (Fig.5.19 **Top**). It can be seen again that the wave behaviour of the measured power at the M1/M2 windows follows the pattern of the VDI source across frequency. Fig.5.19 **Bottom** shows the balance between M1 and M2 for the measured power and from simulations of the fabricated H3N model (Fig.5.6). The standing wave behaviour has a small period; hence it must be between the branch line power divider and the horns. To eliminate this influence, the measured imbalance is fitted with a Fourier filter of third order. The filtered imbalance can be

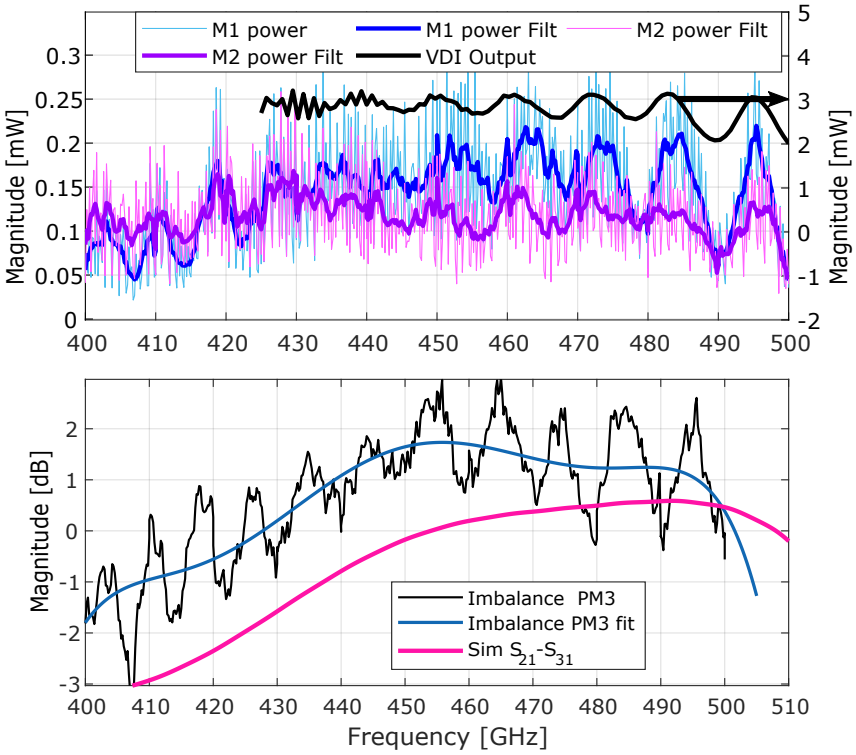

Figure 5.19: Measured power division of branch line power divider H3N-11 with Erickson PM-3. **Top:** Measured power at the window M1 and M2. The solid dark lines are the smoothed data with a moving average filter. The black curve is the available power from the VDI source. **Bottom:** Measured imbalance of the power divider H3N-11. In black is the measured imbalance and in blue is the fitted curve using a Fourier filter. The simulated imbalance obtained from Fig.5.6 **Right top** is plotted in magenta

compared with the results obtained from the simulation of the fabricated model. The results show an increased imbalance between 460 and 500 GHz above 1 dB and the points of equal balance are shifted to 427.8 and 501.6 GHz.

Comparison of the transmission measurements of block 03 and block 02 added to the experimental results obtained with the Erickson PM3 suggest that the reduced transmission in block 3 between $460 - 480$ GHz is not caused by an inherent problem with the transmission parameters of the coupler. Ideally, the IBAMI chips in block .03 would be removed and the power division measuredwith the Erickson PM3. This would allow to find out if there is an unexpected interaction between the beamlead pockets and the coupler. However, removing the IBAMI chips destroys them in the process. Considering that these IBAMI chips are not available in abundance and that these devices are also needed for other experiments required for the CHAI development, it is decided against removing them from block 03. This shifts the experiment of the coupler with an external power detector out of the time frame of this

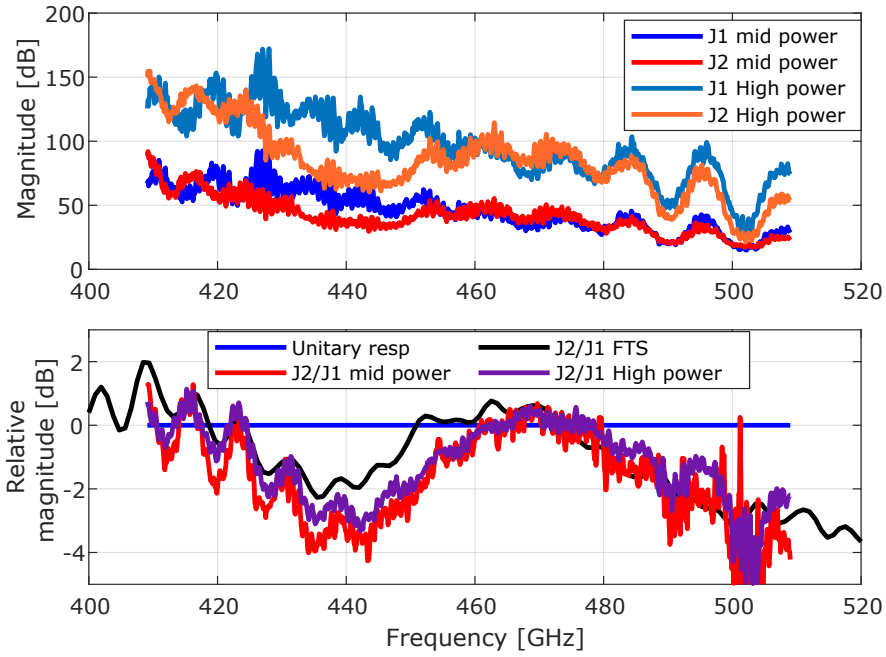

Figure 5.20: C
omparison of the SIS response]Comparison of the SIS response. **Top:** Induced current for a high- and mid-power sweeps. The high and mid-power are classified in function of how large is the current induced in the junctions below the gap voltage (at 2 mV). For high power sweeps $I_{induced} > 150$ μA. The measured high and mid-power sweeps follow the same behaviour. **Bottom:** Relative response for the high and mid-power sweeps plus the FTS measured response. The response of the junctions remains constant across both power sweeps and only differs from the FTS measured response in the $440 - 460$ GHz range, where the junctions' response is more similar to each other

thesis and leaves the uncertainty about what exactly is the cause of the low induced current observed in block 03.

So far the results point to a problem particular to block 03, most likely caused by the added beamlead pockets within block 03. Two possibilities arise then. First, the power divider in a block with beamlead pockets has, contrary to waht is expected form its design, a frequency range where the transmission falls to very low values. The second possibility is that it the combined effect of the power divider, the IBAMI chips and the beamlead pockets creates a network that gives rise to the observed effect of low induced current between $460 - 480$ GHz. Since experiments with the current equipment available would not yield that much more insight into the problem at hand, it is necessary to resort to 3D EM simulations.

5.3.3 Induced current in the junctions at high power

Before moving to the simulatons there is a consideration that must be addressed. It is how the induced current in the junctions behaves at higher LO power coupled to them. One assumption made in this thesis is that the cur-

rent induced has a linear relation to the coupled power. In the non-adjusted LO sweeps, due to the standing waves present in the optic path, there may be frequencies for which the induced current is higher than initially expected and possibly leading to a non linear relation between the input power and the induced current. The linearity is checked by increasing the LO power coupled to the junctions. Fig.5.20 shows the recorded current in the junction for two LO sweeps in the IBAMI test block, one with a LO power that induces a current below 100 μA, or medium level; whereas for the second sweep, it was attempted to couple the largest amount of power without saturating the junctions, so the induced current would be over 150 μ A. This was only achieved at the lower end of the band. Nonetheless, this sweep still represents, or it is close to, the maximum power coupled to the junctions scenario in this thesis work. Fig.5.20 **Top** shows the recorded current in the junctions for both sweeps and the relative response of the junction is shown in Fig.5.20 **Bottom** where it can be seen that both sweeps display a very similar relative response, meaning that, even for the induced current level of the second sweep, the linearity response of the junctions does not change significantly and can be used to assess the power coupled to the junctions when the IBAMI is embedded in the 2-pixel block scenario.

5.4 Simulation of the 2-pixel block

Considering that not much more insight can be gained with further experiments, it is necessary to resort to EM simulations. This would allow for a better understanding of the measurements and attempt a possible deembedding of the parameters of the power divider. The first step is the understanding of how the individual components affect the performance of the 2-pixel block. CST provides a schematic simulator that allows for fast and flexible simulation and some limited experimentation. It does require the 3D simulation results of the main components, which are in this case the 3D model of the branch line power divider, the connecting waveguides and the 3D model of the IBAMI chip. 2 lumped elements ports are used to represent the SIS junctions. In the circuit simulator, the pre-simulated 3D blocks are connected at their ports and there are possibilities to add ideal components to the network. For our purposes, this schematic simulator will be used to study the 2-pixel block and the main components in several scenarios concerning this work.

Fig.5.21 shows the lower half of the 2-pixel block with the main components therein and the representation in a schematic simulator available in CST. Given the complex response of the 3D component of the IBAMI chip, however, first, a simpler circuit is simulated. The first 2-pixel simulation to study consists of a branch line coupler H3N and two theoretical ideal 90° hybrid couplers as a perfectly balanced detector, as a replacement for the actual IBAMI chips. The schematic is shown in Fig.5.22. The adjustable parameters of the ideal coupler are the level of balance between the power at its outputs, the excess loss and its impedance. Since this coupler is meant to replace the branch line coupler in the IBAMI chip, a 90° coupler with a 3 dB balance to both junctions is chosen. Since the IBAMI chip is fabricated in superconducting Nb, no excess loss is added. The impedance of this theoretical coupler is chosen such that it is matched to the waveguide at $480GHz$, meaning $Z_{TE_{10}}(480GHz) = 513\ \Omega$. A CST 3D model of a H3N coupler (S-parameters shown in Fig.5.6 **Right**) and of the connecting waveguides are added to the schematic, which is subsequently simulated in less than a minute. The transmission characteristics to the four "junctions"(J_1, J_2, J_3 and J_4), represented by ports perfectly matched to the ideal couplers, are shown in Fig.5.23. The **Top** graph shows the S- parameters $S_{J_1,In}, \ldots, S_{J_4,In}$ of the schematic model, meanwhile the **Bottom** graph shows the relative response of junctions J_2, J_3, with respect J_1. From the S-parameters (Fig.5.23 **Top**) it can be seen that they are dominated by the transmission characteristics of the branch line coupler H3N (Fig.5.6 **Top right**), as expected. There is

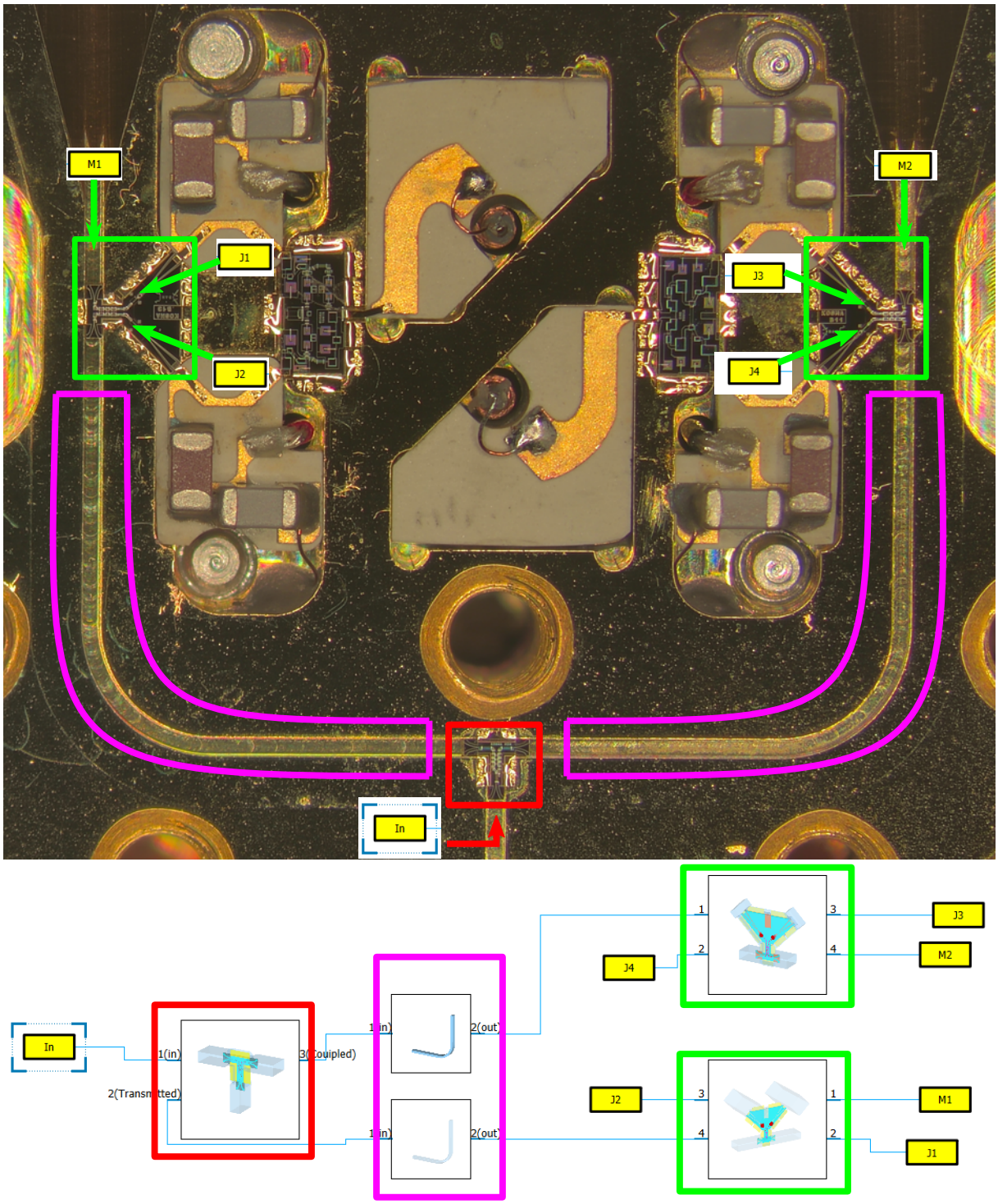

Figure 5.21: Image and schematic of the 2-pixel block **Top:** Photo of the lower half of the 2-pixel block with the main components therein, Namely the two IBAMI chips with the respective IF combiner and the branch line power divider. The yellow boxes indicate where the ports of the piece-wise schematic are located in the 2-pixel block. **Bottom:** The equivalent schematic of the 2-pixel block. Here the branch line power divider(in red), the 2 IBAMI chips (in green) and the waveguides connecting them (in magenta) have been already simulated and the schematic uses its S-parameters to calculate the overall parameters of the network. In the piece-wise schematic, the port's impedance is block dependent, meaning that the ports are matched and do not generate any reflections.

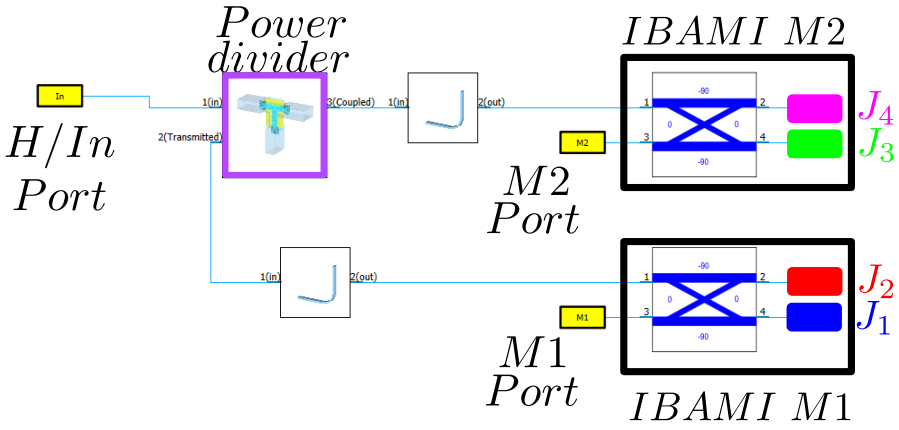

Figure 5.22: Schematic of the 2-pixel block with theoretical mixers. Here the branch line coupler in the IBAMI chips is replaced by a theoretical hybrids, whose parameters can be chosen at will.

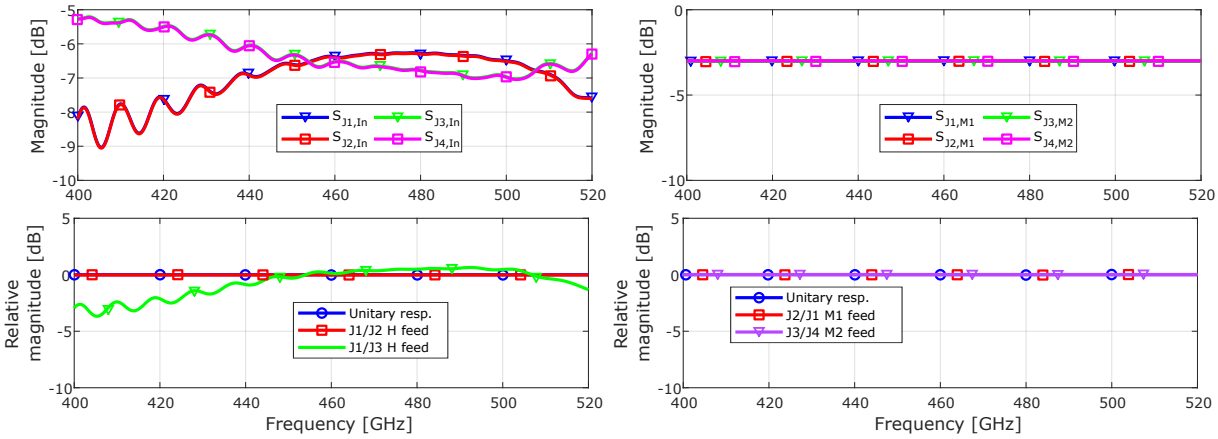

Figure 5.23: Transmission to junctions in the 2-pixel block with theoretical mixers with perfectly matched SIS junctions. Here the branch line coupler in the IBAMI chips is replaced by a theoretical coupler. The ideal hybrids have a -3dB coupling, a constant impedance of 513 Ω, and perfectly matched ports for the 4 junctions and the RF port. **Left top:** Transmission from the H-port (input). **Left bottom:** Relative response of junctions J_2 and J_3 with respect J_1. **Right top:** Transmission to the junctions from M1/M2 ports. **Right bottom:** Relative transmission towards junctions in IBAMI at M1 (J_1/J_2) and M2 -ports (J_4/J_3).

a standing wave pattern between the $400-440$ GHz, with a larger amplitude in the transmission to junctions J_1 and J_2 of the IBAMI M1 (Transmitted port of the H3N coupler). All these features are replicated in the relative response of junctions J_2/J_1 and J_3/J_1. It is observed that the former quantity yields the parameters of the IBAMI chip coupler (ideal -3dB transmission in this case), while, the latter yields similar characteristics to the balance of the coupler as observed in Fig.5.6 **Top right**, with an additional wave pattern embedded.

The cause behind the standing waves pattern is the mismatch between the branch line power divider and the IBAMI chips M1 and M2. (Fig.5.26). The amplitude of the standing wave depends on the level of mismatch between

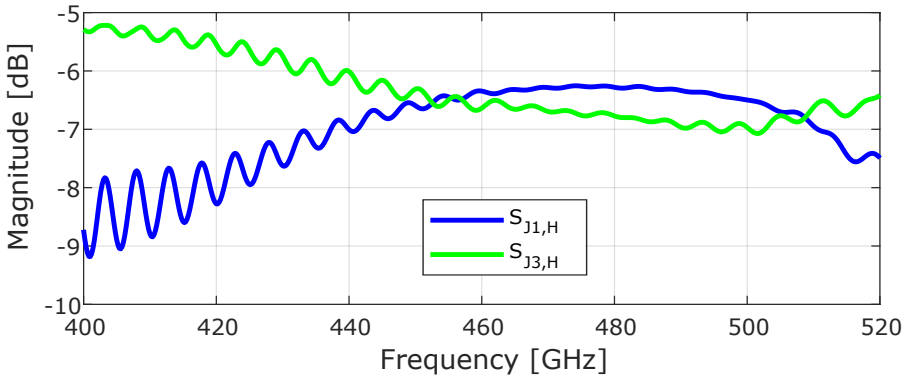

Figure 5.24: Transmission to junctions in the 2-pixel block with theoretical mixers with a longer waveguide. For this simulation, the length of the waveguides between the branch line coupler power divider and the IBAMI mixers M1/M2 is doubled. The consequence is that the wave pattern observed in the transmission from the input port of the coupler to the junctions has its period halved. This supports the hypothesis that the wave pattern is a symptom of the existence of a standing wave between the coupler and the IBAMI M1/M2.

the line and the load, and its period is determined by the length of the line. To check whether or not the wave pattern observed in the transmission to the junctions is caused by a standing wave in the waveguide, their length is doubled and, as a consequence, the resulting wave in the transmission has had its period halved. In our case, these standing waves originate due to the mismatch between the theoretical IBAMI M1/M2 coupler and the waveguide on the one side and the mismatch between the 3D simulated coupler and the waveguide on the other side. The mismatch at the theoretical mixer is because these ideal couplers have a constant impedance and are only matched to the waveguide TE_{10} impedance at 480 GHz. At the lower end of the band, the impedance is $Z_{TE_{10}}(400\ \mathrm{GHz}) = 650\ \Omega$, this produces a reflection coefficient theoretical couplers of $|\Gamma_{dB}| \approx -18$ dB. Comparing the magnitude of the standing waves observed in IBAMI M1 and M2, it is observed that the effect of the standing wave is greater in the junctions J_1, J_2. Since both theoretical couplers are the same, the reason for this difference must lie elsewhere. This difference is caused by the fact the reflection coefficients at the output ports of the branch line power divider are not the same (Fig.5.6 **Bottom right**.)

It is important to notice that, in practice, standing waves are unavoidable and will appear in the transmission lines between two components as long as $\Gamma \neq 0$. Its effect can only be reduced in a given frequency band, by either reducing the mismatches as much as possible and/or introducing loss in the transmission lines. Hence it would be important to know how to minimize its effect. This point is explored later in this text.

The next step to towards a model of the complete 2-pixel block is the inclusion the simulated reflections at the input port of the SIS tuning structure, obtained from [Westig, 2013]. This would replace the ideal resistor of 513 Ω at the junction ports. In this scenario the transmissions from the H port to the junctions are not affected noticeably (Fig.5.25 **Left**). The transmission from M1 and M2 ports, however, shows an interesting change from the very uniform transmission seen in Fig5.23 **Right** to a wavy pattern observed in Fig.5.25 **Right**. The transmission from the M-ports to junctions in the same mixer(pairs J_1, J_2 and J_3, J_4) (Fig.5.25 **Right top**) show an off phase behaviour, meanwhile if junctions from M1 and M2 are compared, it is noticed that the pairs J_1, J_3 and J_2, J_4 show similar behaviour. This is expected since they are junctions that find themselves at equivalent ports in M1/M2. This leads to the term **mirrored/equivalent** junctions, and it refers to junctions that find themselves at equivalent ports in the IBAMI chips at M1/M2-ports and are the pairs J_1-J_3 and J_2-J_4

The wavy pattern in the relative response through the M1/M2 port has the same period as the standing wave in the H port transmission but its magnitude is more or less constant in the complete frequency range. The cause behind this pattern is the existence of standing waves in the waveguide between the mixer and the power divider (labelled as Z_S and Z_L in Fig.5.26). Fig.5.27 depicts the current situation for a M-port sweep. The incoming signal (blue arrow) from M is directed towards the junction ports and it is reflected due $|\Gamma_{J_\iota}| > 0$. The junctions reflect power towards ports H and M (red arrow), and due to the symmetry of the 90° coupler, half of the power ends at port H (green arrow). The first effect of the added reflections at the junctions is, that they indirectly establish a transmission path between the isolated ports (Fig.5.28). Subsequently, the power that gets launched from port H finds itself in the standing wave cavity between the branch line power divider and the IBAMI chip. The reflected power is then fed back to the H port and here it interferes with the original signal from the M port.

In the previous paragraph, it was mentioned how reflections at the junction ports can reduce the isolation of the perfect 90° hybrid, this is due to the reflected waves coming from the junction ports. Fig.5.28 shows the transmission characteristics of a perfect coupler when The SIS ports are not perfectly matched. The SIS reflections are taken from the tuning structure found in [Westig, 2013]. It can be seen how, even with a perfect coupler, the transmission between isolated ports, H and M ports in our case is determined by the reflection parameters at the junctions. This is a dire consequence since it means that, four our case, the isolation between ports H and M in the mixer

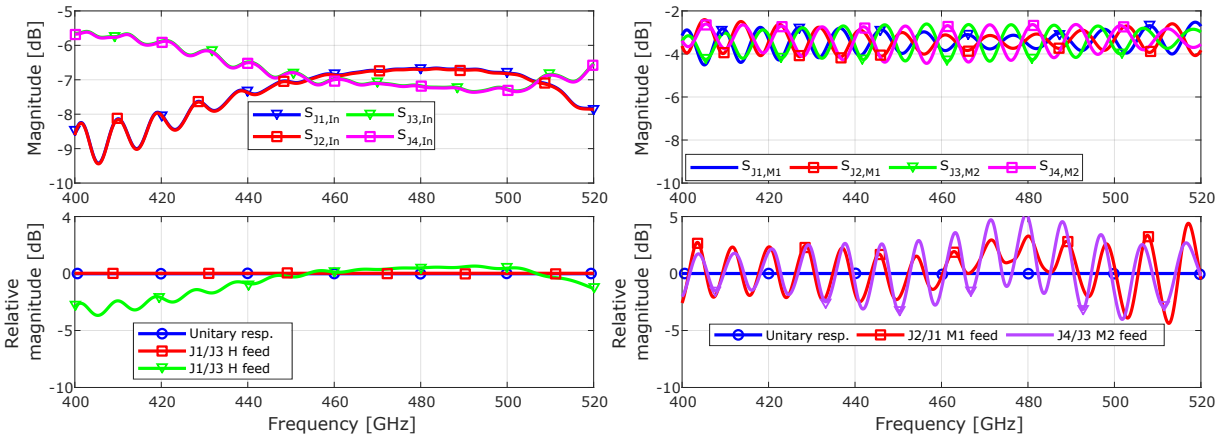

Figure 5.25: Transmission to the junctions in the 2-pixel block with power divider H3N and theoretical IBAMI plus the added reflection of the SIS tuning structure. **Left Top:** Transmission from the input (H-port) to the junctions of the two IBAMI chips. **Left bottom:** Relative transmission towards junctions J_2 and J_3 with respect J_1 . **Right top:** Transmission from the M1/M2 port towards the respective junctions. **Right bottom:** Relative transmission of junctions in the same Mixer.

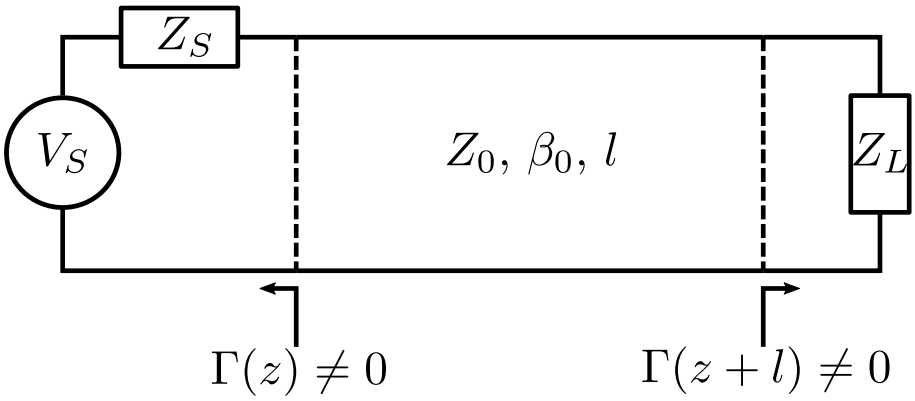

Figure 5.26: Transmission line with generator and load mismatches. For any transmission line which is not perfectly matched the load (Z_L) will generate standing waves in the line. The standing wave is generated by the intereference betweent the incoming wave and the reflected one by the load at $z+l$. In the case where $Z_0 \neq Z_S$, the reflected wave by the load will be again reflected into the line by the mismatch with the source at z. This will interfere with the waves already in the line, enhancing the magnitude of the standing waves.

will be dominated by the reflection at the junction port.

Now that it has been seen that this wave behaviour in the M1/M2 sweeps is caused by the reflections at the SIS junction ports and the phase offset introduced by the 90° coupler in the mixer, it is time to move towards the next step of including the complete 3D simulated IBAMI in the reduced cavity.

The model is shown in Fig.5.29 **Top**. It does not include the complete IBAMI chip. It does not include the 3D model of the tuning structure and the

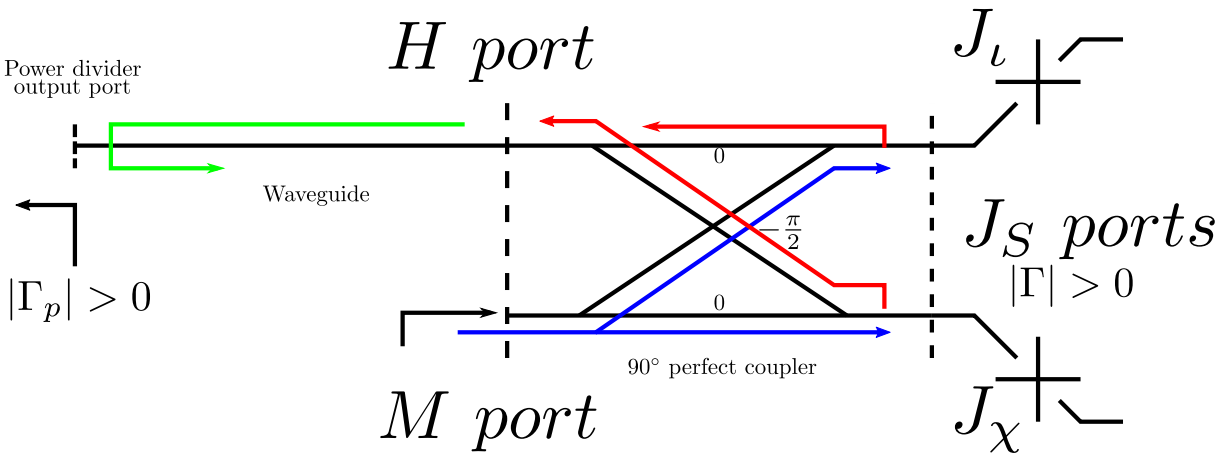

Figure 5.27: M1/M2 feed schematic. A signal is injected at M port and it is equally divided by the perfect 90° coupler towards the junctions port J_ι and J_χ (blue arrow). Here both junctions J_ι and J_χ reflect some power back into the 90° coupler. Half of the total reflected power is redirected to the H port (red arrow). There, the reflected signal enters the waveguide and is reflected into the mixer, generating a standing wave (green arrow). The power entering the H-port interferes with the original signal coming from the M-port and produces the off-phase wave pattern in the transmission from the M port towards the junctions. In the case that the reflection at the waveguide ports of the branch line power divider is zero ($|\Gamma_p| = 0$), no standing wave would be observed.

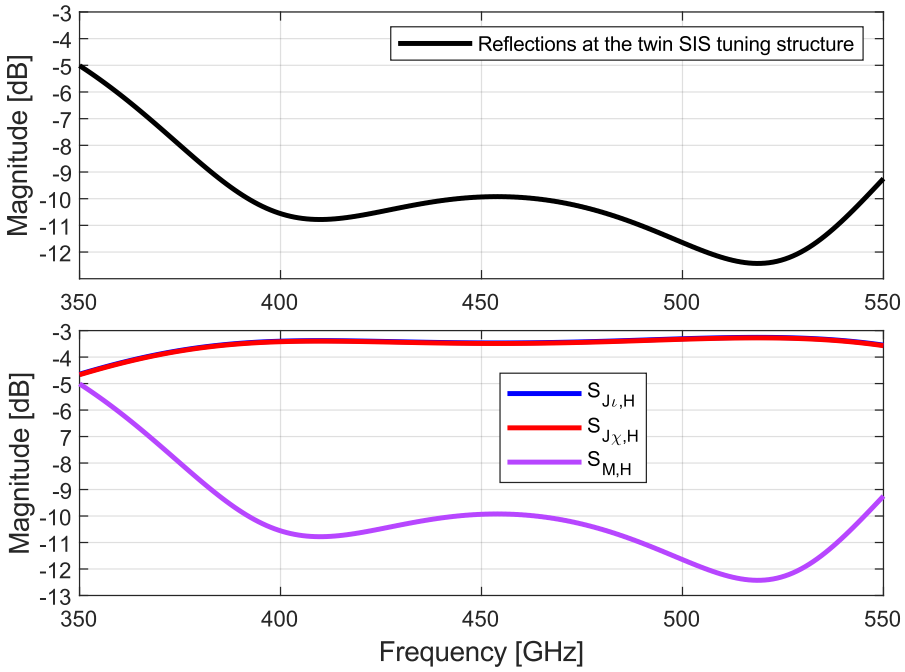

Figure 5.28: Effect of the reflections from the SIS on the parameters of a perfect −3 dB hybrid. **Top:** Reflections from the tuning structure of the twin parallel SIS junctions, obtained from the simulations presented in [Westig, 2013]. **Bottom:** Parameters of a theoretical 90° coupler with junctions at ports 2 and 3 ($|\Gamma_\xi|$,$|\Gamma_\iota| > 0$). The isolation between output ports is worsened by the reflection parameters of the SIS junction

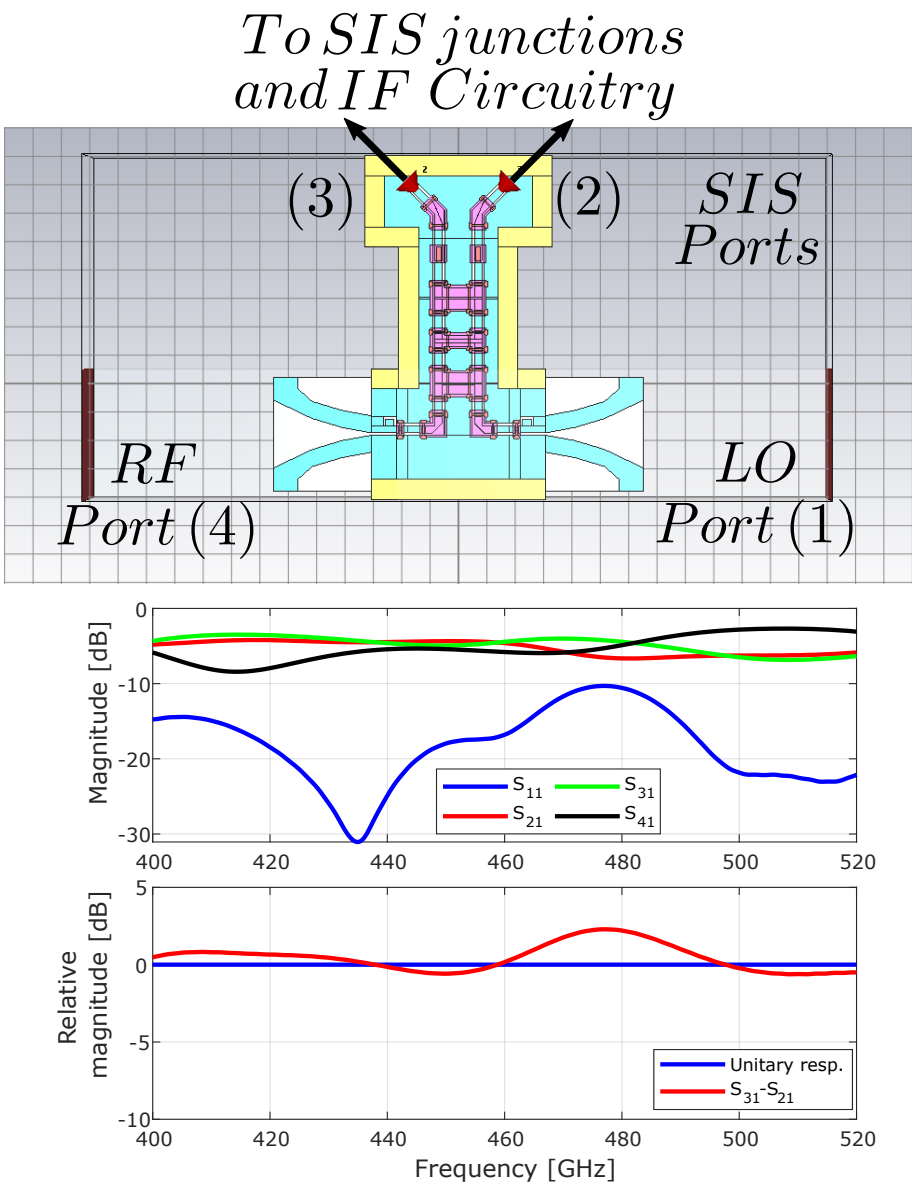

Figure 5.29: Top: CST 3D model of the reduced membrane of the integrated balanced mixer as in [Westig, 2013]. In this model only the branch line coupler cavity is included in the simulation. The *SIS* ports 2 and 3 have an impedance equal to $Z_0 = 42\ \Omega$. **Middle:** S-parameters of the model. **Bottom:** Transmission balance of the model (S_{31}/S_{21})

subsequent IF circuitry. Instead, SIS ports 2 and 3 do have an impedance of 42 Ω, to not generate artificial reflections at the moment of connecting the model to the SIS ports in the 2-pixel schematic. The effect of the SIS tuning structure is included later in a schematic simulation where the SIS ports have the simulated S-parameters obtained form Sonnet (Fig. 5.28).

This model shows a more complex behaviour than the perfect 90° coupler used before (Fig.5.29 **Bottom**). The effects of including this reduced cavity model can be seen in Fig.5.30, where the S-parameters show a more complex behaviour than in 2-pixel block (together with a branch line power divider H3N) with an ideal IBAMI coupler (Fig.5.25). The calculation of the relative

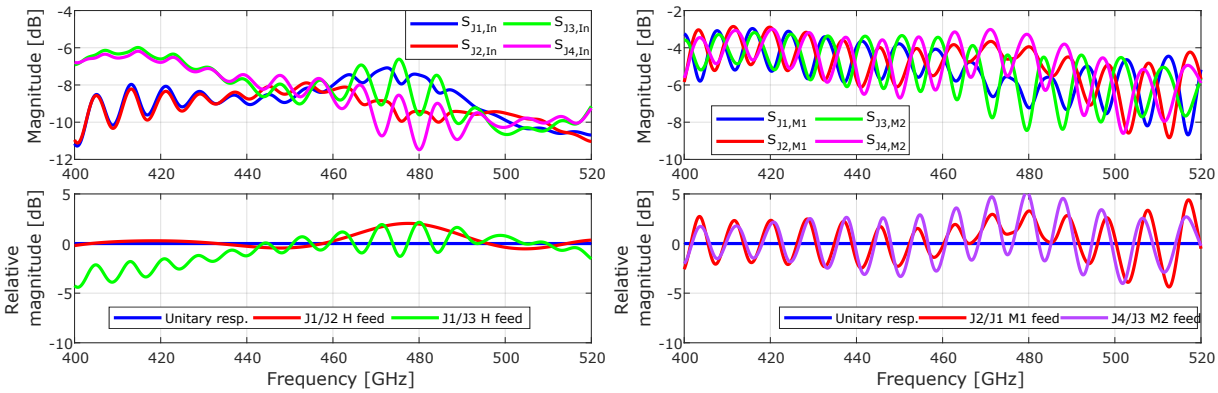

Figure 5.30: Transmission to the junctions in the 2-pixel block with H3N and the reduced IBAMI model plus SIS tuning structure. **Left Top:** Transmission from the input (H-port) to the junctions of the two IBAMI mixers. **Left bottom:** Relative transmission towards junctions J_2 and J_3 with respect J_1 . **Right top:** Transmission from the M1/M2 port towards the respective junctions. **Right bottom:** Relative transmission to junctions of the same mixer.

response, used in the presentation of the measurements of the IBAMI chips (Sec5.3), proves to be useful in this case. The relative response from the H port feed (Fig.5.30 **Left bottom**) yields the same relative response as the IBAMI chip(Fig.5.29 **Bottom**). Meanwhile, for the equivalent junctions, J_1 and J_3, an enhanced standing wave behaviour between $460 - 500$ GHz. This is mainly due to the reflections of the reduced IBAMI cavity model (Fig.5.29 **Bottom**) and the higher reflections at the coupled port of H3N (S_{33} in Fig.5.6 **Bottom right**). The simulation results with the reduced cavity IBAMI show that direct analysis of the S-parameters would be difficult, given how it is influenced by many components and their interaction. The transmission from the M-ports to the junctions shows the same overall behaviour dominated by the off-phase standing wave. For the case of the reduced cavity the standing wave's amplitude is affected by added reflections of the model itself (Γ_{hybrid} and Γ_{SIS}).

The next step is to simulate two models of the, almost complete, IBAMI chip as it would be in blocks 11.110.02 and 11.110.03. The implemented model in CST is shown in Fig. 5.31 and their results in Fig. 5.32. The only difference between models is that the model corresponding to block 11.110.03 has 3 μm beamlead pockets(described in sec.4.2.2). The only missing components in this 3D model are the twin SIS tuning structures. They are replaced by a lumped port of Z_{port} : 10 Ω. This was done to reduce the simulation time of these models (the simulation time of these models took around 150-200 hours of computing time). It is important to notice that this port cannot capture the true behaviour and influence of the impedance of the SIS junctions as they are reduced to a constant 10 Ω impedance across frequency. The inclusion of the SIS junctions into the simulation would be the natural next step.

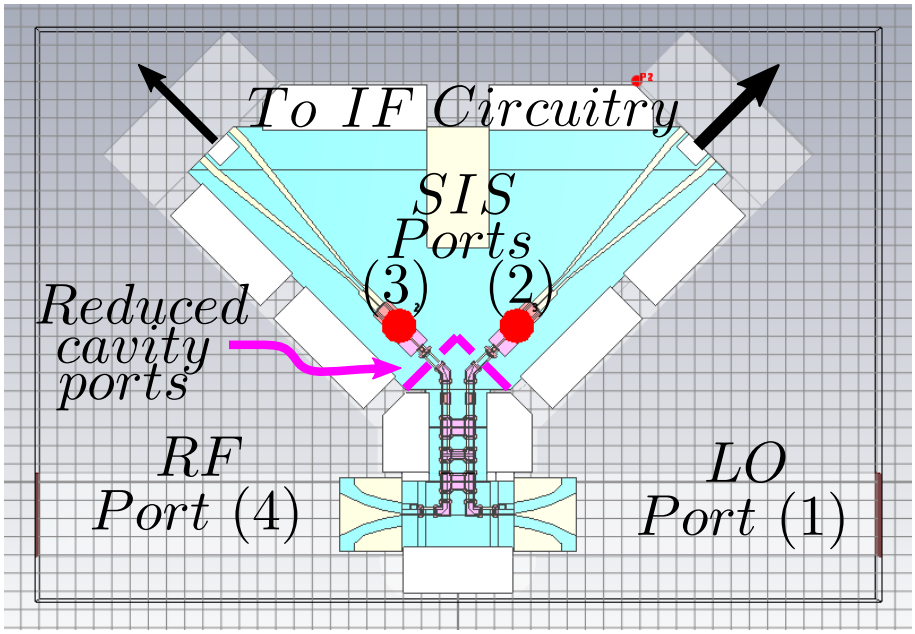

Figure 5.31: CST 3D model of the complete chip of the integrated balanced mixer. The twin SIS tuning structure is replaced by a lumped port of $R : 10\ \Omega$. The magenta dashed lines indicate the position of the $Z : 42\ \Omega$ lumped ports in the reduced cavity model.

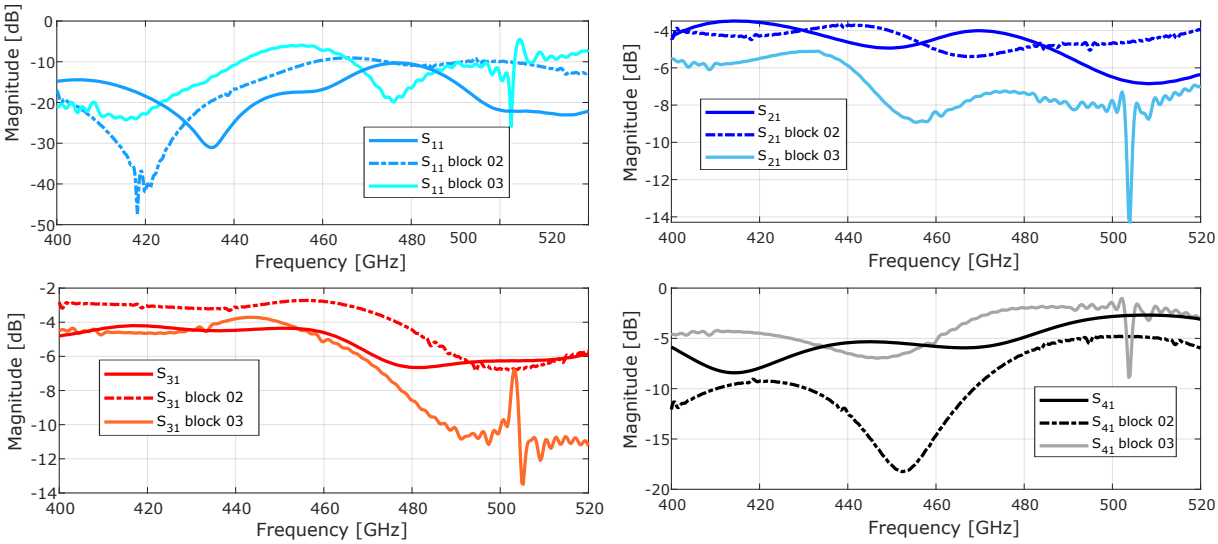

Figure 5.32: S-parameters of the RF components of IBAMI in the three simulated scenarios, in the reduced cavity with only the three branch line coupler, the reduced cavity and the complete cavity without and with the addition of beam lead pockets. **Top left:** Reflections at the input Waveguide port. **Top right:** Transmission from the input waveguide port to the SIS port at the transmitted port.**Bottom left:** Transmission between output waveguide ports **Bottom right:** Transmission from the input waveguide port to the SIS port at the coupled port.

The simulated results for the complete IBAMI chip in blocks 02 and 03 are shown in Fig.5.32 with the results of the reduced cavity IBAMI as well. Comparing the models with the reduced cavity (Fig.5.29) to the complete model in (Fig.5.31) shows significant variations in all S-parameters displayed. It was expected that there would be a difference between the S-parameters of

the IBAMI in the reduced cavity and in the complete cavity models. However, it was not expected that the inclusion of the beamlead pockets would cause such a stark difference between models in blocks 02 and 03. Considering the differences between block .02 and .03, it can be seen that the transmission to junctions decreases significantly, about 5 dB between $460 - 500$ GHz. The reflections at the waveguide port remain around similar levels, with block .03 having the higher overall S_{11}. Finally, the isolation between output ports decreases considerably in block .03, reaching -2 dB at 500 GHz. These results suggest the power is not coupled to the junctions port, but rather it gets reflected and exits through the RF port, hence the low S_{21}/S_{31} and high S_{41}. Another notable feature is the excitation of resonance at 504 GHz that appears in block .03. It was initially thought that this resonant behaviour was directly caused by the addition of beamlead pockets. Closer and more careful inspection reveals that block 02 also exhibits resonances within the band, albeit in smaller magnitude. This suggests that resonances that already exist in the block couple to the beamlead pockets, producing the behaviour seen in the parameters of block .03. An examination of the electric field distribution at 500 GHz (Fig.5.33) shows how the field intensity is the highest in the pockets by the branch line coupler. A cross-section of the cavity where the branch line couple sits shows the field in the cavity. This field resonates in the cavity made between the waveguide and the coupler and hinders the propagation of the CPW mode through it (Fig.5.34).

The simulations of the 2-pixel blocks using the complete cavity IBAMI model in the 2-pixel block show somewhat similar results to the result obtained with the reduced cavity model. Comparing Fig.5.30 and 5.35 it can be seen that for For block 02 the relative response shows that the standing wave pattern in the relative response of J_1/J_3 has increased with respect to the result obtained with the reduced cavity IBAMI model. The reason for this is the greater reflections at the waveguide ports. The M-port sweeps show that the phase between mirrored junctions starts to drift at the high end of the band (Fig.5.35 **Right top**) and that the magnitude of the standing waves in the relative response (Fig.5.35 **Right bottom**) exhibits a larger amplitude towards the high end of the band.

The result for block 03 (Fig.5.36) shows the effects of the lower transmission towards the junctions and higher transmission between the H and M ports of the complete IBAMI models within blocks 02 and 03 (Fig.5.32). This leads to a lower transmission from the H-port (Fig.5.36**Left top**). The transmissions from the M port exhibit lower transmissions, even reaching -10 dB at 460 GHz (Fig.5.36**Right top**). This leads to a very large amplitude of the wave

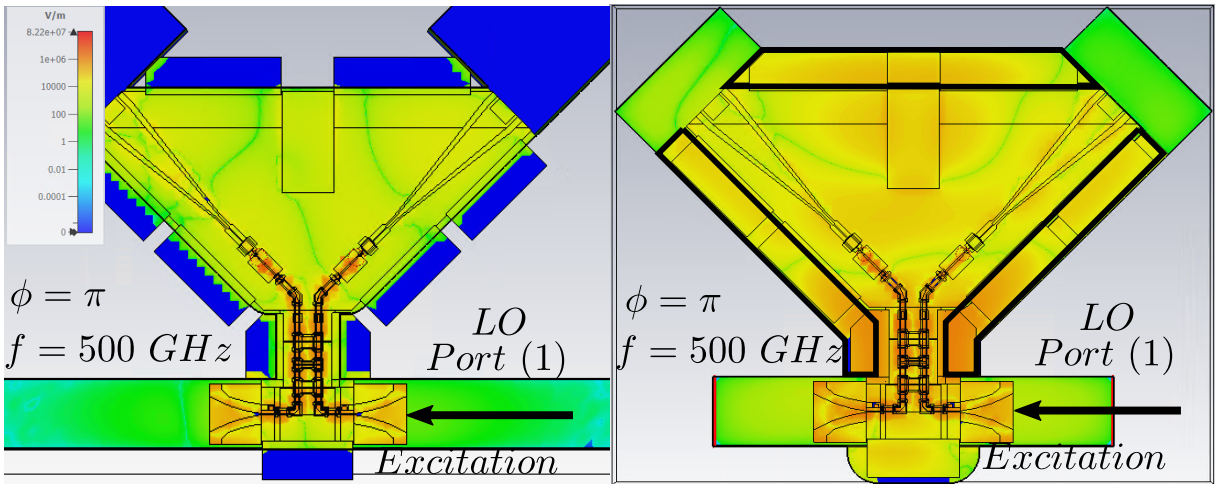

Figure 5.33: E-field intensity at 500 GHz in the RF IBAMI cavity for both blocks, 11.110.02 and 11.110.03. The addition of the pockets(enclosed in black lines) results in a clear resonant behaviour, evidence of this can be seen in the concentration of the E field in the pockets that sit at the side of the branch line coupler.

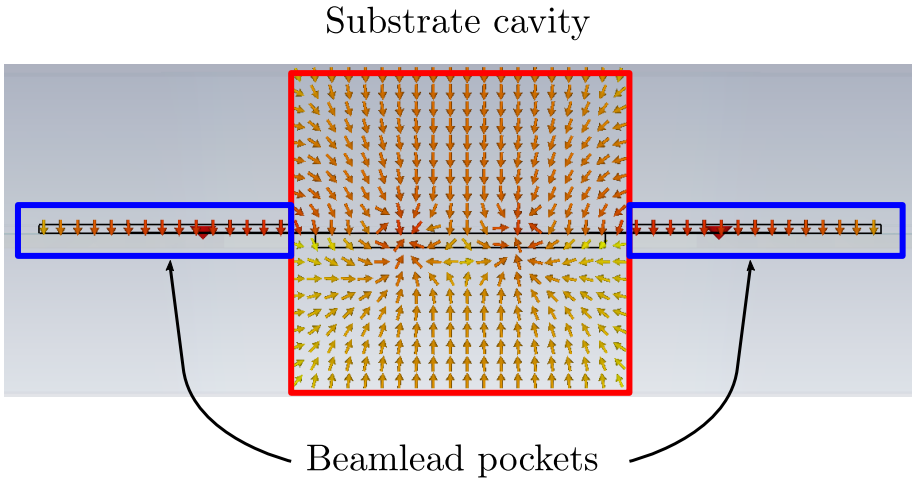

Figure 5.34: E-field vector plot at $f = 500$ GHz block 03, transversal cut of the branch line coupler cavity. It can be seen how the field in the substrate cavity could hinder the propagation of the CPW even mode in the branch line coupler.

pattern in the relative response (Fig.5.36 **Rigth bottom**).

These results were certainly not expected given the results measured in section 5.3, where the IBAMI test block used to measure the reference response also has 5 μm beamlead pockets in it. A comparison between the induced current in the junctions in the IBAMI test block and the simulated transmitted power to the junction ports in the three IBAMI models (Reduced cavity and in blocks 02 and 03) is shown in the next section.

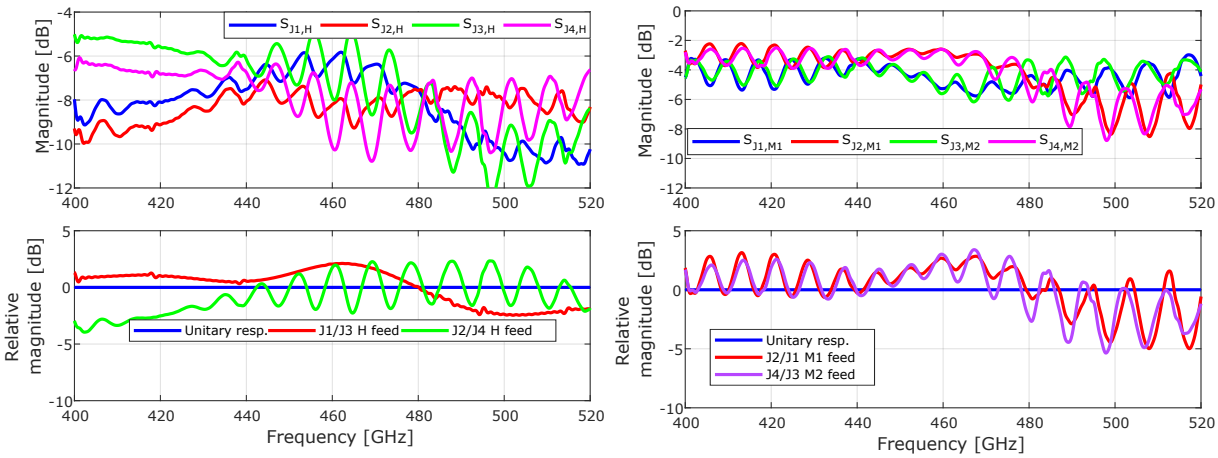

Figure 5.35: Simulated transmission to the junctions in the 2-pixel block with H3N and the complete IBAMI model in block 11.110.02. Here the SIS junctions are summarized as a lumped port of $Z_{SIS} = 10\ \Omega$ **Left Top:** Transmission from the input, H-port, to the junctions the two IBAMI mixers. **Left bottom:** Relative transmission towards junctions J_2 and J_3 with respect J_1 . **Right top:** Transmission from the M1/M2 port towards the respective junctions. **Right bottom:** Relative transmission of junctions of the same Mixer.

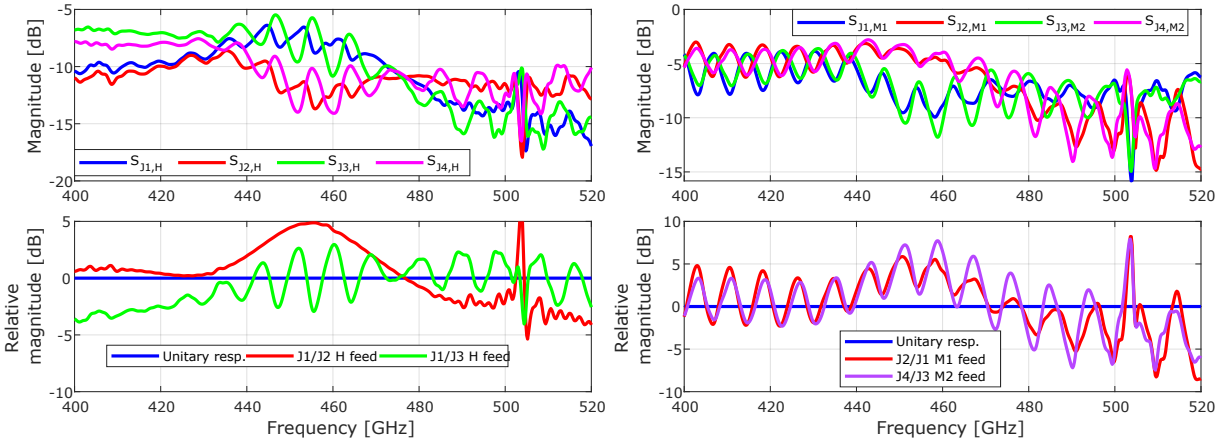

Figure 5.36: Simulated transmission to the junctions in the 2-pixel block with H3N and the complete IBAMI model in block 11.110.03. Here the SIS junctions are summarized as a lumped port of $Z_{SIS} = 10\ \Omega$ **Left Top:** Transmission from the input, H-port, to the junctions the two IBAMI mixers. **Left bottom:** Relative transmission towards junctions J_2 and J_3 with respect J_1. **Right top:** Transmission from the M1/M2 port towards the respective junctions. **Right bottom:** Relative transmission of junctions of the same Mixer.

5.5 Comparison between experimental results and simulations

The only available parameters to compare are the induced currents in the SIS junctions, This quantity depends on the transmission parameters of the IBAMI (S_{21}, S_{31}) and on the incident LO power. To correct for the variation in the incident LO power, the simulated S_{21} and S_{31} are multiplied by the VDI LO power as a function of frequency (Fig.4.19). Additionally, the relative response measured is compared to the simulated S_{21}/S_{31}. The comparisons

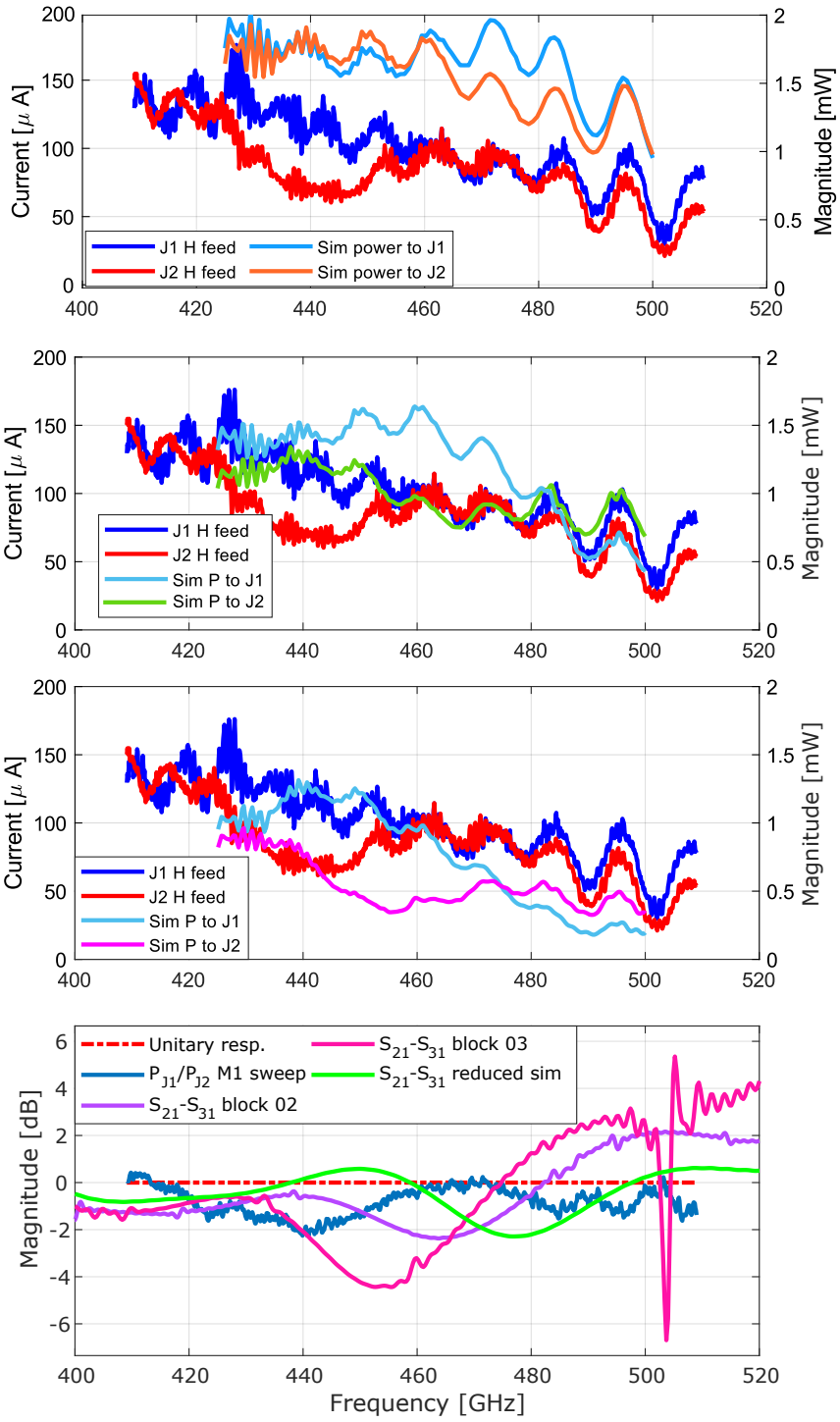

Figure 5.37: IBAMI transmission between waveguide and Junction ports: Measurement vs Simulation. The measured induced current was measured in the IBAMI test block, which is equivalent to the simulated IBAMI in block .03. **Top:** Comparison with a reduced cavity IBAMI. **Middle top:** Comparison with a complete cavity IBAMI without beamlead pockets. **Middle bottom:** Comparison with a complete cavity IBAMI with beamlead pockets. **Bottom:** Comparison between the measured relative response of the junctions and the simulation in the three IBAMI cavities.

between the simulated power transmitted to the junctions and the measured induced current are shown in Fig.5.37.

It can be seen that neither of the models' simulated transmitted power matches what is observed in the IBAMI test block. The reduced cavity model (Fig.5.37 **Top**) matches neither the points of equal balance nor the decrease in induced current seen in the measurements. Blocks .02 and .03 (**Middle top**, **Middle bottom**) display the decreasing power in frequency, however, both of them seem to be shifted in frequency. Additionally, from simulations it is expected that at some point the measured induced current in J_2 would be larger, and remain larger, than in J_1, however, this is not the case and only the between $460 - 480$ GHz, is the current between the junctions similar. This feature is seen more clearly when analyzing the relative response of J_2 (Fig.5.37 **Bottom**). From the measured response the points of equal balance are found at 410 and 470 GHz and neither of the simulated responses matches with experimental results. Another fact is that the resonance seen in the parameters of block .03 is not seen in the measured results. the stark difference between the simulations of block .03 and the experimental measurements is intriguing when considering that the measurements are obtained in a block which also has similar 5 μm beamlead pockets.

When only considering the result at hand, neither of the block simulations corresponds to the measured results and an answer about which IBAMI model to use in the 2-pixel block can not be given with certainty. The reason why the simulation of block .03 does not match the simulation is not currently known. This added to that the only available measured parameters are the transmissions to the junctions, it is hard to give a definite reason for it. The current IBAMI modes in blocks .02 and .03 assume a perfectly tuned SIS junctions pair over the whole frequency range by using an impedance of $Z_{SIS} = 10\ \Omega$. By omitting the detailed structure of the actual tuning circuit of the SIS junctions, the simulation is simplified and accelerated. This simplification is twofold: first, the matching to the SIS is not good enough to allow for neglect of the reflections and assume a constant impedance over the whole frequency range. Secondly, the coupled LO power changes the (quantum) impedance of the SIS, which in turn affects the absorbed LO power. The final absorbed power and thus the induced current needs to be calculated in an iterative procedure. This is a complex interaction is difficult to implement in CST. An possible way to include the dynamic behaviour of the SIS junctions is obtaining the impedance from the induced current LO sweeps, which would involve recording the pumped I-V curves at the measured frequencies. This would allow an approximation of

the embedding impedance of the SIS junctions and use it for the calculation of the RF voltage V_{rf} and current I_{rf}. From these quantities then the Z_{rf} of the SIS could be obtained. It is important to note that this Z_{rf} is dependent on the LO power coupled to the junctions and for accurate measurements, an additional reference power detector is required. This process would yield the impedance Z_{rf} of the twin tuning structure across frequency, ready to be included in CST simulations, with the limitation that this procedure is only a retroactive fitting of the measurements.

On the other hand, the resonant behaviour obtained from the simulation IBAMI chip in block .03 was not expected. The measured induced current in the IBAMI test block does not display any evidence of the behaviour of the sort. The only evidence observed in this thesis that would suggest some sort of resonant behaviour in the IBAMI block was detected in the non-adjusted LO sweeps in block .03, albeit for a different frequency. For all couplers tested in block 03, the LO sweeps over the H port displayed a range of low induced current (Fig.5.38). Additionally, the SIS displayed a broken step I-V characteristic, shown in Fig.5.39, when injecting the LO signal through the LO input port of the 2-pixel block (Fig.4.6) and an F_{LO} within 465 and 480 GHz. Similar phenomena have only been previously detected in [Ermakov et al., 2016]. It was initially thought that the cause for the low induced current ranges was the existence of the broken step IV curves, However, the broken I-V curves are not observed in the entire range between $470-480$ GHz, but at particular frequencies, with the junction displaying the broken step effect but not in the same magnitude. Additionally, broken step IV was recorded even outside of the range of low induced current $470-480$ GHz. These facts suggest that both phenomena are symptoms of the same problem rather than one being caused by the other. To obtain theoretically a pumped curve that looks similar to the one shown in Fig.5.39, a high incident LO power is needed (which is available) and an embedding impedance with a very low real part and a high imaginary part, which points at a resonance in the block.

At this point, even if the simulations and measured results of the IBAMI in block .02 and .03 are very limited, they have the closer correspondence to the actual fabricated devices used. These models are used to compare the measured induced current to simulations for branch line power dividers H3N. H2L and H2S. Since it was already seen that the simulation of the IBAMI does not display a great level of agreement with the measured induced current, only the relative response of the junctions is given, for both, H and M1/M2-port feeds is presented.

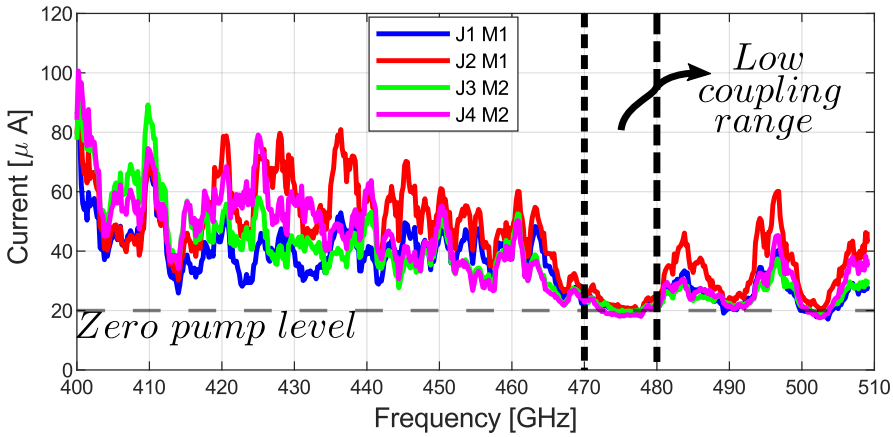

Figure 5.38: Example of an LO sweep through the LO port of block 11.110.03. In the range between 470-480 GHz there is hardly any power coupled to the junctions for this sweep. Afterwards, from 480 to 510 there is a behaviour similar to that of a standing wave.

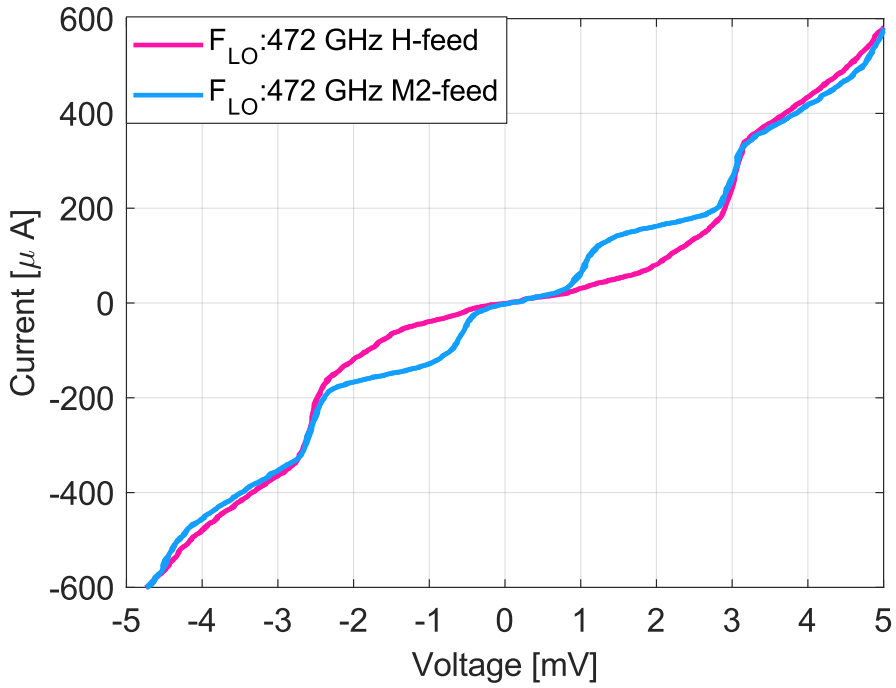

Figure 5.39: Broken step I-V curve recorded in the SIS junctions for a CW signal of 472 GHz feed through two different paths in block 11.110.03. The broken step I-V curve is displayed in the magenta curve. The broken step name comes in the clear break and change in the slope in the middle of the first photon step.

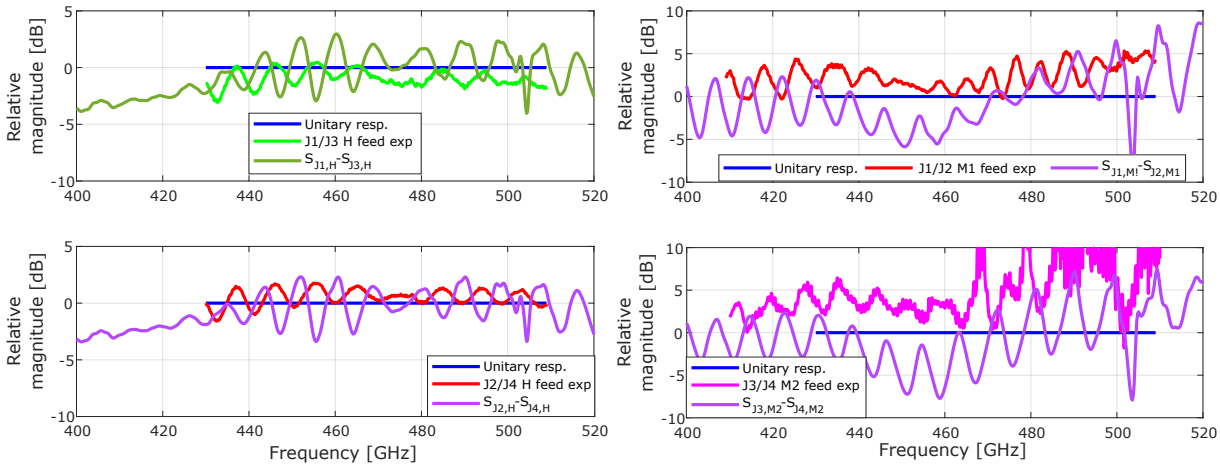

Figure 5.40: Comparison betwwen experimental and simulation results for coupler H3N-13 in block 03. **Left top:**Relative response for mirrored junctions J_1 andJ_3 for an H-port sweep. **Left bottom:** Relative response of mirrored junctions J_2 and J_4 for an H-port sweep. **Right top:** Relative response of junctions in the same IBAMI chip for a M1-port sweep. **Right bottom:** Relative response for junctions on IBAMI chip for a t M2-port sweep.

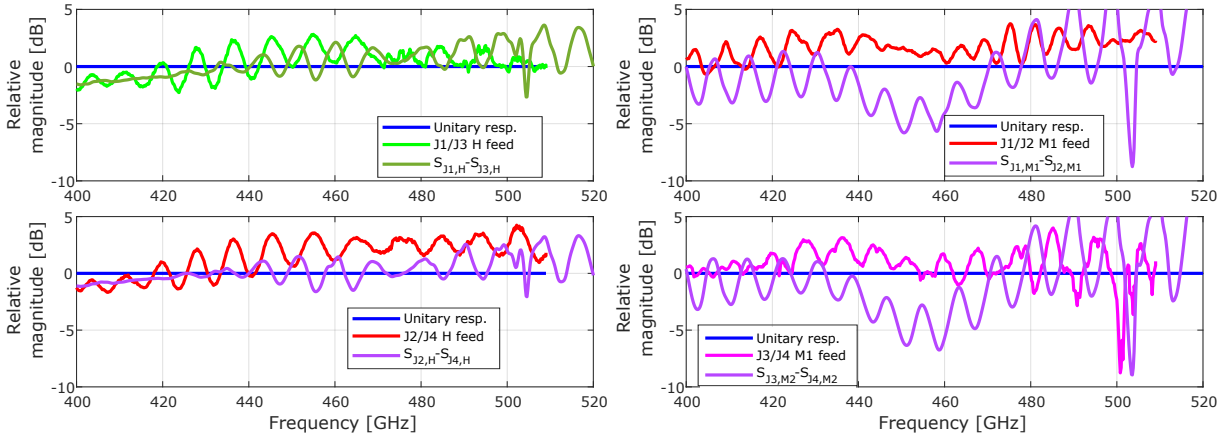

Figure 5.41: Comparison between experimental and simulation for coupler H2L-8 in block 03. **Left top:** Relative response for mirrored junctions J_1 andJ_3 for an H-port sweep. **Left bottom:** Relative response of mirrored junctions J_2 and J_4 for an H-port sweep. **Right top:** Relative response of junctions in the same IBAMI chip for a M1-port sweep. **Rigth bottom:** Relative response for junctions on IBAMI chip for a t M2-port sweep.

For model H3N-13 there is a very limited agreement between simulations and measurement (Fig.5.40). From the H-port sweeps (Fig.5.40 **Left**), the measured relative response is not as large as the expected one. There is an offset between the measured standing waves and the simulated ones and both have a similar period. Additionally, for some of the junction pairs in the IBAMI chips, the standing waves seem to change their frequency, since the relative phase between the simulated and measured relative response changes across frequency. This is seen in the relative response of the IBAMI at M1-port (Fig.5.40 **Right top**). For the case of the M-port sweep for the IBAMI at M2-port, only the frequency of the standing wave matches up to 460 GHz.

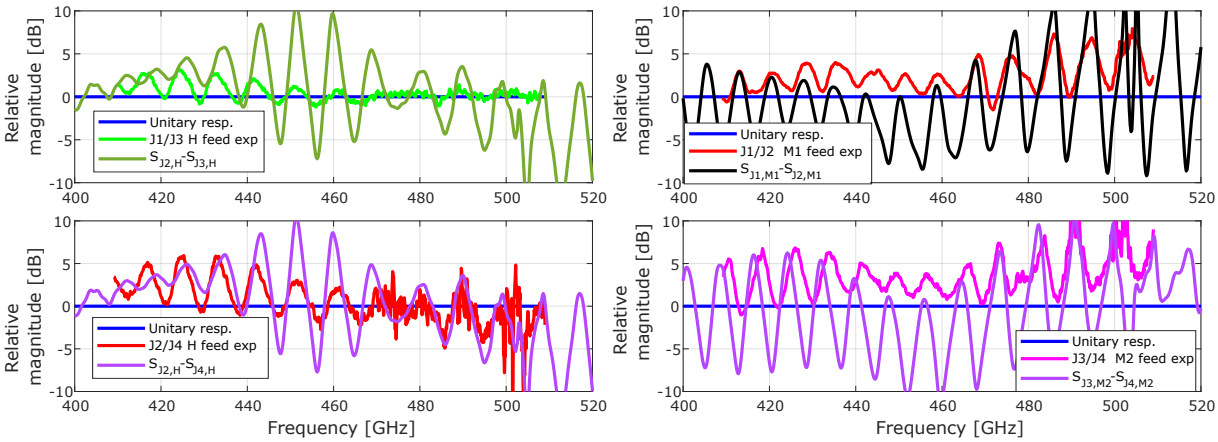

Figure 5.42: Comparison between experimental and simulation for coupler H2S-3 in block 03. **Left top:** Relative response for mirrored junctions J_1 and J_3 for an H-port sweep. **Left bottom:** Relative response of mirrored junctions J_2 and J_4 for an H-port sweep. **Right top:** Relative response of junctions in the same IBAMI chip for a M1-port sweep. **Rigth bottom:** Relative response for junctions on IBAMI chip for a t M2-port sweep.

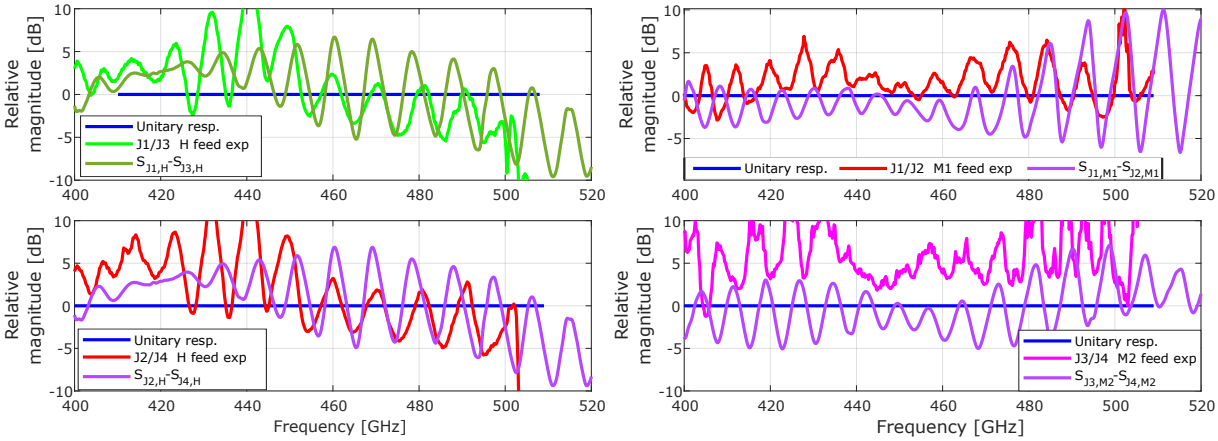

Figure 5.43: Comparison between experimental and simulation for coupler H2S-1 in block 02. **Left top:**Relatice response for mirrored junctions J_1 andJ_3 for an H-port sweep. **Left bottom:** Relative response of mirrored junctions J_2 and J_4 for an H-port sweep. **Right top:** Relativer response of junctions in the same IBAMI chip for a M1-port sweep. **Rigth bottom:** Relative response for junctions on IBAMI chip for a t M2-port sweep.

The results for the LO sweep with branch line power divider H2L-8 in block 03 are presented in Fig.5.41. The H-port sweeps reveal that the imbalance of the measured relative response is larger than the expected from simulation. Additionally, the standing wave in the experimental results is present from 400 GHz up to 460 GHz where the range of low induced current does not allow for further comparison. The frequency of the standing waves is similar but there is a variation on their period with frequency. The M-port sweeps display a large difference between experimental results and simulations. Neither the overall balance in the response nor the magnitude of the standing waves exhibits a match between simulation and experiment. Due to the irregularity of the standing wave in the relative response, it is hard to make a comparison

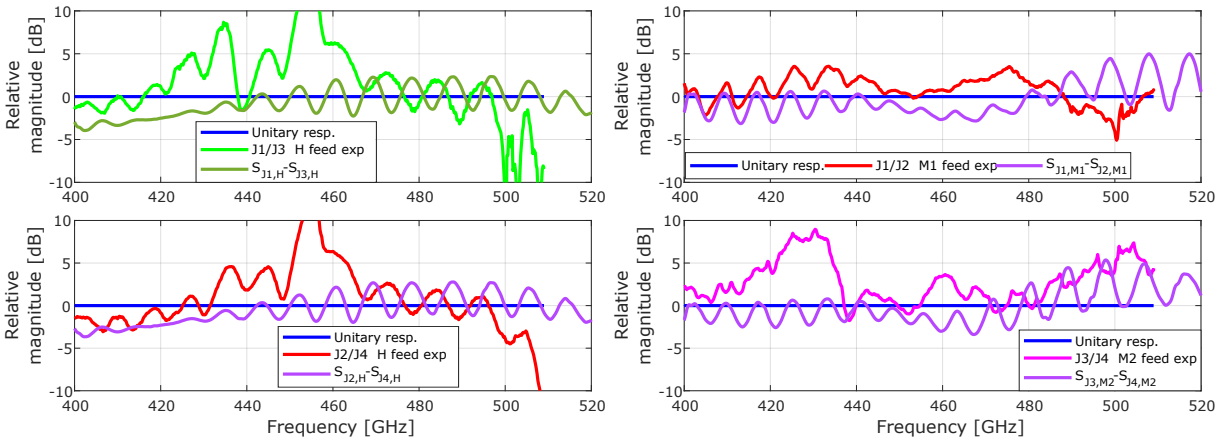

Figure 5.44: Comparison between experimental and simulation for coupler H3N-12 in block 02. **Left top:**Relative response for mirrored junctions J_1 andJ_3 for an H-port sweep. **Left bottom:** Relative response of mirrored junctions J_2 and J_4 for an H-port sweep. **Right top:** Relative response of junctions in the same IBAMI chip for a M1-port sweep. **Rigth bottom:** Relative response for junctions on IBAMI chip for at M2-port sweep

beyond the fact that their periods are similar.

The comparison for branch line power divider H2S-3 in block 03 is shown in Fig.5.42. For H-port sweeps (Fig.5.42 **Left**) the magnitude of the measures standing wave is significantly smaller than the expected simulated one. The period of the standing waves matches between simulation and experimental results, and it is also observed that a change in the frequency of the standing wave is also present. The M-port sweeps (Fig.5.42**Right**) show a measured response whose standing wave amplitude is considerably smaller than the simulated one. Additionally, the measured overall imbalance is higher. The change in frequency in the standing waves is also observed.

The results for the branch line power divider H2S-1 are presented in Fig.5.43. For the H port sweeps it can be seen that the period of the standing waves matches, again, with a change in period across frequency. It is noticed that the measured amplitude of the standing wave in the range $420 - 450$ GHz is of comparable magnitude to the standing waves seen in the simulated results. For the M-port sweeps. The IBAMI at Mixer port M1 displays an overall match in the amplitude of the standing waves observed that matches not only the period but the increase towards the high end of the band. For this sweep, it is noticed a significant drift between experimental and simulated results. For The IBAMI at mixer pot M2, there is hardly any match between simulation and experimental results aside from the period of the standing waves.

The results for the branch line power divider H3N-12 are shown in Fig.5.44.

The fact that the IBAMI chip at mixer port M2 broke during the experimental procedure limits the comparisons for mirrored junctions J_1/J_3 and J_2/J_4 and for J_3/J_4. For the relative response of J_1/J_2 it is observed that the measured and simulated relative response matches in period and amplitude up to 470 GHz.

5.5.1 Discussion

The first important observation that can be made, is that the period of the measured standing wave pattern observed in the relative response of the junctions matches with the period of the simulated one. This supports the idea that is the mismatches between the power divider and the IBAMI chip that produce and allow the existence of standing waves in the waveguide connecting them. In general, the amplitude of the measured standing waves is lower than the simulated ones. It is hypothesized that the reason for this is that the mismatch between components is not as high as the simulation would suggest. Another possibility is that the losses in the waveguides are higher than anticipated. However, the results for model H2S-1 exhibit some sort of agreement between simulations and measurements where both standing waves are of similar amplitude, albeit, not in the same frequency range. This fact makes the idea of high waveguide losses unlikely.

If only experimental results are considered. It can be seen that the magnitude of the standing waves of models H3N-13 and H2L-8 are similar. Given that these two power dividers were tested with the same mixer, it suggests that their parameters are similar and around the same value. In contrast, power divider H2S-3, tested in the same block, displays large standing waves in the relative response J_2/J_4 but not in J_1/J_3. There is a considerable difference between the results of power dividers H2S-3 and H2S-1, tested in blocks .03 and .02 respectively. The standing waves observed in the relative response of J_2/J_4 and J_1/J_3 are considerably larger with power divider H2S-1. However, the suspicion that, at the moment of testing power divider H2S-1, the IBAMI chip was already damaged, limits the comparison with power divider H2S-3. Judging by the amplitude of the standing waves, it can be said that branch line power divider H2S-1/3 has the largest reflections at its output ports, this agrees with the simulated results of the branch line power dividers where the short circuit termination causes the highest reflections at the output ports of the power divider.

Regarding the beamlead pockets and their unexpected effect on the transmission from the H-port. There is a strong argument on the performance side to simply remove them since block 02 did not display such effects. The

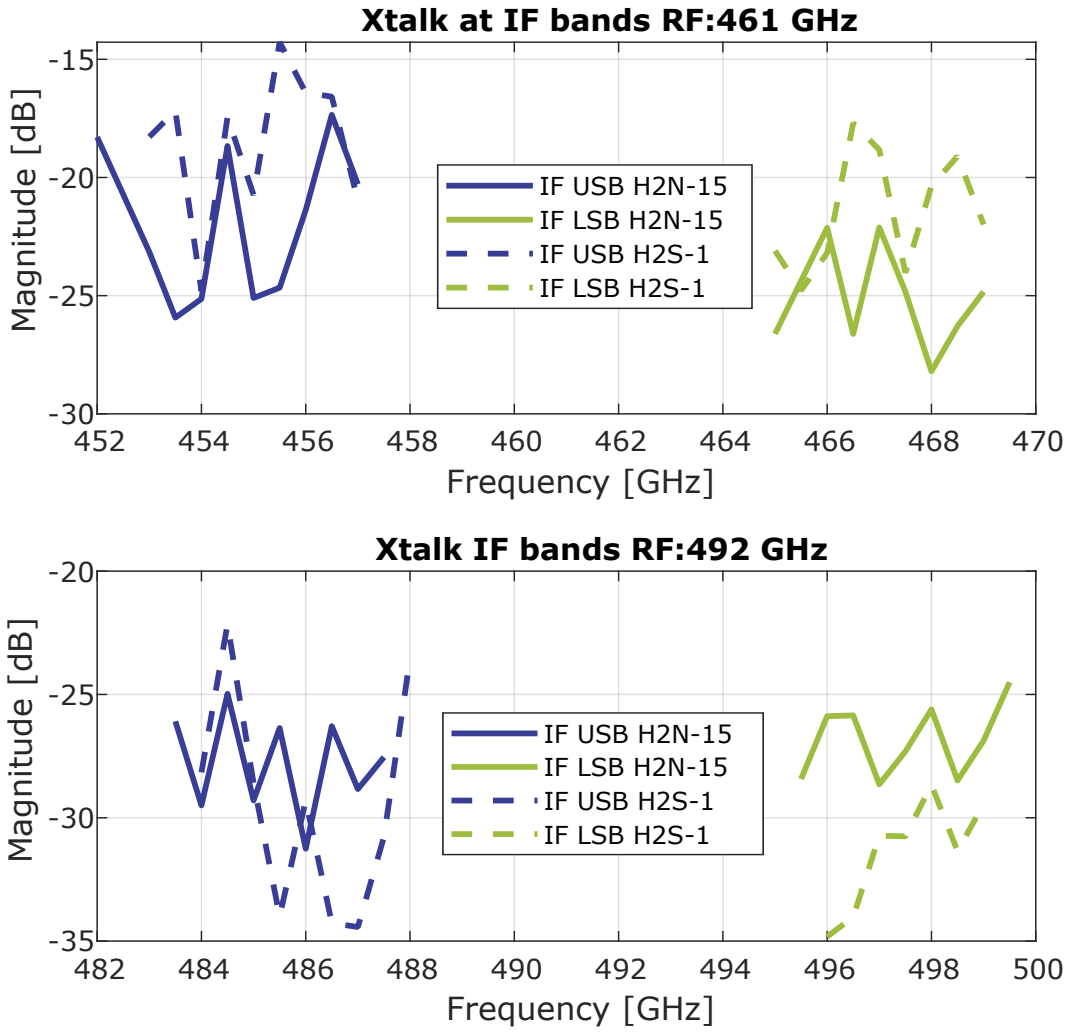

Figure 5.45: Results of the crosstalk between pixels for models H2N-15 and H2S-1. **Top:** results for $F_{Gunn} = 461$ GH. Here the model H2N-15 displays a better crosstalk than model H2S-1. The difference being ~ 5 dB. **Bottom:** results for $F_{Gunn} = 492$ GHz, Foir this frequency, the model H2S-1 displays a better crosstalk than model H2N-15.

consequence of such action would be placing a very short time limit on the lifespan of the IBAMI Chips. It was observed that the IBAMI chips in block .02 were in a bad state after 4 opening/closing cycles, as observed with the measurement of power divider H2S-1. This was due to the waveguide walls pressing the beam leads and forcing them into the waveguide cavity. In turn, this puts pressure on the Si membrane eventually breaking the IBAMI chip. In comparison, the IBAMI chips at block 03 have survived 10 opening/closing cycles without exhibiting signs of decay. This speaks against the removal of the beamlead pockets but for their modification. The simulations of block 03 show where the field is concentrated pointing to possible cavities to eliminate to reduce the chance of the field coupling to the pockets in future blocks.

5.6 Crosstalk over the LO path results

The results of the crosstalk were measured using the IBAMI mixers as coherent detectors. The process was enabled by the CW signal generated by the VDI CW generator used as LO. The signal to detect was the CW signal from the Gunn LO. Two branch line power dividers were tested in this setup, the models were **H2N-15** and **H2S-1**.

The results for the crosstalk measurements are shown in Fig. 5.45. Only the lower and upper sideband range was covered with a resolution of 0.5 GHz. The simulation of the fabricated components shows that the isolation between output ports of the coupler H2N (Fig.5.5) is almost 6 db better than the isolation of coupler H2S (Fig.5.6). A difference like this is only observed for the LSB and USB for the $F_{Gunn} = 461$ GHz, where the model H2N displayed a lower crosstalk than model H2S. For the case of $F_{Gunn} = 492$ GHz, the model H2S displayed a lower crosstalk than model H2N. The exact reason for this was not explored due to the lack of time and the fact that no more experiments of this kind were performed because there was no direct translation from these measurements to the parameters of the branch line power divider.

5.7 Considerations for array receivers

From section 5.5 it was seen how the standing waves present in the waveguide between the branch line power divider and the IBAMI chip generated the wave pattern observed in transmission from the H-port/M-ports to the junctions. This raises the question of how to minimize the effect of the standing waves in the LO path on the transmission to the junctions. The first and most direct approach is the elimination/reduction of the factors that contribute to its existence. These factors are the reflections at their interfaces and the waveguides between the components. The reduction of the reflection at the ports is a viable approach but comes with difficulty that achieving reflections lower than $|\Gamma_{dB}| < -20$ dB is very challenging for complex components, requiring optimization of every individual component to ensure the reflections at every interface are lower than the required value. Additionally, considering that the low noise operation of the SIS junctions does not necessarily mean the lowest level of reflection, the reflections of the LO distribution network become even more critical. To reduce the negative impact of the standing waves, Especially the out-of-phase standing waves, in the power distribution towards the SIS junctions. This prompts the analysis of the phase of the reflected signals, modified by the respective hybrids in the mixer and LO

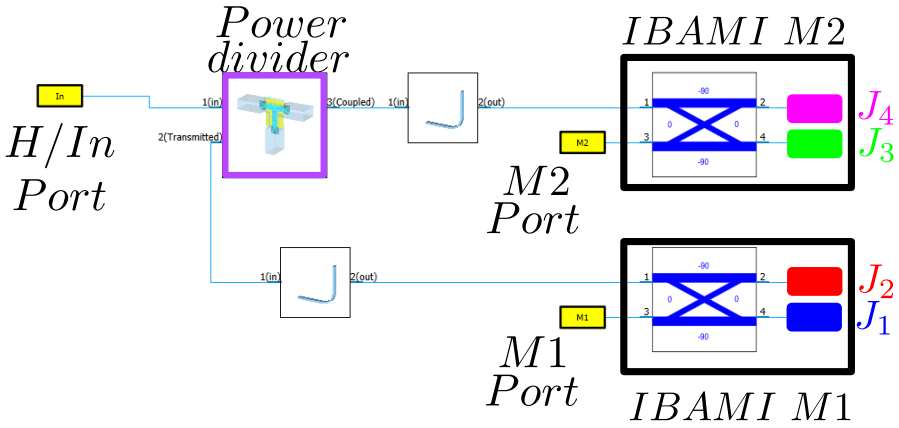

Figure 5.46: Schematic of the 2-pixel block with theoretical mixers. Here the branch line coupler in the IBAMI chips is replaced by a theoretical coupler. One of the parameters of this coupler is the style of coupler, the balance , the loss and the input impedance seen at every port.

divider. In pursuit of the speed of development, various configurations are studied in the schematic solver of CST, using, again, a theoretically balanced mixer like in Fig.5.46. The 90° coupler in the IBAMI chip is replaced with a 180° one while keeping the same level of reflections between components. Its effect of using a 180° coupler in the balanced mixer is tested, in a piece-wise simulation, in conjunctions with an H3N power divider. The schematic of the 2-pixel block is presented again for clarity purposes (Fig.5.46).

Fig. 5.47 shows the transmission characteristics of two IBAMI mixers with a 180° coupler (**Right Top**). It can be seen how the transmission from the H port changes considerably, in comparison with Fig.5.25 **Right top**. Where previously the transmission was dominated by the characteristics of the H3N coupler, now a considerable standing wave pattern can be observed in both mixers. Checking the relative transmission form H-port (Fig.5.25 **Right bottom** to the junctions reveals that these standing waves are only visible when comparing equivalent junctions (meaning J_1-J_3 and J_2-J_4) in different mixers. On the other hand, when observing the transmissions from the M1/M2 ports it can be seen how they are not affected by the standing waves present in the LO path (Fig.5.25 **Left**), being only affected by the parameters of the coupler. From a pragmatical point of view, with the same level of reflections at the input ports, the 180° balanced mixer shifts the effect of the standing wave from transmission from the M-port to the transmission from the H-port. This means the RF signal to both junctions in the mixers will be the same but the LO level will be different. The exact level of imbalance a balanced mixer can tolerate and what are the implications for its noise temperature is a topic not explored in this thesis.

The effect of changing from a 90° based balanced mixer to a 180° one is

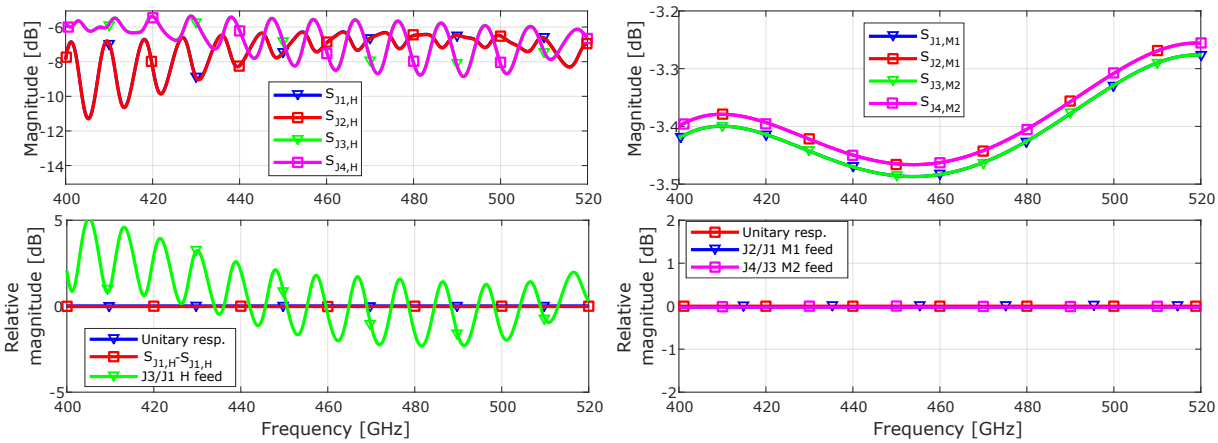

Figure 5.47: 2-pixel block with branch line coupler H3N and a 180° coupler balanced mixer. Due the perfect balance of the theoretical coupler in the IBAMI, the parameters pairs $S_{J1,H}/S_{J2,H}$ and $S_{J3,H}/S_{J4,H}$ are overlapped in top of each other. This is also the case for the $S_{J1...4,M}$ parameters. **Left top:** Transmission from the H-port towards the junctions. **Left bottom:** Relative response for junctions in the same IBAMI chip J_1/J_2 and mirrored pair J_1/J_3. **Rigth top:** Transmission from port M1/M2 towards respective junctions. **Rigth bottom:** Relative response of junctions in the same IBAMI chip.

shifting the effect of the standing wave towards the transmission from port H. From a design point of view, this is an undesired feature since it is desired that both mixers receive the same amount of power. Looking carefully at the transmission in Fig.5.47 it can be seen that the transmissions from the H port towards the junctions are in a $\Delta\phi = 90°$ off phase(Fig.5.47 **Top left**), with a transmission power imbalance of ~ 3 dB. These results suggest that the cause of this counter-phase behaviour in the transmission in the H-port is due to the phase imbalance introduced by the 90°. Hence, a different power divider, where $\Delta\phi = 0°$, is tested to confirm whether or not it is the $\Delta\phi$ introduced by the power divider that causes the observed behaviour in the relative response of the junctions.

The second power divider considered in this thesis is a Wilkinson power divider. The main difference with the 90° branch line coupler is that Wilkinson's outputs have a $\Delta\phi = 0°$ between them. A theoretical Wilkinson power divider is implemented in the schematic simulator, replacing the model of the H3N power divider, with an impedance of $Z_W = 270\ \Omega$. This Z_W generates a reflection coefficient of $\Gamma(480\,GHz) = -10$ dB, at 480 GHz. This impedance is chosen because it would generate reflections equivalent to the maximum reflections generated by the branch line power divider H3N (Fig.5.6 (Right)). The results of the transmission with the theoretical Wilkinson and 180° hybrid balanced mixer is shown in Fig.5.48. It is important to remember that, even if they are theoretical, ideal components, the reflections of the SIS junctions and the mismatch between the waveguide and the Wilkinson power

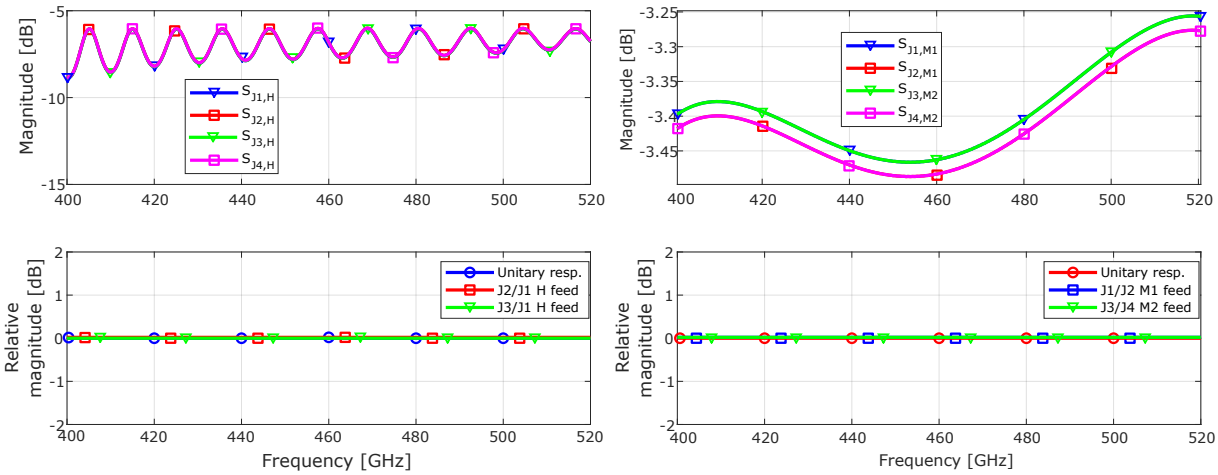

Figure 5.48: 2-pixel block with theoretical wilkinson and a 180° coupler balanced mixer. **Left top:** Transmission from the H-port towards the junctions. **Left bottom:** Relative response for junctions in the same IBAMI chip S_1/J_2 and mirrored pair S_1/J_3. **Rigth top:** Transmission from port M1/M2 towards respective junctions. **Right bottom:** Relative response of junctions in the same IBAMI chip.

divider are still present. The transmission from the H-port to the junction shows the wave pattern caused by the standing waves in the LO path(Fig.5.48 **Left top**), however, it can be seen that the transmission to all junctions has the same magnitude and has the wave behaviour is in-phase. Proof of this is the relative response (Fig.5.48 **Left bottom**) between junctions J_1/J_2 and J_1/J_3. From the transmission to the junctions from the M-port, the results are expected for the 180° hybrid. These results show an improvement over the 2-pixel block with a 90° branch line power divider. For the same level of mismatch between waveguide components, an in-phase power divider ($\Delta\phi = 0°$) transmission manages to eliminate the effect of the standing waves in the relative transmission to the junctions, while a quadrature power divider (($\Delta\phi = 90°$)) maximizes the relative difference in power delivered to the junctions. This configuration would be better than the present one for an array receiver since, even if the standing waves in the LO path cause the power delivered to the junction to vary across frequencies, all junctions would receive an equivalent level of power.

Now that the effects of an in-phase power divider on the power distribution to the junctions are known, the next step is to simulate the theoretical 2-pixel block with the designed microstrip Wilkinson power divider (Section 3.3.2.3) in a theoretical scenario with two ideal IBAMI mixers based on a 90° hybrid. The results obtained are shown in Fig.5.49. The transmissions from the H-port towards the junctions (Fig. 5.49 **Left top**) show that between $400-440$ GHz there is a standing wave behaviour that increases its magnitude towards the low end of the band. This behaviour is caused by the reflections at the output ports of the designed microstrip Wilkinson, which are higher than

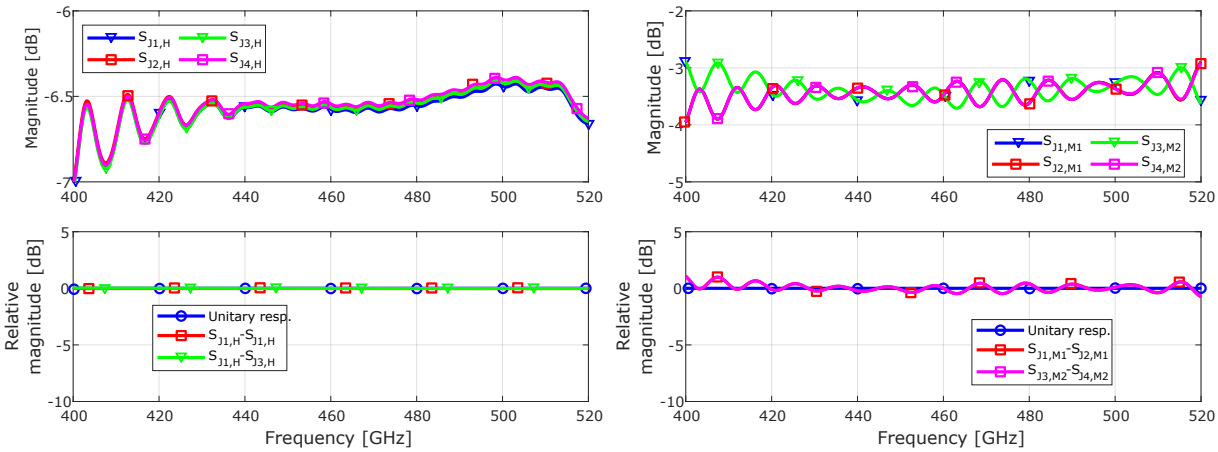

Figure 5.49: 2-pixel block with the microstrip Wilkinson and theoretical IBAMI based on a 90° hybrid. **Left top:** Transmission to the junction from the input port.**Left bottom**, relative transmission from the input port to junctions $J2$ and J_3 with respect to J_1. **Rigth top:** Transmission the the junctions from the M-ports. **Right bottom:** relative transmission to junctions in the same mixer.

the ideal one for this frequency range. The relative response (Fig. 5.49 **Left bottom**) shows no imbalance in the entire band, even at the lower end where the transmission parameters display an increased standing wave behaviour. The transmission from the M-ports(Fig. 5.49 **Right top**, **Right bottom**) shows a standing wave pattern that has an off-phase between the two junctions of the same mixer. This is in agreement with the previously simulated results in Section 5.4. The difference here is that the amplitude of the standing waves with the microstrip Wilkinson is not as large as with the branch line power divider due to the lower reflections of the former in comparison with the latter.

The results obtained from the schematic simulation prompt the testing of the proposed microstrip Wilkinson in a 4-pixel scenario. Here the IBAMI mixers consist of the theoretical 90° Hybrid with an impedance of $Z_{coupler} = 513\ \Omega$. The junctions are summarized as the reflection obtained from the tuning structure from [Westig, 2013]. The 3 power dividers and the 4 IBAMI mixers are connected by waveguides of the same length. The results are shown in Fig.5.50. The relative transmission from the H-port to the junctions has an overall behaviour similar to what was measured with in the 2-pixel scenario (Shown in Fig.5.49). The reflections at the output ports generate the standing wave behaviour in the $400-440$ GHz band(Fig.5.50 **Left top**). The relative response of the junctions is the same in the LFA band(Fig.5.50 **Left bottom**), even in frequencies where there is a substantial standing wave observed in the transmission towards the junctions. The transmission from the M ports shows an enhanced standing wave. In contrast, if the 4-pixel block is populated with 90° branch line power dividers, Like model H3N,

the transmission will suffer due to the standing waves being in off-phase. enhancing the imbalance in the transmisison towards the junctions (Fig.5.51 **Left**). The transmission from the M ports suffers as well, with an imbalance up to ~ 3 dB in the band(Fig.5.51 **Right**).

After having studied the results for the choice of components for heterodyne array receivers, it is seen that and 0° equal power divider in combination with balanced mixers based on a 180° coupler would be the best case scenario. In practice, the performance of these components comes with the a complex design, fabrication and that may have a limited bandwidth. One example of this are the HFA 90° and 180° hybrids designed for the HFA, presented in Chapter 3. At this point it is necessary to evaluate the requirements of the system, and decide for a design contemplating the feasibility of the designs with the current fabrication capabilities at hand.

5.8 Fabricated microstrip Wilkinson

A prototype of the Wilkinson power divider was fabricated by the cleanroom personnel of the I. Physikalisches Institut approximately 3 weeks before the hand-in date of this work. The fabricated is mounted in block 11.110.05, shown in Fig.5.53. This model differs from the proposed model in Chapter 3. The reason for this is that, given the scarcity of time, the model for manufacture had to be simplified to reduce the number of fabrication steps. What this meant is that all the SiO_2 patches had to be 300 nm thick and the SiO_2 patch at the waveguide-CPW transition had to be reduced from 800 to 300 nm. The consequence is that the mode had to be optimized once again, with the results obtained shown in Fig5.54.

The Wilkinson power divider is tested in block 11.110.05. This block, detailed in Chapter 4, has a different beamlead pocket footprint than block .03/.04. This modification was implemented after the simulations of the IBAMI in block .03 showed the field concentrates in the pockets by the side of the branch line hybrid (Fig.5.33). The beamlead footprint in block .05 has had a section removed where the field showed a maximum magnitude in an attempt to reduce its effects on the transmission towards the junctions. The other modification is that there is a step discontinuity in the waveguide interface in the IBAMI, detailed in [Westig, 2013], Section 3.2.8. This additional modification limits the comparison between the results obtained for the branch line power dividers tested in block .03 and the Wilkinson power divider in .05. Hence, it is expected that there are differences between the IBAMI reference response and the relative response obtained from junctions in the

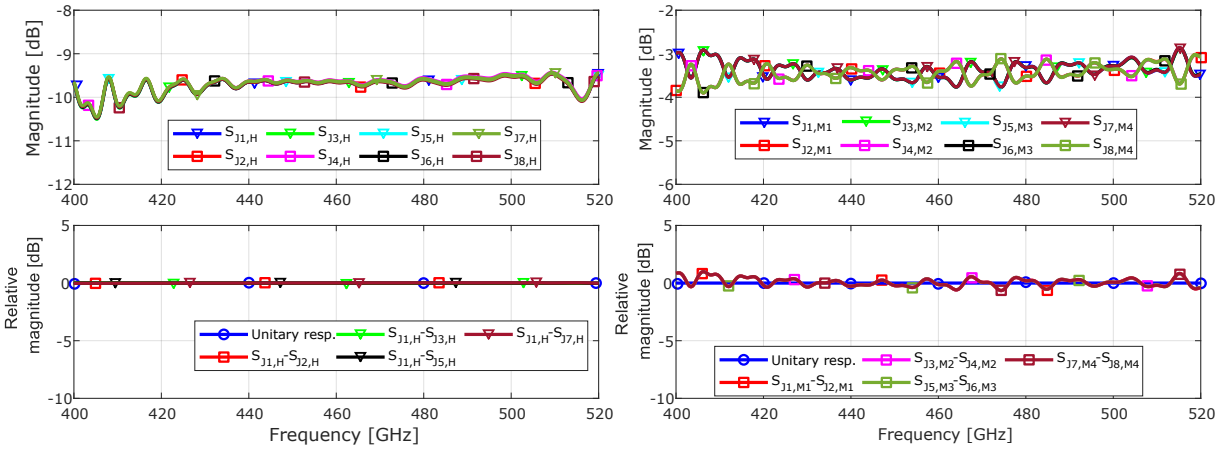

Figure 5.50: 4-pixel block with 3 microstrip Wilkinson power dividers in a cascade configuration and 4 theoretical IBAMI based on a 90° hybrids.**Left top:** Transmission to the 8 junctions from port H. **Left bottom** relative transmission of junctions J_2,J_3,J_5 and J_7 with respect J_1. **Rigth top:** Transmission the the junctions from the M-ports.**Right bottom:** relative transmission to junctions in the same mixer.

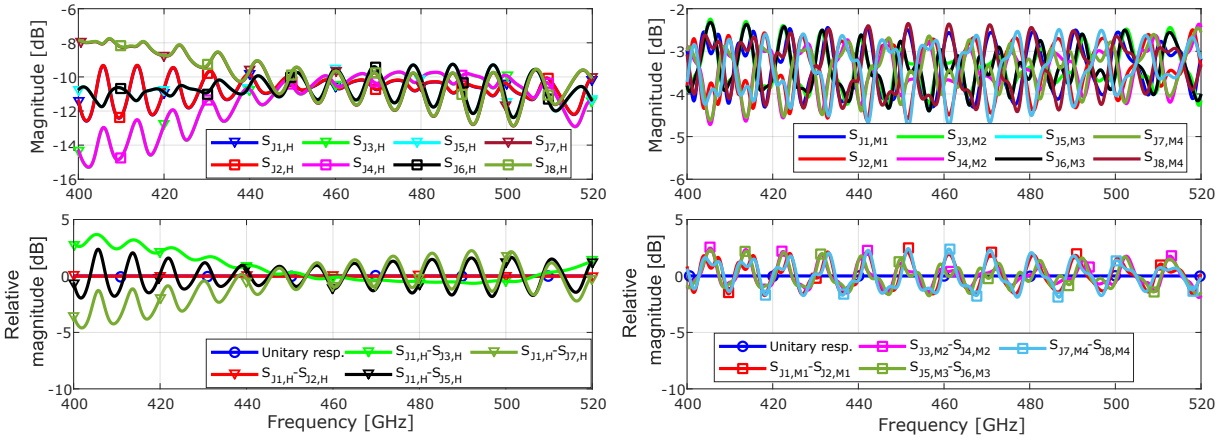

Figure 5.51: 4-pixel block with 3 90° branch line power dividers in a cascade configuration. **Left top:** Transmission to the 8 junctions from port H. **Left bottom** relative transmission of junctions J_2,J_3,J_5 and J_7 with respect J_1.**Right top:** Transmission the the junctions from the M-ports.**Right bottom:** Relative transmission to junctions in the same mixer.

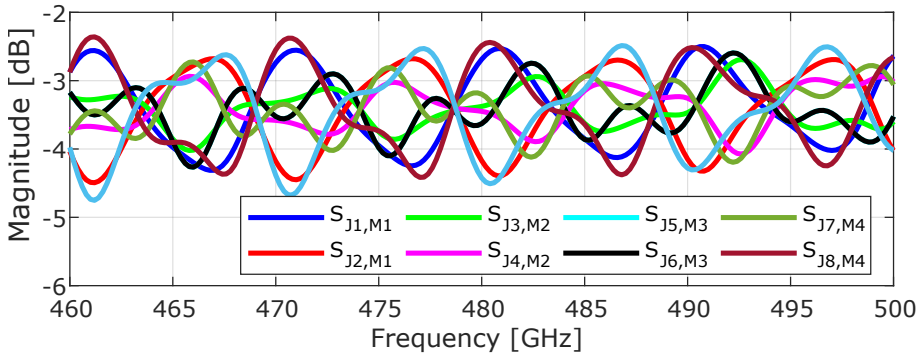

Figure 5.52: Transmission from M-port to junctions in a 4-pixel block with 3 90° branch line power dividers. Here is a zoom into the $460 - 500$ GHz band for the transmission from the M-port towards the respective junctions.

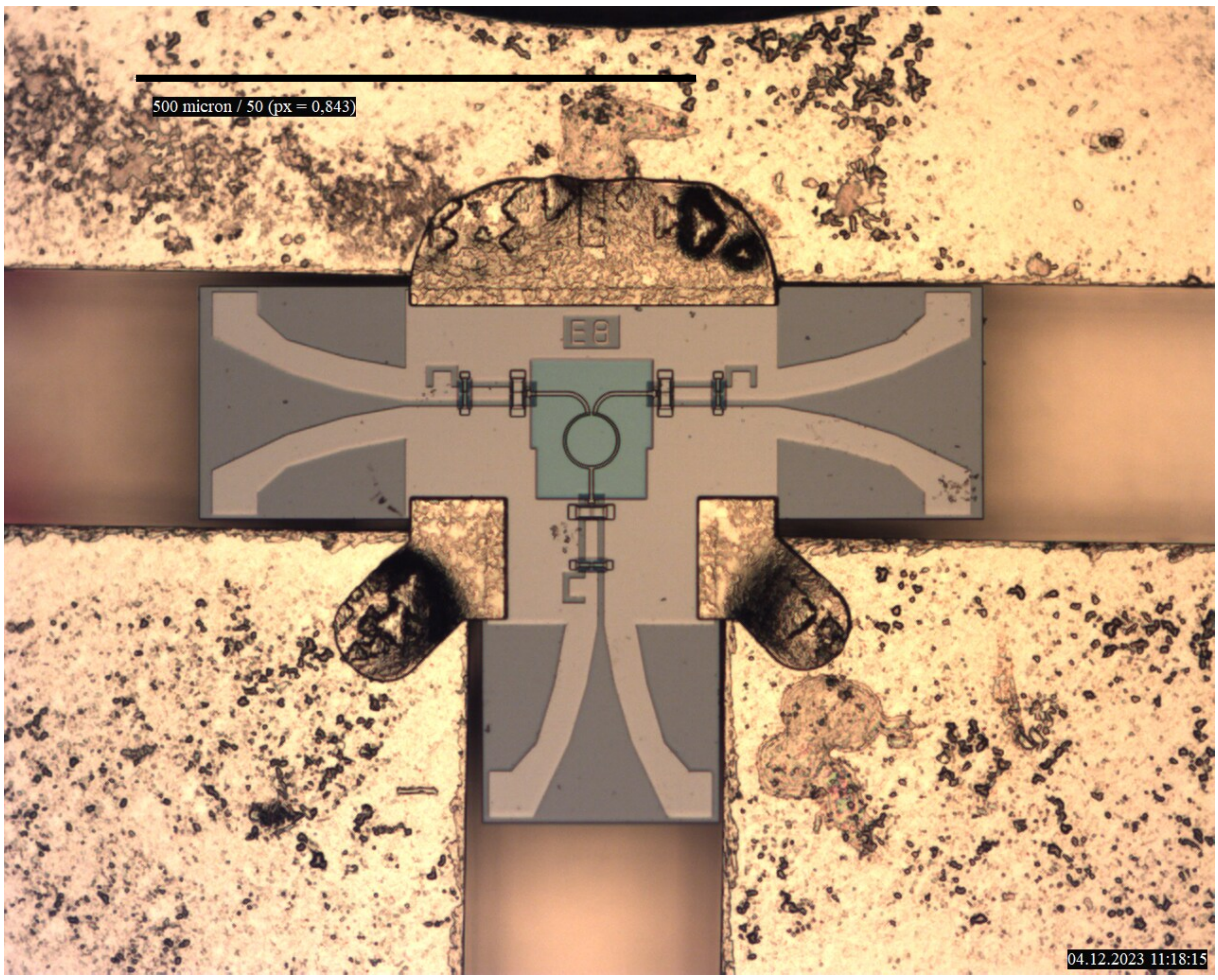

Figure 5.53: Photograph of the fabricated Wilkinson power divider suspended in its waveguide cavity in block 11.110.05.

same IBAMI chip (pairs J_1/J_2 and J_3/J_4). The simulation of the 2-pixel block with the fabricated Wilkinson power divider is done in the schematic simulator with a reduced cavity IBAMI chip. The IBAMI model also has the waveguide step included. The results are shown in Fig.5.55. The effect of the higher reflections at the wilkinson output ports is seen in the standing wave pattern observed in the transmission to the junctions ports(**Left top**). However, due to the Wilkinson is 0° power divider, the standing waves are in phase. This is observed in the relative transmission towards junction J_1 to J_3 (**Left bottom**), where both junctions have the same relative transmission. Analyzing the transmission from the M1/M2 ports (**Right top**), the junctions in the same IBAMI chip display the off-phase behaviour that is clear in the relative response (**Right bottom**). Overall, the simulated results are in line with what is expected for a 2-pixel configuration with an in-phase power divider and a balanced mixer based on a 90° branch line hybrid. Which are the balanced response of mirrored junctions (pairs J_1/J_3 and J_1/J_4) for H-port sweeps and the standing wave pattern in the M1/M2-port sweeps for junctions in the same mixer (pairs J_1/J_2 and J_3/J_4).

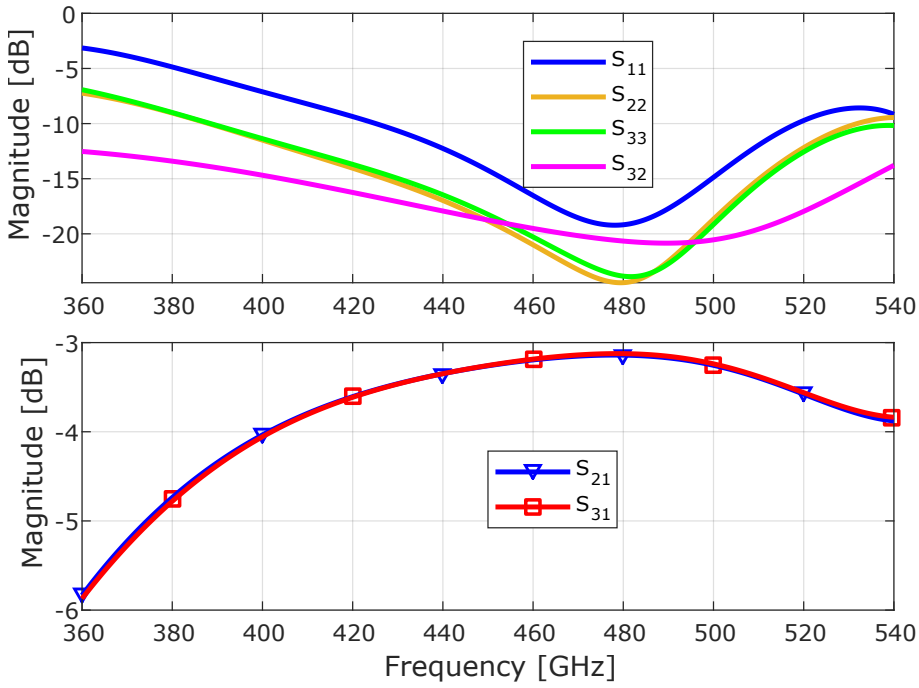

Figure 5.54: S-parameters of the microstrip Wilkinson prototype. **Top:** Reflections at the output ports of the model (S_{ii}) plus transmission between output ports(S_{32}). **Bottom:** Transmission from the input port towards the output ports.

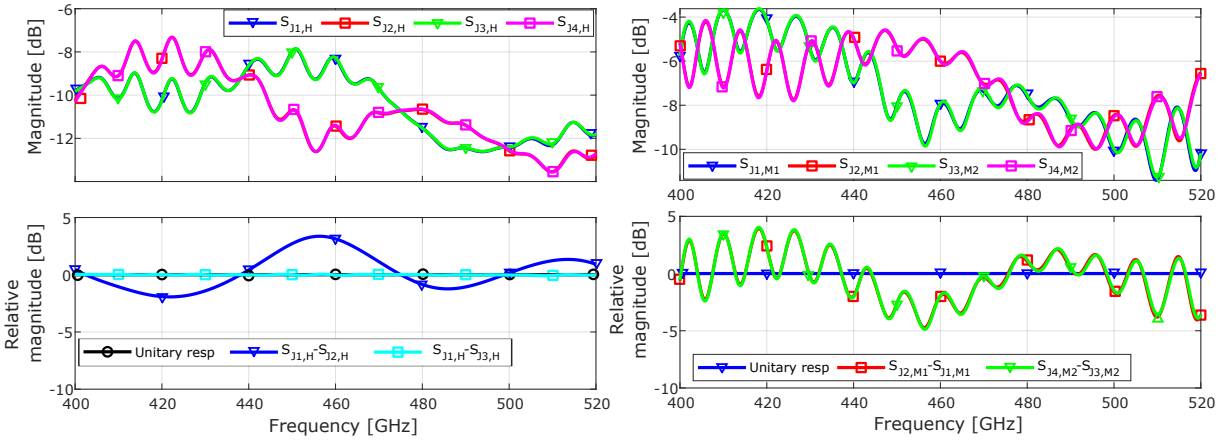

Figure 5.55: Simulated s-parameters of the fabricated Wilkinson power divider the 2-pixel block. The IBAMI model used is a reduced cavity IBAMI with a step discontinuity in the waveguide (Shown in Sec 3.2.8 of [Westig, 2013], sections 3.2.4 and 3.2.8). **Left top:** Transmission from the Input H-port towards the junction ports. **Left bottom:** Relative transmission towards junctions J_1 with respect to junctions J_2 and J_3. **Right top:** Transmissions from the M1/M2 ports towards the corresponding junctions. **Right bottom:** relative transmission to junctions in the same IBAMI.

The results are shown in Fig.5.56 and Fig.5.57. **Left top:** shows the recorded induced current in the SIS junctions, it can be seen that the induced current in all junctions follows the previously observed trend that they decrease towards the high end of the band. The wave pattern caused by the available LO power from the VDI LO is also present. In the $400-450$ GHz range, it can be seen that all four junctions display a different level of induced current. From 450 GHz on, the induced current levels of junctions J_2, J_3 and J_4, display a similar level of induced current and J_1 has an overall lower level. Checking the relative response of junctions in the same IBAMI chip in the **Left bottom** graph shows that the response of the two mixers has an offset with the IBAMI at M2 (pair J_3/J_4) having the more balanced response than the IBAMI chip at M1 (pair J_1/J_2). Moving on to the sweeps from the M1/M2 ports **Right top** it can be seen that the induced currents in junctions of the same IBAMI chip are in off-phase. This is caused by the 90° coupler in the IBAMI, compliant with what is expected (Fig.5.55). it is observed that the mirrored junction pair $J_2/\ J_4$ exhibits almost the same values across the band. This is in contrast to the behaviour of the other mirrored pair $J_1/\ J_3$, where the induced current of both junctions follows the same overall behaviour but there seems to be a constant offset between them. The relative response between the junctions of the same IBAMI for M-port sweeps(**Right bottom**) shows the considerable standing wave pattern with a maximum amplitude of ~ 5 dB. There is a clear minimum in the wave pattern between $450-460$ GHz. Keeping in mind that the amplitude of the standing waves depends on the reflections at the waveguide ports of the power divider and the IBAMI chip, this fact suggests that the reflections between the components are at their minimum.

The relative response two H-port sweeps is plotted in Fig. 5.57. The sweep "H feed 1" refers to the initial sweep (shown in Fig.5.56) where each junction is recorded by its respective bias box. "H feed 2" refers to a LO sweep where J_3 is recorded with bias box 1. It can been seen how the relative response of pair J_1/J_3 differs between the two H port sweeps, especially in the higher end of the band, where the relative response in sweep "H feed 1" falls to ~ -1.9 dB, while the "H sweep 2" the response has its lower value of -1 dB in the $460-500$ GHz. It is observed that the relative response of pair J_1/J_3 for sweep 2 agrees with sweep 1 in the lower end of the band and to the relative response of J_2/J_4 at the high end. The relative response of pair J_2/J_4 is very balanced and close to the unitary response within the LFA band with a maximum difference of 0.5 dB at 500 GHz. This agrees with the simulated relative response of mirrored junctions (Fig. 5.55 **Left bottom** pair). The reason behind the different relative response for mirrored junctions J_1/J_3

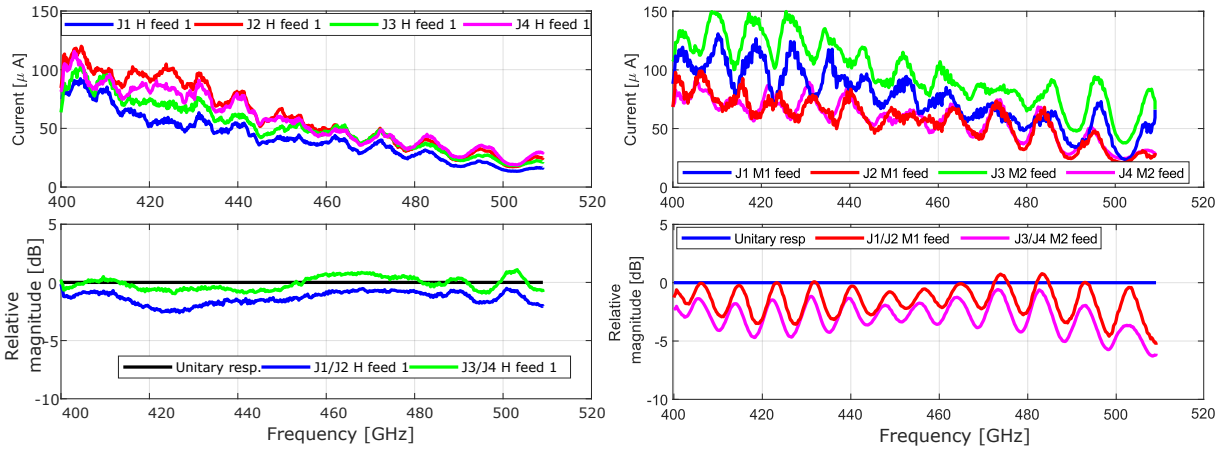

Figure 5.56: LO sweeps in Block 11.110.05 with a microstrip Wilkinson power divider. LO sweeps number 1 through the H-port. **Left top:** Induced current in all junctions. **Left bottom:** The relative response between junctions of the same IBAMI chips. **Right:** LO sweeps through the M-ports. **Right top:** Induced current in all junctions. **Right bottom:** Relative response between junctions in the same IBAMI chip.

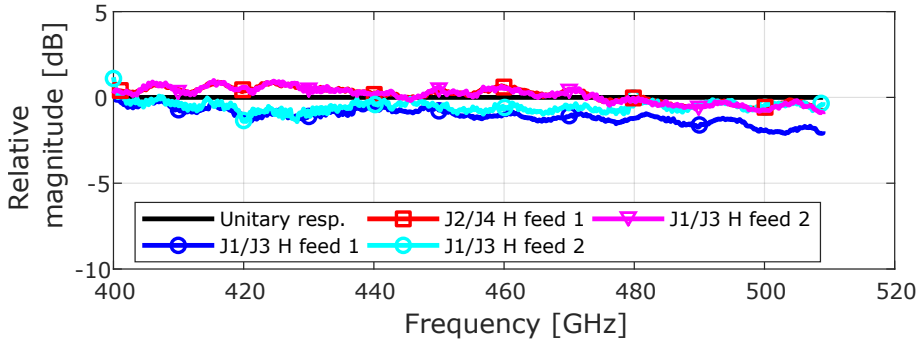

Figure 5.57: Relative transmission for mirrored junctions in block .05 with a Wilkinson power divider. The "H feed 1" and "H feed 2" correspond to two different sweeps. The difference in induced current between J_1 and J_3 measured in sweep "H feed 1" sweep prompted the recording of another sweep (sweep "H feed 2") where J_1 and J_3 are both recorded with Bias box 1.

and J_2/J_4 from the H-port sweep is not exactly known at this point. The experimental results obtained do not allow to discriminate which junctions, either J_1 or J_3, is the one that has a problem

The last point to address is the fact that no range of low induced current nor broken step I-V curves have been detected so far with the Wilkinson power divider. This supports the hypothesis that the properties of the SIS junctions depend on the network they are embedded in. Since the differences between the LO distribution network in blocks 11.110.03 and 11.110.05 are the power divider and the footprint of the beamlead pockets in the IBAMI cavity, it is not possible to pinpoint the cause behind the broken step I-V or the range of low induced current. So far, it seems that the modifications to the beamlead footprint and the Wilkinson power divider prevent the appearance of the range of low induced current and the broken step I-V.

Chapter 6

Conclusions and outlook

6.1 Conclusions

In the framework of this thesis, two power dividers based on superconducting planar technology have been designed, fabricated and partially characterized for the LFA band of the CHAI receiver. Given the required operational temperature of the power divider, SIS junctions are the only feasible detectors within the capabilities at hand that could be used to characterise the power dividers. Considering the availability of the previously developed Integrated Balanced Mixer (IBAMI) chips, it is decided to use the SIS junctions in it as direct power detectors. The power dividers are to be tested in a 2-pixel block, with two IBAMI mixers. This platform has the advantage that it represents half of the 4-pixel block unit, later intended as a building block for the 64-pixel CHAI focal plane array. Before the testing of the power divider in the 2-pixel block, the transmission to the junctions in the IBAMI is measured. First by FTS measurements and secondly by an LO sweep. From these experiments, a reference measurement is obtained to be used in the experiment in the 2-pixel block. At this stage, no problems were detected in the properties of the IBAMI in its test block.

The properties of the SIS in the 2-pixel block proved to be more complex than initially expected. The reason is that their I-V characteristic in the presence of an RF field depends on the network the junctions are embedded in. Essentially, this meant that the power detector properties depended on the components to characterise. These properties complicate the interpretation of the measurements since it is undesired that the properties of the power sensor depend on the device to measure. Clear examples of that are the broken step I-V curves and the range of low induced current detected in the H-port sweeps in block 11.110.03. It was only after testing devices in block 11.110.02 that it was discovered that there was an additional interaction be-

tween the branch line power divider and the IBAMI chip via the beam lead pockets in block 11.110.03. This is a problematic topic since these features may appear in more complex networks, such as the 4-pixel block. The one fairly simple and direct solution of simply removing the beamlead pockets from the IBAMI chip cavity is quickly discarded as the IBAMI chips in block 11.110.02 showed symptoms of mechanical damage after 5 open/close cycles.

Since the experiment could not yield more information about the results obtained in block.03, It attempted to gain insight by comparing measurements and simulations of the 2-pixel block. The IBAMI chip had three models simulated, an IBAMI model with a reduced cavity and the IBAMI chips in the cavities corresponding to blocks .02 and .03. The results of these simulations are compared to the IBAMI reference measured in the IBAMI test block. No simulation was able to reproduce the measured results obtained in the IBAMI test block. It is suspected that the simplification of the SIS junctions to a constant impedance in the IBAMI chip results in the disagreement between the experimental results and simulations. Future work has to consider the variable impedance of the SIS junctions in the simulation, where the RF impedance of the junction depends on the level of the coupled power, to get 3D models that comply with the measured results. This would be of considerable assistance at the moment of debugging and finding the source of problems in more complex components. Even more perplexing at this stage, was that the simulated IBAMI in block .03 did show a resonant behaviour, this simulation was performed only considering the IBAMI chip. The only evidence that could be used to point to some resonant behaviour in the IBAMI cavity were the broken step I-V curves and the range of low induced current.

The testing of the branch line power dividers was limited to the transmission towards the SIS junctions of the two IBAMI chips in the 2-pixel block. The 2-pixel block was not a platform designed to fully characterise a power divider but to yield as much information about the smallest network of the complete 64-pixel array. In this aspect, testing with the 2-pixel block proved to be very useful as the detection of the broken step I-V and the range of low induced current was detected in an earlier stage of development and not later stages where the network would be considerably more complex, like in the 4-pixel block. In the 2-pixel block platform, three out of the four branch line power divider models were tested, these are power dividers H2L, H2S, H3N and at a later stage, the prototype of the Wilkinson in-phase power divider. The power division characteristics were evaluated by studying the relative response of equivalent/mirrored junctions in the two IBAMI chips.

The relative response for three branch line power dividers exhibits a wave pattern across frequency, caused by the standing waves present between the power divider and the IBAMI chips. The fact that for almost every model tested, the period of the standing waves, determined by the long waveguide between IBAMI chips and power divider, matched between simulation and results supports that hypothesis. The simulated model H2S had the standing waves with the largest amplitude for all simulated models. Fabricated power divider H2S-1, tested in block .02 had the largest standing wave's amplitude observed. This agrees with the fact that a short circuit termination would generate the highest reflections at the output ports of the power divider. In light of this fact and the amplitude of the standing waves observed with power divider models H3N and H2L, the idea is that the proposed on-chip TiN loads do work to some extent. However, due to the limitation of not having a reference measurement of the input power to the 2-pixel block and the little agreement with the simulation, the measurements do not allow for a calculation of the exact value of the TiN termination's reflections.

The final experiment that was performed was the crosstalk between IBAMI mixers. An RF continuous wave (CW) signal (generated by a Gunn LO) is injected into one of the M-port and it is detected by the mixers that are activated by the VDI LO. This test is only performed for two frequencies of the RF signal $f^1_{gunn} = 462$ and $f^2_{gunn} = 491$ with the VDI LO sweeping the upper and lower sidebands (USB and LSB respectively). The branch line power dividers tested in this configuration were H2S-1 and H2N-15. The results for both power dividers had similar results for both the LSB and USB for $f^1_{gunn} = 461$ GHz. In the case of $f^2_{gunn} = 492$ GHz, the power divider H2S-1 has a lower crosstalk than model H2N-15 for both the USB and LSB. this means that even for a power divider with a terrible termination the crosstalk is, on average, < -15 dB for $f^1_{gunn} = 461$ and < -20 dB $f^2_{gunn} = 492$.

From the simulation of the 2-pixel block, it was understood that the wave pattern observed in the relative transmission towards the junctions was caused by the standing waves present in the LO path. The effect of this standing wave was that the relative transmission to the junctions was not balanced. This is undesired since in an array scenario means that not every mixer will receive the same amount of power leading to different pixel performances in the array. The first approach is to reduce the reflection at the waveguide interfaces of the components composing the network. Given that the SIS junctions are not operated in the regime that generates the lowest reflections that only leaves the power divider for optimization. Nevertheless, it is possible to reduce the effect of the standing waves in the mixer by having a

180° coupler instead of a 90°, since the phase difference introduced by the coupler cancels the effect of the standing waves in the transmission towards the junctions. A bit more liberty is available at the side of the power divider, the current branch line models could be optimized for the reduction of the reflections at its waveguide interfaces. This process would entail the optimization of every connection between the components, eg. the interface 90° branch line hybrid and the CPW S-bend. This process would be arduous and it is not a guarantee that the final models achieved the desired reflection level. The other option is having a power divider that does not have a phase difference between its outputs. This does not eliminate the standing waves in the network but it reduces its effect since now the transmissions are in-phase and have the same behaviour in frequency. This is proven with a schematic of a 2-pixel block with a Wilkinson power divider that has reflections that are equivalent to the ones simulated from the branch line power dividers, but for the Wilkinson power divider, the relative transmission to the junctions is balanced in the band. This means that if equal transmission between the input ports (H- and M-ports) and the mixers is desired, the ideal choice of components for an array receiver is in-phase power dividers and balanced mixers based on 180° hybrids since this configuration minimizes the effect of the standing waves present in the LO path. On the other hand the current configuration in the 2-pixel block, 90° power dividers and balanced mixers based on 90° hybrids is the configuration that maximizes the effect of the standing waves in the transmission towards the junctions.

6.2 Future work

During the development of this thesis, some topics were not explored due to the lack of time and/or resources. They pertain to the two main points that were not presented in this thesis. The first is the inclusion of the high frequency behaviour of the SIS junctions in the 3D simulation of the Mixers. It could be that this will yield more accurate simulations that will help with the debugging and analysis of experimental results. Continuing with the SIS junctions, the exact cause of the broken step I-V and the range of low induced current requires more investigation. It was possible to avoid their manifestation in block 11.110.05 by changing the beamlead pockets footprint. Nevertheless, they could appear again with a different power divider or with a change in the network. This is particularly the case for more complex LO distribution networks, like in the 4-pixel block.

The second point concerns the development of balanced mixers based on 180° couplers. From the schematic analysis of the 2-pixel network, it was

concluded that a 180° reduces the effect that the standing waves present in the LO path have on the mixers. This comes with the problem that 180° hybrids are hard to implement. An example of this is the CPW hybrids presented in sections 3.4.1 3.4.2, where the overall parameters of the 90° hybrid are better than for the 180° one. It should also be considered that the latter dimensions are smaller than the former and will require higher precision in the manufacturing process. Alternatives to solve or bypass the limitations of the 180° should be looked into to ensure the feasibility of the manufacturing process.

Appendix A

Additional results

In this section additional simulations results that did not fit in the main text are presented. The results are from an unsuccessful $1-4$ power divider in a single chip, plus an alternative design for the HFA 90° balanced mixer tuned to a higher frequency than the model presented in section 3.

A.1 Complete one to four division in one chip for the LFA

The complete power division in one chip was attempted and it is subject to the constraints as the individual power divider. This meant that a special geometry had to be taken so the distance between output waveguides would eb maximizes while trying to keep the footprint as small as possible. The designed $1-4$ power divider is shown in Fig.A.1. Its suffered from cavity resonances, shown in Fig.A.2, with its S-parameters shown in Fig.A.3 . This approach to the power division was discarded since it was not clear at that point if after the removal of the cavity resonances, the performance would be adequate for the 4−pixel block.

A.2 Additional HFA components

For the additional HFA components, a second 90° balanced mixer is presented, here the waveguide transition is based on a slotline antenna with a radial stub instead of a crooked balun. This model is an alternative to the model presented in section 3 in the case a higher operational frequency is desired

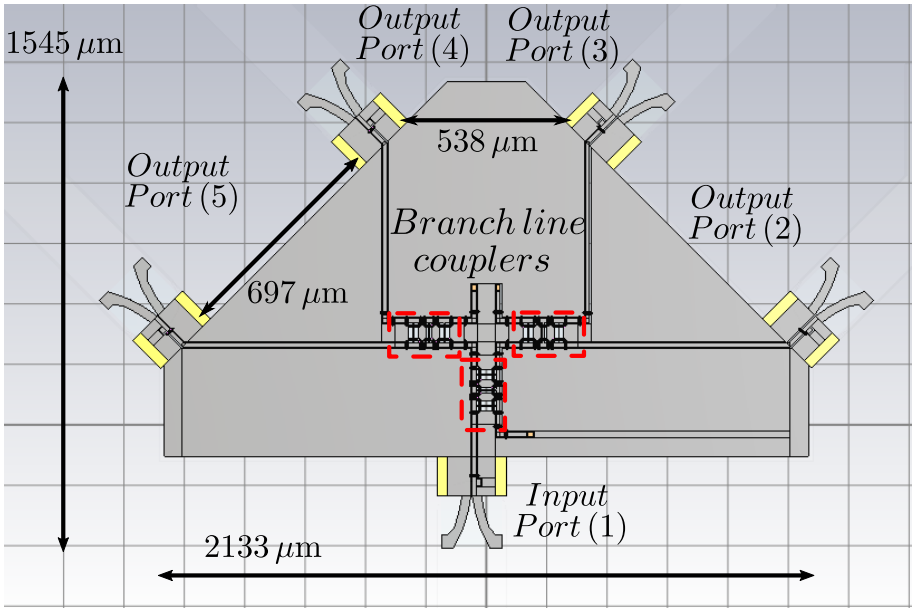

Figure A.1: An integrated single membrane 4-way power divider. This model attemped to eliminate the need of waveguide between the CPW branch line couplers and have the complete 4-way division in one chip. the size of the chip can be explained due the need to have a minimum distance between waveguide of 700 μm.

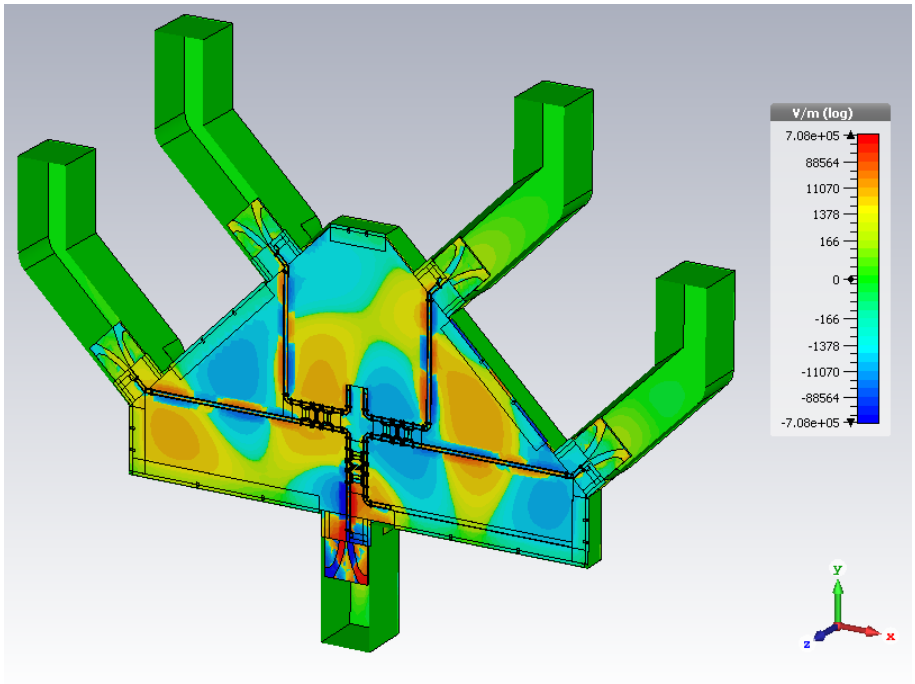

Figure A.2: Shown cavity resonances in the integrated single membrane 4-way power divider. The required distance between the output waveguide is met by increasing the CPw line between the components. This traduces into a larger cavity that suffers from coupling between the odd mode of the CPW and the cavity over it.

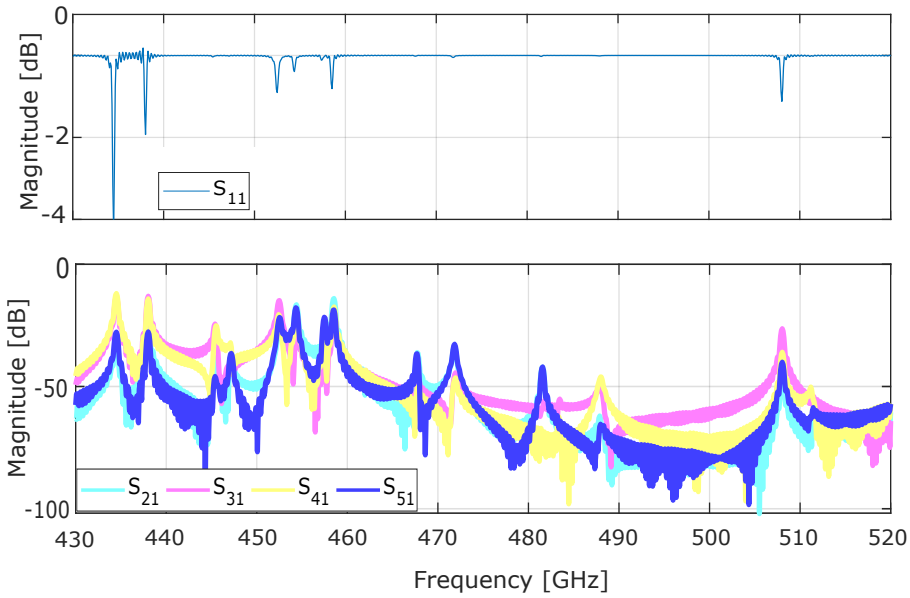

Figure A.3: S-parameters of the the integrated single membrane 4-way power divider.There is an almost complete reflections at the input port and practically no transmission.

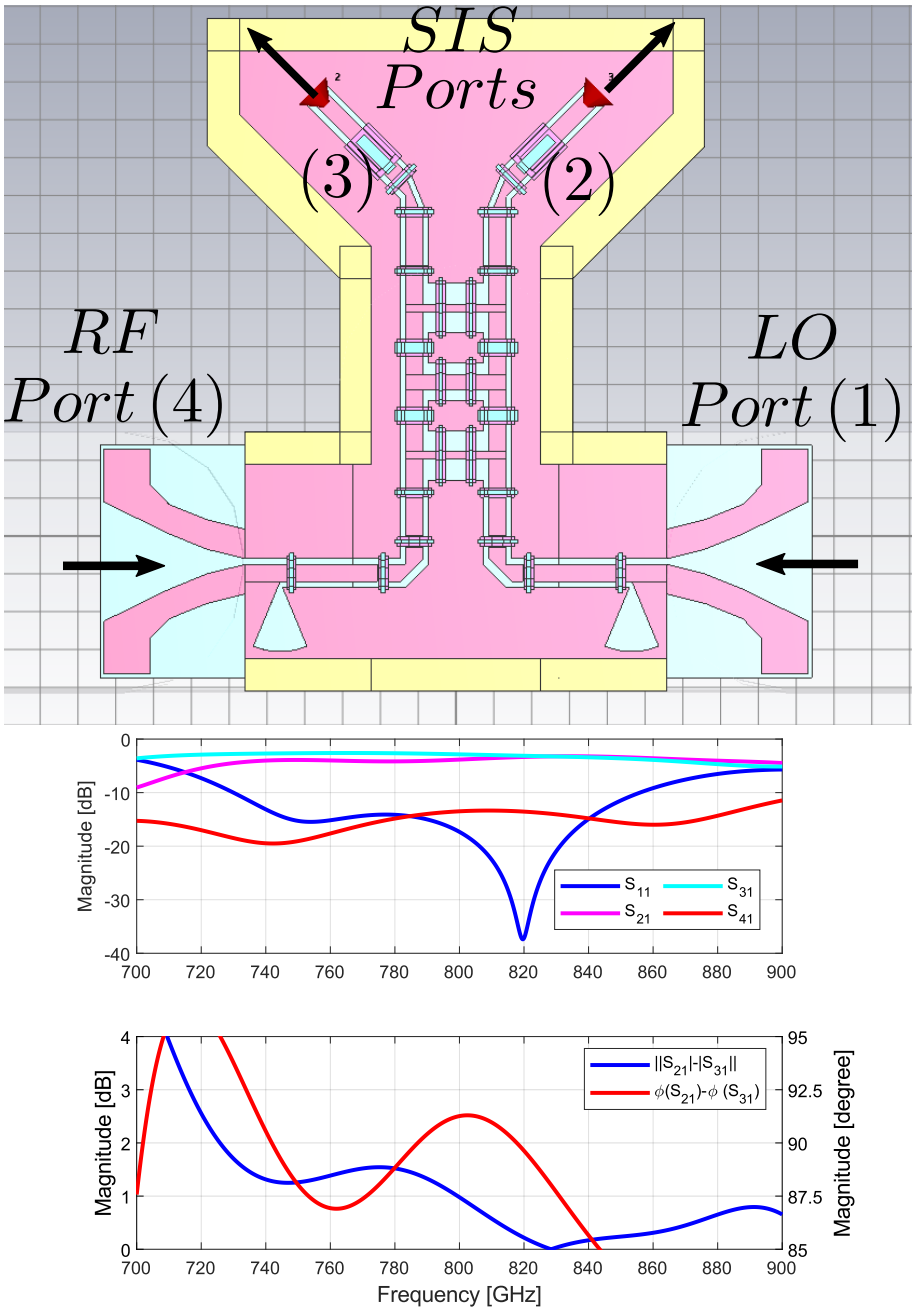

Figure A.4: Alternative branch line coupler. **Top:** CST model of the integrated branch line coupler.**Middle:**S-parameters. **Bottom:** Amplitude and phase imbalance of the branch line coupler. It can be see how the reflection, the amplitude and phase imbalance are centered $\sim$ 820 GHz.

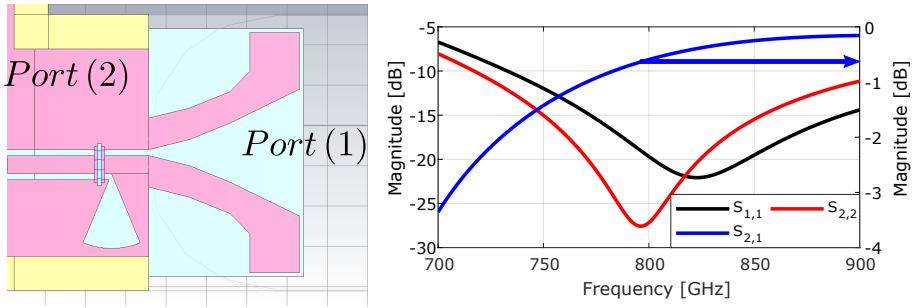

Figure A.5: Waveguide-CPW transition with a radial balun. **Left:** CST model. **Rigth:** S-parameters.

Bibliography

[Acharya et al., 1993] Acharya, P., Ekstrom, H., Gearhart, S., Jacobsson, S., Johansson, J., Kollberg, E., and Rebeiz, G. (1993). Tapered slotline antennas at 802 ghz. *IEEE Transactions on Microwave Theory and Techniques*, 41(10):1715–1719.

[ALMA,] ALMA. Introduction to radio astronomy. `http://www.almaobservatory.org/en/about-alma/how-does-alma-work/technology/antennas`. Accessed: December 8th, 2016.

[Ambegaokar and Baratoff, 1963] Ambegaokar, V. and Baratoff, A. (1963). Tunneling between superconductors. *Phys. Rev. Lett.*, 11:104–104.

[Annett, 2004] Annett, J. (2004). *Superconductivity, superfluids and condensates*. Oxford master series in condensed matter physics. Oxford Univ. Press, Oxford.

[Ashcroft and Mermin, 1976] Ashcroft, N. W. and Mermin, N. D. (1976). *Solid State Physics*. Holt-Saunders.

[Bahl et al., 2013] Bahl, I., Bozzi, M., and Garg, R. (2013). *Microstrip Lines and Slotlines*. 3rd edition.

[Bardeen et al., 1957] Bardeen, J., Cooper, L. N., and Schrieffer, J. R. (1957). Theory of superconductivity. *Phys. Rev.*, 108:1175–1204.

[Bardeen and Pines, 1955] Bardeen, J. and Pines, D. (1955). Electron-phonon interaction in metals. *Phys. Rev.*, 99:1140–1150.

[Barends, 2009] Barends, R. (2009). Photon-detecting superconduicting resonators.

[Barnard, 1899] Barnard, E. E. (1899). Photographs of comets and of the the milky way. *Monthly Notices of the Royal Astronomical Society*, 59(6):354–358.

[Becklin, 2005] Becklin, E. E. (2005). Overview of the sofia science program. In *American Astronomical Society Meeting Abstracts*, volume 207 of *American Astronomical Society Meeting Abstracts*, page 159.02.

[Belitsky et al., 1995] Belitsky, V. Y., Jacobsson, S. W., Filippenko, L. V., and Kollberg, E. L. (1995). Broadband twin-junction tuning circuit for submillimeter sis mixers. *Microwave and Optical Technology Letters*, 10(2):74–78.

[Blackman,] Blackman, E. Half absorption altitutde. `https://www.pas.rochester.edu/~blackman/ast104/windows.htmll`. Accessed: March 7th, 2022.

[Bowen, 1927] Bowen, I. (1927). The origin of the nebulium spectrum. *Nature*, 120(3022):473.

[Braham, 1961] Braham, P. (1961). *Electron. Eng.*, 33:42.

[Broom and Wolf, 1977] Broom, R. F. and Wolf, P. (1977). Q factor and resonance amplitude of josephson tunnel junctions. *Phys. Rev. B*, 16:3100–3107.

[Buckle et al., 2009] Buckle, J. V., Hills, R. E., Smith, H., Dent, W. R. F., Bell, G., Curtis, E. I., Dace, R., Gibson, H., Graves, S. F., Leech, J., Richer, J. S., Williamson, R., Withington, S., Yassin, G., Bennett, R., Hastings, P., Laidlaw., I., Lightfoot, J. F., Burgess, T., Dewdney, P. E., Hovey, G., Willis, A. G., Redman, R., Wooff, B., Berry, D. S., Cavanagh, B., Davis, G. R., Dempsey, J., Friberg, P., Jenness, T., Kackley, R., Rees, N. P., Tilanus, R., Walther, C., Zwart, W., Klapwijk, T. M., Kroug, M., and Zijlstra, T. (2009). Harp/acsis: a submillimetre spectral imaging system on the james clerk maxwell telescope. *Monthly Notices of the Royal Astronomical Society*, 399(2):1026–1043.

[Bustos et al., 2014] Bustos, R., Rubio, M., Otárola, A., and Nagar, N. (2014). Parque astronómico de atacama: An ideal site for millimeter, submillimeter, and mid-infrared astronomy. *Publications of the Astronomical Society of the Pacific*, 126(946):1126–1132.

[Carruthers, 1970] Carruthers, G. R. (1970). Rocket Observation of Interstellar Molecular Hydrogen. *Astrophysical Journall*, 161:L81.

[CCAT-prime, a] CCAT-prime. `http://www.xoptx.com/cornell-caltech-atacama.php`. Accessed: December 15th, 2016.

[CCAT-prime, b] CCAT-prime. CCAT pathfinder kSZ science case: Probing the transition between gravity and dark energy dominated regimes. http://www.ccatobservatory.org/docs/ccat-technical-memos/CCAT-p.kSZ_whitepaper.pdf. Accessed: Juny 20th, 2022.

[CCAT-prime, c] CCAT-prime. Initial Instrumentation Plan for CCAT-Prime. http://www.ccatobservatory.org/docs/ccat-technical-memos/CCAT-p.instruments.160707.pdf. Accessed: December 10th, 2016.

[Chang, 1979] Chang, W. H. (1979). The inductance of a superconducting strip transmission line. *Journal of Applied Physics*, 50(12):8129–8134.

[Collin, 2007] Collin, R. (2007). *FOUNDATIONS FOR MICROWAVE ENGINEERING, 2ND ED.* McGraw-Hill series in electrical engineering: Radar and antennas. Wiley.

[Consortium,] Consortium, C. http://www.ccatobservatory.org/index.cfm/page/about-ccat.html. Accessed: July 4th, 2022.

[consortium,] consortium, C. CCAT consortium:science case for GEco. http://www.ccatobservatory.org/docs/ccat-technical-memos/CCA. Accessed: December 13th, 2016.

[Cooper, 1956] Cooper, L. N. (1956). Bound electron pairs in a degenerate fermi gas. *Phys. Rev.*, 104:1189–1190.

[Cuong et al., 2007] Cuong, N. D., Yoon, S.-G., Kim, D.-J., and Kang, B.-D. (2007). Tin thin film resistors for 20 db pi-type attenuator applications. *Applied Physics Letters*, 90(18):183506.

[de Gennes, 1966] de Gennes, P. (1966). *Superconductivity of Metals and Alloys*. Advanced book classics. W.A. Benjamin.

[de Graauw, Th. et al.,] de Graauw, Th., Helmich, F. P., Phillips, T. G., Stutzki, J., Caux, E., Whyborn, N. D., Dieleman, P., Roelfsema, P. R., Aarts, H., Assendorp, R., Bachiller, R., Baechtold, W., Barcia, A., Beintema, D. A., Belitsky, V., Benz, A. O., Bieber, R., Boogert, A., Borys, C., Bumble, B., Caïs, P., Caris, M., Cerulli-Irelli, P., Chattopadhyay, G., Cherednichenko, S., Ciechanowicz, M., Coeur-Joly, O., Comito, C., Cros, A., de Jonge, A., de Lange, G., Delforges, B., Delorme, Y., den Boggende, T., Desbat, J.-M., Diez-González, C., Di Giorgio, A. M., Dubbeldam, L., Edwards, K., Eggens, M., Erickson, N., Evers, J., Fich, M., Finn, T., Franke, B., Gaier, T., Gal, C., Gao, J. R., Gallego, J.-D., Gauffre, S.,

Gill, J. J., Glenz, S., Golstein, H., Goulooze, H., Gunsing, T., Güsten, R., Hartogh, P., Hatch, W. A., Higgins, R., Honingh, E. C., Huisman, R., Jackson, B. D., Jacobs, H., Jacobs, K., Jarchow, C., Javadi, H., Jellema, W., Justen, M., Karpov, A., Kasemann, C., Kawamura, J., Keizer, G., Kester, D., Klapwijk, T. M., Klein, Th., Kollberg, E., Kooi, J., Kooiman, P.-P., Kopf, B., Krause, M., Krieg, J.-M., Kramer, C., Kruizenga, B., Kuhn, T., Laauwen, W., Lai, R., Larsson, B., Leduc, H. G., Leinz, C., Lin, R. H., Liseau, R., Liu, G. S., Loose, A., López-Fernandez, I., Lord, S., Luinge, W., Marston, A., Martín-Pintado, J., Maestrini, A., Maiwald, F. W., McCoey, C., Mehdi, I., Megej, A., Melchior, M., Meinsma, L., Merkel, H., Michalska, M., Monstein, C., Moratschke, D., Morris, P., Muller, H., Murphy, J. A., Naber, A., Natale, E., Nowosielski, W., Nuzzolo, F., Olberg, M., Olbrich, M., Orfei, R., Orleanski, P., Ossenkopf, V., Peacock, T., Pearson, J. C., Peron, I., Phillip-May, S., Piazzo, L., Planesas, P., Rataj, M., Ravera, L., Risacher, C., Salez, M., Samoska, L. A., Saraceno, P., Schieder, R., Schlecht, E., Schlöder, F., Schmülling, F., Schultz, M., Schuster, K., Siebertz, O., Smit, H., Szczerba, R., Shipman, R., Steinmetz, E., Stern, J. A., Stokroos, M., Teipen, R., Teyssier, D., Tils, T., Trappe, N., van Baaren, C., van Leeuwen, B.-J., van de Stadt, H., Visser, H., Wildeman, K. J., Wafelbakker, C. K., Ward, J. S., Wesselius, P., Wild, W., Wulff, S., Wunsch, H.-J., Tielens, X., Zaal, P., Zirath, H., Zmuidzinas, J., and Zwart, F. The herschel-heterodyne instrument for the far-infrared (hifi).

[Dicke, 1946] Dicke, R. H. (1946). The measurement of thermal radiation at microwave frequencies. *Review of Scientific Instruments*, 17(7):268–275.

[Drude, 1900a] Drude, P. (1900a). Zur elektronentheorie der metalle. *Annalen der Physik*, 306(3):566–613.

[Drude, 1900b] Drude, P. (1900b). Zur elektronentheorie der metalle; ii. teil. galvanomagnetische und thermomagnetische effecte. *Annalen der Physik*, 308(11):369–402.

[Einstein, 1916] Einstein, A. (1916). Strahlungs-emission und absorption nach der quantentheorie. *Deutsche Physikalische Gesellschaft*, 18:318–323.

[Erickson, 2017] Erickson, E. F. (2017). Nasa's kuiper airborne observatory 1974-1995 - twenty one years of discovery. In *American Astronomical Society Meeting Abstracts #229*, volume 229 of *American Astronomical Society Meeting Abstracts*, page 111.02.

[Ermakov et al., 2016] Ermakov, A. B., Belitsky, V., Aghdam, P. Y., Desmaris, V., Ferm, S.-E., Fredrixon, M., Krause, S., Lapkin, I., Meledin, D.,

Pavolotsky, A. B., Rashid, H., Shafiee, S., Strandberg, M., Sundin, E., Saini, K. S., and Bryerton, E. W. (2016). Broken-step phenomenon in sis mixers.

[ESO, 2022] ESO (2022). Alma receiver bands. `https://www.eso.org/public/teles-instr/alma/receiver-bands/`. Accessed: April 14th, 2022.

[Ewen and Purcell, 1951] Ewen, H. I. and Purcell, E. M. (1951). Observation of a Line in the Galactic Radio Spectrum: Radiation from Galactic Hydrogen at 1,420 Mc./sec. *Nature*, 168(4270):356.

[Fan et al., 1995] Fan, L., Kanamalura, S., and Chang, K. (1995). A new wide-band and reduced-size uniplanar magic-t. In *Proceedings of 1995 IEEE MTT-S International Microwave Symposium*, pages 667–670 vol.2.

[Fathi, 2018] Fathi, S. (2018). *Development of Integrated Superconducting Balanced Mixers for THz Focal Plane Arrays*. PhD thesis, Universität zu Köln.

[Field et al., 1969] Field, G. B., Goldsmith, D. W., and Habing, H. J. (1969). Cosmic-Ray Heating of the Interstellar Gas. *Astrophysical Journal*, 155:L149.

[Fontana et al., 2012] Fontana, A. L., Boucher, C., Serres, P., Bortolotti, Y., Cope, F.and Stil, I., Lefranc, B., Garnier, O., Butin, G., Mattiocco, F., Navarro, S., John, D., Navarrini, A., and Schuster, K. F. (2012). A 3mm multipixel SIS receiver for IRAM 30-m Pico Veleta Telescope. In *Proceedings SPIE*, volume 8452, pages 84522E–84522E–11.

[Fontana et al., 2010] Fontana, A. L., Lazareff, B., Navarrini, A., and Bortolotti, Y. (2010). Heterodyne Array Receiver for Radio Astronomy in the 2mm Band. In *Proceedings of the 40th European Microwave Conference (EuMC)*, pages 906–909.

[Fröhlich, 1950] Fröhlich, H. (1950). Theory of the superconducting state. i. the ground state at the absolute zero of temperature. *Phys. Rev.*, 79:845–856.

[F.S., 1984] F.S., H. (1984). *Troposphere - Concise Encyclopedia of Science & Technology*. McGraw-Hill, New York.

[Gao, 2008] Gao, J. (2008). The physics of superconducting microwave resonators.

[Ghigo, 2023] Ghigo, F. (2023). Pre-history of radio astronomy. https://web.archive.org/web/20200615213814/http://www.nrao.edu/whatisra/hist_prehist.shtml.

[Gorter and Casimir, 1934] Gorter, C. and Casimir, H. (1934). Two fluid model. *Z. Phys*, 35:963.

[Graf and Heyminck, 2001] Graf, U. and Heyminck, S. (2001). Fourier gratings as submillimeter beam splitters. *IEEE Transactions on Antennas and Propagation*, 49(4):542–546.

[Graf et al., 2002] Graf, U., Heyminck, S., Michael, E., Stanko, S., Honingh, C., Jacobs, K., Schieder, R., and Stutzki, J. (2002). SMART: The KOSMA Sub-Millimeter Array Receiver for Two frequencies. In *Proceedings of the 13th International Symposium on Space Terahertz Technology*, Cambridge, Massachusetts.

[Groppi et al., 2003] Groppi, C., Walker, C., Kulesa, C., Golish, D., Hedden, A., Gensheimer, P., Narayanan, G., Lichtenberger, A., Graf, U., and Heyminck, S. (2003). DesertSTAR: a 7 pixel 345 GHz heterodyne array receiver for the Heinrich Hertz Telescope. In *Proceedings SPIE*, volume 4855, pages 330–337.

[Groppi et al., 2009] Groppi, C., Walker, C., Kulesa, C., Golish, D., Kloosterman, J., Weinreb, S., Jones, G., Barden, J., Mani, H., Kuiper, T., Kooi, J., Lichtenberg, A., Cecil, T., Narayanan, G., Pütz, P., and Hedden, A. (2009). SuperCam: A 64 pixel heterodyne array receiver for the 350 GHz Atmospheric Window. In *Proceedings of the 20th International Symposium on Terahertz Space Technology*, Charlottesville.

[Gupta et al., 1996] Gupta, K., Grag, R., Bahl, I., and Bhartia, P. (1996). *Microstrip lines and Slotlines*. Artech House, Boston, London, 2nd edition.

[Güsten et al., 1998] Güsten, R., Ediss, G., Gueth, F., Gundlach, K., Hauschildt, H., Kasemann, C., Klein, T., Kooi, J., Korn, A., Kramer, I., LeDuc, R., Mattes, H., Meyer, K., Perchtold, E., Pilz, M., Sachert, R., Scherschel, M., Schilke, P., Schneider, G., Schraml, J., Skaley, D., Stark, R., Wetzker, W., Wiedenhover, H., Wongsowijoto, S., and Wyrowski, F. (1998). CHAMP: the Carbon Heterodyne Array of the MPIfR. In *Proceedings SPIE*, volume 3357, pages 167–177.

[Güsten et al., 2006] Güsten, R., Nyman, L. A., Schilke, P., Menten, K., Cesarsky, C., and Booth, R. (2006). The atacama pathfinder experiment

(apex) – a new submillimeter facility for southern skies. *A& A*, 454(2):L13–L16.

[Harris, 1990] Harris, A. I. (1990). Coherent and incoherent detection. In Kaldeich, B., editor, *Liege International Astrophysical Colloquia*, volume 29 of *Liege International Astrophysical Colloquia*, pages 165–169.

[Hartmann, 1904] Hartmann, J. (1904). Investigations on the spectrum and orbit of delta Orionis. *The Astrophysical Journal*, 19:268–286.

[Heaviside, 1893] Heaviside, O. (1893). *Electromagnetic Theory*. The Electrician, 1st edition.

[Hellwig et al., 1970] Hellwig, H., Vessot, R. F. C., Levine, M. W., Zitzewitz, P. W., Allan, D. W., and Glaze, D. J. (1970). Measurement of the unperturbed hydrogen hyperfine transition frequency. *IEEE Transactions on Instrumentation and Measurement*, 19(4):200–209.

[Hesper et al., 2017] Hesper, R., Khudchenko, A., Baryshev, A. M., Barkhof, J., and Mena, F. P. (2017). A high-performance 650-ghz sideband-separating mixer—design and results. *IEEE Transactions on Terahertz Science and Technology*, 7(6):686–693.

[Heyminck et al., 2012] Heyminck, S., Graf, U. U., Güsten, R., Stutzki, J., Hübers, H. W., and Hartogh, P. (2012). Great: the sofia high-frequency heterodyne instrument. *A& A*, 542:L1.

[Ho et al., 1994a] Ho, C.-H., Fan, L., and Chang, K. (1994a). New uniplanar coplanar waveguide hybrid-ring couplers and magic-t's. *IEEE Transactions on Microwave Theory and Techniques*, 42(12):2440–2448.

[Ho et al., 1994b] Ho, C.-H., Fan, L., and Chang, K. (1994b). New uniplanar coplanar waveguide hybrid-ring couplers and magic-t's. *IEEE Transactions on Microwave Theory and Techniques*, 42(12):2440–2448.

[Huggins, 1864] Huggins, W. (1864). On the spectra of some of the chemical elements. *Philosophical Transactions of the Royal Society of London*, 154:139–160.

[Hunt, 2012] Hunt, B. J. (2012). Oliver heaviside: A first-rate oddity. *Physics Today*, 65(11):48–54.

[infrared laboratories,] infrared laboratories. `https://www.irlabs.com`. Accessed:January 15th, 2023.

[Iqbal, 2012] Iqbal, M. (2012). *An Introduction To Solar Radiation*. Elsevier Science.

[Jansky, 1933] Jansky, K. G. (1933). Radio waves from outside the solar system. *Nature*, 132(3323):66–66.

[Johns, 2006] Johns, M. (2006). The Giant Magellan Telescope (GMT). In Stepp, L. M., editor, *Ground-based and Airborne Telescopes*, volume 6267, page 626729. International Society for Optics and Photonics, SPIE.

[Josephson, 1962] Josephson, B. (1962). Possible new effects in superconductive tunnelling. *Physics Letters*, 1(7):251–253.

[Kamerlingh Onnes, 1911] Kamerlingh Onnes, H. (Nov. 1911). The superconductivity of mercury. *Comm. Phys. Lab. Univ.*, (29):122–124.

[Kapteyn, 1909] Kapteyn, J. C. (1909). On the Absorption of Light in Space. *The astrophysical Journal*, 29:46.

[Kasemann et al., 2006] Kasemann, C., Güsten, R., Heyminck, S., Klein, B., Klein, T., Philipp, S., Korn, A., Schneider, G., Henseler, A., Baryshev, A., and Klapwijk, T. (2006). CHAMP+: a powerful array receiver for APEX. In *Proceedings SPIE*, volume 6275, pages 62750N–62750N–12.

[Kautz, 1978] Kautz, R. L. (1978). Picosecond pulses on superconducting striplines. *Journal of Applied Physics*, 49(1):308–314.

[Kautz, 1979] Kautz, R. L. (1979). Miniaturization of normal-state and superconducting striplines. (84).

[Kawamura et al., 2005] Kawamura, A., Mizuno, N., Yonekura, Y., Onishi, T., Mizuno, A., and Fukui, Y. (2005). Nanten2: A submillimeter telescope for large scale surveys at atacama. *Proceedings of the International Astronomical Union*, 235:275P.

[Kerr, 1999] Kerr, A. (1999). Suggestions for revised definitions of noise quantities, including quantum effects. *IEEE Transactions on Microwave Theory and Techniques*, 47(3):325–329.

[Kerr et al., 2014] Kerr, A. R., Pan, S.-K., Claude, S. M. X., Dindo, P., Lichtenberger, A. W., Effland, J. E., and Lauria, E. F. (2014). Development of the alma band-3 and band-6 sideband-separating sis mixers. *IEEE Transactions on Terahertz Science and Technology*, 4(2):201–212.

[Kerr et al., 2015] Kerr, A. R., Pan, S.-K., and Lyons, W. G. (2015). The

genesis of sis mixers - the legacy of john tucker in radio astronomy. In *2015 IEEE MTT-S International Microwave Symposium*, pages 1–4.

[Kerr and Randa, 2010] Kerr, A. R. and Randa, J. (2010). Thermal noise and noise measurements—a 2010 update. *IEEE Microwave Magazine*, 11(6):40–52.

[Kooi, 2008] Kooi, J. W. (2008). *Advanced receivers for submillimeter and far infrared astronomy*. PhD thesis, University of Groningen.

[Krabbe, 2000] Krabbe, A. (2000). Sofia telescope. In Melugin, R. K. and Roeser, H.-P., editors, *Airborne Telescope Systems*. SPIE.

[Lahiji et al., 2010] Lahiji, R. R., Sharifi, H., Katehi, L. P. B., and Mohammadi, S. (2010). 3-d cmos circuits based on low-loss vertical interconnects on parylene-n. *IEEE Transactions on Microwave Theory and Techniques*, 58(1):48–56.

[Landau and Ginzburg, 1950] Landau, L. D. and Ginzburg, V. L. (1950). On the theory of superconductivity. *Zh. Eksp. Teor. Fiz.*, 20:1064.

[Lea and Lichtenberger, 1996] Lea, D. and Lichtenberger, A. W. (1996). Progress on characterization with integrated test structures of dielectric and superconducting films for sis mixer circuits. *Seventh Int. Symposium on Space Thz Tech.*, pages 356–368.

[Li et al., 2021] Li, R.-Z., Wu, Z., Ji, J., Yin, X., Yan, J., Fang, Y., and Yu, Y. (2021). A wideband termination based on laser-scribed lossy microstrip line structures. *Applied Sciences*, 11(15).

[Lin and Wu, 2001] Lin, T.-H. and Wu, R.-B. (2001). Cpw to waveguide transition with tapered slotline probe. *IEEE Microwave and Wireless Components Letters*, 11(7):314–316.

[Linden et al., 1994] Linden, D., Orlando, T., and Lyons, W. (1994). Modified two-fluid model for superconductor surface impedance calculation. *IEEE Transactions on Applied Superconductivity*, 4(3):136–142.

[London et al., 1935] London, F., London, H., and Lindemann, F. A. (1935). The electromagnetic equations of the supraconductor. *Proceedings of the Royal Society of London. Series A - Mathematical and Physical Sciences*, 149(866):71–88.

[Lopez-Berrocal et al., 2009] Lopez-Berrocal, B., de Oliva-Rubio, J., and

Molina-Fernandez, I. (2009). Design and implementation of dc–20-ghz lumped resistor matched loads for planar microwave circuits. *IEEE Transactions on Microwave Theory and Techniques*, 57(10):2439–2443.

[Matthaei et al., 1980] Matthaei, G., Young, L., and Jones, E. (1980). *Microwave Filters, Impedance-matching Networks, and Coupling Structures.* Artech House microwave library. Artech House.

[Mattis and Bardeen, 1958] Mattis, D. C. and Bardeen, J. (1958). Theory of the anomalous skin effect in normal and superconducting metals. *Phys. Rev.*, 111:412–417.

[Maxwell, 1873] Maxwell, J. C. (1873). *A Treatise on Electricity and Magnetism.* Oxford,Clarendon press series, Londres, 1st edition.

[McKee and Ostriker, 1977] McKee, C. F. and Ostriker, J. P. (1977). Theory of the interstellar medium: three components regulated by supernova explosions in an inhomogeneous substrate. *Astrophysical Journal)*, 218:1.

[Mechanikwerkstatt, 2018] Mechanikwerkstatt, I. physikalishces Institut, U. z. K. (2018). Direct communication.

[Meissner and Ochsenfeld, 1933] Meissner, W. and Ochsenfeld, R. (1933). Ein neuer effekt bei eintritt der supraleitfähigkeit. *Naturwissenschaften*, (21):787–788.

[Mena and Barishev, 2005] Mena, P. and Barishev, A. (2005). Alma memo 513 - design and simulation of a waveguide load for alma-band 9. ALMA MEMO Series.

[Mirzaei et al., 2021] Mirzaei, B., Gan, Y., Finkel, M., Groppi, C., Young, A., Walker, C., Hu, Q., and Gao, J.-R. (2021). 4.7 thz asymmetric beam multiplexer for gusto. *Opt. Express*, 29(15):24434–24445.

[Monje et al., 2005] Monje, R., Vassilev, V., Pavolotsky, A., and Belitsky, V. (2005). High quality microstrip termination for mmic and millimeter-wave applications. In *IEEE MTT-S International Microwave Symposium Digest, 2005.*, pages 1827–1830.

[Nasa, 2008] Nasa (2008). Atmospheric window. `https://commons.wikimedia.org/wiki/File:Atmospheric_electromagnetic_opacity.svgl`. Original image by NASA, Vectorized by Wikipedia user Mysid, Accessed: March 7th, 2022.

[Niemack, 2016] Niemack, M. (2016). Designs for a large-aperture telescope to map the CMB 1x faster. *Applied Optics*, 55:1686.

[Pardo et al., 2001] Pardo, J., Cernicharo, J., and Serabyn, E. (2001). Atmospheric transmission at microwaves (atm): an improved model for millimeter/submillimeter applications. *IEEE Transactions on Antennas and Propagation*, 49(12):1683–1694.

[Payne, 1988] Payne, J. (1988). Multibeam receiver for millimeter-wave radio astronomy. *Review of Scientific Instruments*, 59(9):1911–1919.

[Personnel, 1973] Personnel, U. (1973). *Basic Electronics*. Dover Books on Electronics, Electricity, Electrical Engineering. Dover Publications.

[Pilbratt et al., 2010] Pilbratt, G. L., Riedinger, J. R., Passvogel, T., Crone, G., Doyle, D., Gageur, U., Heras, A. M., Jewell, C., Metcalfe, L., Ott, S., and Schmidt, M. (2010). Herschelspace observatory: An esa facility for far-infrared and submillimetre astronomy. *Astronomy and Astrophysics*, 518:L1.

[Pippard and Bragg, 1950] Pippard, A. B. and Bragg, W. L. (1950). Field variation of the superconducting penetration depth. *Proceedings of the Royal Society of London. Series A. Mathematical and Physical Sciences*, 203(1073):210–223.

[Pippard and Bragg, 1953] Pippard, A. B. and Bragg, W. L. (1953). An experimental and theoretical study of the relation between magnetic field and current in a superconductor. *Proceedings of the Royal Society of London. Series A. Mathematical and Physical Sciences*, 216(1127):547–568.

[Planck, 1901] Planck, M. (1901). Ueber das gesetz der energieverteilung im normalspectrum. *Annalen der Physik*, 309(3):553–563.

[Pozar, 2011] Pozar, D. (2011). *Microwave Engineering*. Wiley, New York, 4th edition.

[Reed and Wheeler, 1956] Reed, J. and Wheeler, G. (1956). A method of analysis of symmetrical four-port networks. *IRE Transactions on Microwave Theory and Techniques*, 4(4):246–252.

[Rida et al., 2009] Rida, A., Margomenos, A., and Tentzeris, M. M. (2009). Wideband mm-wave compensated 90° bends for grounded coplanar waveguide and microstrip transmission lines on flexible lcp substrates. In *2009 59th Electronic Components and Technology Conference*, pages 2000–2003.

[Riechers,] Riechers, D. [cii] 158 um line intensity mapping in the epoch of reionization. `http://www.ccatobservatory.org/docs/ccat-technical-memos/ccatp_im_v2.pdf`. Accessed: December 11th, 2023.

[Risacher et al., 2016] Risacher, C., Güsten, R., Stutzki, J., Hübers, H.-W., Bell, A., Buchbender, C., Büchel, D., Csengeri, T., Graf, U. U., Heyminck, S., Higgins, R. D., Honingh, C. E., Jacobs, K., Klein, B., Okada, Y., Parikka, A., Pütz, P., Reyes, N., Ricken, O., Riquelme, D., Simon, R., and Wiesemeyer, H. (2016). The upgreat 1.9 thz multi-pixel high resolution spectrometer for the sofia observatory. *A& A*, 595:A34.

[Risacher et al., 2017] Risacher, C., Güsten, R., Stutzki, J., Hübers, H. W., Büchel, D., Graf, U., Greiner-Baer, M., Heyminck, S., Honingh, C., Jacobs, K., , Klein, B., Pütz, P., Richter, H., Rothbart, N., and Ricken, O. (2017). The upGREAT THz heterodyne arrays for SOFIA: 1.9 THz and 4.7 THz first results. In *28th International Symposium on Space Terahertz Technology*, Cologne, Germany.

[Rybicki and Lightman, 1985] Rybicki, G. B. and Lightman, A. P. (1985). *Radiative Processes in Astrophysics*. John Wiley & Sons, Ltd, New York, 1st edition.

[Schuster et al., 2004] Schuster, K. F., Boucher, C., Brunswig, W., Carter, M., Chenu, J. Y., Foullieux, B., Greve, A., John, D., Lazareff, B., Navarro, S., Perrigouard, A., Pollet, J. L., Sievers, A., Thum, C., and Wiesemeyer, H. (2004). A 230 GHz heterodyne receiver array for the IRAM 30 m telescope. *Astronomy and Astrophysics*, 423(3):1171–1177.

[Shan et al., 2020] Shan, W., Ezaki, S., Kang, H., Gonzalez, A., Kojima, T., and Uzawa, Y. (2020). A compact superconducting heterodyne focal plane array implemented with hpi (hybrid planar integration) scheme. *IEEE Transactions on Terahertz Science and Technology*, 10(6):677–689.

[Shapiro, 1963] Shapiro, S. (1963). Josephson currents in superconducting tunneling: The effect of microwaves and other observations. *Phys. Rev. Lett.*, 11:80–82.

[Sieth et al., 2014] Sieth, M., Devaraj, K., Voll, P., Church, S., Gawande, R., Cleary, K., Readhead, A. C. S., Kangaslahti, P., Samoska, L., Gaier, T., Goldsmith, P. F., Harris, A. I., Gundersen, J. O., Frayer, D., White, S., Egan, D., and Reeves, R. (2014). Argus: a 16-pixel millimeter-wave spectrometer for the green bank telescope. In *Proceedings SPIE*, volume

9153, pages 91530P–91530P–12.

[Simon et al., 2019] Simon, R., Schneider, N., Bigiel, F., Ossenkopf-Okada, V., Okada, Y., Johnstone, D., Schilke, P., Stacey, G., Röllig, M., Sanchez-Monge, A., Seifried, D., Stutzki, J., Bertoldi, F., Buchbender, C., Fich, M., Herter, T., Higgins, R., and Nikola, T. (2019). Astro2020: The cycling of matter from the interstellar medium to stars and back.

[Simons, 2004] Simons, R. (2004). *Coplanar Waveguide Circuits, Components, and Systems*. Wiley Series in Microwave and Optical Engineering. Wiley, 1st edition edition.

[Simons, 2001] Simons, R. N. (2001). *Coplanar Waveguide Circuits, Components, and Systems*. John Wiley & Sons, Ltd.

[Slipher, 1912] Slipher, V. (1912). On the spectrum of the nebula in the Pleiades. *Lowell Observatory Bulletin*, 2:26–27.

[Slipher, 1911] Slipher, V. M. (1911). Peculiar star spectra suggestive of selective absorption of light in space. *Astronomische Nachrichten*, 189(1):5–8.

[Sunada et al., 2000] Sunada, K., Yamaguchi, C., Nakai, N., Sorai, K., Okumura, S., and Ukita, N. (2000). BEARS: SIS 25-beam array receiver system for the NRO 45-m telescope. In Butcher, H., editor, *Radio Telescopes*, volume 4015 of *Proc. SPIE 4015, Radio Telescopes*, pages 237–246.

[Swetz et al., 2011] Swetz, D. S., Ade, P. A. R., Amiri, M., Appel, J. W., Battistelli, E. S., Burger, B., Chervenak, J., Devlin, M. J., Dicker, S. R., Doriese, W. B., Dünner, R., Essinger-Hileman, T., Fisher, R. P., Fowler, J. W., Halpern, M., Hasselfield, M., Hilton, G. C., Hincks, A. D., Irwin, K. D., Jarosik, N., Kaul, M., Klein, J., Lau, J. M., Limon, M., Marriage, T. A., Marsden, D., Martocci, K., Mauskopf, P., Moseley, H., Netterfield, C. B., Niemack, M. D., Nolta, M. R., Page, L. A., Parker, L., Staggs, S. T., Stryzak, O., Switzer, E. R., Thornton, R., Tucker, C., Wollack, E., and Zhao, Y. (2011). Overview of the atacama cosmology telescope: Receiver, instrumentation, and telescope systems. *The Astrophysical Journal Supplement Series*, 194(2):41.

[Tielens and Hollenbach, 1985] Tielens, A. G. G. M. and Hollenbach, D. (1985). Photodissociation regions. II. A model for the Orion photodissociation region. *Astrophysical Journal*, 291:747–754.

[Tien and Gordon, 1963] Tien, P. K. and Gordon, J. P. (1963). Multiphoton

process observed in the interaction of microwave fields with the tunneling between superconductor films. *Phys. Rev.*, 129:647–651.

[Tinkham, 2004] Tinkham, M. (2004). *Introduction to Superconductivity*. Dover Publications.

[Tolpygo et al., 2018] Tolpygo, S. K., Bolkhovsky, V., Oates, D. E., Rastogi, R., Zarr, S., Day, A. L., Weir, T. J., Wynn, A., and Johnson, L. M. (2018). Superconductor electronics fabrication process with monx kinetic inductors and self-shunted josephson junctions. *IEEE Transactions on Applied Superconductivity*, 28(4):1–12.

[Tucker, 1979] Tucker, J. (1979). Quantum limited detection in tunnel junction mixers. *IEEE Journal of Quantum Electronics*, 15(11):1234–1258.

[Tucker and Feldman, 1985] Tucker, J. R. and Feldman, M. J. (1985). Quantum detection at millimeter wavelengths. *Rev. Mod. Phys.*, 57:1055–1113.

[Tyrrell, 1947] Tyrrell, W. (1947). Hybrid circuits for microwaves. *Proceedings of the IRE*, 35(11):1294–1306.

[Tyson, 2002] Tyson, J. A. (2002). Large synoptic survey telescope: Overview. In Tyson, J. A. and Wolff, S., editors, *Survey and Other Telescope Technologies and Discoveries*. SPIE.

[user Sch,] user Sch, W. Solar spectrum. `https://commons.wikimedia.org/wiki/File:EffectiveTemperature_300dpi_e.pngl`. Original spectrum by M. Iqbal: An Introduction to Solar Radiation Accessed: March 12th, 2022.

[van de Hulst, 1945] van de Hulst, H. C. (1945). Radiogolven uit het wereldruim: II. Herkomst der radiogolvenRadiogolven uit het wereldruim: II. Herkomst der radiogolvenRadio waves from space. *Nederlandsch Tijdschrift voor Natuurkunde*, 11:210–221.

[Van Duzer and Turner, 1981] Van Duzer, T. and Turner, C. (1981). *Principles of Superconductive Devices and Circuits*. Elsevier.

[Walker et al., 2001] Walker, C., Groppi, C., Golish, D., Kulesa, C., Hungerford, A., d'Aubigny, C. D., Jacobs, K., Graf, U., Martin, C., and Kooi, J. (2001). PoleStar: An 810 GHz Array Receiver for AST/RO. In *Proceedings of the 12th International Symposium on Space Terahertz Technology*, San Diego, California.

[Ward,] Ward, P. L. Planck's law. https://ozonedepletiontheory.info/ImagePages/plancks-law-frequency1/. Original image by Ozonedepletiontheory, Accessed: April 14th, 2022.

[Westig, 2013] Westig, M. P. (2013). Quantum limited balanced superconducting 380-520 ghz mixer on a silicon membrane and mesoscopic tunnel devices for terahertz frequencies.

[Wilkinson, 1960] Wilkinson, E. J. (1960). An N-Way Hybrid Power Divider. *IRE Transactions on Microwave Theory and Techniques*, 8(1):116–118.

[Williams, 2003] Williams, D. (2003). Large molecules in space? *Astronomy & Geophysics*, 44(6):6.14–6.21.

[Wilson et al., 1970] Wilson, R. W., Jefferts, K. B., and Penzias, A. A. (1970). Carbon Monoxide in the Orion Nebula. *Astrophysical Journal*, 161:L43.

[Wilson et al., 2009] Wilson, T. L., Rohlfs, K., and Hüttemeister, S. (2009). *Tools of Radio Astronomy*. Springer Berlin Heidelberg, New York, 5th edition.

[Wilson et al., 2013] Wilson, T. L., Rohlfs, K., and Hüttemeister, S. (2013). *Tools of Radio Astronomy*.

[Yassin and Withington, 1995] Yassin, G. and Withington, S. (1995). Electromagnetic models for superconducting millimetre-wave and submillimetre-wave microstrip transmission lines. *Journal of Physics D: Applied Physics*, 28(9):1983.

[Young et al., 2012] Young, E. T., Becklin, E. E., Marcum, P. M., Roellig, T. L., Buizer, J. M. D., Herter, T. L., Güsten, R., Dunham, E. W., Temi, P., Andersson, B.-G., Backman, D., Burgdorf, M., Caroff, L. J., Casey, S. C., Davidson, J. A., Erickson, E. F., Gehrz, R. D., Harper, D. A., Harvey, P. M., Helton, L. A., Horner, S. D., Howard, C. D., Klein, R., Krabbe, A., McLean, I. S., Meyer, A. W., Miles, J. W., Morris, M. R., Reach, W. T., Rho, J., Richter, M. J., Roeser, H.-P., Sandell, G., Sankrit, R., Savage, M. L., Smith, E. C., Shuping, R. Y., Vacca, W. D., Vaillancourt, J. E., Wolf, J., and Zinnecker, H. (2012). Early science with sofia, the stratospheric observatory for infrared astronomy. *The Astrophysical Journal Letters*, 749(2):L17.

[Yu et al., 2002] Yu, L., Newman, N., and Rowell, J. (2002). Measurement of the coherence length of sputtered nb/sub 0.62/ti/sub 0.38/n thin films.

IEEE Transactions on Applied Superconductivity, 12(2):1795–1798.

[Yu et al., 2005] Yu, L., Singh, R., Liu, H., Wu, S., Hu, R., Durand, D., Bulman, J., Rowell, J., and Newman, N. (2005). Fabrication of niobium titanium nitride thin films with high superconducting transition temperatures and short penetration lengths. *IEEE Transactions on Applied Superconductivity*, 15(1):44–48.

[Zheng and Walmsley, 2008] Zheng, X. H. and Walmsley, D. G. (2008). Temperature-dependent gap edge in strong-coupling superconductors determined using the eliashberg-nambu formalism. *Phys. Rev. B*, 77:104510.

[Zou et al., 2010] Zou, H., Zhang, H., Song, C., Wang, H., and Wang, P. (2010). Characterisation and modelling of mitered coplanar waveguide bends on silicon substrate. *International Journal of Electronics*, 97(6):715–727.

Acknowledgments

First of all, I want to thank Professor Dr Jürgen Stutzki for his support and for allowing me the opportunity to work in the development of superconducting devices. A Special thanks to Professor Dr. Lucas Labadie for co-reviewing my thesis and many thanks to Professor Dr. Thomas Michely for chairing the board of examiners and for teaching in Solid state physics.

A very special thanks to my supervisor Dr. Netty Honingh for the continuous support and guidance over the years and whose help was, and still, is invaluable.

A thunderous thanks to the Cleanroom crew: Dr. Karl Jacobs, Dr. Felix Münning, Michael Schulz and Stephan Wulff, who fabricated prepared and mounted the devices presented in this work. Thank you for your labor, because without it, this work could not have been done.

I would also like to thank Drs. Guevara, Kabanovic and Mertens for the help lent in preparing this document. This extends to Dr. Justen as well for his help dealing with the electronics and recording software.

I'm thankful to the people with whom I have shared these years, to Johanna Böhm for helping me in the constant battle against the German language and for all the coffees shared. To Craig Nicholas Yanitski, for helping me with the German bureaucracy.To Xiaodong Ren for his insight on Chinese cuisine and tea. A thank you to Cristian Guevara and Carolina Portilla, for the moments of national camaraderie shared and to Amalia Canes-Napoles for helping me detach myself a little from the world of physics

Financial support

This work is carried out within the Collaborative Research Centre 956, subproject D3,funded by the Deutsche Forschungsgemeinschaft (DFG)- project ID 184018867.

Teilpublikationen:

Konferenzbeiträge

- I.Barrueto et al. "CCAT-prime Heterodyne Instrument (CHAI) advances", In: *47th International Conference on Infrared, Millimeter and Terahertz Waves*. 2022
- I.Barrueto et al. "LO power division circuits for the CCAT-prime Heterodyne Array Instrument (CHAI)", *32nd IEEE International Symposium on Space THz Technology*, Baeza, Spain. 2022.
- I.Barrueto et al, "Superconductive devices for the CCAT-prime Heterodyne Array Instrument", *Physics and Chemistry of Star Formation: The Dynamical ISM Across Time and Spatial Scales-Proceedings of the 7th Chile-Cologne-Bonn-Symposium*, p:346-348. February 2023.

Eidesamtliche Erklärung zur Disseration

Hiermit versichere ich an Eides statt, dass ich die vorliegende Dissertation selbstständigund ohne die Benutzung anderer als der angegebenen Hilfsmittel und Literatur angefertigt habe. Alle Stellen, die wörtlich oder singemäß aus veröffentlichten und nichtveröffentlichten Werken dem Wortlaut oder dem Sinn nach entnommen wurden, sind alssolche kenntlich gemacht. Ich versichere an Eides statt, dass diese Dissertation noch keineranderen Fakultät oder Universität zur Prüfung vorgelegen hat; dass sie - abgesehen vonunten angegebenen Teilpublikationen und eingebundenen Artikeln und Manuskripten -noch nicht veröffentlicht worden ist sowie, dass ich eine Veröffentlichung der Dissertation vor Abschluss der Promotion nicht ohne Genehmigung des Promotionsausschussesvornehmen werde. Die Bestimmungen dieser Ordnung sind mir bekannt. Darüber hinauserkläre ich hiermit, dass ich die Ordnung zur Sicherung guter wissenschaftlicher Praxisund zum Umgang mit wissenschaftlichem Fehlverhalten der Universität zu Köln gelesen und sie bei der Durchführung der Dissertation zugrundeliegenden Arbeiten und derschriftlich verfassten Dissertation beachtet habe und verpflichte mich hiermit, die dortgenannten Vorgaben bei allen wissenschaftlichen Tätigkeiten zu beachten und umzusetzen.Ich versichere, dass die eingereichte elektronische Fassung der eingereichten Druckfassungvollständig entspricht.

Köln, den 18. Dezember 2023